Vol. 272, No. 1, February 1, 1993 ISSN 0003-2670

ANALYTICA CHIMICA ACTA

An international journal devoted to all branches of analytical chemistry

ELSEVIER

ANALYTICA CHIMICA ACTA

Scope. *Analytica Chimica Acta* publishes original papers, preliminary communications and reviews dealing with every aspect of modern analytical chemistry. Reviews are normally written by invitation of the editors, who welcome suggestions for subjects. Preliminary communications of important urgent work can be printed within four months of submission, if the authors are prepared to forego proofs.

Submission of Papers

Americas

Prof. Harry L. Pardue
Department of Chemistry
1393 BRWN Bldg, Purdue University
West Lafayette, IN 47907–1393
USA
Tel:(+1-317) 494 5320
Fax:(+1-317) 496 1200

Computer Techniques

Prof. J.T. Clerc
Universität Bern
Pharmazeutisches Institut
Baltzerstrasse 5, CH-3012 Bern
Switzerland
Tel:(+41-31) 654171
Fax:(+41-31) 654198

Other Papers

Prof. Alan Townshend
Department of Chemistry
The University
Hull HU6 7RX
Great Britain

Tel:(+44-482) 465027
Fax:(+44-482) 466410

Prof. Willem E. van der Linden
Laboratory for Chemical Analysis
Department of Chemical Technology
Twente University of Technology
P.O. Box 217, 7500 AE Enschede
The Netherlands
Tel:(+31-53) 892629
Fax:(+31-53) 356024

Prof. Paul Worsfold
Dept. of Environmental Sciences
University of Plymouth
Plymouth PL4 8AA
Great Britain

Tel:(+44-752) 233006
Fax:(+44-752) 233009

Submission of an article is understood to imply that the article is original and unpublished and is not being considered for publication elsewhere. *Anal. Chim. Acta* accepts papers in English only. There are no page charges. Manuscripts should conform in layout and style to the papers published in this issue. See inside back cover for "Information for Authors".

Publication. *Analytica Chimica Acta* appears in 14 volumes in 1993. The subscription price for 1993 (Vols. 267–280) is Dfl. 4214.00 plus Dfl. 462.00 (p.p.h.) (total approx. US$ 2816.75). *Vibrational Spectroscopy* appears in 2 volumes in 1993. The subscription price for *Vibrational Spectroscopy* (Vols. 4 and 5) is Dfl. 700.00 plus Dfl. 66.00 (p.p.h.) (total approx. US$ 461.50). The price of a combined subscription (*Anal. Chim. Acta* and *Vib. Spectrosc.*) is Dfl. 4592.00 plus Dfl. 528.00 (p.p.h.) (total approx. US$ 3084.25). All earlier volumes (Vols. 1–266) except Vols. 23 and 28 are available at Dfl. 259.50 (US$ 156.25), plus Dfl. 18.00 (US$ 10.75) p.p.h., per volume. The Dutch guilder price is definitive. The U.S. dollar price is subject to exchange-rate fluctuations and is given only as a guide. Subscriptions are accepted on a prepaid basis only, unless different terms have been previously agreed upon.
Our p.p.h. (postage, packing and handling) charge includes surface delivery of all issues, except to subscribers in the U.S.A., Canada, Australia, New Zealand, China, India, Israel, South Africa, Malaysia, Thailand, Singapore, South Korea, Taiwan, Pakistan, Hong Kong, Brazil, Argentina and Mexico, who receive all issues by air delivery (S.A.L.–Surface Air Lifted) at no extra cost. For Japan, air delivery requires 25% additional charge of the normal postage and handling charge; for all other countries airmail and S.A.L. charges are available upon request.

Subscription orders. Subscription orders can be entered only by calendar year and should be sent to: Elsevier Science Publishers B.V., Journals Department, P.O. Box 211, 1000 AE Amsterdam, The Netherlands. Tel: (+31-20) 5803 642, Telex: 18582, Telefax: (+31-20) 5803598, to which requests for sample copies can also be sent. Claims for issues not received should be made within six months of publication of the issues. If not they cannot be honoured free of charge. Readers in the U.S.A. and Canada can contact the following address: Elsevier Science Publishing Co. Inc., Journal Information Center, 655 Avenue of the Americas, New York, NY 10010, U.S.A. Tel: (+1-212) 6333750, Telefax: (+1-212) 6333990, for further information, or a free sample copy of this or any other Elsevier Science Publishers journal.
Advertisements. Advertisement rates are available from the publisher on request.

Detailed "Instructions to Authors" for *Analytica Chimica Acta* was published in Volume 256, No. 2, pp. 373–376. Free reprints of the "Instructions to Authors" of *Analytica Chimica Acta* and *Vibrational Spectroscopy* are available from the Editors or from: Elsevier Science Publishers B.V., P.O. Box 330, 1000 AH Amsterdam, The Netherlands. Telefax: (+31-20) 5862845.

US mailing notice – Analytica Chimica Acta (ISSN 0003-2670) is published biweekly by Elsevier Science Publishers (Molenwerf 1, Postbus 211, 1000 AE Amsterdam). Annual subscription price in the USA US$ 2816.75 (subject to change), including air speed delivery. Second class postage paid at Jamaica, NY 11431. *USA Postmasters*: Send address changes to Anal. Chim. Acta, Publications Expediting, Inc., 200 Meacham Av., Elmont, NY 11003. Airfreight and mailing in the USA by Publication Expediting.

ANALYTICA CHIMICA ACTA

An international journal devoted to all branches of analytical chemistry

(Full texts are incorporated in CJELSEVIER, a file in the Chemical Journals Online database available on STN International; Abstracted, indexed in: Aluminum Abstracts; Anal. Abstr.; Biol. Abstr.; BIOSIS; Chem. Abstr.; Curr. Contents Phys. Chem. Earth Sci.; Engineered Materials Abstracts; Excerpta Medica; Index Med.; Life Sci.; Mass Spectrom. Bull.; Material Business Alerts; Metals Abstracts; Sci. Citation Index)

VOL. 272 NO. 1 FEBRUARY 1, 1993

CONTENTS

(Continued overleaf)

Contents (continued)

ANALYTICA CHIMICA ACTA
VOL. 272 (1993)

ANALYTICA CHIMICA ACTA

An international journal devoted to all branches of analytical chemistry
Revue internationale consacrée à tous les domaines de la chimie analytique
Internationale Zeitschrift für alle Gebiete der analytischen Chemie

Anal. Chim. Acta, Vol. 272 (1993)

ELSEVIER, Amsterdam–London–New York–Tokyo

0003-2670/93/$06.00

Analytica Chimica Acta, 272 (1993) 1–40
Elsevier Science Publishers B.V., Amsterdam

Review

Light scattering and the absolute characterization of macromolecules

Philip J. Wyatt

Wyatt Technology Corporation, Santa Barbara, CA 93103 (USA)

(Received 11th June 1992; revised manuscript received 13th September 1992)

Abstract

Light scattering (LS) has returned to the arsenal of analytical chemists with an impact scarcely imaginable a decade ago. Several important developments have restored this absolute measurement technique to its present status. The advent of HPSEC (high-performance size exclusion chromatography) and a variety of other techniques for macromolecular separation were of particular significance in stimulating the application of low angle laser light scattering (LALLS) for the determination of polymer molecular weights, their averages, and their distributions. However, it has been the more recent introduction of on-line scattering measurements over a broad range of scattering angles (differential LS) that has permitted many important deductions of light scattering theory to be extracted and applied for the *first time*. These include determination of the mean square radius and its various averages, molecular conformation and structure, branching ratios, better characterizations of co-polymers, as well as those polymers soluble only at high temperatures. In addition, some instrumental broadening effects now may be measured directly. Tremendous advances in personal computers, together with flexible and versatile data collection and processing software, have played significant roles as well. This paper summarizes the theoretical basis of the measurements and presents some examples of the application of this theory for the deduction of molecular parameters from unfractionated polymer solutions. In passing, the operating principles of differential refractive index detectors (the most important and commonly used detection system for HPSEC) are described, as well as their importance to differential LS measurements. The general operating characteristics of modern LS detectors/photometers with their associated software and, most importantly, the combination of on-line LS detection and HPSEC separation is discussed with numerous examples of its analytical capabilities.

Keywords: Chromatography; Light scattering; Macromolecules

Since its early development by Einstein [1], Raman [2], Debye [3], Zimm [4,5], and others [6,7], the theory of light scattering from macromolecular solutions and suspensions has represented one of the major successes of chemical physics. Indeed, light scattering is one of the few *absolute* methods available for the determination of molecular mass and structure and certainly is applicable over the broadest range of molecular weights of any method. Until samples could be separated by HPSEC (more commonly called gel permeation [8] chromatography), however, these measurements produced only weight average molecular weights, M_w, and the corresponding z-average square radii $\langle r_g^2 \rangle_z$ together with the second virial coefficient, A_2. The ability to sort molecules one at a time by size for many years may have seemed as difficult as sorting molecules by speed, the latter feat postulated by Maxwell as being directed by a demon. This HPSEC "Maxwell's demon" has resulted in the ability to analyze the distribution of broadly polydisperse samples as well as to obtain details of branching

Correspondence to: P.J. Wyatt, Wyatt Technology Corporation, Santa Barbara, CA 93103 (USA).

and molecular conformations. Thus, weight, number, and z-average values for both mass and size may be obtained for most samples by combining light scattering and HPSEC. Included in such measurements is the ability to calculate both differential and cumulative distributions of the molecular weights and mean square radii. (Other types of liquid chromatography separation techniques, for example, those requiring mobile phase gradients, will not be discussed explicitly in this paper, though their combination with LS will result in similar capabilities.)

Naturally, there are some limitations to the tandem technique of light scattering and HPSEC. Theoretically, light scattering measurements may resolve size down to about a twentieth of the incident wavelength. For a given concentration c (g/ml), the scattered light signal is proportional to cM_w. Thus, for molecular weights below a few thousand, relatively high concentrations may be required in order that the molecules produce a detectable LS signal. In addition, the combined techniques require a parallel or serial determination of mass concentration for each eluting fraction. At high molecular weights and very low concentrations, conventional mass concentration detectors (based on measurement of refractive index change) have difficulty determining concentration values accurately. Finally, an accurate ancillary determination of the refractive index increment with molecular concentration, dn/dc, is required. For heterogeneous co-polymers, this quantity sometimes must be measured at each elution since it may be a function of molecular weight, while for polyelectrolytes, a tedious dialysis step is rigorously required for dn/dc determinations and is often overlooked. Nevertheless, even with these problems, light scattering certainly represents the most accurate and powerful detection technique for HPSEC, as well as for other separation methods. LS is absolute and does not require calibration of the columns. Conventional HPSEC, and companion viscometric techniques combined with HPSEC, require column calibrations, often with standards whose M_w values have been previously measured by LS!

It is important to mention briefly the state of experimental and theoretical conditions [9] that existed in the 1940s and 1950s. Electronic computers were virtually non-existent in those early years, at least by the standards we have today. The same was true of filters, high purity solvents, chart recorders and light sources. Lasers did not exist, so monochromatic light was generally obtained from mercury lamps equipped with optical filters, collimating optics and various neutral density filters. Zimm [10] and others developed particularly innovative instruments for making these measurements, although the Brice-Phoenix instrument developed by Brice, Halwer and Speiser [11] enjoyed the greatest commercial success. Later in the early 1960s, units developed by the French firm SOFICA (*Société Française d'instruments de controle et d'analysis*) enjoyed some commercial success and many are still used (complete with their mercury lamps!) today. The first laser-based system, developed by the author and his colleagues [12], was the *Differential I*, introduced in 1971 by Science Spectrum, Inc. Designed primarily to measure colloidal suspensions, it was rarely applied for determination of polymer molecular weights, except by Paul Bescher at Atlas Chemical (now ICI/America).

Light scattering measurements in the 1950s, therefore, were generally made using the best commercial production photomultiplier tubes available at the time (1P21), electronic circuitry based on vacuum tubes, and galvanometers to measure PMT output current. (In 1948, Zimm [10] used a cathode ray tube display with a preamplified signal to improve the precision of his readings. His instrument and electronics incorporated many unique innovations, but it was never commercialized. A graduate student who could take measurements in the middle of the night when municipal power was most stable generally completed the experimental apparatus. Since galvanometers were difficult to read (at each scattering angle) because of the inevitable presence of dust in the solvent, measurements were often required at high concentrations relative to those associated with the chromatographic separations of today.

Separations. The thought that a chromatographic process could separate polydisperse molecules by mass or size in the manner that the

gedanken Maxwell's demon separated molecules by speed was almost inconceivable. Yet, most theoretical developments were based on the assumption that molecular suspensions could be obtained that were monodisperse. Unraveling the actual size distribution of a polydisperse molecular solution was an extremely difficult and time-consuming procedure often involving weeks of careful fractionation by non-solvent addition to dilute polymer solutions or ultracentrifugation and very careful decanting [13]. This "deconvolution" was rarely performed. Instead, polydisperse samples were measured with light scattering techniques to yield weight average molecular weights and *z*-average [14] square radii. Until the discovery of anionic polymerization by Szwarc [15], truly monodisperse samples were not available. Viscometric measurements, on the other hand, measured viscosity averaged molecular weights and a hydrodynamic size. Attempts to derive distributions on the basis of such measurements were marginally successful. The enormous potentials of gel permeation HPSEC were yet to be developed.

In the next section, the salient features of the theory of light scattering from macromolecular solutions will be reviewed. Some of the instrumentation used during the past few decades is discussed briefly in the *Instrumentation* section together with brief descriptions of two classes of differential refractometers. The *Measurements* section is an exposition of light scattering measurements by reference to examples of experimental results and techniques. Particular emphasis is placed on the use of light scattering instrumentation as a HPSEC detector. The *Concluding Remarks* section summarizes new instrumentation and their capabilities, and discusses future directions for light scattering.

No presentation of light scattering and its relation to molecular characterization can ever be considered complete. Indeed, the discussion presented here is certainly oversimplified and, in many respects, quite cursory. However, it is the author's main objective in writing this monogram to demystify light scattering and encourage the reader to explore and exploit its potentials. There is no more fundamental means for measuring the mass of molecules than LS. It is a time-proven and absolute procedure that should be included among the tools of every physical, polymer, or biological scientist.

SOME THEORY

Following the treatment by Zimm [5], we consider first the scattering of light by a solution of essentially monodisperse molecules within a volume V. The molecular concentration is N and each molecule is assumed to consist of η segments. The probability of finding one such segment in a volume $d\tau$ at a distance r from another segment is, therefore,

$$\eta N\rho(r)d\tau/V \tag{1}$$

where $\rho(r)$ is the radial distribution function of the segments in the molecule (polymer). The excess Rayleigh ratio of the light scattered from a dilute suspension of such molecules (excess of scattering of the molecular solution above that scattered by the solvent itself, all divided by the incident intensity) is given by

$$R_\theta = \frac{K^*\eta^2N^2}{V^2}\int\rho(r)\,\exp(2\pi i\boldsymbol{s}\cdot\boldsymbol{r}/\lambda d)\tau \tag{2}$$

where θ is the angle between the incident and scattered rays, $\boldsymbol{s}$ the vector difference between unit vectors in the directions of the incident and scattered rays, and λ is the wavelength of the incident light in the solvent of refractive index $n_0(\lambda = \lambda_0/n_0)$. The integration is over all orientations as well as magnitudes of $\boldsymbol{r}$ at constant $\boldsymbol{s}$.

The physical constant K^* for vertically polarized incident light is given by

$$K^* = 4\pi^2(dn/dc)^2n_0^2/(N_a\lambda_0^4) \tag{3}$$

where n_0 is the refractive index of the solvent, N_a is Avogadro's number, λ_0 the vacuum wavelength of the incident light, and dn/dc is the refractive index increment of the solution. Note that the concentration c (g/ml) $= NM/VN_a$, where M is the molecular weight of the molecule. The incident light is assumed vertically polarized with respect to the plane containing the incident and scattered rays, i.e. measurement of scattered light is confined to a plane. The $1/\lambda_0^4$ scattering dependence was derived originally by Rayleigh who

showed also that the blueness of the sky was due to the preferential scattering of the shorter wavelengths.

It is important to stress that Eq. (2) is the Born or, more familiarly, Rayleigh-Gans-Debye (RGD), *approximation*. In this approximation, the incident wave is considered essentially unaffected by the scattering molecule. In formal terms, the theory is only valid when

$$|m-1| \ll 1 \text{ and } 2ka|m-1| \ll 1 \qquad (4)$$

where $2a$ is a characteristic diameter of the molecule, m is the refractive index of the solvated molecule relative to that of the solvent ($m = n/n_0$), and $k = 2\pi n_0/\lambda_0$. These two inequalities correspond, respectively, to the conditions that the molecular refractive index is almost indistinguishable from the refractive index of the solvent and the total phase shift of the incident light wave as it passes through the molecule is negligible. On this basis, each element of the molecule is treated as a simple dipole scatterer whose excitation and scattering is independent of any other element of the molecule. For most molecules in solution, these conditions are generally satisfied. The net scattering by the molecule into the direction θ is calculated by summing over each element per Eq. (2) including, thereby, the differences in phase between the excitations of these elements [16,17]. Figure 1 shows a greatly simplified view of a large single polymer molecule confined to a plane illuminated by a plane wave whose maximum amplitudes at a particular moment are indicated by the horizontal lines. The incident wave and the scattered wave (into the θ-direction) are in the directions indicated by the unit vectors $\boldsymbol{i}$ and $\boldsymbol{j}$, respectively. Note that $\boldsymbol{s} = \boldsymbol{i} - \boldsymbol{j}$. Since $\boldsymbol{i}$ and $\boldsymbol{j}$ are vectors of unit length, the *magnitude* of $\boldsymbol{s}$ is just $2 \sin \theta/2$ (from the law of cosines). The form of the intensity distribution function [see Eq. (6), below] is also displayed.

Following Zimm [5], the probability of finding a segment at a distance r from another reference segment in its vicinity is defined by Eq. (1). However, even for very dilute systems, this probability must be divided into two parts: internal and external. The *internal* probability refers to the two segments being in the *same* molecule, while the

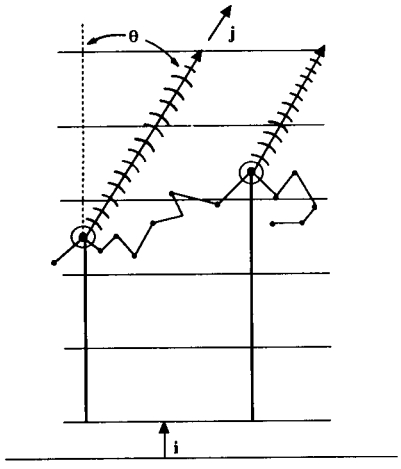

$$P(\theta) = \frac{1}{(N+1)^2} \sum_i \sum_j \frac{\sin \mu r_{ij}}{\mu r_{ij}}, \text{ where}$$

$$\mu = \frac{4\pi n_0}{\lambda_0} \sin(\theta/2) = 2k \sin(\theta/2)$$

r_{ij} = distance between pairs of $N+1$ elements of polymer.

Fig. 1. Scattering of a plane wave from a large macromolecule in the RGD approximation.

external probability refers to the segments being in two separate molecules, i.e.

$$\frac{\eta N \rho(r) d\tau}{V} = \left[\rho_1(r) + \frac{N\rho_2(r)}{V}\right] \eta d\tau \qquad (5)$$

These two probability elements contribute to the Rayleigh ratio, R_θ, of Eq. (2). The *internal* part (i.e. that involving the term ρ_1) may be represented [5] in terms of the normalized intensity distribution function, $P(\theta)$, defined by

$$P(\theta) = \int \rho_1(r) \exp(2\pi i \boldsymbol{s} \cdot \boldsymbol{r}/\lambda) d\tau \qquad (6)$$

In an earlier paper [18], Zimm postulated that two thread-like molecules (random coils) most commonly interact with each other at only one point (the "single contact" assumption). In addition, he considered the limit of very high dilutions which would lead to an expression for light scattering correct to second order in the concentration. On this basis, he was able to show that the *external* part would contribute to the scattering as

$$\int \rho_2^*(r) \exp\left(\frac{2\pi i \boldsymbol{s} \cdot \boldsymbol{r}}{\lambda}\right) d\tau = \eta^2 X P^2(\theta) \qquad (7)$$

where $\rho_2^*(r)$ is the limit of $\rho_2(r)$ as $c \to 0$ and X is an integral representing the short range interaction between pairs of segments. Combining Eqs. (2), (5), (6), and (7) leads to the very important relation

$$R_\theta = K^* McP(\theta)[1 - 2A_2 MP(\theta)c] \quad (8)$$

to order c^2 and noting that the second virial coefficient $A_2 = -N_a\eta^2 X/(2M^2)$. If more than a single molecular weight is present in the solution, then the symbol M must be replaced by M_w, the *weight* averaged molecular weight. Equation (8) was further extended to third order in the concentration (again, assumed vanishingly small by Zimm) by including the *third* virial coefficient A_3 and an additional external contribution to the variation of scattered light $Q(\theta)$ by the expression:

$$R_\theta/(K^*c) = MP(\theta)[1 - 2A_2 MP(\theta)c] + M^2P^2(\theta)[4A_2^2 MP^2(\theta) + 3A_3 Q(\theta)]c^2 \quad (9)$$

In the limit as $\theta \to 0$, both $P(\theta)$ and $Q(\theta) \to 1$. Although the function $P(\theta)$ has been evaluated explicitly for certain simple molecular structures, the actual functional dependence of $Q(\theta)$ for such structures has never been developed.

The excess Rayleigh ratio, R_θ, of light scattered from a small volume V into a detector set at an angle θ with respect to the direction of the incident light beam and collecting light scattered into a solid angle $d\Omega_\theta$ may be expressed in terms of *measurements* of scattered light intensities.

$$R_\theta = f[I(\theta) - I_s(\theta)]/I_0 \quad (10)$$

where $I(\theta)$ is the intensity of scattered light measured from the sample, $I_s(\theta)$ is the intensity of scattered light measured from the pure solvent, I_0 is the incident light intensity per unit projected area of V, and f is an absolute calibration constant derived from the geometry of the experimental apparatus. The detected intensity values include corrections for the finite solid angle $d\Omega_\theta$ subtended by the detector at θ, the variation of the volume element "seen" by the detector due to foreshortening, and the electronic gain (for the case of multiple detectors) of the detector. In general, f will be a function of n_s, the refractive index of the solvent and may depend also on the scattering cell refractive index, structure, and geometry. For the special refraction cell used in the DAWN® instruments (see *Light scattering photometers* in the *Instrumentation* section), the calibration constant f is proportional [19] to $n_s n_g$, where the refractive index of the solvent and cell glass are n_s and n_g respectively. For scattering cells of cylindrical symmetry, the calibration constant may be shown to be proportional to n_s^2. Further discussions may be found in references 20 and 21. Factors contributing to these correction terms include the cell and solvent refractive indices and various Fresnel reflection coefficients at each surface. Effects of the detector field of view and geometrical terms relating to the distances of the various elements from the central scattering volume are generally included in the normalization coefficients corresponding to each angle, θ. Note that conventional instrumentation [comprised of a collimated detector(s) viewing the volume element V] may not compensate directly for the volumetric foreshortening associated with the variation of the contributing scattering volume with scattering angle. A single detector collecting all light scattered from V into the solid angle $d\Omega$ at $\theta = 90°$, for example, would collect (to first order) light scattered at the angle θ from an associated volume $V/\sin\theta$. At very small scattering angles (below, say 15°), this first order correction may be inadequate and higher terms must be introduced. Variations of scattered light collected per Eq. (10) as a function of angle must be corrected during the subsequent data processing to compensate for such foreshortening effects in order that the derived molecular parameters retain their accuracy and that data collected at all scattering angles be usable.

As mentioned above, for certain molecular conformations, the variation of scattered light with angle, $P(\theta)$, may be written in closed form. Debye [22] and Zimm, Stein and Doty [6] showed, for example, that for a random coil molecule, Eq. (6) reduces to

$$P(\theta) = 2(e^{-u} - 1 + u)/u^2 \quad (11)$$

where

$$u = (2k^2/3)b^2\eta \sin^2\theta/2 = \mu^2 b^2 \eta/6 \quad (12)$$

$k = 2\pi n_0/\lambda_0$, $\mu = 2k \sin \theta/2$ and b is a constant depending on the architecture of the molecule. The random coil model assumes that the distribution of molecular segments is Gaussian with respect to the molecular center of mass.

Although this model is very often used to describe a variety of molecules in theta solvents, it is only an approximation and will yield erroneous results if not corrected. On the one hand, the assumption of a Gaussian probability distribution requires that the number of segments be very large and that there are no interactions between them. In addition, the simple model makes no provision for excluded volume effects [23] (links cannot pass through each other) or hindered rotations [24] (links are attached and are not free to rotate unrestrictedly). As the molecular weight falls below that of a few hundred monomers, the molecular structure departs significantly from this random coil model.

The integration of Eq. (6) over some other molecular structures is readily performed to yield, for example:

For a thin rod of length l

$$P(\theta) = \frac{1}{z}Si(2z) - (\sin z/z)^2 \tag{13}$$

where

$$z = kl \sin \theta/2 = \mu l/2 \tag{14}$$

and $Si(x)$ is the sine integral function $\int_0^x \frac{\sin\mu}{\mu} d\mu$

For a sphere of radius a

$$P(\theta) = \left[3(\sin u - u \cos u)/u^3\right]^2 \tag{15}$$

where

$$u = a\mu = 2ka \sin \theta/2 \tag{16}$$

The general form [22] of $P(\theta)$ is

$$P(\theta) = 1 - \alpha_1(2k \sin \theta/2)^2 + \alpha_2(2k \sin \theta/2)^4 - \ldots \tag{17}$$

where

$$3\alpha_1 = (1/V)\int r^2 dV = (1/M)\int r^2 dM = \langle r_g^2 \rangle \tag{18}$$

and the α_n are higher order coefficients proportional to $\int r^{2n} dM$. Note that Eq. (18) is the z-average square radius [13] in the event that a distribution of molecular sizes is present. [See Eq. (64).] Mijnlieff and Coumou [25] have presented an excellent discussion of these higher moments. A discussion concerning the limiting values of $\langle r_g^2 \rangle$ derivable from LS measurements may be found in reference 26.

Alternatively, the integral in Eq. (18) may be used to *define* the so-called *mean square radius*. The integration is over the mass elements of the molecule with respect to the *center of gravity* of the molecule. Thus, each mass element dM of the molecule is weighted by the *square* of its distance from the molecule's center of gravity r^2 and the quantity integrated over all the mass elements. For the simple case of a homogeneous sphere

$$\langle r_g^2 \rangle = \frac{3 \cdot 4\pi}{4\pi a^3}\int_0^a r^4 dr = \frac{3a^5}{5a^3} = \tfrac{3}{5}a^2 \tag{19}$$

The root mean square radius $\langle r_g^2 \rangle^{1/2}$ is often called the "*radius of gyration*," a misnomer that began to appear in the literature in the 1950s. The subscript "g," referring to integration with respect to the center of *gravity*, has been mistakenly associated with the kinematic term "gyration." The radius of gyration refers to the rotation about an axis fixed in space. Thus, any object has an infinite number of radii of gyration as there are an infinite number of axes fixed in space about which a molecule may be rotated. In the simplest case of a homogeneous sphere with an axis passing through its center of gravity, the *radius of gyration* squared with respect to this axis is

$$\langle r_G^2 \rangle = \frac{1}{M}\int r^2 \sin^2 \theta dM = \frac{1}{V}\int r^2 \sin^2\theta dV = \frac{2\pi}{4/3\pi a^3}\int_0^a r^4 dr \int_0^\pi \sin^3 \theta d\theta = 2a^2/5 \tag{20}$$

Contrast this result with that of Eq. (19)! Most articles and books use Debye's definition, Eq. (18), but once in a while, for the case of spheres, those unfamiliar with the definition of Eq. (18) will inadvertently use Eq. (20).

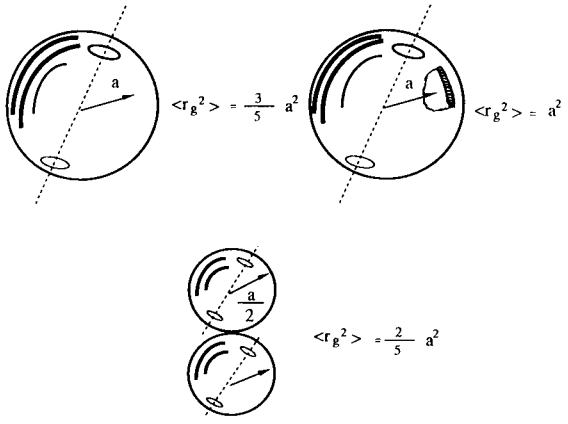

Fig. 2. The mean square radii for three different spherical structures with the same end-to-end dimensions.

Figure 2 presents the geometry and associated mean square radii of three configurations whose effective hydrodynamic radius, or end-to-end size, is the same: a homogeneous sphere, a spherical shell, and an aggregate of two spheres. The maximum dimension of each of these units is $2a$, where a is the radius of the large sphere and the spherical shell. Note that the root mean square radius ("radius of gyration") is quite different for each of these structures, yet their "hydrodynamic" radii are comparable. The root mean square radius thus depends on the internal mass distribution of the molecules and is not generally a measure of the molecule's external geometry. For certain linear molecules, the mean square radius is proportional to the square of the molecule's mean diameter (hydrodynamic diameter). Generally, this is not the case.

Debye's general result was anticipated by Guinier [27] who showed that in the limit as

$$\begin{aligned}&(2k \sin \theta/2)^2\langle r_g^2\rangle = \mu^2\langle r_g^2\rangle \to 0,\\ &P(\theta) \to 1 - (2k \sin \theta/2)^2\langle r_g^2\rangle/3 \\ &\quad = 1 - \mu^2\langle r_g^2\rangle/3\end{aligned} \tag{21}$$

independent of the molecule's shape or conformation. Thus, measurement of the angular variation (slope) near $\theta = 0$ of the Rayleigh ratio, Eq. (10), should permit deduction of the molecular z-average size in the limit of small concentration, c. Of course, the Guinier relation is included in Debye's more general result, Eq. (18). For the case of a random coil and in the limit as $\mu^2\langle r_g^2\rangle \to 0$, Eq. (11) may be expanded for small u to yield

$$\begin{aligned}P(\theta) &= 2(e^{-u} - 1 + u)/u^2\\ &\approx \frac{2}{u^2}\left(1 - u + \frac{u^2}{2!} - \frac{u^3}{3!} - 1 + u\right)\\ &\approx \left(1 - \frac{u}{3}\right)\\ &\approx 1 - \frac{\mu^2 b^2 \eta}{6 \cdot 3}\end{aligned} \tag{22}$$

Comparing this limit with the Guinier result, Eq. (21), yields

$$\frac{b^2\eta}{6} = \langle r_g^2\rangle \tag{23}$$

Equation (23) relates the molecular chain of η segments and characteristic dimension b to the z-average (or mean) square radius given by Eq. (18). However, because of the excluded volume and hindered rotation effects discussed earlier, this relation must be interpreted with caution.

In Zimm's analysis, he considered the higher order contributions by Eq. (5) to Eq. (2) through Eq. (9) since, as has been mentioned earlier, light scattering from solutions of higher concentrations could be measured more easily. For the case of HPSEC measurements, however, where column operating conditions invariably result in very low concentrations at the light scattering detector, Eq. (8) may be considered a practical starting point for the deduction of molecular characteristics from light scattering measurements on such samples. Nevertheless, even for such vanishingly small concentrations, Zimm [5] warned that the approximation in the derivation of Eq. (8) that was most likely to have a serious effect was the single contact approximation. Obviously, for very long and highly coiled molecules this approximation may fail. Zimm suggested that more involved analyses than his (!) or experiments themselves might show the magnitude of the deviations from the approximation. To date, there have been no such analyses or experiments reported.

Equation (9), or its simpler form Eq. (8), relates the unknown (to be determined) quantities on the right to the measured quantities on the left. Implicit within $P(\theta)$ are the Debye coefficients α_1, ..., α_n of Eq. (17). Similar expansions would be expected for $Q(\theta)$, as well. The *analytical* solution of Eq. (8), therefore, would consist of making a series of measurements over a range of scattering angles, θ_i, and (vanishingly small) concentrations, c_j, and then finding a least squares fit (global fit) to the parameters on the right-hand side. Letting

$$Y_{ij} = R(\theta_i)/[K^* c_j] \tag{24}$$

the quantities $R(\theta_i) \equiv R_{\theta i}$ are easily measured per Eq. (10). Historically, the measurements at different θ were made using a scanning photometer of the type developed by Zimm [10] or Brice et al [11]. More recently, photometers [19] containing a fixed array of 15 to 18 detectors (e.g. DAWN®) make such measurements almost simultaneously. The unknowns on the right-hand side of Eq. (8) are M, the weight average molecular weight, A_2, the second virial coefficient, and the coefficients α_1, α_2, ... Implicit in α_1, of course, is the most important mean square radius $\langle r_g^2 \rangle$ per Eq. (18). For small molecules ($r_g < 30$ nm), generally only terms through α_1 are required for $P(\theta)$. As the molecular weight (and size) increases, contributions from terms α_2 and higher may be required. An ideal analytical program will select automatically the order necessary to fit the data. When the addition of higher order terms does not improve the precision of the resulting parameters, then no further approximations need be considered. The conformation of the molecules also affects the selection of the angular expansion. Thus for rodlike molecules, weights as low as 200 kilodalton may require inclusion of 2nd order items in $\sin^2 \theta/2$ for the accurate characterization of data collected at larger scattering angles.

An alternative analytical method was developed by Mijnlieff and Coumou [25]. They begin with the assumption that the molecules are random coils whose scattering function is described by Eq. (11). After finding a best fit to this model, they then introduce a perturbation procedure to correct the coefficient of the linear term of the random coil model to improve the fit to the data for *all angles*. However, when Zimm and his colleagues began making measurements, they did not have the great variety of computer hardware available today. They resorted instead to using certain geometrical constructions and extrapolations to obtain their final results. In particular, Zimm began by considering the *reciprocal* of Eq. (8), *viz.*

$$\begin{aligned}\xi_{ij} = 1/Y_{ij} &= K^* c_j / R(\theta_i) \\ &= \frac{1}{MP(\theta_j)} + 2A_2 c_j - \left[3A_3 Q(\theta_i) \right. \\ &\quad \left. - 4MA_2^2 P(\theta)\{1 - P(\theta_i)\}\right] c_j^2 \end{aligned} \tag{25}$$

At very low concentrations, this may be approximated by the more familiar form

$$\xi_{ij} = \frac{1}{MP(\theta_i)} + 2A_2 c_j = \frac{P^{-1}(\theta_i)}{M} + 2A_2 c_j \tag{26}$$

The chief advantage of Eq. (26) over Eq. (8) is that $P^{-1}(\theta)$ has a greater range of linearity with respect to $\sin^2 \theta/2$. From a *geometrical* point of view, Zimm chose to solve Eq. (26) by means of a double extrapolation to zero scattering angle and zero concentration. We shall return to his formulation presently, but first let us examine Eq. (8) in the Guinier limit, Eq. (22), and show how extrapolations of the data to zero concentration and scattering angle will permit the extraction of the molecular parameters. We shall assume, furthermore, that the molecular suspensions are not generally monodisperse, in which case we replace M by its weight averaged value M_w.

For small $x = (4\pi n_0/\lambda_0)^2 (\sin \theta/2)^2 \langle r_g^2 \rangle /3$, Eq. (8) becomes

$$R_\theta/(K^* c) \approx M_w(1 - x) - 2A_2 M_w^2 c \tag{27}$$

where terms of order xc and x^2 are assumed negligible.

When Eq. (8) was developed by Zimm, it was not practical to solve it numerically by non-linear regression techniques. Noting that $x \to 0$ as $\theta \to 0$, and therefore

$$\lim_{\theta \to 0} R_\theta/(K^* c) = M_w[1 - 2A_2 M_w c] \tag{28}$$

one can extrapolate the data points $R_\theta/(K^*c)$ numerically to obtain the value

$$y_0 = R_0/(K^*c) \text{ at } \theta = 0 \tag{29}$$

where R_0 is the zero angle extrapolated value of R_θ. From this value, Eq. (28) may be solved for M_w to yield

$$M_w = 2y_0/\left(1 + \sqrt{1 - 8A_2cy_0}\right) \tag{30}$$

In the further limit as $c \to 0$, Eq. (30) yields

$$M_w = y_0 + 2A_2cy_0^2 \tag{31}$$

to order c. If the more exact formulation of Eq. (8) is to be fitted, then higher terms must be included to account for the non-linear behavior of measurements of $R_\theta/(K^*c)$ at larger scattering angles.

As mentioned earlier, Zimm noted that Eq. (8) could be extrapolated linearly over a broader range of x and c by considering the expansion of $P^{-1}(\theta)$ to order x

$$\xi = K^*c/R_\theta \approx (1+x)/M_w + 2A_2c \tag{32}$$

when $x \ll 1$ and $2A_2M_wc \ll 1$. Although this approach permits more linear extrapolation in a geometrical sense, it has some shortcomings from an analytical point of view. In particular, Eq. (32) must be applied only when K^*c/R_θ is linear in x and c. This means that data that depart from linearity (higher angle scattering for many classes of molecules) cannot be included in the analysis. If, instead of using Eq. (32), we select a more general polynomial expansion of $P^{-1}(\theta)$, for example, following Debye's Eq. (17), then a least squares fit to a similar generalization of Eq. (8) should produce comparable *analytical* results. Indeed, for high molecular weights, the precision of the intercept ($\theta = 0$, $c = 0$) of Eq. (32) begins to deteriorate significantly since the extrapolated value of K^*c/R_θ is restricted to an ever decreasing range on the ordinate axis.

For very large molecules of non-Gaussian (i.e. *not* random coil) structure, there is another problem associated with using Eq. (26): $P(\theta)$ can become zero or vanishingly small. For example, for spherical molecules, $P(\theta)$ will be zero [see Eq. (15)] whenever $\sin u = u \cos u$. As the size of a spherical molecule increases, this behavior becomes more noticeable. Thus, Eq. (26) cannot be treated *analytically* for all angles in such cases, while there are no such restrictions for Eq. (8). Equation (32) is certainly a useful, valid formulation for most molecules with weights below about 10^6 so long as there are no noticeable departures from linearity at larger scattering angles. If such departures are evident, then the large angle data cannot be used in the formulation of Eq. (32). If all the data are to be used [i.e. $P(\theta)$ will be expanded to include higher order terms], then Eq. (26) must be used instead with the earlier caveats that very small values of $P(\theta)$ be handled appropriately. If non-linear variations in scattering data are observed with changes in *concentration*, then Eq. (8) must be extended to include contributions of the third virial coefficient A_3 and terms to order c^3. However, a word of caution is required. Recall that Eq. (8) was developed by Zimm [5] for the case of vanishingly small concentrations and single point contact (if any) between molecules, generally satisfied in the chromatographic separation process to be discussed later. If the concentration becomes too great, then the additional terms required to characterize fully the light scattering process become very complex and difficult to describe in quantitative terms. The *detection* of such regions of too great a concentration from the light scattering measurements is straightforward, so that experiments should be repeated using lower concentrations to avoid the need to introduce such higher terms. Possible failure of the single contact approximation was discussed earlier.

Returning to Eq. (32) and setting $\xi = K^*c/R_\theta$, then in the limit as $\sin^2\theta/2 \to 0$,

$$\frac{d\xi}{d[\sin^2(\theta/2)]} = \frac{1}{M_w}\frac{4k^2}{3}\langle r_g^2\rangle \tag{33}$$

and, in the limit as $c \to 0$

$$\frac{d\xi}{dc} = 2A_2 \tag{34}$$

Thus, by examining the slope near $\sin^2(\theta/2) = 0$ of the graphically extrapolated zero concentration variation, one may derive the z-average square radius from Eq. (33). The reciprocal weight

average molecular weight $1/M_w$ is calculated from the intercept of Eq. (32) in the limit as θ and $c \rightarrow 0$. The slope of the graphically extrapolated zero scattering angle variation near $c = 0$ yields the second virial coefficient per Eq. (34). Equation (33) is of particular significance because of its universal application to all molecular suspensions satisfying Eq. (4) and in the limit of very low concentration and scattering angle. It should be clearly evident that the $\langle r_g^2 \rangle$ of a molecular solution can generally be obtained (for sufficiently large molecules) *independent* of dn/dc, M_w, or even c (sufficiently small). This is true for all molecular species, including highly branched polymers and some types of co-polymers. All that is required is to have data collected at sufficiently small scattering angles so that Eq. (32) is valid. However, at sufficiently low concentrations, Eq. (8) shows that R_θ is directly proportional to $P(\theta)$. Thus dividing both sides of this simple proportionality by the values corresponding to a *fixed* angle θ (say 90°), the resultant equation

$$\frac{K^*c/R_{\theta_1}}{K^*c/R_\theta} = \frac{R_\theta}{R_{\theta_1}} \approx \frac{P(\theta)}{P(\theta_1)} \tag{35}$$

may be solved numerically to yield the best fit value for α_1 of the Debye expansion, Eq. (17), even if $P(\theta)$ must be expanded to a higher order (say, through α_2). Thus *all* angular data may be used to find a best fit $\langle r_g^2 \rangle$ value, independent of M and dn/dc (assumed constant). Although Eq. (35) shows this independence quite vividly, it is easy to see this same independence from Eqs. (33) and (32) in the limit of very small concentration and small angle. [Note that $1/M_w$ is just the extrapolated value of $\xi(\theta \rightarrow 0) = \xi_0$.]

The ability of light scattering techniques to determine a size-related parameter is of great importance for the determination of molecular conformation. Since r_g will be *proportional* to the geometrical size for linear molecules, a log–log plot of r_g versus M permits the extraction of such information. For spherical molecules (e.g. globulins), the radius is proportional to the cube root of the mass. Thus, measurement of averaged $M - r_g$ pairs for a set of relatively narrow mass distribution samples, will permit a plot of values yielding a line whose slope should be about 0.333. If the molecules are rods, we should derive a slope of unity, while for random coils in a good solvent, it should be between 0.5 and 0.6. Making such determinations becomes particularly simple when a sample has a sufficiently broad range of masses *and* can be separated, e.g. by HPSEC techniques (see the *HPSEC measurements* section). If good mass separation is not possible, then such a plot might yield the wrong conformation slope since each elution slice would itself contain a broad range of masses whose various weighted averages (were they measurable) would be different. This would be particularly true for the case of highly branched materials whose sizes vary negligibly over broad variations of mass.

With an appropriate software program (e.g. ASTRA®) (see the *On-line Zimm plots* section), $P(\theta)$ may be expanded (up to order x^5, if required) and Eq. (8) may be used to generate molecular weight and size parameters for each so-called eluant slice (c is fixed) immediately

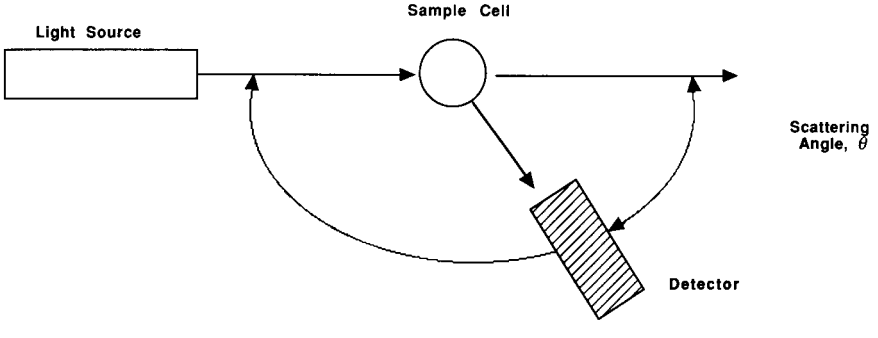

Fig. 3. Schematic representation of traditional light scattering measurement using a scanning goniometer.

following chromatographic separations. This formulation may yield more accurate results at very large molecular weights than Eq. (32) since it permits the incorporation of higher terms in x and the use of data collected at *all* angles. Alternatively, ASTRA will permit solution via a more general expansion [following Eq. (17)] of $P^{-1}(\theta)$ in Eq. (26). For very large molecular weights, Eq. (8) still remains the safest starting point for the *analytical* extraction of molecular parameters.

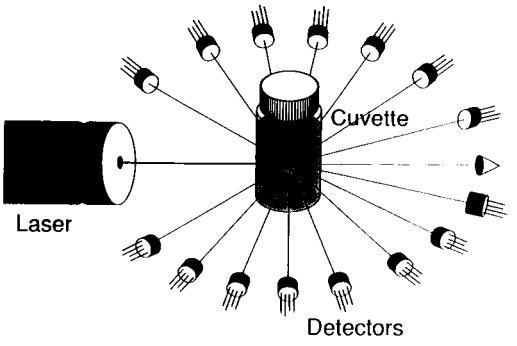

Fig. 4. Schematic representation of multidetector (DAWN) light scattering photometer.

INSTRUMENTATION

Light scattering photometers

Figure 3 presents a schematic representation of the traditional light scattering measurement using a single, collimated detector which moves in an arc about a sample-containing cuvette (scanning goniometer). It is the basic structure that was incorporated into the Zimm [10] instrument, the Brice-Phoenix [11], the SOFICA, and the *Differential I* [12] (the first laser-based system). This structure is still used in scanning goniometers incorporating immersion baths manufactured by Brookhaven Instruments, among others. Zimm's instrument provided for the sample to be immersed in a liquid whose refractive index was the same as the solvent, whereas the SOFICA design selected a liquid to match that of the glass vessel containing the sample. The Fresnel reflections at interfaces between medium discontinuities (for which immersion is supposed to help) do not seem as important as flaring effects caused by debris attached to the interface surfaces. Very clean cells are always the best hope to reduce stray light. In the earlier instruments designed before lasers were developed, the light source usually consisted of a collimated mercury arc lamp with filters to select the wavelength. As discussed briefly in the previous section, because of volumetric foreshortening, a sin θ normalization correction to the detected scattered intensity is usually required. Again, this correction is only valid to first order and may yield some error, especially at small angles. Because of beam flaring effects at the interfaces of the cell containing the sample, goniometers rarely can detect below about 25°. Other corrections, especially as they relate to the Brice-Phoenix instruments, are discussed in some detail by Utiyama [28]. Scanning goniometers represent a rather archaic type of design since all measurements are invariably made at a set of *fixed* angles. Further, because the scattering function $P(\theta)$ for molecules is a smoothly varying function of angle, any set of angles subtending the range required is as good as any other set. The $P(\theta)$'s are easily interpolated, so data between fixed angular locations may be extracted from the measurements at adjacent angles. Since light collection using multidetectors is far more rapid than sequential stopping, collecting, and then moving to the next angle, there are no compelling reasons to remain with single detector instruments for performing classical Zimm plots.

Figure 4 is the schematic representation of a multidetector system such as incorporated in the DAWN® (Wyatt Technology Corporation) instruments for their batch mode configuration. The collimated detectors are placed at fixed angles (θ) about the scattering volume alternating on either side of the sample cell. Since each detector may subtend a different solid angle at the central scattering volume (i.e. foreshortening and possibly different collimation apertures) and have slightly different gains, a more detailed approach is needed for *normalization* than the simple sin θ correction of the old scanning goniometers. In general, this is achieved by preparing solutions of known isotropic scatterers and multi-

plying the excess Rayleigh factors at each detector (scattering angle) by a suitable normalization constant to yield the same value as that measured at the 90° detector, the latter being set equal to unity. A solution of a monodisperse 5000 g/mole polymer provides a good scattering standard for this normalization procedure. More recently, normalization for cylindrically symmetric scattering cells has been achieved using special types of optical glass cylinders (e.g. Magic Glass™) whose Rayleigh ratios are large, yet whose scattering remains isotropic.

Absolute *calibration* of most instruments requires a detailed analysis of all geometrical factors involved as well as *measurement* of the illuminating intensity incident on the sample cell with the *same* detector that will make the scattering measurements. This latter determination is very difficult since the incident beam often must be attenuated by a factor of 10^5 or more and at very high precision. Geometrical considerations include accurate determinations of the field of view of the detector, corrections for refractive indices of cell and solvent, reflection contributions, etc. Kaye et al. [29,30], have described details of these difficult calculations for the single LALLS measurement which confirm the *absolute* nature of the light scattering measurement. On the other hand, the *measured* Rayleigh ratios of pure solvents (e.g. toluene or cyclohexane) themselves may be used as a simpler starting point. Once an instrument has been calibrated with a *single* solvent, the Rayleigh ratio of any other solvent may be determined [19,20] absolutely provided its refractive index is known and the effects of stray light removed. Thus, the calibration constant for the light scattering instrument becomes a relatively simple function of the refractive index of the solvent n_s, the cell and detector geometry, and the cell refractive index n_g. Once calibrated with a single pure solvent, the calibration constant for any other solvent and/or cell geometry may be calculated. Alternatively, a narrow standard (e.g. polystyrene) may be purchased from one of several suppliers (e.g. Pressure Chemical Co., Polymer Standards Service, Scientific Polymer Products, etc.) and then measured in a particular cell and solvent. Thereafter, the *measured* value may be used for subsequent calibrations or to check calibration reproducibility. Invariably, a major source of calibration inconsistency is due to contaminated solvents. Calibration procedures based on using such pure (HPLC grade) solvents are, therefore, a useful means for checking solvent purity. If, for example, a calibration based on the 90° scattering of toluene in a glass cell of refractive index n_g has been used, then measurement of the ratios I_{90}/I_0 for other solvents such as benzene, acetone, water, etc. multiplied by the calibration constant $f(n_{\text{toluene}},n_s,n_g)$ should yield the correct corresponding Rayleigh ratios. Although LALLS type detectors are generally calibrated by direct measurement of the ratio I_θ/I_0 with the single photomultiplier detector, this determination requires extensive calibration of the highly attenuating neutral density filters required to measure I_0 directly. Since attenuations greater than 10^6 may be required, the precision of the I_0 measurements may be somewhat limited. After including the geometrical factors, the LALLS absolute calibration coefficient may then be calculated. The tedious process doesn't stop there. The scattering cell itself must be moved to search for a "spot" of minimal stray light.

Because the light scattering techniques of Zimm discussed in the previous section were developed for use in the limit of small scattering angles and low concentrations, attempts have been made to develop instruments that could attain these limits directly. The Chromatix series of instruments pioneered by Kay and his coworkers [29,30] at Beckman Instruments and refined by Chromatix Corporation staff (for some years a subsidiary of Milton Roy) incorporated a low angle measurement capability by means of specially designed cells and stops. With a single measurement at a scattering angle of about 4°, Eq. (32) requires no extrapolation, since $\sin^2 \theta/2 \approx 1.2 \times 10^{-3}$ and one might, therefore, set $R_{0°} \rightarrow R_{4°}$. Thus, x also is set = 0, and the result is

$$K^*c/R_0 \approx 1/M_w + 2A_2c \qquad (36)$$

Since no angular scattering variations are recorded, such instrumentation cannot produce size information (mean square radius), though some measurements may be made on similar

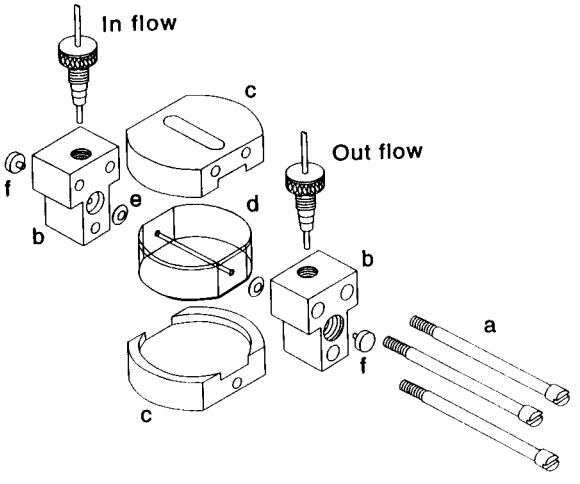

Fig. 5. Exploded view of the refraction cell with manifolds. (a) tie rods; (b) LC manifold; (c) spacer plate; (d) glass cell; (e) seal; (f) window.

samples using the small forward scattered and its complimentary (~ 176°) backscattered intensities. Such measurements are time consuming and difficult to perform, so most units are generally operated at a single scattering angle only. Equally important is the fact that even for angles as low as 4°, once $\langle r_g^2 \rangle 2\ k^2/3$ becomes very large, x itself no longer can be replaced with 0. At very large molecular weights (~ 10^7 g/mole), these errors can become important.

As mentioned earlier, in addition to the problems created by dust and other extraneous particulates in "pure" solvents used for light scattering, the interface itself through which the incident light source passes can often represent a major source of stray light affecting the measurements, especially at small angles. A solution to the beam interface problem was discovered during the development of the refraction cell [31] shown in Fig. 5. The standard configuration of the cell is a right cylinder with a fine polished bore through one diameter. The laser beam enters and leaves the cell via two symmetric manifolds containing chromatographic fittings and Kalrez® sealed windows. Since the glass is chosen of a refractive index significantly greater than that of the solution, rays scattered from the solution at an angle θ refract into the glass at an angle θ'. The cell is surrounded by an array of detectors collimated to detect light from an "object" volume at the center of the cell. Because of refraction, the object volume is displaced slightly from the true center of the cell except for 90° scattering. Figure 6 shows the geometry of the cell refractions of the scattered light intensities. The scattered and refracted rays are related simply by Snell's Law which, expressed in terms of scattering and refraction angles, is just

$$n_g \sin(\pi/2 - \theta') = n_s \sin(\pi/2 - \theta) \tag{37}$$

or

$$n_g \cos \theta' = n_s \cos \theta \tag{38}$$

where the refractive indices of the glass and solvent are, respectively, n_g and n_s. Note that the limiting (smallest) scattering angle corresponds to $\theta = 0°$ and, therefore,

$$\theta' = \cos^{-1}(n_s/n_g) = \theta_c' \tag{39}$$

the supplementary critical angle for the glass–solvent interface.

Equations (38) and (39) confirm that all scattering angles (> 0°) within the solvent correspond to refraction angles greater than θ_c'. Fixing the positions of the detectors about the refraction cell of Fig. 5 as incorporated in a DAWN-F unit, for example, at angles θ' defined by

$$2.0 \geq \cot \theta' \geq -1.4$$
$$\text{(in increments of 0.2)} \tag{40}$$

we see that the 18 locations so-defined will permit a significant range of scattering angles for all

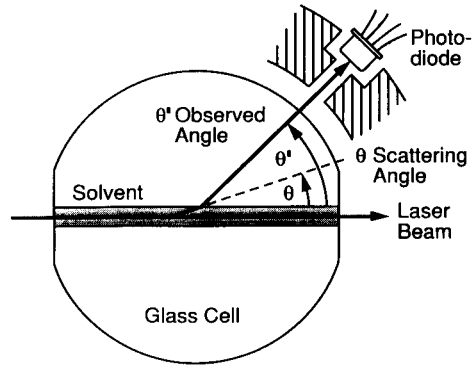

Fig. 6. Section of the refraction cell showing refraction of scattered light during its passage to a detector.

TABLE 1

Refractive indexes of cells available for the DAWN-F system

Glass classification	Refractive index for $\lambda = 632.8$ nm	Refractive index for $\lambda = 488.0$ nm
K5	1.52064	1.52844
F2	1.61656	1.63176
SF10	1.72309	1.74599
SF11	1.77862	1.80586

solvents of refractive index n_s provided that a suitable glass cell of refractive index n_g be selected. At present, cells are manufactured with the corresponding refractive index at $\lambda = 632.8$ and $\lambda = 488.0$ nm shown in Table 1.

Consider, for example, trichlorobenzene of approximate refractive index (at 150°C and $\lambda =$ 632.8 nm) of 1.56. The supplementary critical angle per Eq. (39) attainable for, say, SF10 glass would be given by

$$\theta_c' > \cos^{-1}(n_s/n_g) = \cos^{-1}(1.56/1.72) = 24.9° \quad (41)$$

The lowest fixed refraction angle of the range defined by Eq. (40) corresponds to $\cot^{-1}(2) =$ 26.6°. Thus, the lowest *scattering* angle detected would be 9.5° for *this set of fixed detectors*. [Set $\theta' = 26.6°$ in Eq. (38), and solve for θ.] Were SF11 glass selected instead, only refraction angles

$$\theta_c' > \cos^{-1}(1.56/1.78) = 28.8° \quad (42)$$

could be detected. The *second* fixed detector ($\cot \theta' = 1.8$) would detect light scattered at the angle θ given by

$$n_s \cos\theta = n_g \cos\theta' = 1.78 \cos(29.05°),$$

$$\cos\theta = 0.997,\ \theta = 4.1° \quad (43)$$

The interfaces (windows) through which the laser beam passes are always outside the field of view of any detector for which θ is greater than about 2°. This structure ensures, thereby, that stray light effects caused by such interfaces will be minimal. At very high concentrations, however, n_s changes and the transformed angles are displaced. Care must be exercised to note the occurrence of such phenomena and avoid them.

The refraction cell may be used for both HPSEC measurements (discussed below) as well as static measurements from very small volumes (50 μl). A batch conversion kit permits measurement of larger 10 ml volumes in standard scintillation vials. For such batch measurements, however, there are no refractions and only scattering angles $\theta = \theta'$ defined by Eq. (40) are accessible. For these instrumental configurations operated in a batch mode, therefore, the lowest scattering angle measurable is about 27°. *Extrapolation* to zero angle following Zimm's methods is still quite practical for molecular weights up to a few million, though global fitting approaches, which make use of all angular data, may be preferable.

Differential refractometers: displacement

A key requirement for the determination of molecular weights from light scattering is the numerical value of dn/dc, the change of solution refractive index with respect to a change in concentration of the molecular species being measured [cf. Eq. (3)]. For many molecular species, this value remains constant over a broad range of molecular weights. For others, especially co-polymers, the value can change significantly with molecular weight. Even for homopolymers, as the molecular weight falls below about 10 000 g/mole, the value of dn/dc begins to change appreciably. Average dn/dc values are often sufficient for the determination of weight average molecular weights of bulk samples. However, once the separation of samples via HPSEC techniques is considered, then a value of dn/dc for each elution fraction may be required. For HPSEC measurements combined with light scattering, the absolute concentration of the sample fraction must be known also. Often used are so-called DRI (differential refractive index) detectors which determine the concentration of the particular eluant (solution) through the relation

$$n_s = n_r + (dn/dc)\Delta c \quad (44)$$

where n_r is the refractive index of the pure solvent (reference), n_s is the solution refractive index, and dn/dc is determined by calibration of the unit for each sample and solvent. Thus

$$\Delta c = (n_s - n_r)/(dn/dc) \quad (45)$$

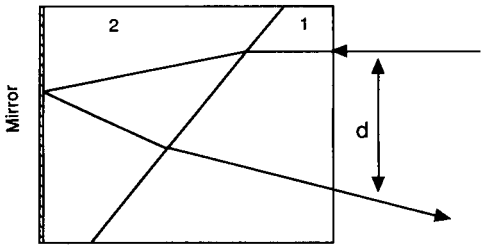

Fig. 7. Conventional split prism cell refractometer based on beam displacement.

The voltage output of a DRI detector generally has a value proportional to $n_s - n_r = \Delta n$. If dn/dc is not constant throughout the separated sample, then the derived concentrations may be erroneous. *Any* measurement technique, even indirect approaches such as viscometry, which require concentration values derived from DRI detector responses is intimately dependent on any changes in dn/dc.

Figure 7 shows schematically the simplified structure of a split prism device used to measure the difference of the refractive indices of two liquids contained, respectively, in the regions 1 and 2. For small refractive index differences between the liquids, it may be shown that the displacement of the incident light beam is

$$d \approx \alpha(n_s - n_r)/n_s \approx \alpha\ \Delta n/n_r \qquad (46)$$

where α is a geometrical constant related to the structure of the cell and the reference and solution refractive indices are n_r and n_s, respectively. Note that the displacement d is directly proportional to the difference of the refractive indices of the solutions. Most commercial DRI detectors are based upon variations of this principle (often involving multiple paths through the cell) and produce an output proportional to the measured displacement. (A Fresnel type DRI detector such as manufactured by Milton Roy is also available wherein the transmitted beam intensity is monitored. As the refractive index of the two liquids differ, the light transmitted through the interface is decreased due to Fresnel reflection losses at the interface.) In order to use a displacement DRI detector as a concentration detector, we rewrite Eq. (46) as

$$d = \alpha\ \Delta n/n_r = \alpha(\Delta n/\Delta c)\ \Delta c/n_r \qquad (47)$$

where Δc is the concentration increment relative to the pure solvent. Thus, for small Δc (generally the case for HPSEC separations), Eq. (47) becomes

$$d = \alpha(dn/dc)\ \Delta c/n_r \qquad (48)$$

Since the output of a DRI detector is typically a voltage change, ΔV, which is directly proportional to the beam deflection d, we may rewrite Eq. (46) as

$$d = \Delta V/\beta = \alpha\ \Delta n/n_r \qquad (49)$$

or

$$\Delta V = \gamma\ \Delta n \qquad (50)$$

where β is the constant relating displacement to voltage change and $\gamma = \beta\alpha/n_r$. The DRI instrument constant is often defined as the product γn_r. Note that $\gamma = \gamma(n_r)$ is a function of n_r. Expressed in terms of *concentration*, Eq. (50) may be rewritten as

$$\Delta V = \gamma\ \Delta c dn/dc \qquad (51)$$

Alternatively,

$$\Delta c = \frac{\Delta V}{\gamma dn/dc} \qquad (52)$$

It is important to note that the response of a conventional (displacement) DRI detector depends explicitly upon the refractive index of the solvent, n_r, as may be seen from Eqs. (48) and (51). This variation requires that the DRI detector be recalibrated each time the solvent is changed. In addition, examination of these equations reveals immediately the need to maintain very precise temperature control, since n_r will vary with temperature. Operation at a different temperature also requires a different calibration constant. Note also that the use of a DRI detector to measure solute concentration is critically dependent on measurement of dn/dc. The user of such instruments should be aware, in addition, that the DRI instrument constants provided by the manufacturers are often in error by amounts exceeding 50% even with the same solvent. They should always be checked by calibrating the DRI unit explicitly for each solvent used, using fixed concentrations of well defined solutes with known dn/dc values.

Differential refractometers: interferometric

A different type of DRI detector with more stable operating characteristics is based on a wave front shearing (rotation) technique used somewhat similarly in interference microscopy. Two nearly coherent and linearly polarized beams of light pass, respectively, through two parallel flow cells: one contains a reference fluid, the other a sample bearing fluid. The two beams are polarized at right angles to one another and are produced from a single incident light wave polarized at 45° passing through a Wollaston prism (see Fig. 8). Any difference in refractive index between the two fluids results in a phase shift of one beam relative to the other. This phase shift is directly proportional to the refractive index difference of the fluids. A conventional interferometer would combine two beams of identical polarization to produce a modulated *intensity* that varies with the phase shift. The interferometric refractometer, on the other hand, responds to the phase difference between the two orthogonally polarized beams by producing a single plane polarized beam of light that has been rotated relative to the initial incident beam (45° polarization) through an angle exactly equal to *one-half* of the phase shift introduced by the difference of the two fluid paths. The angle of rotation is readily measured by means of another plane polarizing element.

Figure 8 shows a schematic of the first part of the interferometer. A light source is masked and collimated before passing through a polarizer oriented at 45° to the horizontal (instrument base). The linearly polarized beam then strikes a Wollaston prism which splits it into two orthogonally polarized beams of equal intensity. The beams then are focused by the lens and pass, respectively, through a reference cell and a sample cell. The light passing through the reference cell is vertically polarized, while the beam passing through the sample cell is horizontally polarized. As the beams enter the cells, they are in phase with one another.

Each cell of Fig. 8 has a length l. Let the refractive index of the fluid in the reference cell be n_r and that of the sample n_s. This means that in the reference cell, there will be l/λ_r wavelengths present, where

$$\lambda_r = \lambda_0/n_r \tag{53}$$

and λ_0 is the vacuum wavelength of the incident light. In the sample cell, there will be l/λ_s wavelengths. Upon emerging from the two cells, the two waves will again have the *same* wavelength (the medium external to the cells is air) but will differ in phase (i.e. be out of step) by an amount

$$l/\lambda_s - l/\lambda_r = l(1/\lambda_s - 1/\lambda_r) \text{ wavelengths} \tag{54}$$

This phase difference is usually expressed in angular or radian units by noting that each wavelength difference introduces a 360° angular phase difference between the waves. Since 2π radians $= 360°$, the phase difference φ between the two waves in radian measure is just

$$\begin{aligned}\varphi &= 2\pi l(1/\lambda_s - 1/\lambda_r)\\ &= 2\pi l(n_s/\lambda_0 - n_r/\lambda_0)\\ &= 2\pi l\,\Delta n/\lambda_0\end{aligned} \tag{55}$$

where $\Delta n = n_s - n_r$. Thus, by measuring φ, we

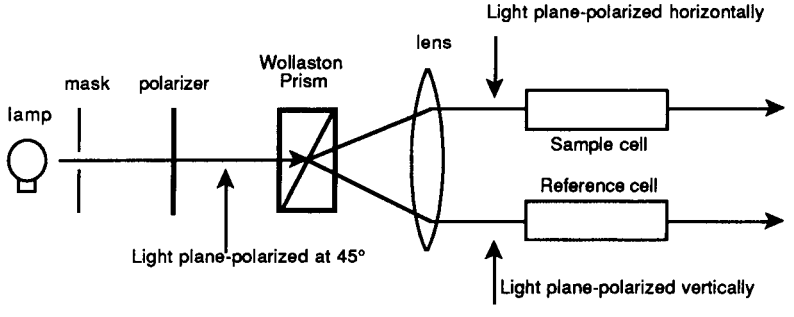

Fig. 8. Production of two orthogonal plane polarized beams from a single plane polarized beam by means of a Wollaston prism.

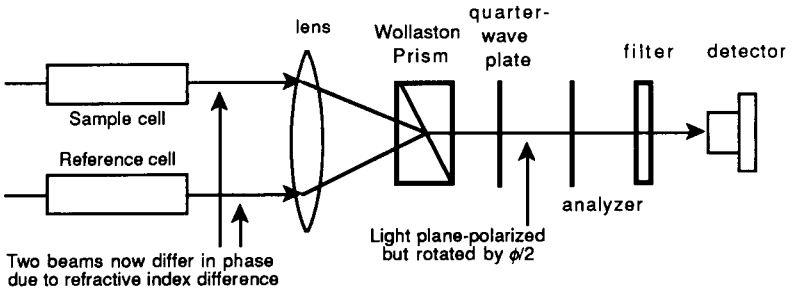

Fig. 9. Recombination of two beams at the second Wollaston prism. The quarter wave plate converts each plane polarized component into a left and a right circularly polarized beam, respectively.

have a direct measure of Δn independent of n_r. [Contrast Eq. (49).] The interferometric refractometer makes this final determination as follows.

Figure 9 shows the second half of the interferometer whereby the sample and reference beams are focused onto a second Wollaston prism which compensates for their earlier separation. A quarter wave plate is placed after the Wollaston prism with its fast axis at 45° with respect to the horizontal. The horizontally polarized sample beam emerges circularly polarized in the counterclockwise direction, while the vertically polarized reference beam emerges circularly polarized in the clockwise direction. Since the two circularly polarized waves rotate at the same frequency in opposite directions and are of equal intensities, they combine to form a plane polarized beam once again. It is easily shown [32] that this beam has been rotated $\varphi/2$ with respect to the incident 45° plane polarized beam.

Following the quarter wave plate is an analyzer (plane polarizer) placed at an angle of $90° - \beta$ with respect to the axis of the incident plane polarizer. The relationship between the planes of polarization of the beams, angles, and analyzer is shown in Fig. 10. The angle β is chosen so that for $\varphi = 0$, the unattenuated incident beam would be reduced in intensity (after passing through the analyzer) to a value of about 35% of its incident intensity. In this manner, the linear range of the instrument will be extended.

Thus, if the incident intensity is I_0 and $\varphi = 0$, the angle β would be defined by

$$I/I_0 = \cos^2(\pi/2 - \beta) = \sin^2\beta = 0.35 \qquad (56)$$

The angle between the combined beam and the analyzer will be, in general,

$$\pi/2 - \beta - \varphi/2 \qquad (57)$$

and, therefore,

$$I/I_0 = \sin^2(\beta + \varphi/2) = [1 - \cos(2\beta + \varphi)]/2 \qquad (58)$$

where I is the intensity of the combined beam whose plane of polarization has been rotated $\varphi/2$ due to the phase difference φ between beams emerging from the reference and sample cells. By measuring the intensity relative to I_0, the phase angle $\varphi/2$ may be deduced by the instrument and hence Δn calculated.

An interference filter, placed just before the detector of Fig. 9, selects the measuring wavelength, λ_0. For use with a standard He–Ne laser-based photometer/detector, this filter is selected

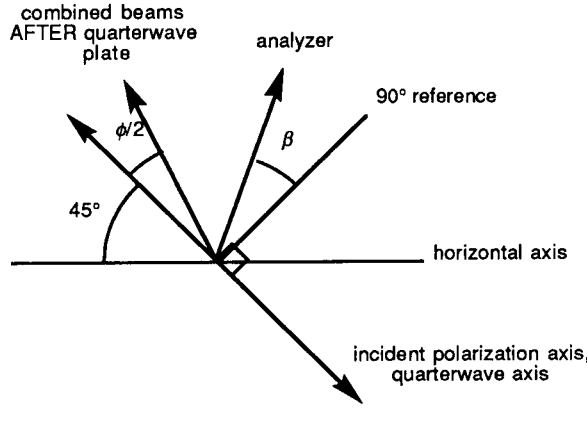

Fig. 10. Upon recombining, the resultant beam is plane polarized at an angle $\varphi/2$ with respect to the incident beam.

at 630 ± 5 nm (He–Ne laser wavelength is 633 nm), or at 488 ± 5 nm for detectors operating at the blue line produced by an argon ion laser.

Since the response of the interferometric refractometer is independent of the refractive index of the reference solvent, n_r, as indicated in Eq. (55), the requirement for temperature regulation is not as stringent as it is for conventional DRI detectors. Not only is the interferometric refractometer stable over a wider range of temperature fluctuations than conventional DRI detectors, but it is also less susceptible to pressure pulses (caused by pump pulsations) since the outlets of the reference and sample cells are connected. Note again that from Eq. (55) we may write an expression for the *concentration* difference between the two cells

$$\Delta c = \varphi\lambda_0/(2\pi l dn/dc) \qquad (59)$$

Although the analyzer angle β is selected so that the linear response of the instrument extends over a broader range (than setting $\beta = 0$), the usual software generates the phase shift values from Eq. (58) directly, a *non*-linear relation valid over an even greater range of values of φ than a simple linear result. The concentration has to be kept low enough, however, so that the signal produced is a monotonic function of φ. As the refractive index difference increases beyond these limits, the intensity response will become sinusoidal. Phillips and Borchard [33] have taken advantage of the periodicity associated with these much larger refractive index differences to increase the precision of the measurement, especially when operated as an on-line DRI detector for chromatography. Fringes are always present as the interferometer becomes "overloaded" and each new fringe corresponds to an increase of φ by 2π.

MEASUREMENTS

Zimm plots: M_w, $\langle r_g^2 \rangle_z$ and A_2

The usual method for preparing a Zimm plot from a polydisperse solution is to prepare samples over a range of low concentrations spanning at least an order of magnitude. By "low" one usually means values that satisfy Zimm's criterion of "vanishingly low," though from a practical

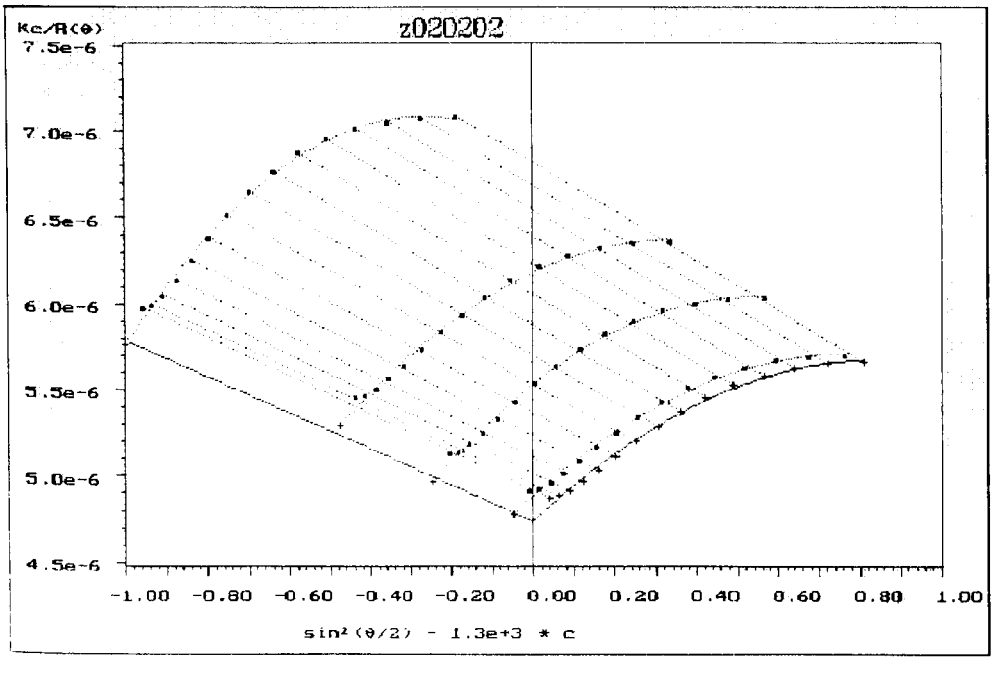

Fig. 11. Zimm plot for conducting polymer data of Table 2.

point of view, the highest value selected may be somewhat outside this range. From light scattering data collected at various angles for various solute concentrations, one obtains the weight average molecular weight, z average square radius (mean square radius), and second viral coefficient. For the multiangle DAWN systems, such samples may be prepared in thoroughly cleaned scintillation vials and run directly in the DAWN-B instrument or a batch configuration of the DAWN-F. Alternately, the samples may be injected sequentially in *ascending* order of concentration into the DAWN-F system with an injection loop and pump or simply a syringe pump (see the section: *HPSEC measurements*). Data may be collected at each concentration while the sample is flowing (once a steady state has been achieved) or in a "stop-flow," static mode. Recently, new size exclusion chromatography software (ASTRAURdinary™) has been developed to permit direct Zimm plots from single chromatographic injections using an in-line system *without* a refractive index detector and without a set of columns (see the section: *On-line Zimm plots*).

A graphical representation (cf. Fig. 11) of the extrapolations of Eqs. (32) through (34) is achieved by plotting K^*c/R_θ versus $\sin^2\theta/2 + Sc$ for each (θ,c) point measured. The stretch factor S is selected so that the data points are sufficiently spread out to produce a well-defined plot. The choice of S, of course, should not affect the final result. S is chosen to give approximately equal weight to angular and concentration terms. The factor may be positive or negative. When Zimm originally developed his technique, and for many years after, the standard data reduction equipment required was a straight edge, a pencil, and a good eraser. Points that did not seem to "fit" because of obviously high noise (dust) contributions were adjusted to lie along a linear line or dropped. The small angle data were extrapolated to 0° for each concentration, and the data at each angle were extrapolated to zero concentration. The common intercept of the two extrapolated curves yields the reciprocal molecular weight. The slope of the $c = 0$ curve near $\sin^2\theta/2 = 0$ yields the square mean radius per Eq. (33) while the slope of the $\sin^2\theta/2 = 0$ curve near $c = 0$ yields the second virial coefficient per Eq. (34). Alternatively, numerical analysis of all data collected permits the introduction of quadratic and higher order fits to the K^*c/R_θ data. From these latter procedures, the coefficient of the term linear in $\sin^2\theta/2$ may be extracted to yield $\langle r_g^2 \rangle$. [Cf. Eq. (17).] Since Eq. (8) is valid over the entire range of angles [at least at low concentrations and for particles/molecules satisfying the Rayleigh-Gans-Debye approximation criteria of Eq. (4)], it is possible to solve for the best values of M_w, $\langle r_g^2 \rangle$ and A_2 using non-linear regression techniques [34] or global fitting. No matter how the molecular parameters are extracted, the creation of a Zimm plot (or its reciprocal Debye plot) is a useful means for examining all data points simultaneously to simplify the search for outlying data. Solution by extrapolation to zero scattering angle and zero concentration permits the application of linear regressions; however, most of the higher angle data are discarded by these traditional methods. As mentioned earlier, a more powerful technique that permits the use of all angular data to find the coefficient of the *linear* term in Debye's expression, Eq. (17), has been developed by Mijnlieff and Coumou [25]. Consider now the production and interpretation of a Zimm plot.

An excellent example of a Zimm plot is shown in Fig. 11. This measurement was made with a batch system using dilutions prepared in standard 20 ml scintillation vials. It is based on the parameters summarized in Table 2. Measurements of the rod-like conducting polymer were made in tetrahydrofuran (THF) at the four concentrations indicated (g/ml). Absolute calibration was based on the Rayleigh factor (14.06×10^{-6} cm^{-1}) for toluene at 633 nm.

The DAWN-B systems have a fixed set of 15 detectors equidistantly spaced in $\sin\theta/2$ between 0.2 and 0.9 in intervals of 0.05. Figure 11 presents the traditional Zimm plot of K^*c/R_θ against $\sin^2\theta/2 + Sc$. The final extrapolations should be independent of the value of S chosen. *Care must be taken, especially in computer-generated results, that this factor does not affect the final results.* At each concentration, the data as a function of

TABLE 2

Zimm plot parameters and results corresponding to Fig. 11

Zimm plot file: z020202
Data file: 02021989
Data identif.: conducting polymer
Detectors: 1 2 3 4 5 6 7 8 9 10 11 12 13 14 15
Absolute calibration constant = $3.000 \cdot 10^{-5}$
Solvent refractive index = 1.404
$dn/dc = 0.350$
Angular curve interpolation degree = 2
Concentration curve interpolation degree = 1

Set	Concentration (g/ml)
24	$3.625 \cdot 10^{-5}$
13	$1.865 \cdot 10^{-4}$
4	$3.626 \cdot 10^{-4}$
8	$7.600 \cdot 10^{-4}$

M_{w_1} (g/mol)	M_{w_2} (g/mol)	r.m.s. radius 1 (nm)	r.m.s. radius 2 (nm)	2nd virial coeff. (cm^3 mol/g^2)
$2.111 \cdot 10^5$	$2.111 \cdot 10^5$	43	43	$6.895 \cdot 10^{-4}$

$\sin^2\theta/2$ are extrapolated to zero value. Similarly, at each value of $\sin^2\theta/2$, the *concentration* values are extrapolated to zero. These two sets of extrapolated values correspond to the two limiting curves displayed and bracketing the data from above and below. A least squares grid has been added to identify the data points more clearly. Note that the Zimm plot methodology is based on *linear* extrapolations to zero concentrations and zero scattering angles of Eq. (32). Extraction by analytic procedures (globel fitting) of the coefficient of the $P(\theta)$ series linear in $\sin^2\theta/2$ also will permit similar determinations. Although the plot shown involves *second* order terms in $P(\theta)$, which are responsible for the curvature (non-linear behavior) of the data points at higher scattering angles and concentrations, only the coefficients of the linear term of $P(\theta)$ per Eq. (17) or the linear extrapolations near zero yield the key molecular parameters sought: M_w, $\langle r_g^2 \rangle$, and A_2. As mentioned above, the coefficients of the higher order terms, of course, are related to other important parameters of molecular structure [22].

The Zimm plot shown in Fig. 11 incorporates a *negative* stretch factor S. Note the extrapolations to *zero angle* lie to the left of the ordinate axis while the extrapolations to zero *concentration* lie to the right. The data plotted, therefore, have the appearance of an opened "fan". This form of the Zimm plot is particularly instructive for large molecular weights or conformations where the angular variations depart from straight lines.

Returning to the approximation of Eq. (32), we see that the intercept of the zero angle and zero concentration curves with the ordinate axis ($x = 0$, $c = 0$) yields the reciprocal weight average molecular weight, $1/M_w$. The slope with respect to $\sin^2\theta/2$ of the zero concentration curve near $x = 0$ yields the factor $4k^2\langle r_g^2 \rangle/(3M_w)$ per Eq. (33), while the slope with respect to c of the extrapolated zero angle curve per Eq. (34) yields $2A_2$. The key molecular parameters, therefore, may be determined from these extrapolations following Zimm's methodology. However, Eq. (26) has a greater range of validity than the limiting, near zero form of Eq. (27). Again, it is important to stress that $\langle r_g^2 \rangle$ may always be obtained analytically or from the linear extrapolation *independent* of dn/dc, M, or n. (Again, an exception is heterogeneous copolymers.)

The critical molecular parameters derived from the data shown in Fig. 11 (remember the results must/should be independent of the stretch factor) are shown at the bottom of Table 2. The two values shown for the molecular weight correspond to the two extrapolated lines ($c = 0$ and $\sin\theta/2 = 0$) and the corresponding sizes calculated from Eq. (32) for each of these masses. If the analysis has been performed suitably, these masses must *always* be the same.

Despite their relatively low molecular weight (250 kilodalton), these rigid rod molecules have an r_g value of 43 nm corresponding to a length of 86 nm. For a molecule of this size, the simple linear approximation to Eq. (33) must fail for all but the smallest scattering angles. For example, consider the result for $\theta = 90°$:

$$x = (2k \sin\theta/2)^2\langle r_g^2 \rangle/3$$

$$= \left(\frac{4\pi 1.402}{632.8\sqrt{2}}\right)^2 (43^2)/3 = 0.24 \qquad (60)$$

Thus, for $\theta > 90°$ at $\lambda_0 = 632.8$ nm and a THF

($n_s = 1.402$) solvent, x is *not* very small compared to unity. This value is not small enough to drop higher order terms in $P(\theta)$ which must be kept to characterize the molecular scattering at larger angles. For the Zimm plot data shown in Fig. 11, the analysis included terms to second order in $\sin^2\theta/2$.

The non-linear appearance of the Zimm plot shown in Fig. 11 confirms the need to be able to include higher terms in x and further emphasizes the importance of making measurements over a broad range of angular values. Even though the key molecular parameters may be derived from the near zero extrapolations per the Zimm plot techniques, more general fitting procedures will yield more consistent and reliable results. This is particularly true when the molecules are very large and/or low angle scattering data are noisy, as is often the case with dust-laden preparations. In the absence of dust noise, measurements at a single, low angle (LALLS) can yield molecular weight data, but neither size nor conformation data. We shall discuss the latter in the next section.

When molecules are very small ($r_g \ll \lambda/20$), the angular dependence of $P(\theta)$ becomes unimportant since the scattering is essentially isotropic. For these cases (e.g. various types of compact proteins), the measurement of scattered light may be performed at *any* angle. As long as the appropriate geometrical factors associated with the detector at each scattering angle are suitably calculated and, therefore, the appropriate corresponding geometrical and normalization constants determined for the detector position selected, measurement of the absolute scattered intensity permits an immediate deduction of M_w at a fixed concentration if that concentration is low enough to ensure that the $2A_2c$ term is very small compared to $1/M_w$. On the other hand, by preparing samples at various concentrations and making measurements at a selected single angle, one may extract the second virial coefficient by making a simplified Zimm plot based on this single angle. This latter procedure has been a standard for many years using the LALLS instruments [29,30]. The advantage of using a *larger* angle (than the 3° to 7° range for LALLS) is that the effects of dust may be reduced. Thus, single angle laser light scattering (SALLS) may be used effectively for very small molecules, i.e. when $P(\theta) = 1$. If one makes the light scattering measurements at *several* angles, however, even though the scattering is isotropic, the resultant measurements may be combined to yield more accurate values for the derived molecular weights. In addition, of course, if the molecular suspensions contain larger aggregates, the detection of angular dissymmetry (by making measurements at several angles) is one of the simplest means for confirming this.

Since single angle measurements may be made using any monochromatic light source, a diversity of other types of instruments may be used including all scanning goniometers incorporating either lasers or mercury arc lamps with filters. For flow geometries (see *HPSEC measurements*) even fluorometers [35] detecting light at 90° have been tried with incident and detected wavelengths being set equal. For small molecules, this technique has been used to obtain *relative*, but not absolute, molecular weights. Recently right angle (90°) devices using solid state lasers have been introduced to determine molecular weights of very small molecules for which $P(\theta) = 1$. These and other 90° SALLS systems have been tried since the concept was introduced in the 1930s by Putzeys and Brosteaux [36]. Although the dust effects are smaller at 90° than at 3°, such right angle measurements share the most important shortcomings of LALLS measurements, i.e. they lack relative precision and yield no size information.

For the case of small molecules, and particularly random coils of molecular weights below about 600K g/mole as well as most proteins, the variation of scattered light intensity with angle should be described well by including the term linear in $\sin^2\theta/2$ and using Eq. (32). Neglecting the effects of experimental uncertainties, the linear fit required to extract M_w, $\langle r_g^2 \rangle$ and A_2 could be achieved using only *two* detectors. The miniDAWN® incorporates *three* angles (approximately 45°, 90°, and 135°) and the flow cell of Fig. 5. On this basis, the precision of the measurement, even for very small molecules where $P(\theta) = 1$, is almost double that of a SALLS device. Incorporating a 20-mW solid state GaAs

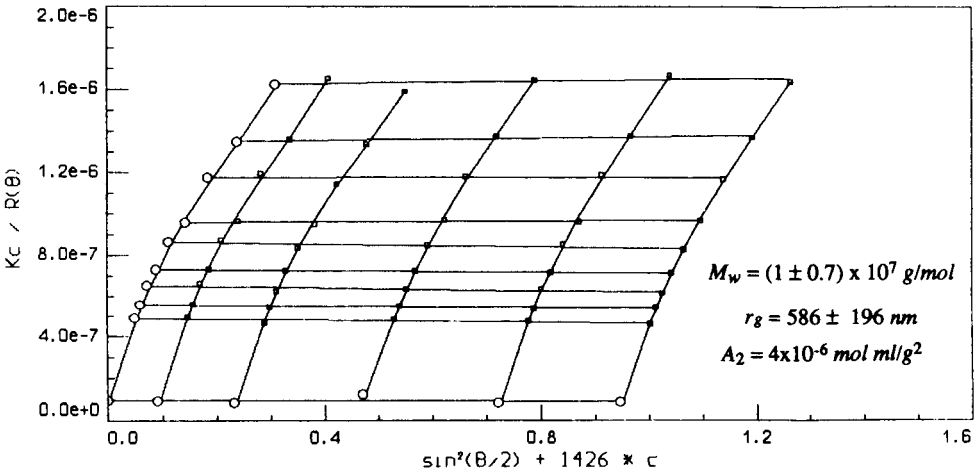

Fig. 12. Zimm plot (lowest nine angles) for a very large polymer molecule.

laser operating at 690 nm, the three angle device is capable of being used in the micro-batch mode to produce data for 3 angle Zimm plots. Although the 15 detector configuration will yield a precision more than double that of the 3 detector system, for molecular weights below a million the three detector instrument is quite useful for a variety of routine applications and especially for quality control. If aggregates are present or if the sample consists of rodlike structures, the accuracy of a three detector system will begin to diminish as r_g increases above about 50 nm. However, the three angle configuration permits deduction of the presence of structures of far greater size by examination of the departure from linearity of the least square fit of the data. The miniDAWN® has sufficient angular resolution to permit calculation of the so-called dissymmetry ratio $R(45°)/R(135°)$, a quantity sometimes used to characterize molecular structure. The 18 detector DAWN systems can also determine dissymmetry ratios and, in addition, deduce a variety of other structurally dependent characteristics for both large molecules and even very large particles whose scattering properties cannot be characterized by the simple RGD approximation.

As mentioned earlier, the Zimm plot methodology is very effective as long as $P(\theta)$ is close to unity and the molecular weights are not too great. When this is not the case, the Zimm plots have large uncertainties associated with extracting both $1/M_w$ from the ordinate intercept per Eq. (32) or the mean square radius per Eq. (33). Figure 12 presents a Zimm plot corresponding to the scattering from a suspension of very large molecules with all but the lowest 9 angles discarded. The angular data were fitted to *third* order in $\sin^2\theta/2$. Because of very slight experimental uncertainties of the data points and the huge molecular size, the exact location of the intercept is highly uncertain. The plot, furthermore, produces an unreasonably large mean square radius. However, if we return to Eq. (8), expand $P(\theta)$ to fourth order in $\sin^2\theta/2$, again keeping the smallest 9 angles, and plot $R(\theta)/(K^*c)$ as a function of c and $\sin^2\theta/2$, we produce the plot of Fig. 13. This Debye plot permits [through an analytical application of Eq. (17)] the extraction of the molecular weight $(4.2 \pm 0.3) \times 10^6$ and root mean square radius of the molecule (232 ± 20) nm while minimizing singularities and uncertainties. The second virial coefficient is essentially zero $(-3 \pm 10) \times 10^{-6}$ cm³ mol/g². Although the commonly used Zimm plot technique is usually effective in yielding r_g and M_w values, once the *linear* expansion/approximation of Eq. (32) has failed for most angles, the

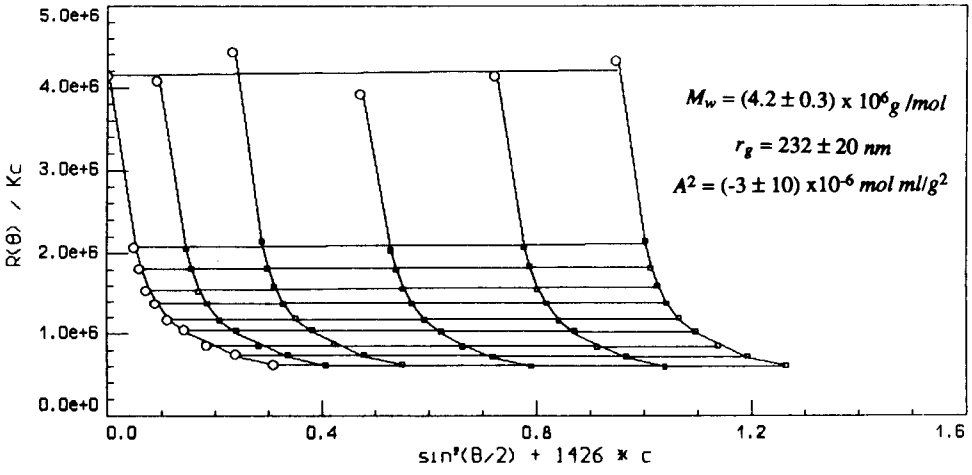

Fig. 13. Debye plot (lowest nine angles) from the same measurements as Fig. 12.

non-linear Debye plot of Eq. (8) generally will be preferable to extract values corresponding to very high molecular weights and large r_g values.

HPSEC measurements

Gel permeation (or high-performance size-exclusion) chromatography (HPSEC) is a well-known separation technique [8,37] whereby molecular species are separated primarily on the basis of their hydrodynamic size: the largest molecules sweep through the porous columns first, followed by the smaller species that have diffused into and further penetrated the interstices of the column gel. The smallest species are, therefore, retained the longest and elute last. For well-fabricated columns, there is an approximate linear relationship over a wide range between the logarithm of molecular size or weight and the elution volume. Traditional HPSEC techniques have exploited this relationship to deduce molecular *weight* based on the *time* a given fraction requires to traverse the column following injection. Since pumping rates are assumed to be constant, this time factor is converted into the elution volume, i.e. the amount of solution pumped until the particular size elutes. Columns are calibrated in terms of the logarithm of the eluting *mass* as a monotonic function of the elution volume. Standards of different masses for certain types of molecules, e.g. polystyrene, are used for this calibration. In addition, since pump rates may not be constant, these standards must be remeasured whenever day-to-day or run-to-run data are compared. The relation between such known calibration masses and the masses associated with an eluting unknown are vague, at best. If the molecular configuration of the unknown is not the same as the calibration standards, very large errors can occur. However, since (as we have seen) light scattering measurements can determine molecular weights absolutely and independently of any calibration or reference standards, the addition of a light scattering detector to a HPSEC separation results in the ability to classify each fraction of an eluting sample. All that is necessary is that the *concentration* of each eluting fraction be known as well as the differential refractive index increment, dn/dc. For most types of homopolymers as well as many types of co-polymers, the value of dn/dc remains essentially constant over the range of masses measured. Thus, making an off-line measurement of dn/dc from the bulk, unseparated solution is often sufficient to characterize the entire sample. There are exceptions, however, and these include some co-polymers as well as samples whose molecular weights are below several thousand g/mole.

As we have seen in the Instrumentation section, a differential refractive index detector is sufficient to measure (at low solute concentrations) the concentration change of an eluting

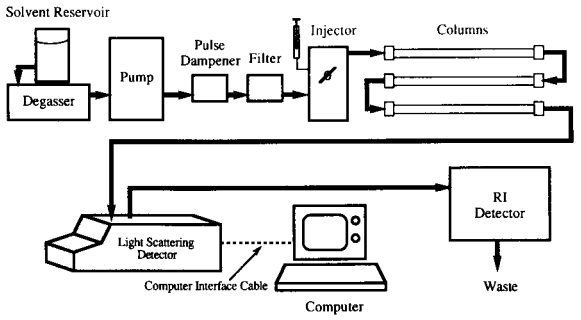

Fig. 14. Incorporation of a light scattering detector for HPSEC measurements.

fraction [see Eq. (52) or Eq. (59)]. This requires measurement of dn/dc, however, which is also a requirement for determining the light scattering constant K^*. Alternatively, $n_s - n_r$, the refractive index change [see Eq. (45)] may be measured if the concentration change is known. Thus, the suitable functioning of a light scattering detector for the measurement of molecular weight and size fractions requires a concentration detector if dn/dc is constant over the sample elution and can be determined off-line. For some co-polymers and other molecular species where dn/dc undergoes large variations over the sample elution, a third detector (UV, infrared, or mass) may be required. For the present, we shall consider only the configuration shown in Fig. 14. The first practical implementation of this configuration was achieved by Chromatix in what was certainly one of the most significant achievements for light scattering in the field of chromatography.

The HPSEC configuration presented in Fig. 14 shows the light scattering detector placed between the traditional DRI detector (used here as a concentration detector) and the separating columns. When the eluant leaving the column flows through a refraction cell of the type shown in Fig. 5, light scattering measurements are made almost simultaneously at each of the different angles. Data collection and processing are generally under the control of a PC-type computer (e.g. driven by the Wyatt Technology Corporation ASTRA® or ASTRette™ program). For the remainder of this section, we shall review a selection of data generated in this manner.

The output intensity (usually in volts) of the light scattering and DRI detectors are collected and stored in a personal computer for later processing. For the DAWN systems, 16 light intensity values as well as an amplified DRI signal are collected. The light intensity values include the intensities detected at the user selected 15 contiguous scattering angles (out of 18 total angles available) and the incident laser monitor, the latter being proportional to I_0. Typically, for

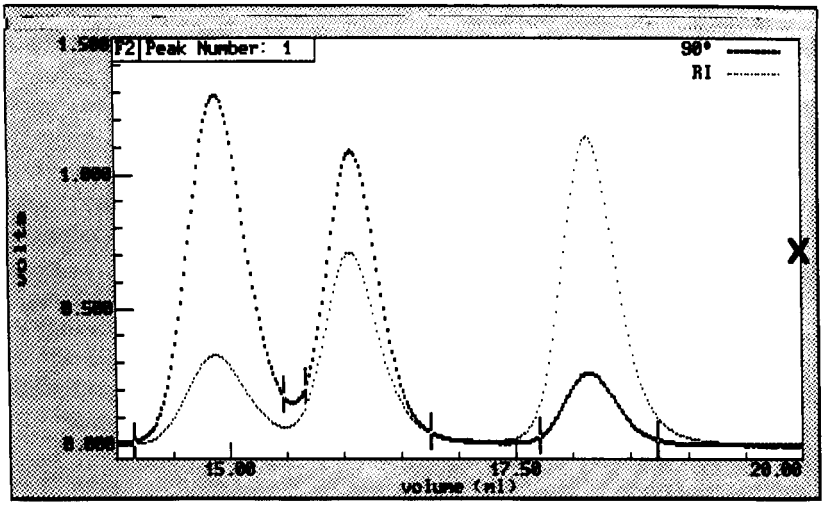

Fig. 15. Superposition of 90° light scattering and DRI signals for three narrow polystyrene standards in THF (nominal molecular weights 600, 200 and 30 kilodalton).

broad molecular weight samples, collections are made at one-second intervals, corresponding to slice volumes of about 15 μl (1 ml/min flow rate). During each collection, 50 to 100 measurements are made at each angle and averaged. Figure 15 shows the DRI and 90° scattered signals from a mixture of three narrow polystyrene standards in THF. Also shown in the figures are the limits (short vertical bars) selected for each of the three peaks to be processed. These limits define the central regions of the peaks and eliminate regions of overlap. The volumetric delay between the two signals (173 μl) has been determined (to be discussed later) and corrected by the software, so that the elution volume shown in the figure corresponds to the same sample volume (absent band broadening) for both detectors. The separation was achieved using two mixed bed Showdex® KF80M columns (Showa Denko KK, Japan). The nominal molecular weights of the mixed very narrow standards were 600 kilodalton, 200 kilodalton, and 30 kilodalton and they were prepared at concentrations of 0.1%, 0.2%, and 0.3%, respectively. Using a 100 μl injection loop resulted in the corresponding injected masses of 0.1, 0.2, and 0.3 mg. The flow rate was 1 ml/min and the DRI detector was a Waters 410.

Note that the DRI peak height increases directly as the concentration while the LS peaks are proportional to the product of concentration times the molecular weight. From the Rayleigh-Gans-Debye approximation, each molecule scatters light directly proportional to the *square* of its molecular volume (generally proportional to the square of its molecular weight). In a solution, therefore, the scattering per unit solution volume would be directly proportional to NM^2, where N is the number of molecules per unit volume. Since $c = NM$, we obtain the result cited, viz. the scattering per unit volume is directly proportional to cM.

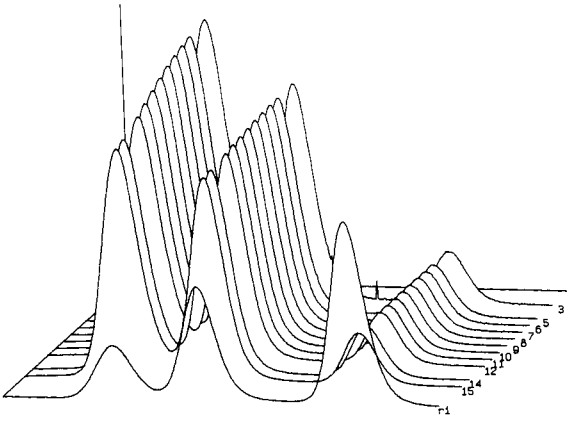

Fig. 16. Elution curves from the three narrow polystyrene standards at 15 different scattering angles with aligned DRI output signal as the first curve in the foreground of the figure. Injection concentrations 0.1%, 0.2%, and 0.3%, respectively.

Figure 16 presents a three-dimensional plot of the normalized scattered light intensity data from the mixture of three narrow polystyrene standards. Each chromatogram corresponds to a different scattering angle. The separated curve in the foreground is the DRI detector signal. The data from some detectors have been dropped.

In a HPSEC separation, it is generally assumed that each slice contains molecules of a single, or at least very narrow, molecular weight, M_i. Therefore, once a separation has been achieved and the collected data processed, the effective mass and size moments may be calculated over each peak selected from the following relations:

Mass

Number average:
$$\overline{M_n} = \frac{\Sigma c_i}{\Sigma \frac{c_i}{M_i}} \tag{61}$$

Weight average:
$$\overline{M_w} = \frac{\Sigma c_i M_i}{\Sigma c_i} \tag{62}$$

z average:
$$\overline{M_z} = \frac{\Sigma c_i M_i^2}{\Sigma c_i M_i} \tag{63}$$

The corresponding mean square radius moments are not analogous, primarily because the quantity measured [13] by LS from a distribution of molecules is given by Eq. (66), below.

Mean square radius

Number average:
$$\langle r^2 \rangle_n = \frac{\Sigma \langle r_g^2 \rangle_i c_i / M_i}{\Sigma c_i / M_i} \tag{64}$$

Weight average: $$\langle r^2 \rangle_w = \frac{\Sigma \langle r_g^2 \rangle_i c_i}{\Sigma c_i} \quad (65)$$

z average: $$\langle r^2 \rangle_z = \frac{\Sigma \langle r_g^2 \rangle_i c_i M_i}{\Sigma c_i M_i} \quad (66)$$

Here, M_i and $\langle r_g^2 \rangle_i$ are the molecular weight and mean square radius, respectively, of slice i at a concentration c_i. The size moments displayed in Eqs. (64) through (66) are somewhat artificial as they involve mixed mass and size terms inconsistent with the standard mathematical definitions [38] of weighted moments of a distribution. The "culprit", of course, is Eq. (66) which is the quantity measured [13] by light scattering from a polydisperse sample. For the case of an ideal random coil, M is proportional to $\langle r_g^2 \rangle$ and thus

TABLE 3

Slice-by-slice details from part of the first peak of Fig. 16

Slice Index	Time (s)	Volume (ml)	Molecular wt. (g/mol)	r.m.s. (nm)	Conc. (g/ml)
262	873.48	14.56	$5.761 \cdot 10^5$	31.7	$5.452 \cdot 10^{-5}$
263	874.52	14.58	$5.786 \cdot 10^5$	31.1	$5.995 \cdot 10^{-5}$
264	875.57	14.59	$5.824 \cdot 10^5$	31.4	$6.558 \cdot 10^{-5}$
265	876.61	14.61	$5.858 \cdot 10^5$	31.5	$7.125 \cdot 10^{-5}$
266	877.65	14.63	$5.886 \cdot 10^5$	31.8	$7.704 \cdot 10^{-5}$
267	878.70	14.65	$5.930 \cdot 10^5$	32.5	$8.267 \cdot 10^{-5}$
268	879.74	14.66	$5.926 \cdot 10^5$	31.3	$8.835 \cdot 10^{-5}$
269	880.78	14.68	$5.956 \cdot 10^5$	31.5	$9.382 \cdot 10^{-5}$
270	881.83	14.70	$5.978 \cdot 10^5$	31.5	$9.909 \cdot 10^{-5}$
271	882.87	14.71	$6.013 \cdot 10^5$	32.0	$1.041 \cdot 10^{-4}$
272	883.92	14.73	$6.031 \cdot 10^5$	31.7	$1.088 \cdot 10^{-4}$
273	884.96	14.75	$6.066 \cdot 10^5$	32.2	$1.131 \cdot 10^{-4}$
274	886.00	14.77	$6.069 \cdot 10^5$	31.6	$1.168 \cdot 10^{-4}$
275	887.05	14.78	$6.076 \cdot 10^5$	31.5	$1.202 \cdot 10^{-4}$
276	888.09	14.80	$6.098 \cdot 10^5$	31.6	$1.229 \cdot 10^{-4}$
277	889.13	14.82	$6.122 \cdot 10^5$	31.9	$1.252 \cdot 10^{-4}$
278	890.18	14.84	$6.137 \cdot 10^5$	31.6	$1.266 \cdot 10^{-4}$
279	891.22	14.85	$6.145 \cdot 10^5$	31.6	$1.277 \cdot 10^{-4}$
280	892.26	14.87	$6.167 \cdot 10^5$	31.9	$1.280 \cdot 10^{-4}$
281	893.31	14.89	$6.175 \cdot 10^5$	31.6	$1.277 \cdot 10^{-4}$
282	894.35	14.91	$6.184 \cdot 10^5$	31.6	$1.267 \cdot 10^{-4}$
283	895.39	14.92	$6.199 \cdot 10^5$	31.9	$1.251 \cdot 10^{-4}$
284	896.44	14.94	$6.185 \cdot 10^5$	31.5	$1.230 \cdot 10^{-4}$
285	897.48	14.96	$6.197 \cdot 10^5$	31.7	$1.203 \cdot 10^{-4}$
286	898.53	14.98	$6.187 \cdot 10^5$	31.5	$1.173 \cdot 10^{-4}$
287	899.57	14.99	$6.185 \cdot 10^5$	31.8	$1.137 \cdot 10^{-4}$
288	900.61	15.01	$6.173 \cdot 10^5$	31.7	$1.098 \cdot 10^{-4}$
289	901.66	15.03	$6.158 \cdot 10^5$	31.9	$1.056 \cdot 10^{-4}$
290	902.70	15.05	$6.132 \cdot 10^5$	31.7	$1.013 \cdot 10^{-4}$
291	903.74	15.06	$6.119 \cdot 10^5$	32.0	$9.672 \cdot 10^{-5}$
292	904.79	15.08	$6.074 \cdot 10^5$	31.6	$9.211 \cdot 10^{-5}$
293	905.83	15.10	$6.049 \cdot 10^5$	31.7	$8.728 \cdot 10^{-5}$
294	906.87	15.11	$6.028 \cdot 10^5$	32.0	$8.257 \cdot 10^{-5}$
295	907.92	15.13	$5.990 \cdot 10^5$	31.9	$7.788 \cdot 10^{-5}$
296	908.96	15.15	$5.953 \cdot 10^5$	31.8	$7.329 \cdot 10^{-5}$
297	910.00	15.17	$5.910 \cdot 10^5$	31.5	$6.877 \cdot 10^{-5}$
298	911.05	15.18	$5.875 \cdot 10^5$	31.5	$6.444 \cdot 10^{-5}$
299	912.09	15.20	$5.819 \cdot 10^5$	31.1	$6.030 \cdot 10^{-5}$
300	913.14	15.22	$5.820 \cdot 10^5$	32.6	$5.631 \cdot 10^{-5}$

an expression proportioned to Eq. (63) would be obtained. The similarity ends there since the weight and number averages are obtained by division of the numerator and denominator sums by M_i to follow the forms of Eqs. (62) and (61), respectively. Note that only the z averaged mean square radius may be determined without the use of a DRI detector. In the limit of very small concentration, the light scattering signal R_θ/K^* extrapolated to zero scattering angle is equal to cM [see Eq. (8)]. Thus from each slice producing an extrapolated LS signal, the z averaged mean square radius of Eq. (66) may be formed immediately without the DRI signals. The local $\langle r_g^2 \rangle$ values, of course, may be calculated as discussed earlier [see Eq. (35)].

The data shown in Figs. 15 and 16 may now be processed peak-by-peak using Eq. (8). After setting an appropriate baseline on the chromatogram produced by each detector and normalizing, the excess Rayleigh ratio (signal minus background, all times the calibration constant and normalization factor, and divided by the incident intensity) may be calculated at each slice. Table 3 presents a small section (from the first peak) of the detailed output available on a slice-by-slice basis with the concentration being obtained directly from the DRI detector. These details include the slice number, elution time, elution volume (time times flow rate), molecular weight, root mean square radius (r.m.s.), and slice concentration. From these slice-by-slice details, application of Eqs. (61) through (66) will yield the results of Table 4 for the data shown in Figs. 15 and 16.

TABLE 4

Molecular weight and size moments

Peak 1, Polydispersity ($\overline{M}_n / \overline{M}_w$) = 1.0035	
$\overline{M}_n$ = 593,000	$\sqrt{\overline{r}_n^2}$ = 31.7
$\overline{M}_w$ = 595,000	$\sqrt{\overline{r}_w^2}$ = 31.7
$\overline{M}_z$ = 597,000	$\sqrt{\overline{r}_z^2}$ = 31.7
Peak 2, Polydispersity = 1.0032	
$\overline{M}_n$ = 213,000	$\sqrt{\overline{r}_n^2}$ = 17.1
$\overline{M}_w$ = 214,000	$\sqrt{\overline{r}_w^2}$ = 17.1
$\overline{M}_z$ = 215,000	$\sqrt{\overline{r}_z^2}$ = 17.1
Peak 3, Polydispersity = 1.0016	
$\overline{M}_n$ = 31,000	$\sqrt{\overline{r}_n^2}$ = 2.5
$\overline{M}_w$ = 31,020	$\sqrt{\overline{r}_w^2}$ = 2.7
$\overline{M}_z$ = 31,060	$\sqrt{\overline{r}_z^2}$ = 2.8

The size resolution limit of a single light scattering measurement depends on signal strength, relative noise or extraneous background contributions, and the *duration* of the measurement. This latter factor affects the means by which the precision of the measurement may be determined. Typically, values of the order of $\lambda/20$ are reported. Smaller results are shown in Table 4 based on averaging hundreds of measurements and the corresponding statistical improvements. The size moments calculated for the 30 kilodal-

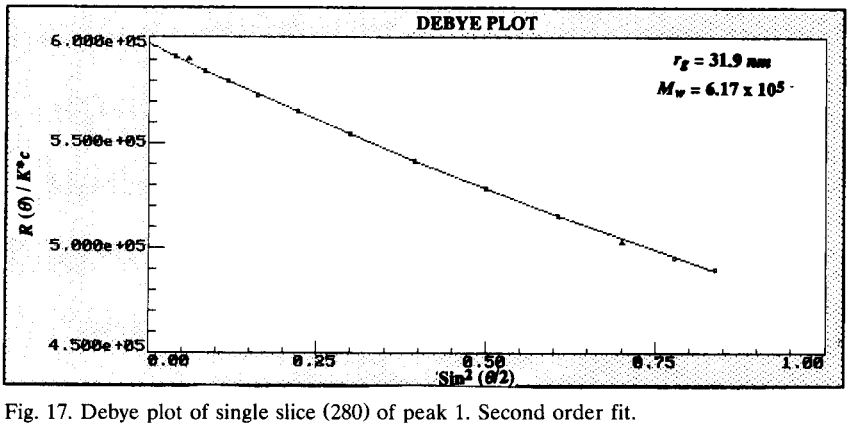

Fig. 17. Debye plot of single slice (280) of peak 1. Second order fit.

ton molecular weight fraction are based on the statistical averaging over $\langle r_g^2 \rangle$ values, both positive and *negative*. The average should be very close to zero if suitable detector normalization was implemented. These small values may be in error by a few nm.

Figure 17 presents the Debye plot $[R_\theta/(K^*c)$ vs. $\sin^2\theta/2]$ of a single slice from the high molecular weight peak of Table 4 as generated by ASTRA. The slope of the line near the origin is directly proportional to the mean square radius while the intercept (at very low concentration) yields the mass directly [see Eq. (31)]. Figure 18 contrasts the corresponding Zimm plot $[K^*c/R_\theta$ vs. $\sin^2\theta/2]$ for the same slice. Although it is somewhat difficult to see from the figures, the Debye plot required a second order fit while the Zimm plot only required terms linear (i.e. first order) in $\sin^2\theta/2$. Both *final* results agree to within experimental error. Analytically, there is no difference between the methods. Once the angular variation begins to depart from linearity, the Zimm plots must drop the higher angle contributions if a *linear* fit is to be used. (Contrast the results of Figs. 12 and 13.) As molecular weights become very large, the application of Eq. (8) to extract the molecular parameters becomes preferable to (and safer than) Eq. (26). Figures 17 and 18 each disclose another very important feature of the multiangle measurement technique. The data collected at the lowest two angles have been dropped (indicated by the triangle symbols), i.e. they are not included in the data used for the least squares linear (Fig. 18) or quadratic (Fig. 17) fits. As is clearly evident from examination of these points (and corresponding ones for other slices in this peak), some column debris appeared simultaneously with the sample and affected these angles, or the angles were normalized incorrectly. In any event, they are easily dropped without any significant effect since the other data points are sufficient to derive the results required.

As discussed in the theoretical section, the determination of $\langle r_g^2 \rangle$ is generally independent [see Eq. (35)] of c, M and dn/dc for homopolymers at concentrations low enough to drop terms in the second virial coefficient, A_2. Figure 19 presents a plot of the logarithm of the root mean square radius $r_g = \langle r_g^2 \rangle^{1/2}$, as a function of elution volume for the sample peaks as defined in Fig. 15. Note that there is a great variation (fluctuation) in these values at the smallest (30 kilodalton) sample because of resolution limitations already discussed. Figure 20 presents the corresponding mass variations with elution volume for the two largest masses and four selected delay volumes between the LS and DRI detectors. Also plotted are the four DRI signals, typically the only detector used for HPSEC. This former "spider" plot confirms the critical depen-

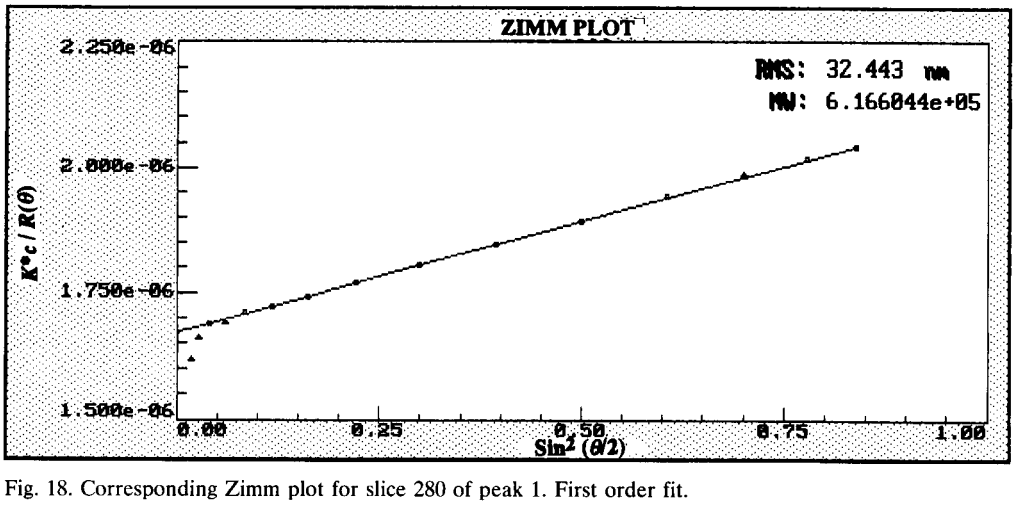

Fig. 18. Corresponding Zimm plot for slice 280 of peak 1. First order fit.

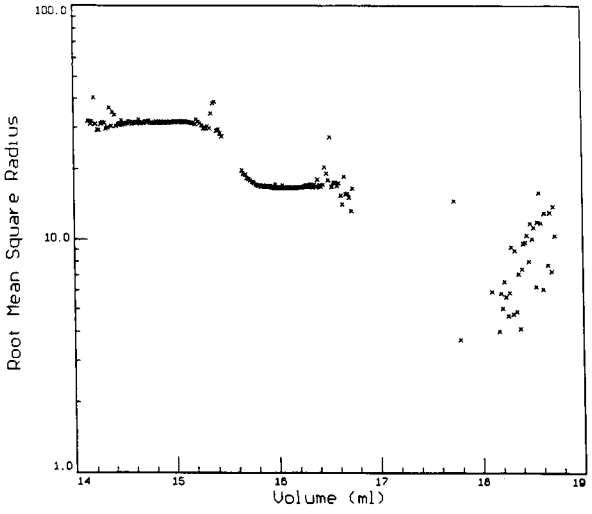

Fig. 19. Logarithm of r.m.s. radius (r_g) versus elution volume for the three polystyrene standards of Fig. 16.

dence of the calculated mass on the corresponding concentration/DRI values. Since the sizes are effectively constant over the peak regions selected, the corresponding masses must be constant, i.e. only [39] the delay volume of 173 μl is satisfactory. Yet even this value does not produce correspondingly constant mass values, indicative of slight instrumental broadening [39]. Note that the 139 μl delay volume yields mass vs. elution

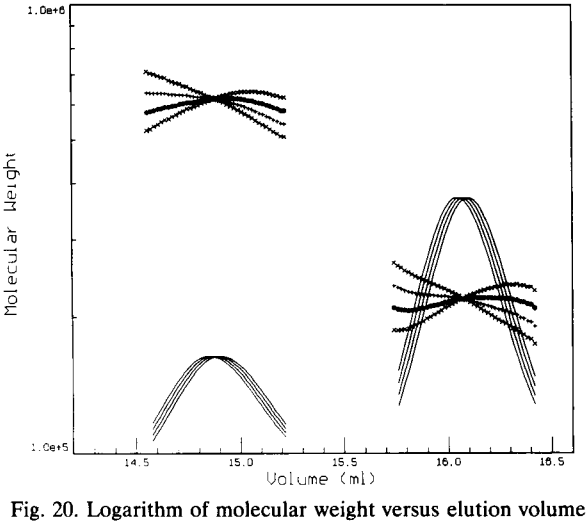

Fig. 20. Logarithm of molecular weight versus elution volume for the two largest polystyrene standards of Fig. 16 at four different delay volumes. The DRI signals are also shown.

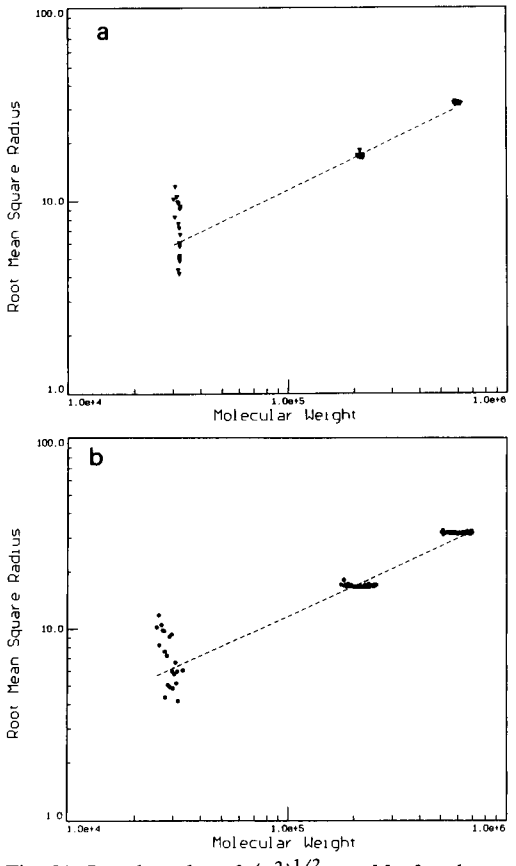

Fig. 21. Log–log plot of $\langle r_g^2 \rangle^{1/2}$ vs. M_w for the two delay volumes 173 μl and 139 μl of Fig. 20.

volume curves identical to the traditional HPSEC "calibration" curves, yet it would yield a mass *variation* inconsistent with the nearly monodisperse character of the standards used.

Figure 21 presents a plot of log r_g as a function of log M for the two delay volumes of 173 μl and 139 μl, respectively. Although both yield "conformation" slopes between 0.52 and 0.54, corresponding to the expected variation of a random coil molecule, only the 173 μl delay volume produces a plot consistent with the "constant-size-means-constant-mass" thesis. Indeed, the narrow standards used elute over a range of volumes considerably broader than the volume of the injection loop (100 μl) because of instrumental broadening in the columns. The separation process itself dilutes the samples injected even if

the masses are identical throughout the sample, i.e. the columns do *not* concentrate molecules of the same molecular mass and size. Note also that a conformation plot based on only two clusters of points is of only limited value, as slight variations of the data points can result in drastically changed slopes. With the addition of other masses to the plot, a slope closer to 0.57 would be obtained.

Plots of log r_g as a function of log M are of great use in other applications. For example, for the study of branched polymers, plots of both the branched and linear polymers can be used to generate the so-called branching ratios for each mass fraction. This ratio at a given mass M is just the ratio of the corresponding $\langle r_g^2 \rangle$ values. Thus, if plots of log r_g versus log M are superimposed on the same graph, then the branching ratio at the mass M is defined [40] as the ratio

$$\rho_M = \langle r_g^2 \rangle_{br} / \langle r_g^2 \rangle_{lin} = \frac{\int_{br} r^2 dm}{\int_{lin} r^2 dm} \qquad (67)$$

where the subscripts *br* and *lin* refer to the values of the branched and linear molecules, respectively. For the same mass, it would be expected that the structure of the branched polymer would be more compact than that of the corresponding linear polymer. Thus the mean square radius of the branched polymer should be less than that of the linear polymer, again for the same mass. Before the advent of HPSEC, application of Eq. (67) had to be made using narrow monodisperse fractions for which $M \approx M_w \approx M_z$. As Stockmayer and Fixman [41] pointed out, one cannot obtain accurate branching ratios from light scattering unless the ratio of Eq. (67) is calculated for the *z*-average *molecular weight*. However, in the HPSEC context (extremely narrow monodisperse fractions assumed in each slice), obtaining the branching ratio from light scattering is much to be preferred [38,40] over indirect viscometric derivations based on concepts of universal calibration [42]. Once the branching ratios are calculated, the branching frequency may be calculated based on a priori knowledge of the type of branching present.

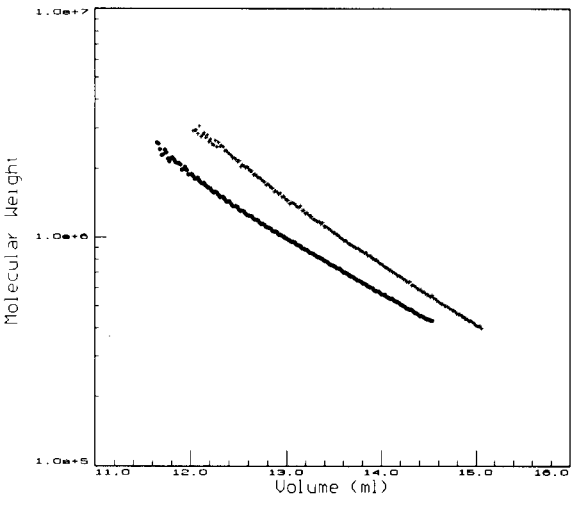

Fig. 22. Mass elution versus volume for two samples of PMMA of comparable masses. The branched material elutes later.

Fig. 22 shows the HPSEC elution chromatograms from two samples of PMMA of comparable molecular weights (calculated from LS measurements). Note that the sample eluting later must be of smaller hydrodynamic size, and indeed it corresponds to the branched material. This is a vivid example of why ordinary HPSEC techniques based on calibration standards are ineffective and often may yield erroneous mass distribution results if the standards and the sample are of different conformations. Figure 23 shows the log mass versus log radius plots confirming that the branched material corresponds to a tighter binding within the molecule (smaller r_g for the same mass). The branching ratios per Eq. (67) are now directly calculable from these data, though it may be appropriate to smooth out the branched data analytically first because of the apparent fluctuations of the radius values shown in Fig. 23. Note that the variation of mass of the branched material is almost independent of the corresponding root mean square radii. The linear sample has a slope corresponding to a random coil configuration while the slope of the branched material is very much smaller.

Departures of molecular solutions or suspensions from a simple linear conformation are easily visualized from log–log plots of r versus M. For example, Fig. 24 presents these plots for a series

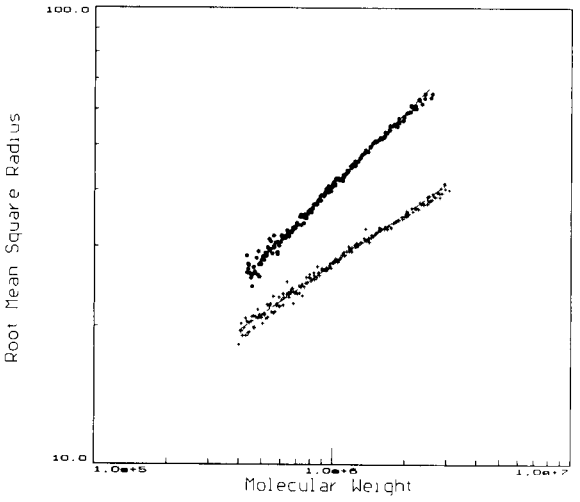

Fig. 23. Conformation plots of linear and branched samples of PMMA. Branching ratios may be calculated directly from these results.

of polystyrene fractions, each of which contains gels [43]. The departures, especially for the higher molecular weights, of these curves from the standard straight line behavior characteristic of random coils is noteworthy and immediately suggestive of the onset of different polymerization processes. Matsumoto [44] has developed a theory of microgel formation that predicts the effects shown in Fig. 24. For relatively broad standards, the log–log plots may yield straight lines or regions whose slopes are less than 0.33 (the value ex-

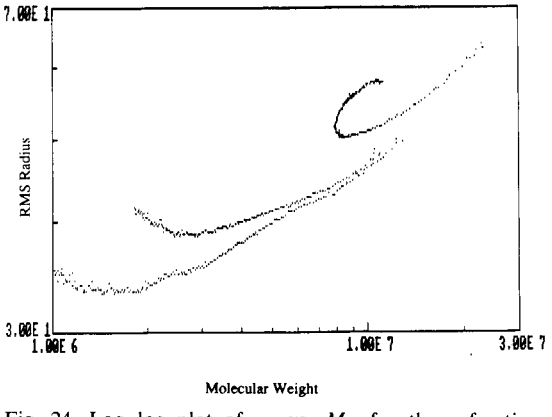

Fig. 24. Log–log plot of r_g vs. M_w for three fractions of polystyrene containing gels.

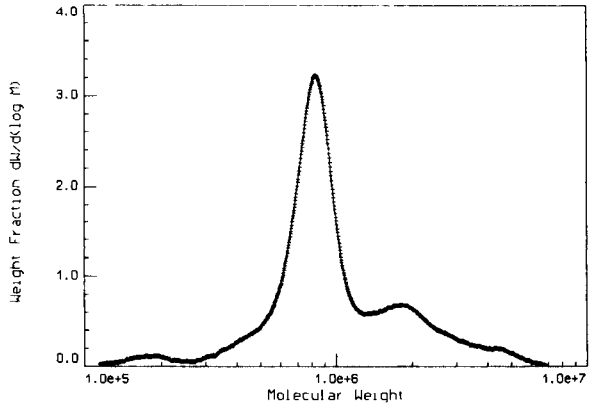

Fig. 25. Differential molecular weight distribution derived from thyroglobulin generated LS data using a three angle (~ 45°, 90°, 135°) detector at 680 nm.

pected for the most compact homogeneous spherical molecule). Such values immediately imply that branching is present for certain types of polymers produced by anionic polymerization [15] which should correspond to random coils (with slope between 0.5 and 0.6). A slope less than 0.50 for such species also is indicative of branching presence.

The application of light scattering is not restricted to simple macromolecules in organic solvents. Jackson, Nilsson and Wyatt [45] have presented the results of light scattering measurements on a variety of biopolymers. Figure 25 shows an example of a derived differential mass distribution for sample of the protein thyroglobulin. The aggregation of some of these narrow distribution molecules is clearly evident at the higher molecular weights. The LS data for this sample were collected at *three* angles only using the miniDAWN® system described earlier. Figure 26 is a particularly interesting example of this "aggregation aggravation". Figure 26 shows a plot of LS elution curves at the angles selected for the same commercially produced immunoglobulin. The scattering from the monomeric component is at the right and it elutes long before this component is the aggregate shown at the left. It is an extremely large structure (r_g ~ 120 nm) showing a variation of scattered intensity angle with a *minimum* around $\sin^2\theta/2 = 0.75$, i.e. $\theta \sim 120°$. In the

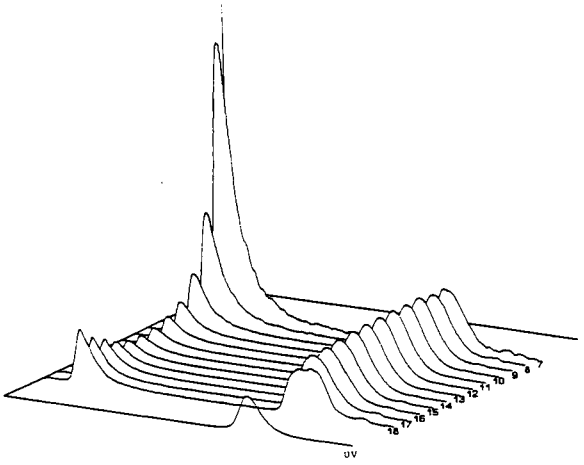

Fig. 26 Light scattering elution curves for an immunoglobulin preparation showing presence of aggregates undetected by UV detector.

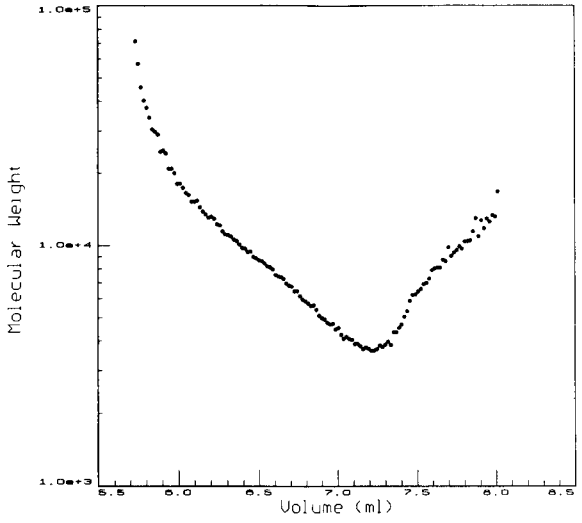

Fig. 28. Log M versus elution volume for the heparin sample of Fig. 27.

foreground is the UV detector recording. Note the absence of any signal at the aggregate elution.

Figure 27 presents an interesting example of the further potential of LS techniques combined with HPSEC. Here we see a chromatogram of the 90° scattering from an unrefined sample of the polysaccharide heparin. Note that the light scattering chromatogram shows two features not seen by the DRI detector: the large mass fraction at the left arising from an aggregated fraction and the noticeable increase in the light scattering signal just beyond the DRI peak. Because there is no DRI signal for the aggregate precursor, its concentration (very low) could not be estimated and, therefore, its corresponding molecular weight moments could not be calculated. However, for the succeeding slices, this was not the case since Fig. 28 clearly shows an *increase* in molecular weight, corresponding to the increase noted in the light scattering signal beyond the DRI peak. This type of behavior echoes the mass versus elution volume results implicit in Fig. 24

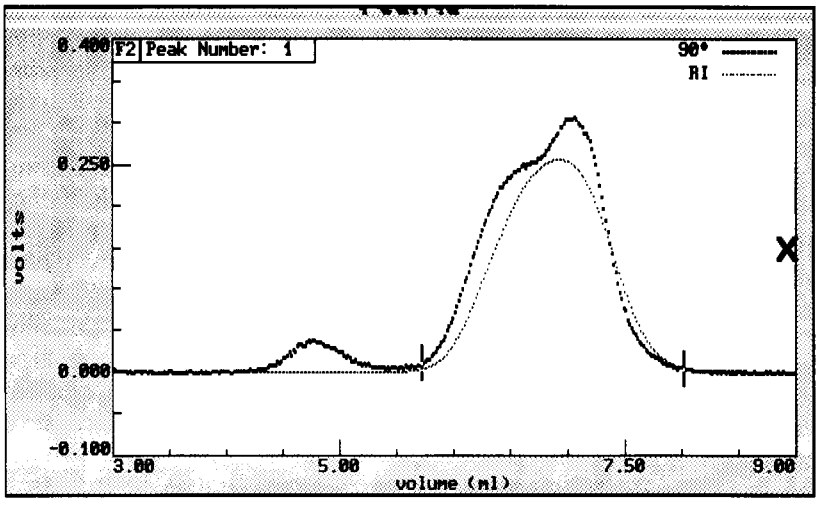

Fig. 27. Chromatogram for 90° scattering contrasted with the DRI signal for a preparation of heparin.

for the case of polystyrene microgels. The apparent heparin microgels are so small, however, that their size could not be estimated. The *z*-average root mean square radius of the aggregate peak, on the other hand, yields a value of about 40 nm.

One of the most difficult of biopolymers to analyze has been the mucopolysaccharide hyaluronic acid. Only with the advent of multi-angle measurement systems combined with HPSEC have definitive molecular weight and structural analyses of this complex biopolymer become practical. Measurements of hyaluronic acid by Yu, Masi and Burns [46] have shown that the derived distributions of molecular weights depend critically on the pH and molality and type of the buffer.

As mentioned earlier, dn/dc may change with molecular weight for certain types of heterogeneous co-polymers. For other copolymers of regular structure, dn/dc is relatively constant over a broad range of molecular weights. The analysis of co-polymers is a most difficult undertaking that is becoming increasingly important with recent emphasis on the development of new materials and blends. Light scattering is an essential tool for such analyses but often must be combined with additional measurements [47–50]. If dn/dc is essentially constant over the co-polymer distributions present, then the light scattering analysis may be performed in the usual manner. But, if the compositions are highly heterogeneous and the monomeric components have significantly different dn/dc values, then these additional measurements are needed so that the concentration, c, and dn/dc may be determined for each slice [51]. Note that a DRI detector can determine only one of these quantities so additional detectors must be used. Gores et al. [52] have suggested in the referenced abstract that a viscometer combined with LS and DRI will suffice, yet at this writing, their work has not been completed.

Light scattering techniques are often criticized as being difficult or inapplicable for the characterization of polymers of molecular weights much below 10 kilodalton. Actually, light scattering measurements may be made at very low molecular weights for sufficiently high concentration and/or dn/dc values. Figure 29 is an example of

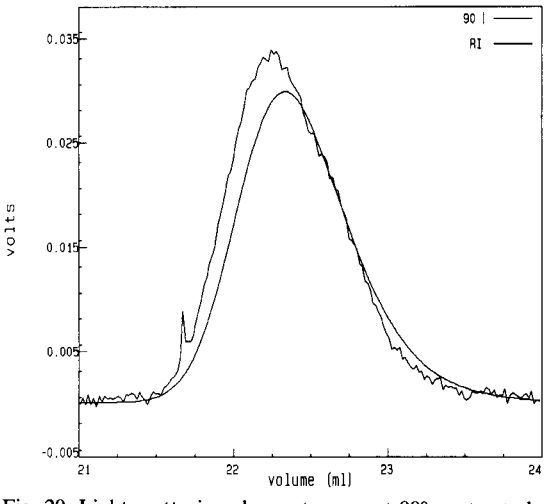

Fig. 29. Light scattering chromatogram at 90° contrasted with DRI signal for a polystyrene sample of nominal molecular weight of 800 g/mole.

a LS chromatogram from a polystyrene sample of nominal molecular weight of 800 g/mole. Measurements were made in THF using a standard vertically polarized 5 mW He–Ne laser, two PSS columns (10^6 Å and 10^4 Å), and an injected mass concentration of about 2% (total mass injected was 2.3 mg). Table 5 presents the derived molecular weight moments assuming $dn/dc \approx 0.168$ ml/g, which may be slightly too high since this corresponds to the value for polystyrene of $M_w \sim$ 10 kilodalton. The improved sensitivity of the hybrid transimpedance photodiodes used for detectors is clearly evident from these measurements. Typical LALLS instruments still incorporate photomultipliers whose performance in the red spectral region has always been very marginal because of poor quantim efficiency. The relative sensitivity of such photomultipliers is a factor of two to five *less* than the corresponding photodiode. In addition, the photodiodes have much

TABLE 5

Molecular weight moments for a low (800 g/mole) molecular weight polystyrene

M_n	808
M_w	853
M_z	899

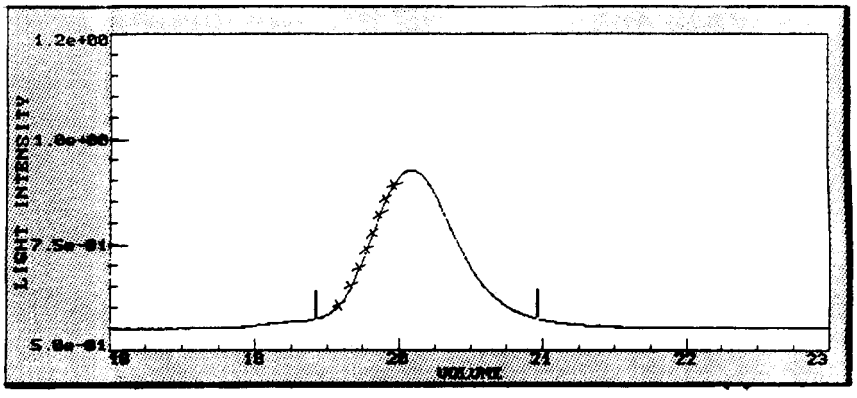

Fig. 30. The 90° light scattering chromatogram for an integrated nominal 1 M g/mole polystyrene sample in THF showing seven different concentrations regions marked on the ascending slope.

greater linear dynamic range and far less temperature dependence.

On-line Zimm plots

The configuration of an on-line light scattering detector combined with separation by HPSEC as shown in Fig. 14 leads to a new and very attractive approach for simplifying and improving the fundamental Zimm-plot procedure. If the columns were absent or if the sample were not separated (for example, for sample fractions beyond the exclusion limit of the columns), then each slice would contain the same unseparated sample (same M_w) but at *different concentrations*. The serial concentration detector (DRI) could provide the concentration at each unseparated slice, though as we shall see shortly, even this is not necessary. But this is exactly the information required to make a Zimm plot (see the first section of *Measurements*), i.e. a series of dilutions of the same unfractionated sample. Thus, with suitable software presently available and a sufficient dilution range, one could generate the data *on-line* to produce a Zimm plot directly *without preparing individual dilutions*. Figure 30 shows such a sample chromatogram from the 90° light scattering peak of an unseparated nominal one million molecular weight polystyrene standard in THF. Marked on-screen are the seven concentrations to be used in the Zimm plot. Figure 31 presents the Zimm plot (contrast Fig. 11) created by the program ASTRAURdinary™ from these

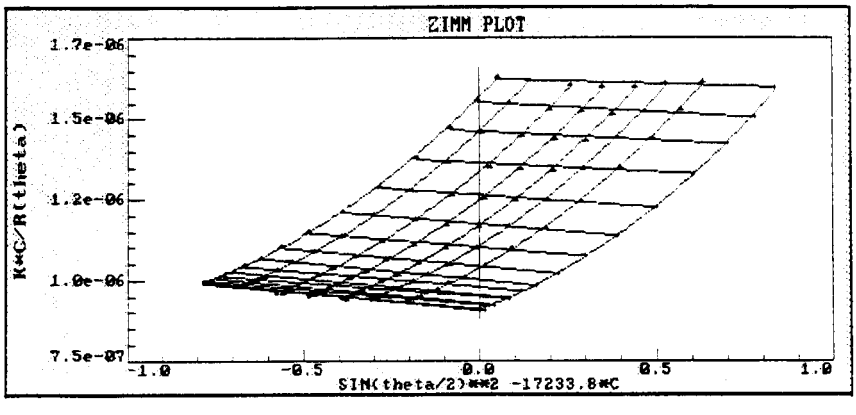

Fig. 31. Zimm plot generated from seven of the eight concentrations specified in Fig. 30.

data, each selected concentration having been averaged over five slices. From this plot, the weight average molecular weight and root mean square radius were 1.26×10^6 g/mole and 51 nm, respectively. The second virial coefficient, A_2, was 3×10^{-4}. The ease and apparent simplicity of this approach deserves further investigation.

If the sample is not separated, each slice contains the same distribution of molecular weights, and the LS signals are directly proportional to $c_i M_w$, where c_i is the mass concentration at the slice i and M_w is the weight average molecular weight of the sample. If we know the total injected mass, say, M_I, then we have

$$M_I = \Delta v \Sigma c_i \tag{68}$$

where Δv is the volume of each slice. However, if we consider the scattering at a *single* angle, say 90°, then

$$R_i(90°) = Bc_i \tag{69}$$

i.e. the measured excess Rayleigh factor at 90° of slice i is directly proportional to the concentration, c_i. In the highly dilute HPSEC limit, $2A_2Mc$ is assumed to be very small compared to 1 and may be dropped [see Eq. (8)]. Here, B is the constant of proportionality and includes a contribution directly proportional to M_w. On summing over each slice, we have

$$\begin{aligned} B &= \Sigma R_i(90°)/\Sigma c_i \\ &= \Sigma R_i(90°)/(M_I/\Delta v) \\ &= \Delta v \Sigma R_i(90°)/M_I \end{aligned} \tag{70}$$

Thus

$$\begin{aligned} c_i &= R_i(90°)/B \\ &= R_i(90°)/(\Delta v \Sigma R_i(90°)/M_I) \\ &= M_I R_i(90°)/[\Delta v \Sigma R_i(90°)] \end{aligned} \tag{71}$$

Thus, for an unseparated sample, the concentration at a particular slice i is readily calculated from the known injected mass M_I and the measured Rayleigh excess ratio per Eq. (10) at a fixed angle, say 90°, at that slice. The peak limits must be selected so that ΣR_i (90°) includes *all* contributions of the injected mass. In addition, no mass fractions must remain in the columns.

Although it is possible to produce an unseparated sample (as just described), if the concentration points were selected and had been on the descending side of the peak, the results would not have been as good due to sample separation by hydrodynamic effects within the connecting tubing itself. Such separations may be minimized by using short leads of tubing between the injector and light scattering photometer and introducing a mixer just before the photometer.

Returning now to the standard Zimm plot procedure of preparing discrete concentrations, the HPSEC configuration with DRI detection offers another important advantage. With a flow cell firmly in place, discrete concentrations of the prepared polymer may be injected sequentially without any columns while the data are collected in a traditional chromatography mode. Figure 32 shows the 90° LS chromatogram produced using a

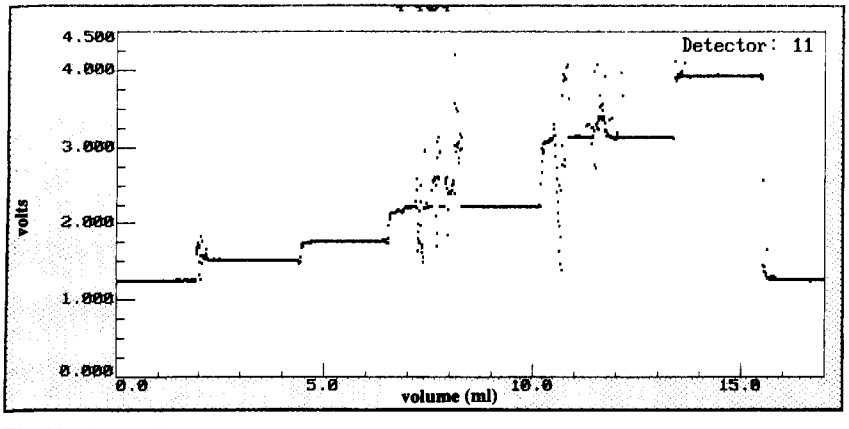

Fig. 32. The 90° light scattering chromatogram produced during the sequential injection of five distinct concentrations of a nominal 1 M molecular weight polystyrene sample in toluene.

syringe pump. The data collection begins with a syringe containing only the solvent (toluene for this example). After a good baseline has been obtained, each of the five concentrations is injected in ascending order alternating between a pair of syringes loaded from cuvettes containing the suitably prepared concentrations. Each injection (at 1 ml/min) is allowed to proceed until a flat plateau is reached and then data collection continues for a few minutes. Each syringe is fitted with a 0.45 μm filter to remove large dust particles. Note that collection continues uniformly even though the flow is intermittently interrupted during the changing of the syringes. Between plateaus, referring to Fig. 32, one sees the noise created during syringe changing, much of which arises from the introduction of bubbles between samples. After the measurement of the final concentration, the pure solvent is introduced again and a final baseline plateau of data is collected.

The data may now be processed as though the sample corresponded to a single sample injection described earlier. The baselines are set. However, the data collected by the DRI detector are replaced by the 90° data since the concentration at each plateau is known a priori. This set of 90° signals will serve no function except to permit the setting of a DRI baseline, required by the chromatography software. Once the baselines are set and the entire range of the measurements ascribed to a single peak, the HPSEC program will calculate the excess Rayleigh ratios per Eq. 10 for each point. In the ASTRAURdinary™ sub directory, a section from each plateau is selected corresponding to a set of 11 slices within a smooth region of each peak. The data are averaged (for each angle) over the 11 slices and then transferred to the Zimm-plot routine (e.g. AURORA). The injection concentration corresponding to each plateau value is entered manually and a result such as shown in Fig. 33 is produced. The excellent appearance of this Zimm plot is due in large measure to two factors: the fixed scattering geometry (no changing of the sample containing cell) and the precision of the sample preparation.

CONCLUDING REMARKS

Light scattering has been confirmed as the method of choice for molecular mass and size characterization by virtue of new instrumentation

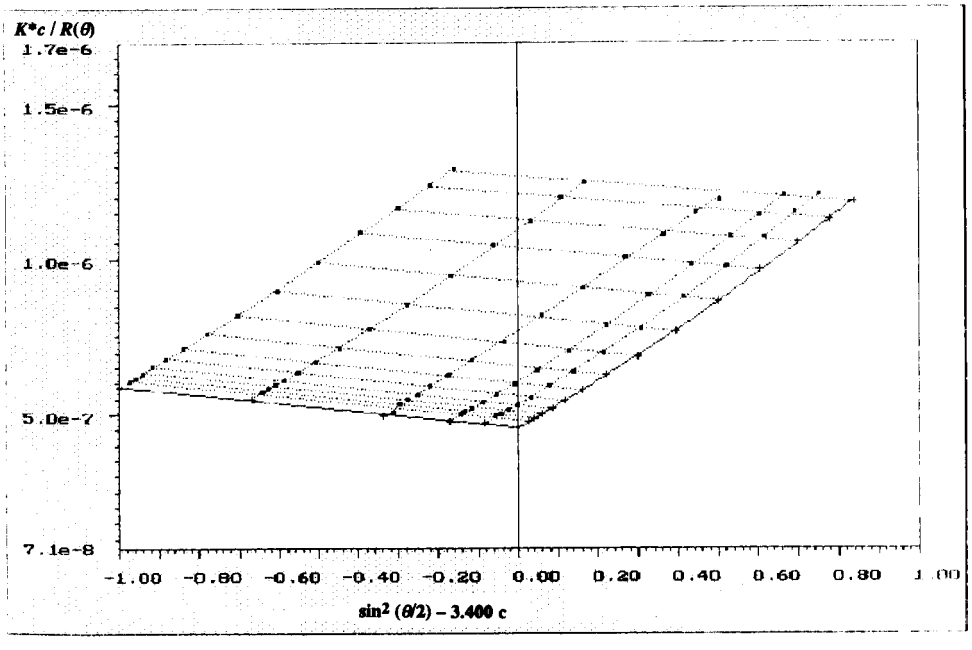

Fig. 33. Zimm plot of the ASTRA-collected data of Fig. 32.

and new techniques. On the one hand, light scattering photometers have now been developed that can measure the angular variation of the scattered light intensity at 15 distinct scattering angles simultaneously and repeatedly. For smaller molecules, a 3-detector system will suffice. This has ensured a high degree of experimental precision in the deduction of key molecular parameters from the measured scattered light intensities. New and improved electronics have increased sensitivity significantly while decreasing detector drift and other temperature dependent effects. The separation techniques of (size exclusion) chromatography, coupled with this dramatically improved detector sensitivity have provided an ideal vehicle for macromolecular characterizations. For the first time, it is now possible to derive molecular mass and size distributions of samples for which only mass determinations were previously available. The further development of an interferometric refractometer operating at the same wavelength as the laser light scattering photometer permits the absolute measurement of the refractive index increment, dn/dc, of the dissolved polymer with high accuracy. This basic quantity is required both for light scattering measurements and the correct interpretation of the output signals from conventional DRI detectors.

Differential (multiangle) light scattering measurements combined with HPSEC represent, therefore, fundamental tools for macromolecular investigations. Although there are important classes of molecules whose size is so small that a measurement at a single angle may be sufficient to derive their mass, the added versatility and precision associated with the simultaneous measurement at many angles should not be overlooked. Continuing improvements in software ensure that even the most complex light scattering measurement and interpretation may be performed by technicians and scientists even when their knowledge of the subject matter may not be extensive. "User friendly" software is a term that has become a requirement of HPSEC analysis.

HPSEC represents only one, albeit an important one, of the many techniques being developed for separating macromolecules. Among the newer techniques for which light scattering measurements will play an increasingly important role are sedimentation and thermal field flow fractionation (SFFF, ThFFF), temperature rising elution fractionation (TREF), charge affinity and reverse phase chromatography, capillary electrophoresis, and ion exchange chromatography. The actual time of elution (elution volume) is irrelevant for light scattering mass determinations of weight average molecular weights, as long as the concentration, dn/dc, and (if needed) the second viral coefficients are known. Indirect techniques such as viscosity that depend critically on calibration standards become inadequate with increasingly complex molecular structure.

In passing, a few words should be said concerning intrinsic viscometric measurements combined with HPSEC. They enjoy considerable popularity because the apparatus is simple and the measurements seem easy to perform. Although they are mistakenly believed to be useful for lower molecular weight characterization (in a HPSEC configuration) than light scattering detectors, they have an upper molecular weight limit one to two orders of magnitude *below* light scattering. At low molecular weights, the detection sensitivity of the two methods are comparable since the LS signal is proportional to M and (for random coils) the viscometer signal is proportional to $M^{0.7}$. The shear rate dependency of high molecular weight ($> 10^6$ g/mole) polymers also poses problems for viscometric detectors. This is less important for LS/HPSEC, as long as there is also no (irreversible) degradation. Indeed, even at molecular weights below 10 kilodalton, viscometers also fail badly because the Mark-Houwink coefficients become functions of molecular weight and dn/dc begins to change rapidly. (The latter affects the concentration derived from the conventionally used DRI detectors.) In his classical text *Molar Mass Measurements in Polymer Science* [38], Billingham makes the point that viscosity is probably the *least* satisfactory method for determining molar masses of polymers. Among the unsatisfactory elements he singles out for criticism are: (a) reliance on the so-called universal calibration (the use of a semi-empirical relation between intrinsic viscosity and

molar mass), (b) the calibration is difficult and imprecise, and (c) the molar masses derived are of doubtful value. Indeed, tremendous amounts of time are required for calibration each time a column is replaced or a mobile phase changed, or whenever the resolution of a column set deteriorates. The viscometric method is, of course, not absolute but rather a relative mass measurement of the viscosity average molecular weight, M_v.

If a column is calibrated to produce a universal calibration curve [42] using well defined calibration standards, then from the previously established Mark-Houwink coefficients of the standards, one obtains a monotonic relationship between the logarithm of the product of the molecular weight and the intrinsic viscosity, and the elution volume. Once such a universal calibration has been achieved, light scattering measurements which yield directly the weight average molecular weight at each elution volume can be used in many cases to deduce the associated intrinsic viscosity without a viscometer [53].

Below about 10 nm, the precision of the root mean square radius derived from light scattering at 633 nm begins to deteriorate rapidly. Only by slowing the pump rate down, increasing the mass injected, and increasing the number of measurements can this precision be improved. Alternatively, since there should be a simple linear relation between the logarithm of molecular weight versus elution volume, a plot of a relatively broad weight distribution polymer can be effectively extrapolated through lower molecular weights as shown in Fig. 34 for the broad polystyrene standard NIST SRM706. Naturally, the extrapolation cannot be made below the total penetration limit.

Considerable improvements in both instrumentation and software are expected in the years ahead. But, while those events continue, far greater attention is needed for the interpretation of the light scattering results. The accurate confirmation of the Einstein-Raman-Debye theory in the RGD approximation implies that higher moments of the mass distributions may be derived directly from the light scattering measurements. Instead of extrapolating to zero scattering angle and zero concentration, the full angular variation of the scattered intensities with scattering angle

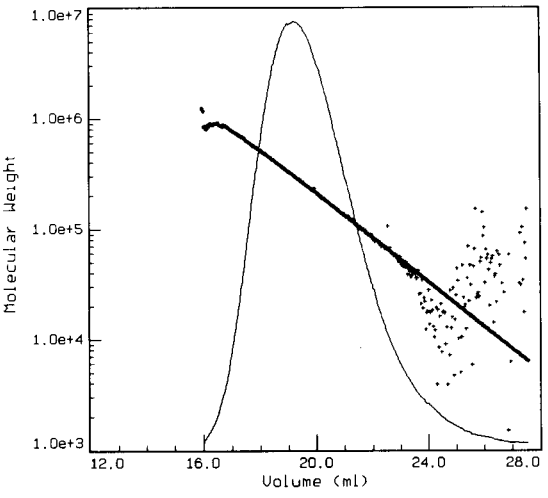

Fig. 34. Log molecular weight versus elution volume for NIST SRM706 with extrapolation through the smaller molecular weights. The DRI signal is superimposed.

as indicated explicitly by Eq. (17) may be applied to extract higher mass distribution moments. Naturally, after a separation (such as HPSEC), the concentration of each slice is fixed and cannot be extrapolated to a zero value. Nevertheless, these concentrations are generally so small that the near zero concentration approximations to the theory may be used. As discussed earlier in this paper, Zimm's original procedure was based on linear extrapolations to extract the molecular mass, size, and second virial coefficient. With the advent of precision instruments, such as the DAWN, non-linear regression techniques permit the extraction of these higher moments by making use of the entire angular variation of the scattered light. In addition, for large enough molecules, it is now possible to derive the third virial coefficient to which, historically, very little attention has been paid. Finally, more complex and larger molecules, as well as large colloidal particles and even single cell organisms, may now be measured and characterized by light scattering [16,54–58].

The author would like to acknowledge the contributions of Lena Nilsson, Janet Howie, James King, Richard Thomas and Dr. Hemnalini Kumar for the extensive development and meas-

urement programs that formed the basis for much of the material reported here. Special thanks go to Dr. Louis A. Papazian of the American Cyanamid Company who has never given up on my continuing education in polymer characterization and HPSEC. Finally, these acknowledgments would not be complete without mention of Dr. David Shortt and Dr. Gary Janik whose keen insights have helped mightily in the development of the instrumentation and its underlying analytical achievements.

REFERENCES

1 A. Einstein, Ann. Phys., 33 (1910) 1275.
2 C.V. Raman, Indian J. Phys., 2 (1927) 1.
3 P. Debye, J. Appl. Phys., 15 (1944) 338.
4 B.H. Zimm, J. Chem. Phys., 13 (1945) 141.
5 B.H. Zimm, J. Chem. Phys., 16 (1948) 1093.
6 B.H. Zimm, R.S. Stein and P. Doty, Polymer Bull., 1 (1945) 90.
7 M. Fixman, J. Chem. Phys., 23 (1955) 2074.
8 J.C. Moore, J. Polym. Sci., A2 (1964) 835.
9 W.H. Stockmayer and B.H. Zimm, Ann. Rev. Phys. Chem., 35 (1984) 1.
10 B.H. Zimm, J. Chem. Phys., 16 (1948) 1099.
11 B.A. Brice, M. Halwer and R. Speiser, J. Opt. Soc. Am., 40 (1950) 768.
12 D.T. Phillips, BioScience, 21 (1971) 865.
13 M.J.R. Cantow (Ed.), Polymer Fractionation, Academic Press, New York, 1967.
14 P. Kratochvil, in M.B. Huglin (Ed.), Light Scattering from Polymer Solutions, Academic Press, New York, 1972, p. 333.
15 M. Szwarc, Carbanions, Living Polymers and Electron Transfer Processing, Interscience, New York, 1968.
16 H.C. van de Hulst, The Scattering Light by Small Particles, Wiley, New York, 1957.
17 P.J. Wyatt, Appl. Opt., 7 (1968) 1879; Appl. Optics (erratum), 8 (1969) 485.
18 B.H. Zimm, J. Chem. Phys., 14 (1946) 164.
19 DAWN-F Instruction Manual, Wyatt Technology Corporation, Santa Barbara, CA, 1991.
20 D.J. Coumou, J. Colloid Sci., 15 (1960) 408; D.J. Coumou, E.L. Mackor and J. Hijmans, Trans. Faraday Soc., 60 (1964) 1539; D.J. Coumou and E.L. Mackor, Trans. Faraday Soc., 60 (1964) 1726.
21 C.I. Carr, Jr. and B.H. Zimm, J. Chem. Phys., 18 (1950) 1616.
22 P. Debye, J. Phys. Colloid Chem., 51 (1947) 18.
23 O.B. Ptitsyn, Z. Fiz. Khim., 31 (1957) 1091.
24 P. Debye, in D. McIntyre and F. Gornick (Eds.), Light Scattering from Dilute Solutions, Gordon and Breach, New York, 1964, pp. 139–147.
25 P.F. Mijnlieff and D.J. Coumou, J. Colloid Interface Sci., 27 (1968) 553.
26 P.J. Wyatt, J. Liquid Chromatogr., 14 (1991) 2351.
27 A. Guinier, Ann. Phys., 12 (1939) 161.
28 H. Utiyama, in M.B. Huglin (ed.), Light Scattering from Polymer Solutions, Academic Press, London, 1972, p. 41.
29 W. Kaye and A.J. Havlik, Appl. Opt., 12 (1973) 541.
30 W. Kaye and J.B. McDaniel, Appl. Opt., 13 (1974) 1934.
31 U.S. Pat., 4616927, Sample Cell for Light Scattering Measurements, 1986.
32 Wyatt/Optilab 903 Instruction Manual; Appendix A, Wyatt Technology Corporation, Santa Barbara, CA, 1992.
33 T. Phillips and W. Borchard, Eur. Polym. J., 26 (1990) 1289.
34 S.T. Balke, Quantitative Column Liquid Chromatography, Elsevier, New York, 1984.
35 G. Dollinger, B. Cunico, M. Kunitani, D. Johnson, and R. Jones, J. Chromatogr., 592 (1992) 215.
36 P. Putzeys and J. Brosteaux, Trans. Faraday Soc., 31 (1935) 1314.
37 W.W. Yau, J.J. Kirkland and D.D. Bly, Modern Size-Exclusion Liquid Chromatography, Wiley, New York, 1979.
38 N.C. Billingham, Molar Mass Measurements in Polymer Science, Wiley, New York, 1977.
39 P.J. Wyatt and L.A. Papazian, J. Liq. Chromatogr., in press; see also P.J. Wyatt, J. Chromatogr., in press.
40 B.H. Zimm and W.H. Stockmayer, J. Chem Phys., 17 (1949) 1301.
41 W.H. Stockmayer and M. Fixman, Ann. N.Y. Acad. Sci. 57 (1953) 334.
42 Z. Grubisic, P. Rempp and H. Benoit, Polym. Lett., 5 (1967) 753.
43 C. Johann and P. Kilz, J. Appl. Polym. Sci., 48 (1991) 111.
44 A. Matsumoto, ACS National Meeting, Sept. 1990, Washington, DC.
45 C. Jackson, L.M. Nilsson and P.J. Wyatt, J. Appl. Polym. Sci., 43 (1989) 99.
46 L.P. Yu, L. Masi and J.W. Burns, Polym. Prepr., 30 (1989) 360.
47 R. Tremblay, M. Rinfret and R. Rivest, J. Chem. Phys., 20 (1952) 523.
48 W.H. Stockmayer, L.D. Moore, M. Fixman and B.N. Epstein, J. Polm. Sci., 16 (1955) 517.
49 H. Benoit and D. Froelich, in M.B. Huglin (Ed.), Light Scattering from Polymer Solutions, Academic Press, London, 1972, p. 467.
50 T. Dumelow, J. Macromol. Sci. Chem., A26 (1989) 125.
51 H.H. Stuting and I.S. Krull, Ann. Chem., 62 (1990) 2107.
52 F. Gores, C. Johann and P. Kilz, Am. Chem. Soc. PMS&E abstracts, 65 (1991) 106.
53 P.J. Wyatt and D.W. Shortt, Proc. 1991 Waters International GPC Symposium, San Francisco, CA, 1991.

54 B.H. Zimm and W.B. Dandliker, J. Phys. Chem., 58 (1954) 644.
55 M. Kerker, The Scattering of Light and other Electromagnetic Radiation, Academic Press, New York, 1969.
56 P.J. Wyatt, in J.R. Norris and D.W. Ribbons (Eds.), Methods in Microbiology, Vol. 8, Academic Press, New York, 1973, p. 183.
57 P.J. Wyatt and C. Jackson, Limnol. Oceanogr., 34 (1989) 96.
58 I.C. Felkner and B.E. Worthy, J. Anal. Chem., 338 (1990) 489.

Analytica Chimica Acta, 272 (1993) 41–51
Elsevier Science Publishers B.V., Amsterdam

Expert systems in chromatography. Results of the ESCA project

L. Buydens

Department of Analytical Chemistry, Katholieke Universiteit Nijmegen, Toernooiveld, 6525 ED Nijmegen (Netherlands)

P. Schoenmakers

Philips Research, P.O. Box 80000, 5600 JA Eindhoven (Netherlands)

F. Maris and H. Hindriks

Organon International BV, Analytical R & D Laboratories, P.O. Box 20, 5340 BH Oss (Netherlands)

(Received 9th July 1992)

Abstract

The final results of the ESCA project (Expert Systems for Chemical Analysis) are presented. This is one of the major projects in the field of expert systems for chromatography. Expert systems have been developed that cover the important areas of method development in LC. In the last part of the project attention was concentrated on two issues, the study of integration possibilities of the different stand-alone systems and the important aspect of validation and evaluation of the developed expert systems. The integration studies and the results of the validation and evaluation are discussed.

Keywords: Expert systems; Liquid chromatography; ESCA project

The results of automation efforts by manufacturers of chromatographic instruments have led to an increased applicability of chromatographic instruments for routine analysis. The bottleneck of analysis is situated mainly in the development of an optimum method and in the interpretation of the results. These processes usually require a lot of expertise and experience to solve the problems that arise for each particular case. Also, the quality control stage becomes an increasingly important aspect to be automated. As a result of automation, the numbers of analyses and results have grown so much that automatic quality monitoring is necessary. In view of the increasing demands of good laboratory and management practice (GLP and GMP), this aspect will become even more important. The incorporation of expertise and experience in instruments is therefore the next step to be taken.

Expert systems are software programs in which human expertise is implemented. Therefore, they seem to be the right approach for further automation of instruments. In other areas of chemistry they have already been demonstrated to be useful [1–3]. In chromatography, a large amount of research has been carried out in a joint re-

Correspondence to: L. Buydens, Department of Analytical Chemistry, Katholieke Universiteit Nijmegen, Toernooiveld, 6525 ED Nijmegen (Netherlands).

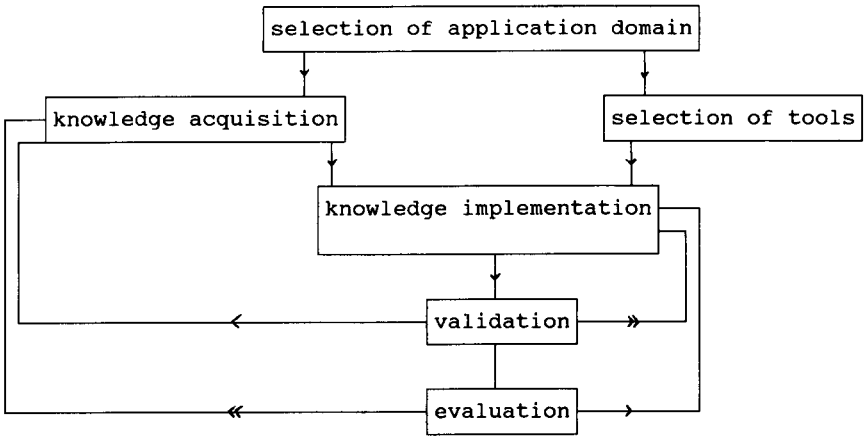

Fig. 1. Different steps in the development process of expert systems.

search project on the applicability of expert systems in chemical analysis (ESCA) [4]. Partners from industry and universities have cooperated to study the possibilities of the expert system approach in LC. In the first stage the development of LC methods for pharmaceutical compounds was selected as an application area. Within this area expert systems were developed that are representative of the whole area of method development: selection of initial method parameters, optimization of selectivity and instrumentation and finally validation of the method obtained. As part of the project all aspects of the expert system building process have been investigated. Aspects of integration and cooperation of expert systems have also been covered.

The project started in May 1987 and officially finished in May 1990. During this period intermediate results and findings have been communicated by means of presentations and so far about 25 papers have been published in international journals and numerous lectures and posters have been presented. In this paper an overview of the most important results is presented.

EXPERT SYSTEM DEVELOPMENT PROCESS

The process of the development of expert systems consists of several stages and has many different aspects. It requires close cooperation between workers who have the necessary application knowledge and expertise and those responsible for the implementation of the expert systems ("knowledge engineers"). The different tasks are shown schematically in Fig. 1. It shows clearly the sequence that has to be followed, the interaction between tasks and the loops that can occur.

The aim of the project was to study and demonstrate the application of expert systems in chromatography. Therefore, it was felt that a single application was too limited to demonstrate the objective. For that reason, a number of (relatively) small domains were selected based on criteria of usefulness, difficulty and variety. These domains were derived from LC method development as shown in Fig. 2. This process resulted originally in four expert systems.

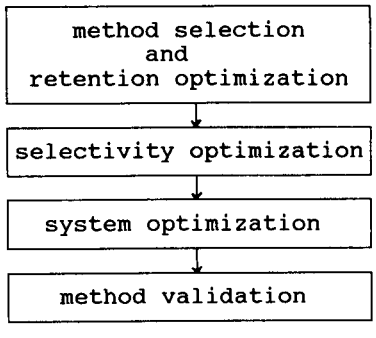

Fig. 2. Stages in the chromatographic method development.

Knowledge acquisition is the process of extracting knowledge as complete as possible from the chromatography expert. This knowledge should then be implemented in a choosen tool by the knowledge engineer, which in this instance was either a chemometrician or a software specialist. The latter requires more time to become familiar with the domain knowledge, but may realise better systems in terms of completeness, consistency and appearance. Chemometricians, on the other hand, can acquire more chemical knowledge in a shorter period of time, but the quality of the resulting software can be inferior.

To implement expert systems in a computer, a software tool is required. This tool can be a standard computer language such as Pascal or C. However, the implementation of expert systems with classical languages requires considerable software engineering experience and a large effort in terms of manpower. In recent years dedicated tools for developing expert systems have become available. These tools are often referred to as "expert system shells". The available tools range from simple to very sophisticated. One of the purposes of ESCA was also to evaluate the suitability of these tools. Therefore, it was necessary to select some suitable tools to implement the applications.

This selection was based on the implementation of a small test knowledge base in different tools of varying size (large, mid-sized and small; see Table 1). The test knowledge base contained essential features of the final knowledge and was obtained from earlier work by De Smet et al. [5].

TABLE 1

List of tools evaluated

Size	Name	Origin	Running on
Small	Delfi 2	Netherlands	PC
Medium	Goldworks [a]	USA	PC
	KES [a]	USA	PC
	Mylog	France	PC
	Nexpert object [a]	USA	PC
Large	S1	USA	Workstation
	KEE	USA	Workstation
	Knowledge Craft	USA	Workstation

[a] These were the tools selected.

TABLE 2

Summary of development environment of the expert systems

Domain	Shell	Expertise centre [a]	Knowledge engineering centre [a]
Method selection and retention optimization	KES	VUB Organon	VUB
Optimization systems:			
Selectivity optimization	KES	VUB Philips NL	VUB
System optimization	Nexpert object + Pascal	Philips NL	Philips Hamburg
Method validation systems:			
Repeatability system	Goldworks	Unicam UK	KUN
Ruggedness system	Goldworks	Unicam UK	KUN

[a] VUB = Free University Brussels, Belgium; KUN = Catholic University Nijmegen, Netherlands; Philips NL = Research Lab., Eindhoven, Netherlands; Philips Hamburg = Research lab., Hamburg, Germany; Organon = Analytical R&D Labs., Oss, Netherlands; Unicam UK = Unicam, Cambridge, UK.

In general, it was concluded that large tools such as KEE or Knowledge Craft were too complicated. They also require large workstations or microcomputers to run on. The small tools were clearly not adequate, e.g., limited implementation possibilities, limited or no access to external databases and poor quality of the end user and knowledge engineering interface. It was finally decided to use a selected group of mid-sized tools, which had the additional advantage of running on normal PCs [6]. Table 2 summarizes the eventual tools from which the systems were built.

Expert systems can only be expected to be useful in practice if they are reliable. Conventional software products can be tested thoroughly through a number of standard procedures. However, for testing expert systems no standard procedures exist. With expert systems both the software and the knowledge base must be reliable and correct. The fact that the knowledge base often contains a lot of heuristic knowledge poses specific problems to the testing phase [7,8]. Considering the increasing demands of GLP, this part in the development process cannot be overesti-

mated. In view of this, considerable effort was devoted to the validation and evaluation of expert systems during the last part of the ESCA project.

EXPERT SYSTEMS OF ESCA

The expert systems that were developed in the ESCA project can be divided into two categories: stand-alone systems and integrated systems. A complete overview is given in Table 3. In this section the stand-alone systems are considered.

Method selection always starts with the choice of the chromatographic mode, be it GC or LC. In LC a further refinement can be made by choosing, for example, the normal- or reversed-phase mode, and further a C_8 or a cyano phase. In this way a decision tree can be built.

DASH (Drug Analysis System in HPLC) is the system that assists in the selection of LC starting conditions for the purity check of pharmaceutical compounds. Because of the complexity of the relationship between the structure (input) and suitable percentage of modifier (output), this system was developed only for heterocyclic basic compounds. As most of these compounds are new chemical entities, there is no literature available on LC analyses for these compounds [9].

LABEL is an expert system that was developed by one of the partners (VUB) before ESCA started. It selects a method for the LC of drugs in pharmaceutical formulations (label claim analysis) [5]. It was included in the project because it covers the situation that one sample must be analysed for different compounds. This is in contrast to DASH. Compounds that are subjected to a purity check usually contain less then 5% of unknown impurities. Optimization is then usually not required. LABEL was added to be able to study the integration of method selection systems with optimization expert systems.

LIT is a small expert system that helps to select all important parameters of a literature method and that checks whether a literature method can be treated by SLOPES.

When the experimental results are not satisfactory, all three expert systems have an extension by which adaptations of the method are suggested in order to obtain an acceptable retention range of the compounds.

The next step in method development is selectivity optimization. This step typically involves the optimization of the mobile phase composition in order to obtain an optimum distribution of the peaks over the chromatogram.

SLOPES (SeLectivity OPtimization Expert System) is an expert system which typically addresses one of the important aspects of selectivity optimization. Initially attention was focused on the selection of an appropriate optimization criterion. In the past, many optimization criteria have been put forward. However, it should be recognized that a single criterion is not always the best one in all situations [10]. SLOPES will help the chromatographer to select the most appropriate criterion, which will then be used to judge the quality of the chromatogram [11]. This selection of a criterion depends, for example, on the selected experimental design and on the objective of the optimization (e.g., best spreading of peaks

TABLE 3

Overview of the ESCA expert systems

Method development stage	Stand-alone expert systems [a]	Integrated expert systems (INT) [a]	
1. Initial method selection and retention optimization	DASH, LABEL, LIT	INT I: DASH LABEL LIT +	
2. Selectivity optimization	SLOPES	SLOPES	
3. System optimization	SOS	INT II	INT III
4. Validation	REPS RES	SOS + REPS	SOS + RES

[a] Names are explained in the text.

or minimum analysis time). Once the optimum selectivity has been obtained the mobile phase composition and stationary phase are kept constant for the next step, system optimization.

SOS (System Optimization expert System [12]) can be used here to select a column with the shortest analysis time from a column set given by the user. In addition, the user should also provide a set of available detector cells and a list of allowed time constants. Finally, some limits should be given, such as the required minimum resolution between a relevant pair of peaks, maximum pressure drop and maximum flow-rate. Within these constraints SOS recommends the column, instrument parameters and optimum flow-rate. It predicts also the required analysis time and the critical resolution. A result of a consultation and the experimental verification is shown in Fig. 3.

The final step in method development is the validation of the method. This means that the quality of the results should be guaranteed to a certain extent. The importance of validation is still increasing in view of increasing GLP demands. The level of validation depends mainly on the intended use of the method. A higher level of validation is required if, for example, the method is to be used in a large number of laboratories over a long period of time. Methods to be used for regulatory analysis need the highest level of

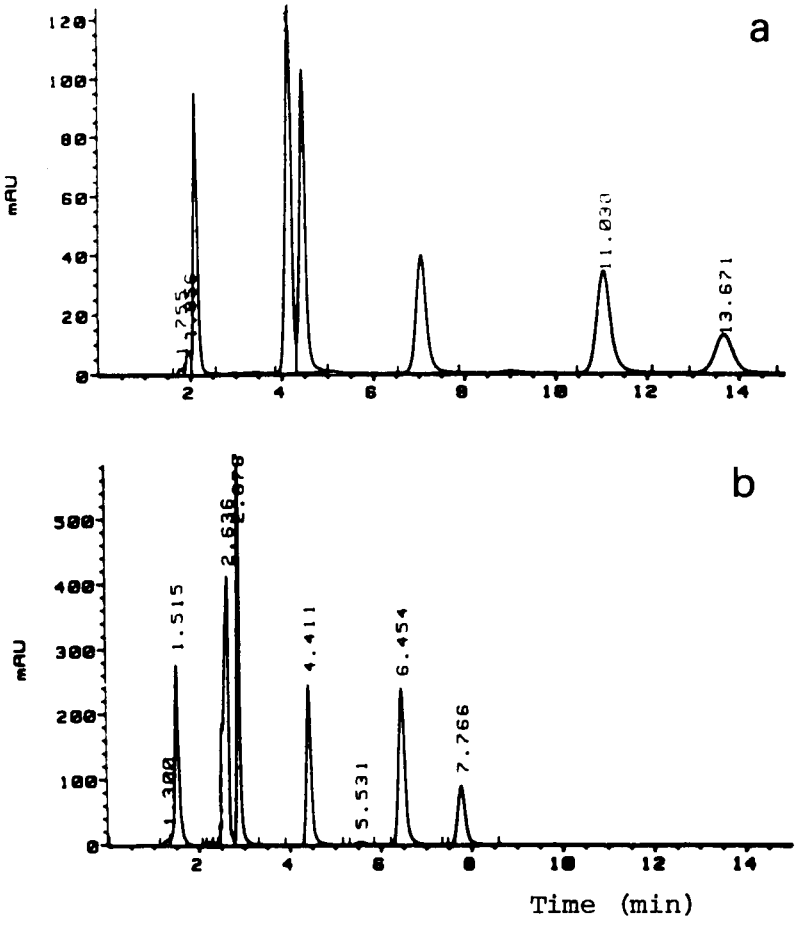

Fig. 3. Optimization with the SOS expert system. (a) Chromatogram before optimization; (b) chromatogram obtained with the conditions as advised by SOS, by which an analysis time and a resolution of 6.2 min and 1.6, respectively, were predicted.

validation. Validation of a method requires the testing of its specificity, precision, accuracy and limitations. These so-called performance characteristics may be tested by validation procedures. Many of these procedures make use of complex mathematics and rely on statistical designs, such as the Plackett–Burman design (e.g., for precision testing). Expert systems can be of great help here in guiding the (inexperienced) user in the set-up of such advanced designs, in the calculation and in the interpretation of the results. In the ESCA project, precision testing was chosen as the most challenging item in method validation to demonstrate the applicability of expert systems. Precision testing involves, in fact, three separate parts: repeatability, reproducibility and ruggedness. In the repeatability test the analysis is repeated a number of times under identical conditions. This is in contrast to the reproducibility test, where different conditions, e.g., different instruments in different laboratories, are applied. Finally, in a ruggedness test the effect of small changes in the operating conditions, i.e., temperature, flow-rate and mobile phase composition, on precision is tested. Repeatability and ruggedness testing were the subject of different expert systems.

REPS (Repeatability testing System [13,14]) is an expert system in which Goldworks software is combined with the Lotus 1–2–3 spreadsheet package. The expert system is used to select test procedures for repeatability. Based on the usage requirements, an experimental design is set up. The spreadsheet can run the algorithms and calculates the variances for peak areas and heights and retention times. The expert system is able to interpret the results and to perform a diagnosis based on how the above parameters vary together. An example of a rule can illustrate how a diagnosis proposal is reached. For instance, if the variance of retention time and the variance in peak areas are large, and the variance of peak heights is small, then it is concluded that the problem of repeatability is imprecision of the flow-rate.

RES (Ruggedness Expert System [15,16]) is a modular expert system in which the Goldworks software is combined with the procedural language C. It is intended to assist in the proper set-up of a complete ruggedness test. This involves heuristical (experience-based) knowledge to select the proper factors (and appropriate levels) to which the method should be rugged. Statistical knowledge is necessary to choose a proper design based on the selected factors and the intended usage of the method. The experimental results are interpreted. If applicable system suitability criteria are provided, factors that cause problems are identified.

INTEGRATION STUDIES [17,18]

The stand-alone expert systems described above all tackle a specific sub-problem of the method development process. These systems are implemented in different shells and run on different hardware. Ideally, the chromatographer should be able to consult the system that is needed in a specific situation as part of a complete method development expert system. Also, from the viewpoint of the knowledge engineers it was seen as a challenging task to integrate stand-alone systems of different origins. Because of the three knowledge engineer centres involved in the project, it was decided to study three partial integrations (see Figs. 4–6).

There are two important aspects to this. First, the analytical experts had to realize that to produce meaningful integrations it was necessary to fill knowledge gaps between the different stand-alone systems, so that additional knowledge acquisition was inevitable. This resulted in considerable extensions of the existing systems and in the addition of new expert systems, such as LABEL and LIT. Second, the knowledge engineers had the difficult task of linking sub-systems of different origins into an acceptable architecture.

INT I [17]. The structure of the architecture of INT I is given in Fig. 4. In this scheme the supervisor is the essential part, having the strategic knowledge to route the end user to the different expert systems. INT I is a typical example for which relatively much additional knowledge was necessary for the integration and integration was necessary in order to obtain a suitable system. As

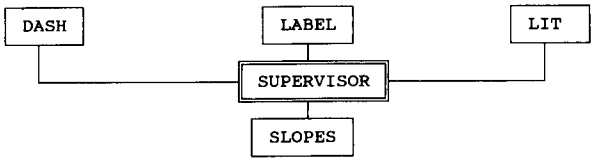

Fig. 4. Structure of the integrated system 1 (INT I).

an extension, it is felt that the integration with the SOS system is necessary because using SOS strongly influences the selection of the optimization criterion.

INT II [19]. Figure 5 shows the structure of the second integrated system. Two of the five subsystems (REPS and SOS) are the original stand-alone systems whereas the other modules were built to add flexibility to the system. This architecture allows the user to consult the system in three different situations. It can be used to assess the repeatability of a new method or to check the repeatability of a previously validated method. Also, the possibility of using the system as a trouble-shooting tool turned out to be a valuable feature.

INT III. Another possibility to link stand-alone expert systems is shown in Fig. 6. In the ruggedness expert system (RES) the system optimization system (SOS) is incorporated as an extra module. The scheduler has knowledge on when to activate which module. The different modules take care of the different tasks in the ruggedness test and the SOS module has been added to provide solutions for problems that have been detected by the diagnosis module. SOS can be used in a number of situations. Primarily, SOS can help to improve a method when the resolution has fallen below a critical level during the ruggedness testing. SOS can then propose new conditions based on the requirement for higher resolution. Both systems had to be adapted slightly and/or extended in order to make a sensible integration.

These studies show that integration often results in complex structures, i.e., they are less user friendly. This endorsed in fact the original decision to build limited stand-alone systems. On the other hand, it was shown that integration is useful in situations where the chromatographer often has to switch between systems. Similar conclusions have also been reported elsewhere [20].

VALIDATION AND EVALUATION OF THE ESCA EXPERT SYSTEMS

Considerable attention was paid to the testing of the expert systems [21,22]. It is important to note that systems were tested with special emphasis on their performance rather than on appearance aspects such as a nice user interface. The latter should, however, be of sufficient quality to make an understandable system. Two main stages have been distinguished, the validation and the evaluation stage.

The validation process involved checking the software and testing the knowledge base by the responsible expert. The procedure that was followed involved the selection of a number of test cases by the expert. The expert solved the test cases manually, while the expert system was also

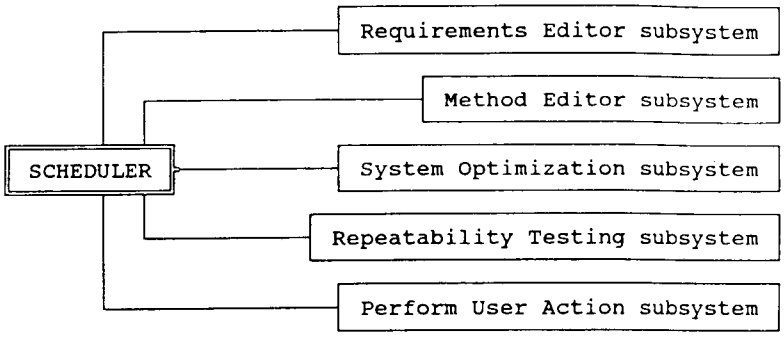

Fig. 5. Structure of the integrated system 2 (INT II).

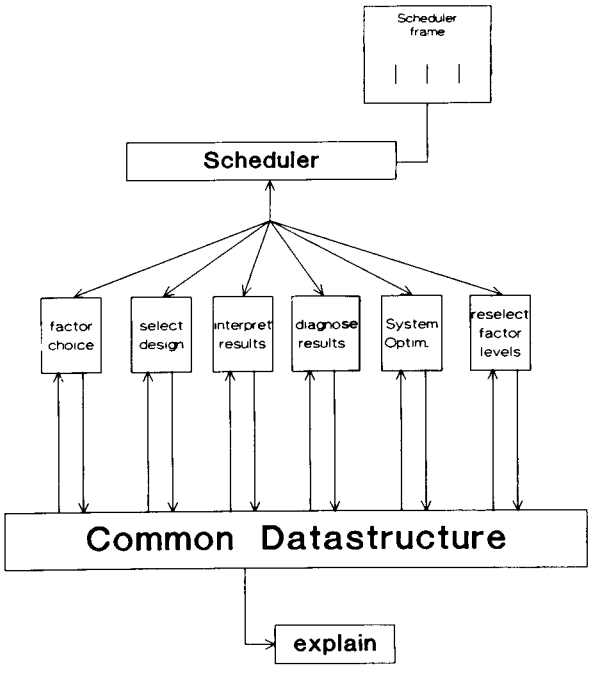

Fig. 6. Structure of the integrated system 3 (INT III).

consulted. The test cases were selected within the scope of the systems and to make use of as much of the knowledge base as possible. Whenever differences between the expert systems solution and that of the expert were seen, the cause of the discrepancy was identified. This led to the addition of missing knowledge or to the correction of existing knowledge. To decide on the proper performance of the systems, a set of pass/fail criteria were defined by the knowledge engineer and the expert prior to testing. The systems were improved until agreement was reached between the expert and the expert system. After validation the systems were subjected to the second stage, the external evaluation.

The evaluation phase consisted of testing the expert system in practical situations, to evaluate the system's performance in daily practice. Generally, these tests were performed by external evaluators, i.e., chromatographers not involved in building the system. Unbiased problem cases were put to the expert system. All inputs and outputs of the systems were registered and, whenever possible and appropriate, verified with experiments. A list of performance criteria were identified by the knowledge engineers and the experts for each system. These criteria took into account aspects of the man/machine interface, the consistency of the system and its limitations. A list of criteria is given in Table 4.

The evaluations were carried out by different persons, ranging from experts in method development to students with little or no experience. Summarizing the evaluations of the three integrated systems the following conclusions can be drawn. The user friendliness expressed among others in a good user interface, clear screen text and easy help functions was judged to be good in

TABLE 4

Example of evaluation criteria

Man–machine interface (user interface)	Choice of phrases
	Explanation
	Operation (mouse, keyboard, file input, etc.)
	Usability/ease of use
Consistency testing	Accuracy (correct answer, quality of advice)
	Reproducibility (repeatability, same input same output)
	Robustness of software (does the system lock up or fall over)
	Ruggedness (small changes in input small changes in output, similar cases, similar answers)
System limits	Conflict (two rules with the same input give a different output)
	Missing rules (input leads to no realistic output)
	Are essential parts missing?
	Are there examples of strange answers in extreme cases, e.g., incomplete input, nonsense output?
	Technical content: do the systems do a useful job?

INT III and INT III. Some of these aspects are closely related to the quality of the shell. KES (INT I) belongs to the older generation of shells in which the above features can be improved.

With respect to the knowledge, a great variety exists between the systems. The knowledge collected in INT I is most complex and generally of heuristic nature. Although this system was restricted to basic pharmaceutical compounds, there is still a lot of chemical and analytical knowledge to add. The knowledge in the other systems is better defined and proved to be complete in a broad field of applications. The evaluators found the item "factor choice in the ruggedness module very flexible. On the other hand, they asked for more flexibility in the experimental design.

Case study: pH optimization

In the following example an interesting application of expert systems is shown in which algorithmic-based knowledge is combined with heuristic knowledge. The complexity of some steps in the method development process will be demonstrated.

INT I deals with method selection and selectivity optimization. In this system three modules are present for the method selection and subsequent retention optimization. After an experiment it has to be decided whether the selectivity has to be optimized. The expert system adequately helps to select a method for the selectivity optimization, viz., sequential or simultaneous approach, and which parameters have preferably

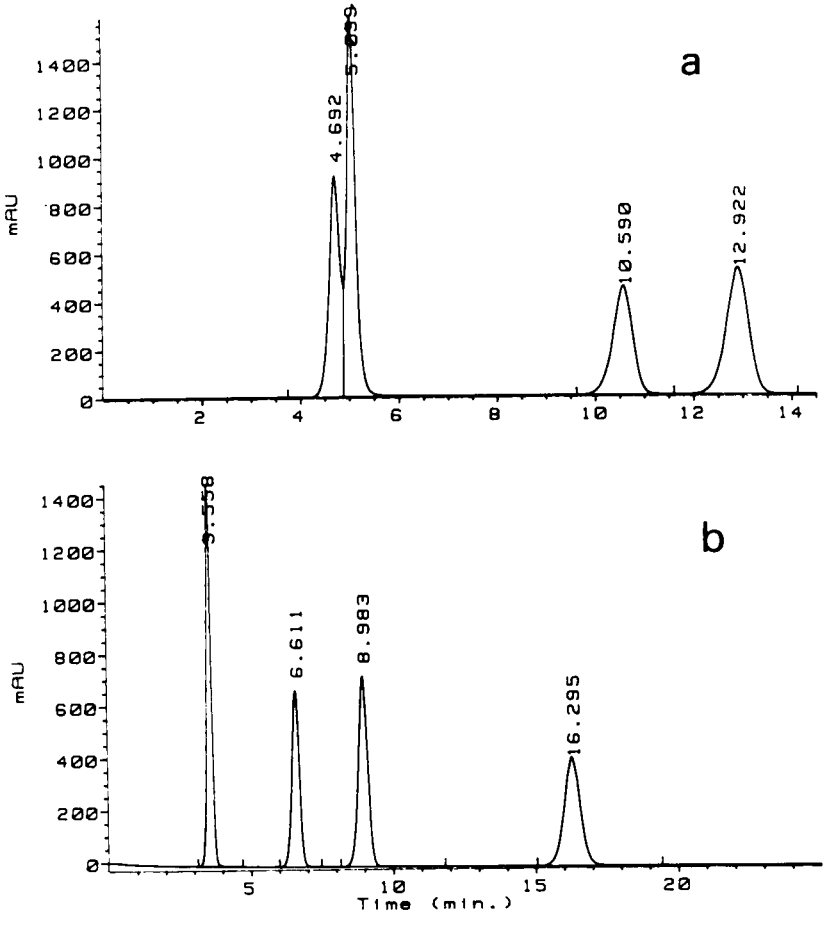

Fig. 7. Optimization with SLOPES. (a) Chromatogram in one of the experiments; (b) result obtained after optimization with SLOPES.

to be optimized, viz., percentage of modifier, mixture design, temperature, pH. The next step is to carry out the optimization. It was chosen to implement only the software tools to carry out pH optimization in a simultaneous approach. The pH optimization was selected because this is a relatively new area. For other types of optimization one can use commercially available software tools.

Before the experiments for the pH optimization can be carried out, the parameter space has to be defined, an experimental design has to be selected and a criterion has to be chosen for the calculation of the optimum. In these three modules heuristic knowledge for the selection of parameter space for acids and for bases, chemometric knowledge for the selection of an appropriate design and algorithmic knowledge for the calculation of the optimum is used.

In Fig. 7, two chromatograms are shown, one before and one after pH optimization. The optimization was done by means of SLOPES. The main limitation of the system is to describe accurately the retention behaviour of each solute over the parameter space selected (retention surface). It is well known that the relationship between retention and pH is an S-shaped curve. The calculation of the retention surface through the measuring points cannot be done by a quadratic function. However, to keep the number of measurements small it was decided to fit a quadratic function through the data points and to study the pH variation over only a small pH range of 3 units. By this means a reasonably accurate pH optimization could be achieved.

Main results of the evaluation

Expert systems can provide very powerful assistance during method development because of the heuristic knowledge (expertise and experience of a specialist) that is implemented in these systems. However, during the evaluation phase of all the expert systems it became clear that the attitude towards expert systems is strongly dependent on the expertise level of the evaluator. The accessibility of the specialist's expertise was clearly appreciated by inexperienced users. The introduction of the expert systems resulted for those users in a considerable amount of time saving in the development process. Experienced users could appreciate the quality of advice given by the systems. They are more interested, however, in comparing the expertise in the systems with their own experience. When the strategy implemented in the system did not agree with their own expertise, it resulted in dissatisfaction with the expert system, because their own experience, probably better adapted to their specific situation, is not considered by the system. This is especially the case when the knowledge domain of the expert system is strongly susceptible to individual opinions. This gives rise to a second aspect, that at present expert systems are not flexible enough. (Minor) changes that could result in a better performing expert system for a particular situation may be impossible to make by the user. Only the knowledge engineer who is aware of the structure of the knowledge base is able to make such changes without unexpected consequences.

A third conclusion of the evaluation is that the main attention should be devoted to the integration of expert systems with laboratory instruments. When this is realized, expert systems can be used to obtain rapidly accurate advice while the user remains free to choose his or her own approach.

Conclusions

The ESCA project can be considered as a pioneer project for the application of expert system technology in analytical chemistry. Method development in LC was selected as the application expertise area. The expertise that has been considered in the project covers the important areas of method development in LC.

It was only possible to cover this large area because many recognized experts participated in the project. It would be almost impossible to find a single expert to cover all the different aspects of method development.

Different expert systems resulted from the project. Most of these are still in the research phase, but a few have been further developed for commercialization (system optimization system, ruggedness system). From the results of valida-

tion and evaluation it can be concluded that expert systems are potentially very useful for method development in LC. The benefits of the systems are that method development can be done more consistently and more efficiently and that better optimized and validated methods are produced. Even when the systems were not yet complete this conclusion became clear.

Expert systems still have to find their way into the chromatographic laboratory. Users will have to accept computer programs that assist during tasks such as method development. This requires, as stated above, expert systems that are flexible and easy to integrate. It should be possible to add new knowledge or to adapt the system according to changes in the application environment. Research on this subject remains necessary.

This research project was partly funded by the EEC, as ESPRIT project P1570 ESCA. T. Blaffert, A. Cleland, T. Hamoir, G. Kateman, J.A. van Leeuwen, D.L.M. Massart, M. Mulholland, H. Pirijns, B.G.M. Vandenginste, N. Walker and all other temporary participants are acknowledged for their contributions which made this final report possible.

REFERENCES

1 B.A. Hohne and T.H. Pierce (Eds.), Expert System Applications in Chemistry (ACS Symposium Series, No. 408), American Chemical Society, Washinghton, DC, 1989.
2 J.W. Dolan, L.R. Snyder and M.A. Quarry, Chromatographia, 24 (1987) 261.
3 S.S. Williams, Trends Anal. Chem., 9 (1990) 63.
4 D. Goulder, T. Blaffert, A. Blokland, L. Buydens, A. Chhabra, A. Cleland, N. Dunand, H. Hindriks, G. Kateman, H. van Leeuwen, D. Massart, M. Mulholland, G. Musch, P. Naish, A. Peeters, G. Postma, P. Schoenmakers, M. de Smet, B. Vandeginste and J. Vink, Chromatographia, 26 (1988) 237.
5 M. De Smet, A. Peeters, L. Buydens and D.L. Massart, J. Chromatogr., 457 (1988) 25.
6 J.A. van Leeeuwen, B.G.M. Vandeginste, G.J. Postma and G. Kateman, Chemom. Intell. Lab. Syst., 6 (1989) 239.
7 P. Politakis and S.M. Weiss, Artif. Intell., 22 (1984) 23.
8 R. Wehrens, L. Buydens and G. Kateman, Chemom. Intell. Lab. Syst., 12 (1991) 57.
9 H. Hindriks, F. Maris, J. Vink, A. Peeters, M. De Smet, D.L. Massart and L. Buydens, J. Chromatogr., 485 (1989) 255.
10 P.J. Schoenmakers, The Optimization of Chromatographic Selectivity; a Guide to Method Development, Elsevier, Amsterdam, 1986.
11 A. Peeters, L. Buydens, D.L. Massart and P.J. Schoenmakers, Chromatographia, 26 (1988) 101.
12 P.J. Schoenmakers, N. Dunand, A. Cleland, G. Musch and T. Blaffert, Chromatographia, 26 (1988) 37.
13 M. Mulholland, J.A. van Leeuwen and B.G.M. Vandeginste, Anal. Chim. Acta, 223 (1989) 183.
14 M. Mullholland, N. Dunand, A. Cleland, J. van Leeuwen and B. Vandeginste, J. Chromatogr., 485 (1989) 283.
15 J.A. van Leeuwen, L.M.C. Buydens, B.G.M. Vandeginste, G. Kateman, P.J. Schoenmakers and M. Mulholland, Chemom. Intell. Lab. Syst., 10 (1991) 337.
16 J.A. van Leeuwen, L.M.C. Buydens, B.G.M. Vandeginste, G. Kateman, P.J. Schoenmakers and M. Mulholland, Chemom. Intell. Lab. Syst., 11 (1991) 37.
17 P. Conti, H. Piryns, N. Vandendriesche, M. Desmet, T. Hamoir, F. Maris, H. Hindriks, P. Schoenmakers and D.L. Massart, Chemom. Intell. Lab. Syst., 11 (1991) 27.
18 L. Buydens, J. Van Leeuwen M. Mulholland, B. Vandeginste and G. Kateman, Trends Anal. Chem., 9 (1990) 58.
19 M. Mulholland, N. Walker, F. Maris, H. Hindriks, L. Buydens and T. Blaffert, J. Chromatogr., 550 (1991) 257.
20 F.A. Settle and M.A. Pleva, Chemom. Intell. Lab. Syst., 11 (1991) 13.
21 J.A. van Leeuwen, L. Buydens, B.G.M. Vandeginste, G. Kateman, A. Cleland, M. Mulholland, C. Jansen, F.A. Maris, P.H. Hoogkamer and J.H.M. van den Berg, Chemom. Intell. Lab. Syst., 11 (1991) 161.
22 F. Maris, H. Hindriks, J. Vink, A. Peeters, N. Vandendriesche and D.L. Massart, J. Chromatogr., 506 (1990) 211.

Analytica Chimica Acta, 272 (1993) 53–59
Elsevier Science Publishers B.V., Amsterdam

Condition index evolving profile library searches: gas chromatography–Fourier transform infrared spectrometry application

Taura D. Jarvis and John H. Kalivas

Department of Chemistry, Idaho State University, Pocatello, ID 83209 (USA)

(Received 25th June 1992; revised manuscript received 4th September 1992)

Abstract

A procedure for library searching gas chromatography–Fourier transform infrared spectra is presented. Complete chromatographic resolution is not necessary for correct identification of components present. Simultaneously, spectral similarities create no obstacles for accurate detection. The procedure is based on condition index evolving profiles. Condition index evolving profiles result from performing singular value decomposition of library spectra with sample spectra as they evolve over time. The procedure is demonstrated to successfully identify components present in two-, three-, and four-component samples.

Keywords: Gas chromatography; Infrared spectrometry; Condition number; Library searching; Singular value decomposition; Spectral library

Computerized qualitative analysis based on Fourier transform infrared (FT-IR) spectroscopic measurements has become an important tool in many analytical laboratories. Three primary strategies exist for computer evaluation of spectra. They consist of library searching, pattern recognition, and knowledge-based methods (expert systems) [1]. This paper concentrates on library searching. Some library search methods identify analytes by searching files containing peak positions, intensities, and widths [1]. other algorithms use the entire spectrum to recognize analytes [1]. Still others use a combination of both procedures [1]. Regardless of the library searching approach, the problem of identifying components present in mixtures persists. When a sample contains numerous components at concentrations ranging from trace levels to the major component, the probability of incorrect identifications greatly increases. Even the presence of impurities in simple one-component samples can cause false identifications.

To circumvent this mixture identification problem, components constituting samples are often separated by gas chromatography (GC) before identification of the components by library searching. However, GC peaks are not always completely resolved, so mixtures will still exist [2,3]. In a recent report, a new library searching algorithm is described. This procedure does not require simple one-component samples and is not influenced by weakly absorbing impurities [4]. The procedure is based on condition index evolving profiles (CIEPs) from singular value decomposition (SVD) of sample spectra and library spectra, i.e., sample spectra of GC peaks are library searched as they evolve over time. Approximations of chromatographic elution profiles are also possible as a consequence of CIEP. This

Correspondence to: J.H. Kalivas, Department of Chemistry, Idaho State University, Pocatello, ID 83209 (USA).

paper describes work applying CIEP to GC–FT-IR spectra with unresolved chromatographic peaks.

OPERATION OF CIEP

The fundamentals of how CIEPs operate have been thoroughly presented and only a brief description is given here. Let **D** designate a $p \times t$ spectrochromatogram matrix for the analysis sample where p symbolizes the number of wavelengths at which measurements are made and t represents the total number of spectral scan sets collected across the chromatogram. Each library spectrum is compared to every spectral scan comprising **D** by performing SVD [5] on a $p \times 2$ matrix, **L**, composed of a spectrum from **D** and a library spectrum. The SVD will calculate two singular values for **L**. The match indicator is the condition index computed from the maximum singular value of **L** divided by the smallest singular value, known as the condition number. Condition indexes are calculated from the maximum singular value divided by all singular values individually [6]. Because only two singular values are available, two condition indexes are computed. One condition index will equal 1 while the other is the condition number. This process is repeated t times until each library spectrum has been compared to all t spectral time slices. Identification of components and estimation of their corresponding elution profiles occur by plotting respective match indicators versus time. Substantially large CIEPs signify potential candidates present, while smaller CIEPs imply spectrally similar components which could be present.

After a component has been identified by CIEP, CIEP is used for subtracting its contribution to **D** and another series of library searches is then performed. This process continues until no more components can be identified. The subtraction process as described previously [4] requires that pure-component spectrochromatograms, **P**, of identified components be available. Essentially, after subtracting a fraction of a pure-component spectrochromatogram, $\alpha\mathbf{P}$, from **D**, each spectral time slice of the residual or difference spectrochromatogram, $\mathbf{R} = \mathbf{D} - \alpha\mathbf{P}$, is sequentially compared to the identified component's library spectrum. The α symbol denotes a scalar or the amount of **P** to remove from the sample spectrochromatogram. The sequential comparison produces t condition indexes for each respective α, which are plotted versus time. When the appropriate amount has been subtracted, the condition indexes primarily remain constant across the estimated elution profile. This mechanism was found to operate as well as or better than rank annihilation factor analysis [4].

EXPERIMENTAL

The search library consisted of 116 reference spectra selected from the Sadtler collection of vapor-phase IR reference spectra (Bio-Rad, Sadtler Division, Philadelphia, PA). This set contains spectra of structurally and spectrally similar molecules supplying worst-case scenarios for examination.

All computations utilized built-in functions supplied with MatLab (The MathWorks, Natick, MA). Condition indexes plotted in the figures were normalized to the largest condition index computed over all time intervals and a complete library search. Condition indexes plotted for CIEP subtraction were normalized to the maximum condition index determined over all α values.

The first sample used was diluted to 170 ng μl^{-1} (1-hexanol), 130 ng μl^{-1} (cyclohexanol) and 175 ng μl^{-1} (5-methyl-2-hexanone) with hexane. The second sample used was diluted to 170 ng μl^{-1} each for 1-hexanol, 1-octanol, and 1-nonanol. A 1.0-μl sample was injected into a Hewlett Packard (HP) 5890 gas chromatograph (Hewlett Packard, Palo Alto, CA). Separations were performed isothermally using a 30 m long, 250 μm thick layer of DB-5 (5% dimethyl polysiloxane and 95% diphenyl polysiloxane) stationary phase (J&W Scientific, Folsom, CA) at a temperature of 180°C. Infrared spectra were measured using the HP IRD GC–FT-IR interface. Spectra were recorded from 4000 cm^{-1} to 750 cm^{-1} at 2 cm^{-1} increments every 0.25 s and transferred from HP format to ASCII format via Lab Calc (Galactic

Industries, Salem, NH) file converter. The IR spectra were baseline corrected prior to library searching.

RESULTS AND DISCUSSION

To assess the abilities of CIEP to function with GC–FT-IR data, reconstructed spectrochromatograms of pure components were summed to generate multicomponent spectrochromatograms. By shifting one pure-component spectrochromatogram relative to another, a simple mechanism to vary chromatographic resolution is provided. Condition index evolving profile library searches were then performed on these multicomponent spectrochromatograms.

Simulated spectrochromatograms

Figure 1 shows two individual chromatographic peaks measured at 2900 cm^{-1} of 1-hexanol and cyclohexanol injected with equal concentration and plotted after shifting the time axes so that they severely overlapped as determined by inspection. Figure 1 also shows the summed chromatogram which simulates what may have been measured had the analytes been co-injected. Some representative CIEP library search results are illustrated in Fig. 2. The fact that the CIEP for 1-hexanol has the largest values indicates the presence of 1-hexanol. The double-peaked elution curve is indicative of a second component present which is spectrally similar to 1-hexanol. The higher CIEP for 1-hexanol, compared to the CIEP for cyclohexanol, results from the small region between $t = 13$ and $t = 15$ shown in Fig. 1 where 1-hexanol elutes with larger absorbance values. Similarly, if the 1-hexanol chromatogram was shifted slightly to the left so that $t = 13$ thru 15 were under the cyclohexanol chromatogram, cyclohexanol would be identified first. For the present simulation, cyclohexanol exhibits the next highest CIEP curve suggesting that it is present as well. However, the CIEP library search also implies that the mixture could include 1-bromooctane and methylcyclohexane due to the magnitudes of the respective CIEP. The CIEPs that extend along the baseline in Fig. 2 (and other CIEP plots) represent spectrally dissimilar species.

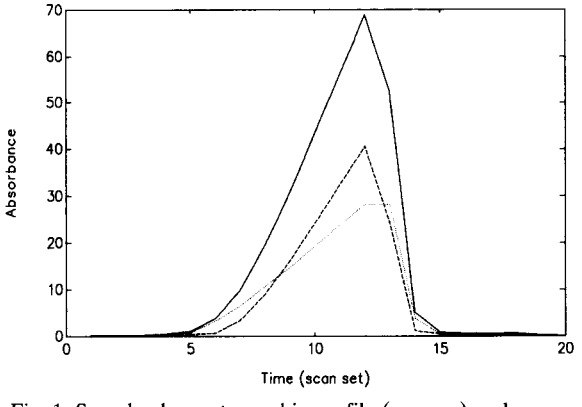

Fig. 1. Sample chromatographic profile (———) and component chromatographic profiles measured at 2900 cm^{-1} for components (·····) 1-hexanol and (— — —) cyclohexanol at a concentration ratio of 1:1.

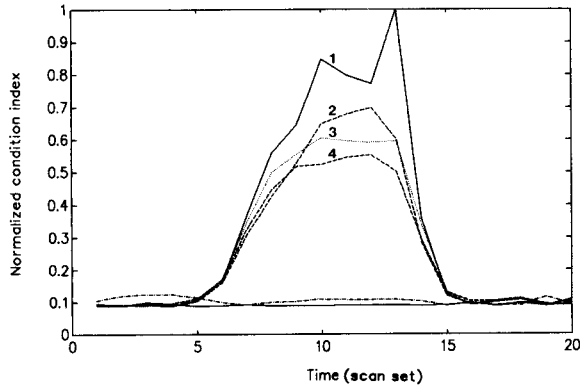

Fig. 2. Normalized condition indexes from a CIEP library search of the sample spectrochromatogram containing 1-hexanol and cyclohexanol as shown in Fig. 1. Labeled CIEPs are library searches for (1) 1-hexanol, (2) cyclohexanol, (3) 1-bromooctane, and (4) methylcyclohexane. The CIEPs extending along baseline are spectrally dissimilar species.

To determine which of the above mentioned potential candidates actually compose the mixture, the contribution of 1-hexanol must first be removed followed by another CIEP library search. Shown in Fig. 3 are the CIEP subtraction results. At $\alpha = 1.0$, the CIEP substantially leveled off signifying that the proper amount of 1-hexanol's contribution has been eliminated. Conducting a CIEP library search on the remaining mixture

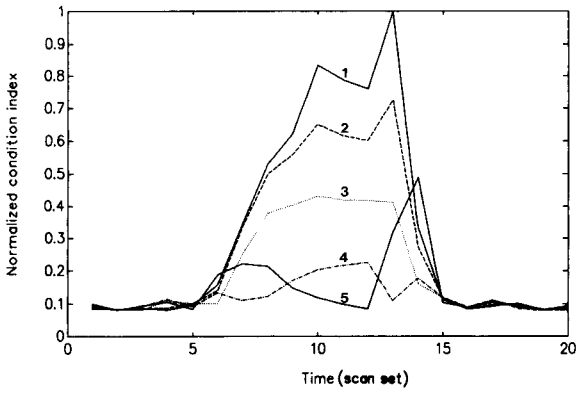

Fig. 3. CIEP subtraction variation of normalized condition indexes with respect to α while subtracting the pure-component spectrochromatogram for 1-hexanol. For the plot 1, 2, 3, 4, and 5, the value of $\alpha = 0.0$, 0.5, 1.0, 1.5, and 2.0, respectively.

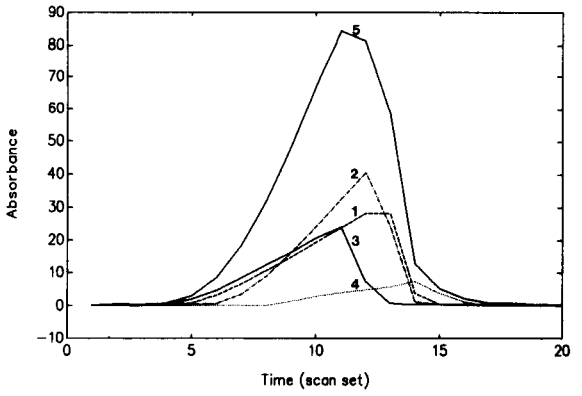

Fig. 5. Sample chromatographic profile and individual chromatographic profiles measured at 2900 cm^{-1}. Numbers correspond to (1) 1-hexanol, (2) cyclohexanol, (3) 1-bromooctane, (4) 2,5-hexanedione, and (5) sample at concentration ratio 1:1:1:1.

spectrochromatogram resulted in Fig. 4. The largest CIEP corresponds to cyclohexanol and provides evidence that it is present in the analysis sample mixture. The small CIEPs for 1-bromooctane and methylcyclohexane suggest their absence in the sample mixture.

Figure 5 displays chromatograms for a four-component mixture composed of 1-hexanol, cyclohexanol, 1-bromooctane, and 2,5-hexanedione. Representative CIEP library search curves are shown in Fig. 6. The component 2,5-hexanedione is easily identified as a contributor to the sample spectrochromatogram due to its larger chromatographic elution peak in the vicinity of $t = 14$ as shown in Fig. 5. Its spectral dissimilarity with the other four components contributes strongly to the high CIEP values. The curves in Fig. 6 suggest the presence of 1-bromooctane and 1-hexanol. The CIEP in Fig. 6 for 1-bromooctane between $t = 5$ and $t = 10$ marks the second largest curve. This is expected because Fig. 5 reveals that 1-

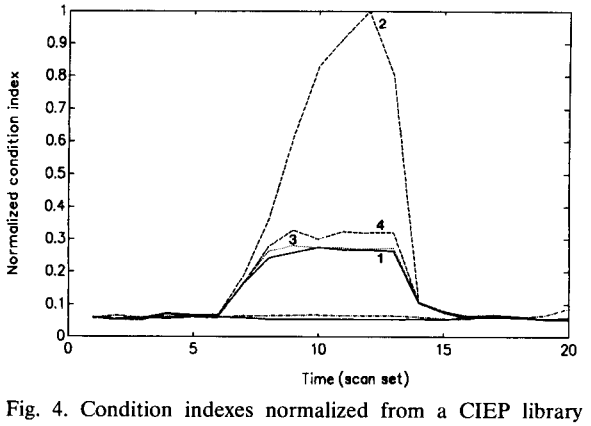

Fig. 4. Condition indexes normalized from a CIEP library search of the analysis sample in Fig. 1 with 1-hexanol removed. Labeled CIEPs are library searches for (1) 1-hexanol, (2) cyclohexanol, (3) 1-bromooctane, and (4) methylcyclohexane. The CIEPs extending along baseline are spectrally dissimilar species.

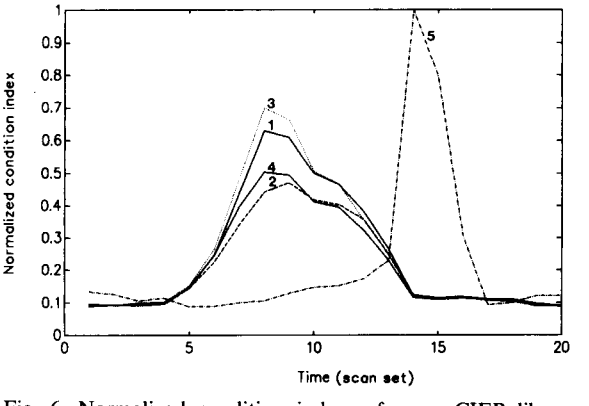

Fig. 6. Normalized condition indexes from a CIEP library search of the sample spectrochromatogram containing components as indicated in Fig. 5. Labeled CIEPs are library searches for (1) 1-hexanol, (2) cyclohexanol, (3) 1-bromooctane, (4) methylcyclohexane, and (5) 2,5-hexanedione.

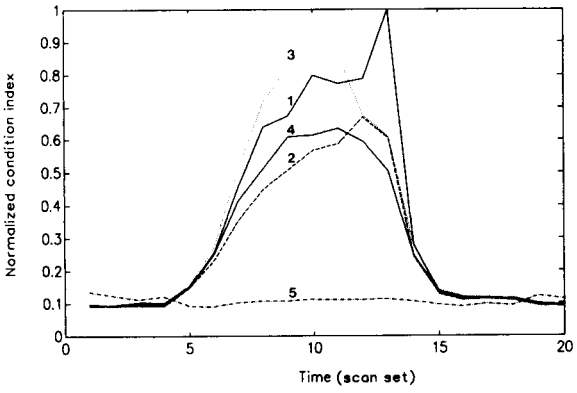

Fig. 7. Normalized condition indexes from a CIEP library search of the sample spectrochromatogram containing components as indicated in Fig. 5 after removing 2,5-hexanedione. Labeled CIEPs are library searches for (1) 1-hexanol, (2) cyclohexanol, (3) 1-bromooctane, (4) methylcyclohexane, and (5) 2,5-hexanedione.

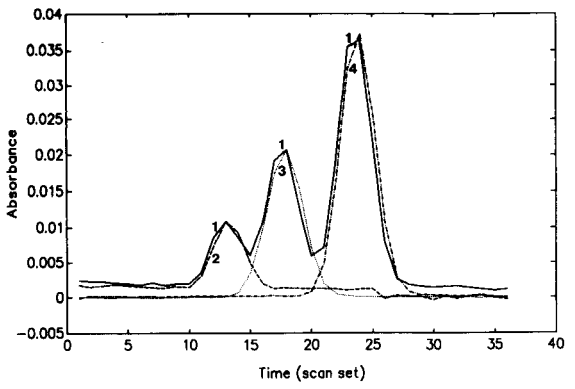

Fig. 8. Sample chromatogram (1) and pure-component chromatograms measured at 2900 cm^{-1} for (2) 5-methyl-2-hexanone, (3) 1-hexanol, and (4) cyclohexanol.

bromooctane has the largest chromatographic elution profile during these times. Figure 7 presents the CIEP library search results after subtracting 2,5-hexanedione. This plot identifies the presence of 1-hexanol and possibly 1-bromooctane. The identification of 1-bromooctane was established with a CIEP search following mathematical removal of 1-hexanol from the sample spectrochromatogram. Unlike Fig. 6, Fig. 7 actually shows a separation of elution profiles for 1-hexanol and 1-bromooctane. Because 2,5-hexanedione has been removed, the CIEP process can now distinguish between the chromatographic elution profiles for 1-bromooctane and 1-hexanol shown in Fig. 5. Note that Figs. 6 and 7 suggest that methylcyclohexane is present due to its relatively large CIEP. After subsequent removal of 1-hexanol and 1-bromooctane the CIEP no longer indicates methylcyclohexane as a potential candidate.

Actual spectrochromatograms

Figure 8 displays the chromatogram for a three-component sample composed of 1-hexanol, cyclohexanol, and 5-methyl-2-hexanone. The results of a CIEP library search are presented in Fig. 9. Normalized condition indexes suggest the presence of all three components. A CIEP subtraction of these three components removes respective contributions and generates a residual spectrochromatogram to search in order to determine the presence of additional components at lower concentrations. In this case, other components were not recognized. Because the retention times were not exactly reproducible to within 0.5 s between sample and pure-component spectrochromatograms as required for subtraction, it was necessary to adjust retention time positions of pure components to match those of the sample as depicted in Fig. 8.

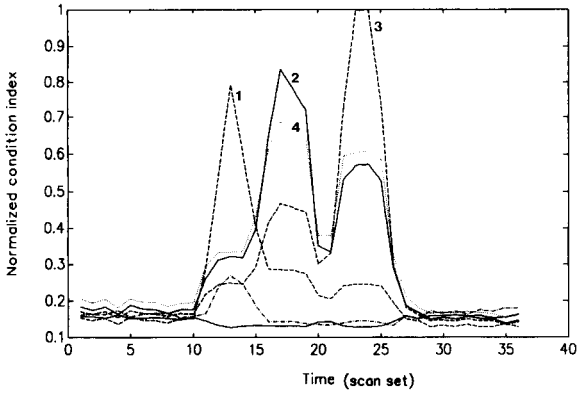

Fig. 9. Normalized condition indexes from a CIEP library search of the spectrochromatogram containing components as indicated in Fig. 8. Representative library searches shown correspond to (1) 5-methyl-2-hexanone, (2) 1-hexanol, (3) cyclohexanol, and (4) 1-bromooctane.

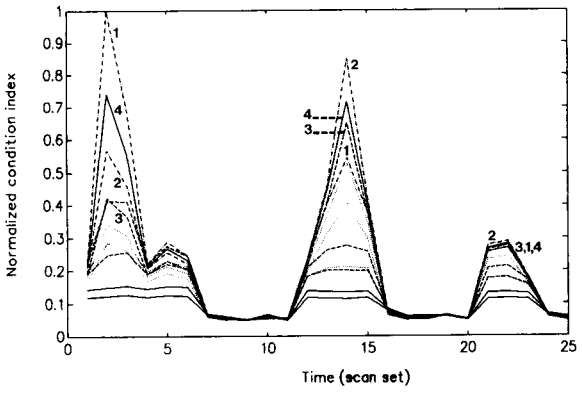

Fig. 10. Normalized condition indexes from a CIEP library search of a sample containing 1-hexanol, 1-octanol, and 1-nonanol as described in Fig. 11. Representative searches shown correspond to (1) 1-hexanol, (2) 1-octanol, (3) 1-nonanol and (4) 1-heptanol.

Another sample containing equal amounts of 1-hexanol, 1-octanol, and 1-nonanol was studied. A library of straight-chain alcohols ranging from 1-methanol to 1-dodecanol was used. Results of the CIEP library search are pictured in Fig. 10 disclosing the presence of both 1-hexanol (first CIEP) and 1-octanol (second CIEP). However, 1-nonanol (third CIEP) is not positively identified. Figure 10 indicates that the third CIEP identifies several potential candidates including 1-nonanol due to the closeness of their CIEPs.

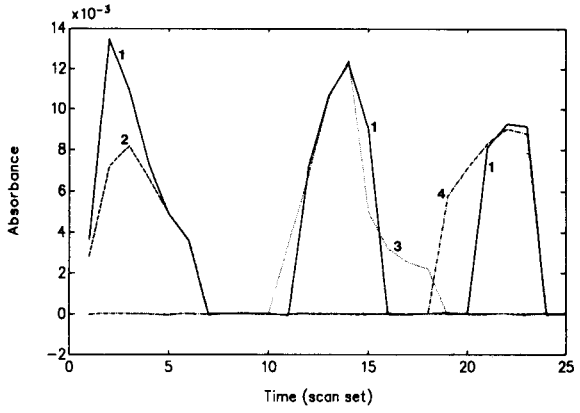

Fig. 11. Sample chromatogram (1) and respective pure-component chromatograms measured at 2900 cm^{-1} for (2) 1-hexanol, (3) 1-octanol, and (4) 1-nonanol.

This can be attributed to the spectral similarity of the straight-chain alcohols identified.

Normally, the next phase involves performing CIEP subtractions on the sample removing contributions of identified components 1-hexanol and 1-octanol followed by another library search. The CIEP subtraction could not be performed for this sample because the chromatograms of the pure components are much broader and different in shape than those of the sample. Figure 11 illustrates the complication.

For this sample, a comparison was made between CIEP, Euclidean distance [1,7], and the dot product [1,8]. The Euclidean distance and dot

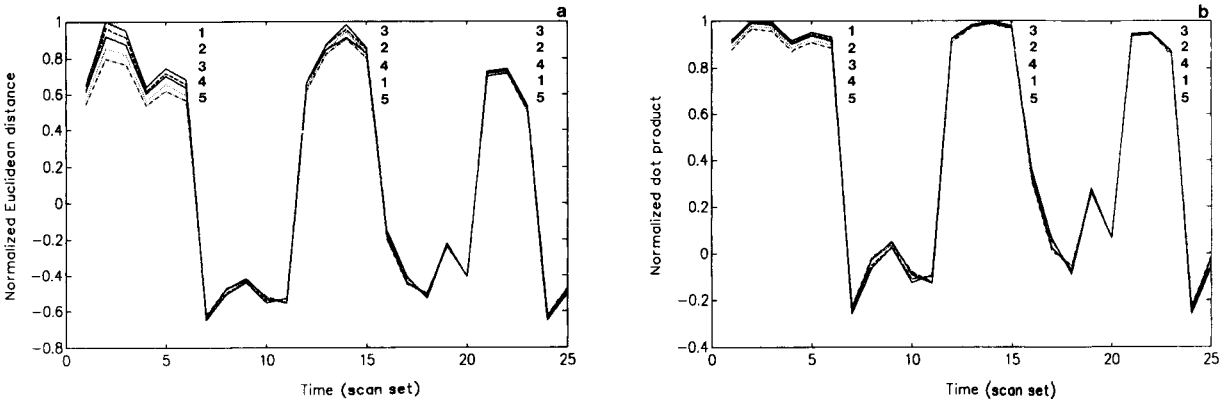

Fig. 12. (a) One minus normalized Euclidean distance evolving profiles and (b) normalized dot product evolving profiles from a library search of the sample described in Fig. 11. Numbers correspond to (1) 1-butanol, (2) 1-hexanol, (3) 1-nonanol, (4) 1-heptanol, and (5) 1-octanol.

product represent two frequently utilized match indicators in spectral library searching. Figure 12a and b displays a few of the predominant evolving profiles. The Euclidean distance plotted is one minus Euclidean distance for easy comparison with CIEP and the dot product. The superior distinguishing ability of CIEP compared to the Euclidean distance and dot product is demonstrated. The Euclidean distance and dot product are not able to discern the differences between the spectrally similar straight chain-alcohols as well as CIEP (Fig. 10).

The research was supported by Idaho EPSCoR-NSF Grant No. RII-8902065. The authors would like to gratefully acknowledge Peter R. Griffiths for his helpful discussions, Erik J. Hasenoehrl for obtaining the data, and Hewlett Packard for their generous donation of the HP-IRD.

REFERENCES

1 H.J. Luinge, Vib. Spectrosc., 1 (1990) 3.
2 S.R. Lowry and D.A. Huppler, Anal. Chem., 53 (1981) 889.
3 P.T. Richardson and J.A. de Haseth, Anal. Chem., 60 (1988) 366.
4 T.D. Jarvis and J.H. Kalivas, Anal. Chim. Acta, 266 (1992) 13.
5 E.R. Malinowski, Factor Analysis in Chemistry, Wiley, New York, 2nd edn., 1991.
6 D.A. Belsley, Conditioning Diagnostics: Collinearity and Weak Data in Regression, Wiley, New York, 1991.
7 S.R. Lowry, D.A. Huppler and C.R. Anderson, J. Chem. Inf. Comput. Sci., 25 (1985) 235.
8 J.W. Sherman, J.A. de Haseth and D.G. Cameron, Appl. Spectrosc., 43 (1989) 1311.

Analytica Chimica Acta, 272 (1993) 61–72
Elsevier Science Publishers B.V., Amsterdam

Quantitative calibration of multi-component systems with a known range of possibly co-existing species

Yu-Long Xie, Yi-Zeng Liang and Ru-Qin Yu

Department of Chemistry and Chemical Engineering, Hunan University, Changsha 410082 (China)

(Received 13th June 1991; revised manuscript received 30th June 1992)

Abstract

The quantitative calibration of multi-component spectrophotometric systems with a known range of possibly co-existing species was studied. A modified stepwise regression method (MSR) was used for treating such systems. Compared with conventional stepwise regression (CSR), the MSR method does not use an *F*-test in the variable selection process and the result of selection is an optimum sequence of regression equations with all possible numbers of variables. The Akaike information criterion (*AIC*) was used for the evaluation of a variable's contribution in the stepwise process and as a criterion for choosing the best equation from the optimum sequence. A numerical example is treated to show the essential difference between MSR and CSR and how MSR works. Spectrophotometric data for real analytical systems were treated by the proposed method, and the results of simultaneous detection and determination were satisfactory.

Keywords: Multivariate calibration; UV–Visible spectrophotometry; Stepwise regression

Quantitative calibration of complex multi-component systems is an important problem in chemometrics. According to the a priori knowledge of qualitative chemical composition in analytical systems, they were previously divided into three classes, the so-called "white", "grey" and "black" analytical systems [1]. The "white" analytical systems are those where one knows well how many and which components exist and only needs to quantify all or part of them, and the "black" systems refer to those without any a priori knowledge concerning their composition. The "grey" analytical systems are somewhere in between and characterized by incomplete a priori qualitative knowledge. Generally, there is more or less a priori information about the analytical systems under study, so "grey" analytical systems represent the most common cases.

Usually, one knows the range of possible co-existing species in an analytical sample, but the exact number and identities are not known. The primary step in calibrating such systems is to identify the number and identities of the truly existing species in the sample. Target transformation factor analysis (TTFA) can be used in such a situation [2], and each suspected component is taken as a test vector to see if it actually exists in the mixtures. However, the application of TTFA requires an analytical data matrix experimentally measured with a series of mixtures containing the same species but in different concentrations; this makes the use of TTFA unfeasible because usually only one sample is available for analysis. This problem was treated as a process of selecting the optimum subset for regression and two methods were introduced, the conventional stepwise re-

Correspondence to: Ru-Qin Yu, Department of Chemistry and Chemical Engineering, Hunan University, Changsha 410082 (China).

gression (CSR) method [3] and the branch-bound algorithm [4]. These have been used successfully for analytical systems with only one sample spectrum.

The CSR method is computationally simple and usually provides an optimum or quasi-optimum regression equation. In practice, to judge whether a variable should be introduced into or rejected from the regression equation with CSR, one relies on an F-test on the corresponding variable under a given significance level α. However, making use of an F-test in variable selection has some drawbacks. The correct conditional distribution of variables to be tested when some variables have already entered the regression equation may not be an F distribution as one assumed [5,6], so in practical usage, an arbitrary critical F value is adopted and just taken as a threshold for the variable selection and one does not pay much attention to the selection of significance level α. However, unfortunately, the variables selected by CSR may be different with different critical F values (an example is given in the Results section). Moreover, a certain fixed critical F may completely prohibit some variables from entering the model, but these variables may happen to be the members of the best model even though they cannot pass the F-test [7,8]. For component identification in a "grey" analytical system using CSR, a suitable critical F value must be chosen through trials on a specific analytical system, which unavoidably brings in some subjectivity [3].

To overcome the defects of CSR, some revision was made and a modified stepwise regression (MSR) was proposed. First, the Akaike information criterion (AIC) was taken as the criterion for variable selection instead of using an F-test, which would alleviate the problem of selecting a critical F value. Second, the stepwise procedure was followed in a different way from CSR, mainly in the stage of variable rejection. The least important variable in the current regression model was deleted one by one as long as it was not the variable just inserted. This would provide chances of entering the regression equation for some variables for which it would be impossible to enter the model under a certain fixed critical F value in CSR. The selected result was a sequence of models with all possible variables instead of a single equation as in CSR. and the model with the most appropriate number of variables was then selected from it. In this paper, the theoretical background and the algorithm will be presented first, and a numerical example will be given to show the essential difference between MSR and CSR and how the method works. The results of treatment of a set of spectrophotometric data for a real analytical system will also be presented.

THEORY AND ALGORITHM

Basic concepts

According to Beer's law and the spectral additivity principle, the mathematical model of the spectrophotometric determination of a "grey" analytical system can be expressed as follows:

$$\boldsymbol{y} = c_0 + \boldsymbol{x}_1 c_1 + \boldsymbol{x}_2 c_2 + \ldots + \boldsymbol{x}_n c_n + \boldsymbol{e}$$

$$= c_0 + \sum_{i=1}^{n} \boldsymbol{x}_i c_i + \boldsymbol{e} = c_0 + \boldsymbol{X}\boldsymbol{c} + \boldsymbol{e} \qquad (1)$$

where $\boldsymbol{y}$ is the mixture (sample) absorbance vector measured at m wavelengths, $\boldsymbol{x}_i (i = 1, \ldots, n)$ is the standard spectrum vector of the possible existing species i in the same wavelength range, c_i $(i = 1, \ldots, n)$ is the relative concentration of the ith species in the mixture, c_0 is the intercept and $\boldsymbol{e}$ is the error vector, which is assumed to be normally distributed with zero mean and constant variance σ^2.

For a specific mixture containing q $(1 \leqslant q \leqslant n)$ components, $\boldsymbol{y}$ in Eqn. 1 consists only of $q + 1$ terms (q $c_i\boldsymbol{x}_i$ terms and an intercept term, c_0). One has to determine the value of q and find q components actually existing in the mixture before quantifying them. This can be treated as a problem of selecting the optimum subset of regression variables, and CSR is a widely used technique.

The basic idea of CSR is to insert in or reject variables from the regression model step by step

according to their contribution to regression. One of the measures of such a contribution of variable i is the partial sum of squares due to regression, Q_i (some analogous statistics, e.g., the partial correlation coefficients or their squares, have also been adopted in the literature), defined as [6]

$$Q_i = S_{reg} - S'_{reg} \quad (2)$$

where S_{reg} is the sum of squares due to regression provided by k variables, $x_1, \ldots, x_k$, and S'_{reg} is the sum of squares due to regression provided by $k-1$ variables. $x_1, \ldots, x_{i-1}, x_{i+1}, \ldots, x_k$ ($1 \leqslant k \leqslant n$). It is obvious that the larger the value of Q_i, the more important the variable i is in the regression equation.

In CSR, the most important variable is chosen, according to their Q_i (or other quantities), from the variables not yet in the current regression equation and then an F statistic is calculated and compared with a preselected critical F_{in} to check if the variable is significant and should be selected and added to the model. A variable entering at an earlier stage may become superfluous because of the correlation with subsequently included variables in the regression equation. Hence at any stage all variables incorporated in the model are checked for retention, the least important variable present in the model is picked out and its F statistic is evaluated and compared with a preselected critical F_{out}. If this tested variable shows an insignificant contribution, it is removed from the model. The procedure is repeated until no variable in the current equation can be removed and no new candidate variable should be added to the equation.

As stated before, an F-test may suffer from some drawbacks and some modification was adopted in MSR [9]. No matter whether it passed the F-test or not, the variable outside the current regression equation with the largest contribution (this can be judged by Q_i or AIC defined below) is added to the model, and the least important variable in the present model is removed from the model. When the least important variable is rejected, the deletion procedure is continued until the next least important variable in the current model is the one just inserted. The process is repeated until all variables are selected. In this way, one could avoid the situation that some variables might have no chance of entering the model in CSR where a certain fixed critical F was adopted. In such a stepwise process, several models with the same size might be calculated, but only the best of them would be recorded and retained, so the result of the stepwise procedure is an optimum or quasi-optimum sequence of equations with all possible variables. The model with the most appropriate number of variables is chosen from this sequence by using AIC or together with other criteria based on residual sum of squares (RSS).

Akaike [10] proposed an information criterion for the identification of an optimum model from a group of competing models, which can also be used for variable selection in regression. Under the aforementioned error assumption, it is easy to obtain the AIC for a model including p variables (see Appendix A):

$$AIC_q = m \log \sigma^2 + 2q \quad (3)$$

where $q = p + 1$ and p is the number of variables in current equation. Together with AIC_q, one can also use some criteria based on RSS to select the suitable model from the optimum sequence provided by the stepwise procedure, e.g., residual mean squares (RMS_q) or mean square error of prediction (S_q) [6]:

$$RMS_q = RSS_q/(m-q)$$

$$S_q = RMS_q/(m-q-1) \quad (4)$$

As will be shown below, during the stepwise selection process, additional computation is not necessary in calculating AIC_q and other related values.

Algorithm

The algorithm of MSR is almost the same as that of CSR. First, n variables x_i and y were centred and normalized to unit variance, and a correlation coefficient matrix $\boldsymbol{R}$ was constructed:

$$\boldsymbol{R} = \begin{pmatrix} X'X & X'y \\ y'X & y'y \end{pmatrix} \quad (5)$$

As the number of variables in the regression equation is increased or decreased only by one after each regression step in MSR (CSR), the adoption of a sweep operator [11], *SW*, on $\boldsymbol{R}$ substantially simplifies the regression process:

$$\boldsymbol{R}^{(l)} = SW_k \boldsymbol{R}^{(l-1)} \tag{6}$$

$$\begin{cases} r_{kk}^{(l)} = 1/r_{kk}^{(l-1)} & \\ r_{ik}^{(l)} = -r_{ik}^{(l-1)}/r_{kk}^{(l-1)} & i \neq k \\ r_{kj}^{(l)} = r_{kj}^{(l-1)}/r_{kk}^{(l-1)} & j \neq k \\ r_{ij}^{(l)} = r_{ij}^{(l-1)} - r_{ik}^{(l-1)} \times r_{kj}^{(l-1)}/r_{kk}^{(l-1)} & i, j \neq k \end{cases} \tag{7}$$

where the rs are elements of matrix $\boldsymbol{R}$, k, the index of the variable being inserted in or rejected from the equation, represents the pivotal element of sweep operation and l is the counting number of sweep operation. At the start, $\boldsymbol{R}^{(0)} = \boldsymbol{R}$.

By using the sweep operator, each regression step with one variable k inserted or removed will be accomplished by sweeping the pivotal element associated with this variable instead of doing a whole new regression including variable k and all variables already in the model. *SW* automatically provides process quantities such as RSS_q and the regression coefficients. The features of *SW* are shown in Appendix B; details can be found elsewhere [11,12].

In the stepwise process, the contribution of the variable k, Q_k, can easily be calculated before *SW* is carried out:

$$Q_k^{(l)} = \frac{\left[r_{k(n+1)}^{(l-1)}\right]^2}{r_{kk}^{(l-1)}} \tag{8}$$

One can substitute AIC_k for Q_k as a criterion for evaluating the contribution of variables. It can be proved that, after inserting the variable which has the largest Q among all candidates or rejecting the variable which has the smallest Q among all current variables, the resultant regression equation has the smallest value of *AIC* value. The value of *AIC* in the stepwise procedure can also easily be calculated [13] (a brief description is given in Appendix A):

$$AIC_k^{(l)} = m \log\left\{ r_{(n+1)(n+1)}^{(l-1)} - \frac{\left[r_{k(n+1)}^{(l-1)} r_{(n+1)k}^{(l-1)}\right]}{r_{kk}^{(l-1)}} \right\} - m \log(m - v) + m \log s^2 + 2v + C \tag{9}$$

where s^2 is the variance of variable y [$s^2 = \Sigma(y_i - \bar{y})^2$, v equals $q + 2$ when considering variable insertion and q for variable rejection and C is a constant independent of q. In this way, one always looks for the variable that provides the smallest *AIC* in both insertion and rejection steps.

If the sweep operation has been exerted $l - 1$ times and there are q variables in the current equation, the lth sweep operation for calculating a new regression equation should be done according to the following steps.

(i) The values of *AIC* of variables outside the current equation are computed based on $\boldsymbol{R}^{(l-1)}$ and the variable k with the smallest value of *AIC* is selected. A regression-incorporated variable k is obtained by sweeping on the pivotal element $r_{kk}^{(l-1)}$ and a regression equation of size $q + 1$ is thus obtained. Denote the just inserted variable k as k_l. If the *AIC* value of the current model of size $q + 1$ is smaller than that of other models with the same size so far calculated (if they exist as such), or if the current model is the first one with this number of variables, the variable indices of this model and its *AIC* value are recorded as the best representative of models of size $q + 1$ up to now, and this model is expected to be replaced in subsequent calculation steps or retained to the end.

(ii) The values of *AIC* of variables inside the current equation are calculated based on $\boldsymbol{R}^{(l)}$ and the variable t which provides the smallest value of *AIC* is chosen. If $t \neq k_l$, i.e., the least important variable t in the current model is not the variable k_l just inserted, variable t is removed from the current equation through SW_t, and a model of size q is obtained again. Compare the value of *AIC* of this q variable model with that of the best model of size q up to now; if it is

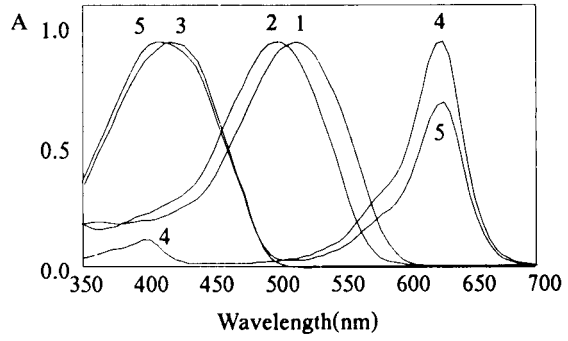

Fig. 1. Spectra of dyes: 1 = amaranth; 2 = coccinellin; 3 = tartrazine; 4 = brilliant blue; 5 = apple green.

smaller, the best model of size q is replaced with this model and its variable indices and *AIC* value are stored.

(iii) Repeat (ii) until $t = k_l$.

(iv) If $q < n$, go back to (i), or stop the selection process and go to (v). In the selection process, the equations of different size having the smallest *AIC* are stored, together with their *AIC* and variable indices. A sequence of optimum equations is thus obtained.

(v) Calculate quantities such as RMS_q and S_q for each equation in the optimum sequence. Choose the equation which shows a minimum value of the criteria as calibration model and calculate the regression coefficient corresponding to each variable in this equation, i.e., concentrations of the species to be determined.

EXPERIMENTAL

Apparatus

A model U-2000 UV–visible spectrophotometer (Hitachi) and a Macintosh II microcomputer were used.

Experimental systems

The dyes amaranth, coccinellin, tartrazine, brilliant blue and apple green were dried at 65–85°C for 6 h. Solutions of each individual dye and some two- and three-component mixtures were prepared with deionized water. The absorbance was measured at 5-nm intervals between 350 and 700 nm. The standard spectra of these five dyes are shown in Fig. 1.

RESULTS AND DISCUSSION

Numerical example

In order to show the distinction between MSR and CSR and how MSR works, the data in a four-variable ($n = 4$) problem given by Hald [14] were taken as an example. This particular problem was chosen because it illustrates some typical difficulties that occur in regression analysis and is widely quoted in statistical textbooks.

The four variables were denoted by x_1, x_2, x_3 and x_4, and y refers to the dependent variable. The data are listed in Table 1.

When using CSR with different critical F values, one would obtain different regression equations. If $F_{in} \geqslant 5.026$, one would obtain

$$y = 103.0974 + 1.4400x_1 - 0.6140x_4$$

If $F_{in} \leqslant 5.025$ and $F_{out} \geqslant 1.87$, one would obtain

$$y = 52.5773 + 1.0683x_1 + 0.6623x_2$$

However, if $F_{in} \leqslant 5.025$ and $F_{out} \leqslant 1.86$, one would obtain

$$y = 71.6483 + 1.4519x_1 + 0.4161x_2 - 0.2365x_4$$

Hence, it was difficult to set an appropriate critical F for CSR.

The selection result of MSR is shown in Table 2. The variable selected was denoted by 1 and unselected variables by 0, an optimum sequence of four regression equations of size 1–4 was ob-

TABLE 1

Data of Hald [14]

No.	x_1	x_2	x_3	x_4	y
1	7	26	6	60	78.5
2	1	29	15	52	74.3
3	11	56	8	20	104.3
4	11	31	8	47	87.6
5	7	52	6	33	95.9
6	11	55	9	22	109.2
7	3	71	17	6	102.7
8	1	31	22	44	72.5
9	2	54	18	22	93.1
10	21	47	4	26	115.9
11	1	40	23	34	83.8
12	11	66	9	12	113.3
13	10	68	8	12	109.4

TABLE 2

Selection results with MSR

No.	x_1	x_2	x_3	x_4	AIC	RMS_q	S_q
1	0	0	0	1	61.0233	80.3515	8.0352
2	1	1	0	0	28.8307	5.7904	0.6434
3	1	1	0	1	29.7543	5.3303	0.6663
4	1	1	1	1	33.2559	5.9830	0.8547

tained together with their AIC values, and so on. It was unequivocal to choose the subset including variables x_1 and x_2 as the best regression model by using AIC and S_q, and this result was in accord with that of all possible regressions [5,6]. RMS_q showed a minimum for the three-variable model x_1–x_2–x_4, which was an inconsistent result. According to the detailed analysis by Draper and Smith [5], it was preferable to choose the two-variable model x_1–x_2 in this situation even though it had a larger RMS_q, which gave an heuristic suggestion of selecting the model as economically as possible on the premise of the value of criteria tending to a minimum, in order to avoid overfitting.

The number of regressions (sweep operation) was eight, which was obviously less than that of an enumerative calculation of $2^4 - 1$.

The stepwise procedure with this data set was followed after normalizing X and y to zero mean and unit variance as below.

Step 1. At the very beginning, there are no variables in the regression equation and the AIC values of four candidates are computed from the correlation matrix: $AIC(.x_1) = 65.6912$, $AIC(.x_2) = 61.3497$, $AIC(.x_3) = 71.2391$ and $AIC(.x_4) = 61.0233$. x_4 is selected and the corresponding regression is completed by sweeping the pivotal element r_{44}. Then, x_4 is taken as the best representative of one-variable models. Here, the variables before the dot (or the oblique line used below) are the indices of variables present in the current model, the variable following the dot is that to be included and the variable following the oblique line refers to the variable to be removed from the model. For the sake of simplicity, the superscript r which denotes the number of SW is omitted throughout the description below.

Step 2. The current model contains only one just selected variable x_4, so no variable rejection is considered. We then calculate the following AIC: $AIC(x_4.x_1) = 32.1524$, $AIC(x_4.x_2) = 64.0401$, $AIC(x_4.x_3) = 43.2633$. It is obvious that x_1 should be added to the regression equation and the second SW with pivotal element r_{11} is applied. Then, x_1–x_4 is used as the best model of size 2 up to now.

Step 3. There are two variables in the current model and the values of AIC after deleting one of them are $AIC(x_4x_1/x_1) = AIC(x_4) = 61.0233$ and $AIC(x_4x_1/x_4) = AIC(x_1) = 65.6912$. As the less important variable is the variable x_1 just inserted, no deletion is needed.

Step 4. The AIC values of two variables remaining outside the model are $AIC(x_4x_1.x_2) = 29.7543$ and $AIC(x_4x_1.x_3) = 30.5080$, x_2 is introduced in the model and the third SW is run on pivotal element r_{22} and x_1–x_2–x_4 is the best three-variable model up to now.

Step 5. Considering variable rejection we obtain $AIC(x_4x_1x_2/x_2) = AIC(x_4x_1) = 32.1524$, $AIC(x_4x_1x_2/x_1) = AIC(x_4x_2) = 64.0401$ and $AIC(x_4x_1x_2/x_4) = AIC(x_2x_1) = 28.8307$. The least important variable, x_4, which is not the one just added should be rejected by sweeping the pivotal element r_{44}. A new two-variable model x_1–x_2 is thus obtained. Since $AIC(x_1x_2) < AIC(x_1x_4)$, we substitute x_1x_2 for x_1x_4 as the best model of size 2.

Step 6. Continue to check if a further deletion is needed for the remaining two variables and compute the corresponding values of AIC: $AIC(x_1x_2/x_2) = AIC(x_1) = 65.6912$ and $AIC(x_1x_2/x_1) = AIC(x_2) = 61.3497$. Variable x_1 should be removed by sweeping the pivotal element r_{11}. The best one variable model of x_4 should not be

TABLE 3

Selection results for dye mixtures by MSR

No.	A [a]	B [b]	Model [c]	Values of criteria			C [d]
				AIC	$RMS_q \times 10^6$	$S_q \times 10^7$	
1	b (19.00)	9	a	−96.6	39006.28	1390.85	b (18.94
	c (30.80)		bc	−370.1	5.37	1.99	c (30.72)
			abc	−367.5	5.49	2.11	
			abce	−364.4	5.69	2.27	
			abcde	−381.6	3.05	1.27	
2	a (13.90)	9	d	−99.8	35130.59	1254.66	a (13.79)
	c (30.80)		ac	−371.7	5.25	1.89	c (30.71)
			ace	−368.8	5.26	2.02	
			acde	−389.2	2.55	1.02	
			abcde	−398.8	1.76	0.73	
3	d (9.60)	9	c	−156.8	5591.50	1997.00	d (9.55)
	e (4.10)		de	−397.1	2.25	0.83	e (4.09)
			ade	−394.9	2.26	0.87	
			bcde	−392.5	2.30	0.92	
			abcde	−389.4	2.38	0.99	
4	a (13.90)	5	b	−152.1	6505.21	2323.29	a (14.41)
	b (19.00)		ab	−408.5	1.46	0.56	b (18.36)
			abc	−404.1	1.89	0.66	
			abce	−405.9	1.49	0.60	
			abcde	−402.7	1.55	0.64	
5	d (19.10)	5	d	−147.4	7559.19	2699.75	d (19.03)
	e (2.05)		de	−419.7	1.09	0.40	e (2.12)
			bde	−418.6	1.08	0.41	
			bcde	−416.0	1.07	0.43	
			abcde	−415.5	1.03	0.43	
6	a (13.90)	5	b	−126.1	24309.66	7596.77	a (13.94)
	b (19.00)		be	−177.9	5222.42	1684.65	b (18.79)
	e (4.10)		abe	−431.0	3.57	1.18	e (4.12)
			abde	−428.0	3.67	1.27	
			abcde	−433.2	2.99	1.07	
7	a (13.90)	9	a	−74.3	106705.20	33345.37	a (13.58)
	b (19.00)		bd	−184.8	4287.47	1383.06	b (19.39)
	d (19.10)		abd	−425.7	4.16	1.39	d (18.89)
			abde	−424.9	4.02	1.38	
			abcde	−422.0	4.12	1.47	
8	a (13.90)	5	c	−110.6	37832.48	11822.65	a (13.81)
	c (30.80)		ac	−126.6	22612.64	7294.40	c (30.04)
	d (4.10)		ace	−416.8	5.36	1.79	e (4.08)
			acde	−416.1	5.16	1.78	
			abcde	−413.2	5.30	1.89	
9	b (19.10)	5	c	−102.4	47869.65	14959.27	b (19.10)
	c (30.80)		bc	−124.8	23812.26	7681.37	c (30.22)
	e (4.10)		bce	−415.2	5.60	1.87	e (4.07)
			bcde	−413.4	5.57	1.92	
			abcde	−410.6	5.71	2.04	
10	b (19.10)	5	d	−105.8	43610.86	13581.84	b (18.69)
	d (19.10)		bd	−133.2	18750.92	6048.68	d (18.87)
	e (4.10)		bde	−432.1	3.46	1.15	e (4.07)
			abde	−431.0	3.37	1.16	
			abcde	−428.8	3.39	1.21	
11	a (13.90)	9	d	−115.5	32889.45	10277.95	a (13.95)
	c (30.80)		ac	−166.0	7343.89	2369.00	c (31.47)
	d (19.10)		acd	−438.2	2.91	0.97	d (18.81)
			abcd	−444.6	2.29	0.79	
			abcde	−441.4	2.36	0.84	

TABLE 3, continued

No.	A [a]	B [b]	Model [c]	Values of criteria			C [d]
				AIC	$RMS_q \times 10^6$	$S_q \times 10^7$	
12	b (19.00)	5	d	−105.6	43665.07	13645.3	b (18.73)
	c (38.00)		bd	−151.7	11035.02	3560.0	c (30.83)
	d (19.10)		bcd	−409.5	6.80	2.26	d (18.86)
			abcd	−410.5	5.71	1.97	
			abcde	−410.0	5.80	2.07	
13	c (19.10)	5	c	−254.8	612.18	191.30	c–d
	d (19.10)		cd	−403.8	8.23	2.65	
	e (4.10)		cde	−410.0	6.55	2.18	
			bcde	−420.1	4.60	1.58	
			abcde	−425.0	3.78	1.35	
14	c (19.10)	7	c	−261.0	514.76	160.86	d–e
	d (19.10)		de	−420.6	5.09	1.64	
	e (4.10)		bde	−437.7	2.94	0.98	
			bcde	−437.7	2.79	0.96	
			abcde	−438.5	2.57	0.92	
15	c (19.10)	7	c	−260.4	523.49	163.59	c–d
	d (19.10)		cd	−409.8	6.92	2.23	
	e (4.10)		cde	−428.4	3.84	1.28	
			acde	−430.7	3.40	1.17	
			abcde	−431.2	3.17	1.13	

[a] A = components actually existing in the mixtures and their concentrations in ppm (in parentheses). [b] B = number of sweep operations. [c] a = Amaranth; b = coccinellin; c = tatrazine; d = brilliant blue; e = apple green. [d] C = components selected with MSR and the corresponding estimate of concentrations in ppm (in parentheses).

replaced by the new one variable model, x_2, because $AIC(x_2) > AIC(x_4)$.

Step 7. The insertion process is continued and x_1 is added once again since $AIC(x_2.x_1)$ (28.8307) is smaller than $AIC(x_2.x_3)$ (54.40) and $AIC(x_2.x_4)$ (64.0401), and the sixth *SW* on the pivotal element r_{11} is performed. The status of the best two-variable model of x_1x_2 is unchangeable as the new two-variable model is also x_1–x_2.

Step 8. The candidate for rejection is x_1 and it should not be removed.

Step 9. x_4 is added in this step because $AIC(x_1x_2x_3) = 29.7916$ and $AIC(x_1x_2.x_4) = 29.7543$, and the seventh *SW* with the pivotal element r_{44} is completed. The status of the best three-variable model of x_1–x_2–x_4 is unchangeable.

Step 10. The candidate for deletion for this three-variable model is x_4 and no removal will occur. Then the last variable outside the model, x_3, is added, which corresponds to the eighth *SW* with the pivotal element r_{33}, and no deletion takes place because $AIC(x_1x_2x_3x_4/x_3)$ is the smallest among $AIC(x_1x_2x_3x_4/x_4)$ (29.7916), $AIC(x_1x_2x_3x_4/x_3)$ (29.7543), $AIC(x_1x_2x_3x_4/x_2)$ (30.5080) and $AIC(x_1x_2x_3x_4/x_1)$ (35.3563). The stepwise process is terminated, and an optimum sequence of models is obtained (see Table 2).

In total, eight sweep operations (i.e., eight regressions) have been carried out.

Real analytical systems

Without variable selection and using all suspected species as regression variables, none of the mixtures of five possible dyes could be analysed with satisfactory concentration estimates for all the components. The analytical results were also unsatisfactory when the Kalman filter method was used. A variable selection process was essential for building the calibration model of "grey" analytical systems.

Table 3 lists some representative results for fifteen mixtures containing two or three of five

possibly existing dyes obtained by using MSR. The selected components for each mixture and their concentration estimates are shown together with the optimum sequence and the values of the criteria. The number of *SW* applied is also given.

Inspecting the values of the criteria in the optimum sequence, there are abrupt decreases in these values when the number of variables of the models increased from a lower value to the correct value, and there is a minimum coincident with the model of the correct number of variables in the sequence of most mixtures in Table 3. This characteristic arises because there exists a best variable subset corresponding to real components in the mixtures and an intrinsically linear relationship characterized by Beer's law. If there is no significant collinearity among the variables (the spectra of components), this variable subset should be much more suitable for the regression equation than all other models except those with more variables included, so *RSS* will decrease drastically when the number of variables changes from a lower value to this correct value, and a further increase of variables on the basis of this model will cause only a slight decrease in *RSS*. As a consequence of the continuing decline of *RSS* and the successive increase in the number of variables in the optimum sequence, the minimum of AIC_q and other analogous criteria would be expected for the model which most closely reflects reality [5,6], and this makes an ultimate unambiguous decision possible.

The situation described above should be regarded as an overall tendency and no absolute consistency would be pursued in practice because of the complexity of real systems, e.g., all independent variables suffer from errors and collinearity exists among variables. More generally, when the actually existing variables have been included in the model, the values of these criteria will tend to a minimum and stabilize as further variables are added. This can be seen from Table 3, where some mixtures show more than one minimum and others give a single minimum pointing to the correct model. However, it can be clearly seen from the sequences in Table 3 that the values of these criteria show only minor differences after the correct model was obtained, especially for RMS_q and S_q. Hence on this occasion one should select the model in the beginning of the stabilized region in the sequence in order not to include more variables than necessary and avoid overfitting.

It should be remembered that the proposed procedure does not work for all situations. Three mixtures consisting of tartrazine (c), brilliant blue (d) and apple green (e) with different concentration ratios were prepared and analysed by the proposed method. It was assumed that the possibly co-existing species were amaranth (a), coccinellin (b) and c, d and e. The optimum sequences obtained for these mixtures are (see Nos. 13–15 in Table 3 also):

(i) c, c–d, c–d–e, b–c–d–e, a–b–c–d–e
(ii) c, d–e, b–d–e, b–c–d–e, a–b–c–d–e
(iii) c, c–d, c–d–e, a–c–d–e, a–b–c–d–e

respectively. Two variables were chosen and these results were obviously incorrect.

The condition numbers of spectral matrices of all possible two- and three-component combinations of these five species were calculated and it was discovered that all combinations had condition numbers smaller than 10 except the c–d–e combination, which had a much higher condition number of 203. This implied that the spectra of these three components overlapped heavily and serious multi-collinearity existed. One could verify this from Fig. 1. If one ignored the incorrect number of components given by the MSR method and took the correct number of species (three) for mixtures (i) and (iii), one should have the correct calibration model (c–d–e) for both cases; the relative errors in the concentration estimation for c, d and e were (i) 51.71, 35.70, −41.48 and (iii) 16.47, −8.80, −11.75, respectively. These results indicated that one could not obtain correct results even using the correct model for such ill-conditioned systems. One partial solution of this problem is to use a biased estimation method. The problem of the interpretation of an ill-conditioned "grey" analytical system when only one analytical sample is available requires further investigation.

In conclusion, MSR alleviates the problems associated with the *F*-test in CSR and provides a feasible means of finding the optimum calibration

model. It can be used in the identification of co-existing components in "grey" analytical systems.

This work was supported by the National Natural Science Foundation of China.

APPENDIX A

Computation of AIC_q in a stepwise process

Akaike's information criterion (AIC) is defined as [10]

$$AIC = -2\log(\text{maximum likelihood}) + 2(\text{number of independent parameters}) \quad (A1)$$

From the error assumption $e \sim N(0, \sigma^2)$ of a general linear regression model:

$$y = \beta_0 + x_1\beta_1 + x_2\beta_2 + \ldots + x_p\beta_p + e \quad (A2)$$

Let $X = (\mathbf{1}, x_1, x_2, \ldots, x_p)$ and $\boldsymbol{\beta} = (\beta_0, \beta_1, \beta_2, \ldots, \beta_p)'$, then the likelihood function of $\boldsymbol{\beta}$ and σ^2 is:

$$L(\hat{\boldsymbol{\beta}}, \hat{\sigma}^2, y) = (2\pi\hat{\sigma}^2)^{-\frac{m}{2}} \exp\left[-\frac{1}{2\hat{\sigma}^2}\| y - X\hat{\boldsymbol{\beta}} \|^2\right] \quad (A3)$$

Since the maximum likelihood estimates of $\hat{\boldsymbol{\beta}}$ and $\hat{\sigma}^2$ are

$$\hat{\boldsymbol{\beta}} = (X'X)^{-1}X'y \quad (A4)$$

$$\hat{\sigma}^2 = \left\{y'\left(I - X(X'X)^{-1}X'\right)y\right\}/m \quad (A5)$$

one will obtain

$$\log L(\hat{\boldsymbol{\beta}}, \hat{\sigma}^2, y) = -\frac{m}{2}\log(2\pi) - \frac{m}{2}\log(\hat{\sigma}^2) - \frac{m}{2} \quad (A6)$$

and consequently

$$AIC_q = m \log \hat{\sigma}^2 + 2q + C \quad (A7)$$

where $q = p + 1$ and $C = m \log(2\pi) + m$; the latter is a constant not related to p and is often ignored.

For a model containing n variables such as Eqn. 1, if q variables were selected in the equation in the former $l-1$ SW, then in the lth SW one calculates the contribution of the remaining $n-q$ variables outside the equation from the result of the $l-1$th sweep operation and looks for a variable k:

$$Q_j^{(l)} = \frac{\left[r_{j(n+1)}^{(l-1)}\right]^2}{r_{jj}^{(l-1)}} \quad (A8)$$

If one introduced a variable j into the equation, the variance of the dependent variable y would change to

$$(\hat{\sigma}^2)_j^{(l)} = \frac{1}{m-q-2} r_{(n+1)(n+1)}^{(l)} = \frac{1}{m-q-2}\left(r_{(n+1)(n+1)}^{(l-1)} - \frac{r_{(n+1)j}^{(l-1)} r_{j(n+1)}^{(l-1)}}{r_{jj}^{(l-1)}}\right) = \frac{1}{m-q-2}\left[r_{(n+1)(n+1)}^{(l-1)} - Q_j^{(l)}\right] \quad (A9)$$

and

$$AIC_j^{(l)} = m \log(\hat{\sigma}^2)_j^{(l)} + 2(q+2) + C = m \log\left[r_{(n+1)(n+1)}^{(l-1)} - Q_j^{(l)}\right] - m \log(m-q-2) + 2(q+2) + C \quad (A10)$$

If $Q_k^{(l)} = \max[Q_j^{(l)}]$, then $AIC_k^{(l)} = \min[AIC_j^{(l)}]$.

When the $q+1$th variable k is inserted into the equation, the contribution of q variables already in the equation is

$$Q_i^{(l+1)} = \frac{\left[r_{i(n+1)}^{(l)}\right]^2}{r_{ii}^{(l)}} \quad (A11)$$

If a variable i of these q variables is removed from the equation in the $l+1$th step, then

$$(\hat{\sigma}^2)_i^{(l+1)} = \frac{1}{m-q-1} r_{(n+1)(n+1)}^{(l+1)} = \frac{1}{m-q-1}\left[r_{(n+1)(n+1)}^{(l)} - \frac{r_{(n+1)i}^{(l)} r_{i(n+1)}^{(l)}}{r_{ii}^{(l)}}\right] = \frac{1}{m-q-1}\left\{r_{(n+1)(n+1)}^{(l)} + \frac{\left[r_{i(n+1)}^{(l)}\right]^2}{r_{ii}^{(l)}}\right\} = \frac{1}{m-q-1}\left[r_{(n+1)(n+1)}^{(l)} + Q_i^{(l+1)}\right] \quad (A12)$$

and

$$AIC_i^{(l+1)} = m \log\left[r_{(n+1)(n+1)}^{(l)} + Q_i^{(l+1)}\right] - m \log(m-q-1) + 2(q+1) + C \quad \text{(A13)}$$

If $Q_t^{(l+1)} = \min[Q_i^{(l+1)}]$, then $AIC_t^{(l+1)} = \min[AIC_i^{(l+1)}]$.

So far, we have shown that the resultant equation has the smallest AIC value after inserting the variable which has the largest contribution Q of all candidates or rejecting the variable which has the smallest contribution Q of all current variables.

Summing up all the relationships described above, one obtains the AIC expression in the lth step of the stepwise process:

$$AIC_k^{(l)} = m \log\left[r_{(n+1)(n+1)}^{(l-1)} - \frac{r_{k(n+1)}^{(l-1)} r_{(n+1)k}^{(l-1)}}{r_{kk}^{(l-1)}}\right] - m \log(m-v) + m \log s^2 + 2v + C \quad \text{(A14)}$$

where s^2 is the variance of variable y: $s^2 = \Sigma(y_i - \bar{y})^2$, the estimate of the noise variance of the original model is s^2 times of that the model after normalization in MSR, so a term $m \log s^2$ is added in Eqn. A14 for compensation. The parameter v equals to $q+2$ or q depending on whether the k is introduced into or rejected from the equation.

APPENDIX B

Sweep operation

For an n by n square matrix, $A = (a_{ij})_{n\times n}$, sweep operation with the pivotal element a_{kk}, SW_k, was defined as

$$B = SW_k A \quad \text{(B1)}$$

and

$$\begin{cases} b_{kk} = 1/a_{kk} & \\ b_{ik} = -a_{ik}/a_{kk} & i \neq k \\ b_{kj} = a_{kj}/a_{kk} & j \neq k \\ b_{ij} = a_{ij} - a_{ik} \times a_{kj}/a_{kk} & i, j \neq k \end{cases} \quad \text{(B2)}$$

An SW has the following features. First, it is reversible and exchangeable, i.e.,

$$SW_k SW_k A = A \quad \text{(B3a)}$$

$$SW_i SW_j A = SW_j SW_i A \quad \text{(B3b)}$$

Second, assuming that X and y in Eqn. 1 have been mean centred, separate X into two blocks as:

$$X = (X_p \mid X_r) \quad \text{(B4)}$$

where $p + r = n$, $X_p(X_r)$ is a submatrix consisting of $p(r)$ columns of X. Let

$$D = X'X = \begin{pmatrix} X_p'X_p & X_p'X_r \\ X_r'X_p & X_r'X_r \end{pmatrix} = \begin{pmatrix} D_{11} & D_{12} \\ D_{21} & D_{22} \end{pmatrix} \quad \text{(B5)}$$

and

$$A = \begin{pmatrix} D & X'y \\ y'X & y'y \end{pmatrix} = \begin{pmatrix} D_{11} & D_{12} & X_p'y \\ D_{21} & D_{22} & X_r'y \\ y'X_p & y'X_r & y'y \end{pmatrix} \quad \text{(B6)}$$

then

$$SW_1 SW_2 \ldots SW_p A = \begin{pmatrix} D_{11}^{-1} & * & D_{11}^{-1}X_p'y \\ * & * & * \\ * & * & y'y - y'X_p D_{11}^{-1} X_p'y \end{pmatrix} \quad \text{(B7)}$$

Here, $D_{11}^{-1}X_p y'$ is just the least-square estimate of c_p, the regression coefficients of the selected model consisting of p variables, and $y'y - y'X_p D_{11}^{-1} X_p y'$ is the corresponding RSS_p, and $*$ denotes the unnecessary sub-blocks omitted.

Based on the above two features, one can obtain the primary statistics such as RSS_p and c_p of the selected model by using SW.

REFERENCES

1 Y.-Z. Liang, Y.-L. Xie and R.-Q. Yu, Chemistry (China), No. 8 (1989) 4.
2 E.R. Malinowaski and D.G. Howery, Factor Analysis in Chemistry, Wiley, New York, 1980.
3 Y.-Z. Liang, Y.-L. Xie and R.-Q. Yu, Acta Pharm. Sin., 24 (1989) 537.

4 Y.-Z. Liang. Y.-L. Xie and R.-Q. Yu, Acta Chim. Sin., 48 (1990) 472.
5 N.R. Draper and H. Smith, Applied Regression Analysis, Wiley, New York, 1981.
6 X.-R. Chen and S.-G. Wang, Modern Regression Analysis, Anhui Education Publishing House, Hefei, 1987.
7 E.M.L. Beale, Technometrics, 12 (1970) 909.
8 N. Mantel, Technometrics, 12 (1970) 621.
9 H.-Q. Pan and P.-Z. Shi, Math. Theory Pract. (China), No. 2 (1987) 54.
10 H. Akaike, IEEE Trans. Autom. Control. AC-19 (1974) 716.
11 M. Shatzoff, S. Fienberg and R. Tsak, Technometrics, 10 (1968) 769.
12 G.M. Furnival and R.W. Wilson, Technometrics, 16 (1974) 499.
13 C.-X. Mao, Math. Theory Pract. (China), No. 4 (1987) 20.
14 A. Hald, Statistical Theory with Engineering Applications, Wiley, New York, 1952.

Analytica Chimica Acta, 272 (1993) 73–81
Elsevier Science Publishers B.V., Amsterdam

Comparison of immobilization methods for the development of an acetylcholinesterase biosensor

Kathrin Stein and Georg Schwedt

Institut für Anorganische und Analytische Chemie der Technischen Universität Clausthal, Paul-Ernst-Str. 4, W-3392 Clausthal-Zellerfeld (Germany)

(Received 17th July 1992; revised manuscript received 16th September 1992)

Abstract

Different methods for the immobilization of acetylcholinesterase (AChE); viz., co-cross-linking at the surface of a pH electrode, co-cross-linking in a membrane and trapping in a polyacrylamide membrane, are described. The immobilization products are compared with respect to the response times, the reproducibility of the preparation and the applicability in a biosensor. For detecting AChE inhibitors the suitability of the immobilization products in combination with a pH electrode was tested with the organophosphorus pesticide dichlorvos.

Keywords: Biosensors; Enzymatic methods; Acetylcholinesterase; Dichlorvos; Immobilization methods; Pesticides

So far biosensors have been mainly developed for the measurement of concentrations of biological compounds in medical analysis, e.g., monitoring of blood sugar levels [1,2]. Biosensors are made of a biochemical or biological component (receptor component), e.g., an enzyme, antibody, cell or microorganism, and a transducer. The transducer sends the signal formed by the receptor component to the transducing system. For biosensor electrodes, field-effect transistors, fibre-optic devices, thermistors or piezoelectric crystals can be used as transducers [1–4]. Normally the receptor component is directly coupled to the transducer [2].

If acetylcholinesterase (AChE) is used as the biochemical component, the enzymatic hydrolysis of acetylcholine (ACh) produces acetic acid and choline. The activity of the enzyme can be measured by the potentiometric detection of the protons formed by the acetic acid produced.

In an AChE biosensor, immobilized AChE is contacted with the pH-sensitive surface of an electrode (transducer). After connecting the "enzyme electrode" to a pH meter, the enzymatic reaction can be monitored. The enzyme is reversibly inhibited by insecticide *N*-methylcarbamates and irreversibly inhibited by organophosphorus esters and, after the conversion into the oxones, by organothiophosphorus esters. An AChE biosensor is suitable for the screening of plant-protection agents of these classes in drinking water by detection of the inhibition effect.

The immobilization reaction fixes the water-soluble enzyme at or in a water-insoluble matrix. The result is an artificial decrease in the mobility of the enzyme with a transition from homogeneous to heterogeneous catalysis. When choosing a suitable immobilization technique it is important that the reaction required for the immobilization does not significantly decrease the catalytic activity of the enzyme.

Correspondence to: G. Schwedt, Institut für Anorganische und Analytische Chemie der Technischen Universität Clausthal, Paul-Ernst-Str. 4, W-3392 Clausthal-Zellerfeld (Germany).

The aim of this work was the development of an immobilization technique that is suitable for producing stable and long-lived immobilization products rapidly and in expensively. For use of an electrode as the transducer of a biosensor, the immobilization product must be contacted with the ion-sensitive surface of the electrode. If the immobilization forms a stable membrane, it can be easily fixed to the surface of the electrode with a rubber-band or a nylon net [5,6]. Co-cross-linking with glutaraldehyde and albumin and trapping in a polyacrylamide gel lattice was compared with respect to applicability in a biosensor.

EXPERIMENTAL

Reagents

All chemicals were of analytical-reagent grade. The following were used: cellulose nitrate membrane filter, 1.2 μm (Sartorius SM 11303 047N), cellulose nitrate membrane filter, 0.45 μm (Sartorius SM 11106 047M), cellulose acetate membrane filter (Macherey–Nagel ST 69), acetylcholinesterase (AChE) of electric eel type VI-S with 200–400 U mg^{-1} solid, AChE of electric eel type III with 909.09 U ml^{-1} (both from Sigma), AChE of bovine erythrocytes, 2 U mg^{-1} solid (Serva), bovine serum albumin fraction V (Merck), 1% (v/v) solution of glycine (Merck) in phosphate buffer (buffer: 2.84 g NaCl, 0.2 g KCl, 0.36 g $Mg_2Cl_2 \cdot 6H_2O$, 1.6 g $Na_2HPO_4 \cdot 2H_2O$ and 0.2 g NaN_3 in 2 l of water, pH adjusted to 7.4 with concentrated HCl), 25% (v/v) solution of glutaraldehyde in water (Serva), acetylcholine chloride (Serva), 2% (v/v) dimethyldichlorosilane in 1,1,1-trichloroethane (Reppel-Silan) (LKB Pharmacia), acrylamide monomer (Merck), *N,N'*-methylenebisacrylamide (BIS) (Merck), *N,N,N',N'*-tetramethylethylenediamine (Temed) (Merck), ammonium peroxodisulphate (Riedel-de Haën) and inhibitor stock solution containing 1 g l^{-1} dichlorvos (Riedel-de Haën) in buffer.

Apparatus

A pH electrode with a spherical surface (N61, Schott Geräte), flat-surface pH electrode (403-S7/165, Ingold), a pH meter (Metrohm), a magnetic stirrer (Metrohm) and an *X–Y* recorder (Asea Brown Boveri) were used.

Immobilization procedure

Co-cross-linking on to the surface of the electrode [7]

About 50 U of AChE (from bovine erythrocytes) and 175 mg of albumin are dissolved in 2 ml of the phosphate buffer in a 3-ml beaker. To start the co-cross-linking reaction, 70 μl of the glutaraldehyde solution are added. The solution is stirred carefully (no bubbles). After 3 min the carefully cleaned and dried electrodes (with spherical surface, Schott Geräte N61) are dipped into the immobilization solution with the pH-sensitive surface three to five times (how often depends upon the viscosity of the solution). Until complete gelation (ca. 15 min) of the enzymatic membrane the electrodes must be rotated at an angle of 45°. Finally, the enzyme membrane is attached by means of a rubber-band. The enzyme electrodes produced are dipped in each case for 15 min in distilled water, in 1% (v/v) glycine solution to remove the excess of glutaraldehyde and again in distilled water. The enzyme electrodes are stored at 4°C in buffer until the measurement.

Co-cross-linking in a membrane

Method 1. About 1000 U of AChE (from electric eel type VI-S) and 875 mg of albumin are dissolved in 10 ml of the phosphate buffer. To start the co-cross-linking reaction, 350 μl of the glutaraldehyde solution are added. The solution must be carefully stirred, avoiding bubbles. After 3 min the membrane filters (cellulose nitrate, 1.2 μm) are dipped into the solution to wet them completely. Until complete gelation the filters are fixed with a pin, e.g., on a pasteboard, so that the membranes make no contact with anything. After drying they are dipped in each case for 15 min in distilled water, in 1% (v/v) glycine solution to remove the excess of glutaraldehyde and again in distilled water. The membranes are stored at 4°C in the phosphate buffer.

Method 2. Four membrane filters (cellulose nitrate, 1.2 μm; cellulose acetate, 1.2 μm) are

placed in the 25% (v/v) glutaraldehyde solution for 1 h, 390 U of AChE (from electric eel type VI-S) and 175 mg of albumin are dissolved in 2 ml of the phosphate buffer and the membrane filters are then removed from the glutaraldehyde solution and moistened with the enzyme–albumin–buffer solution. The membranes are placed on a glass plate, covered with a second plate and stored overnight in a refrigerator. The next morning the membranes are carefully removed from the glass plates, dipped in distilled water (15 min), 1% (v/v) glycine solution to remove the excess of glutaraldehyde and again in distilled water (in each case 15 min). The membranes are stored at 4°C in the phosphate buffer.

Immobilization by trapping in polyacrylamide

General procedure. Acrylamide monomer and BIS are dissolved in 2 ml of the phosphate buffer in a 3-ml beaker and the enzyme AChE is added. Two glass plates are rubbed with Reppel-Silan and the membrane filters are placed on the first plate. Then 2 μl of Temed and 8 μl of ammonium peroxodisulphate solution [20% (v/v) in the phosphate buffer; storable for 1 week] are added to the polymer–enzyme solution and subsequently this solution is poured over the membrane filters on the glass plate. The second glass plate is placed on the first and they are pressed together strongly with clamps. After 30 min the clamps can be removed. The enzyme membranes are stored at 4°C in the phosphate buffer.

Method 1. $T = 15\%$, $C = 5\%$ ($\%T$ = total concentration of solid, $\%C$ = percentage of cross-linker): 300 mg of acrylamide monomer and 16 mg of BIS are dissolved in 2 ml of the phosphate buffer, the 120 U of AChE (electric eel type VI-S) are added. The subsequent procedure is the same as described above.

Membranes with different polymer composition. To prepare a polymer stock solution (solution A), 1.520 g of acrylamide monomer and 80 mg of BIS are dissolved in 2 ml of the phosphate buffer. To prepare an enzyme stock solution (solution B), 240 U of enzyme (electric eel type VI-S) are dissolved in 2 ml of the phosphate buffer.

For the preparation of the different polymers, the polymerization solutions are combined according to the following scheme (volumes in μl):

	Solution A	Solution B	Water
$T = 40\%$, $C = 5\%$:	250.0	250.0	0
$T = 30\%$, $C = 5\%$:	187.5	250	62.5
$T = 20\%$, $C = 5\%$:	125.0	250	125.0
$T = 10\%$, $C = 5\%$:	62.5	250	187.5

To each of these solutions 1 μl of Temed and 4 μl of ammonium peroxodisulphate solution are added. The membrane filter (cellulose acetate, 1.2 μm) is cut in the middle and placed on the first glass plate; 250 μl of the same polymer solution are pipetted on to the two membranes at a time, giving two enzyme membranes for each polymer composition. The subsequent procedure was the same as described above.

$T = 20\%$, $C = 5\%$: 380 mg of acrylamide monomer, 20 mg of BIS and 157.2 U of AChE (electric eel type VI-S) are dissolved in 2 ml of the phosphate buffer. A 245-μl volume of this solution is pipetted on to each of eight membranes lying on the first glass plate. The subsequent procedure is the same as described above.

Method 2. A 380-mg amount of acrylamide monomer and 20 mg of BIS are dissolved in 2 ml of the phosphate buffer and 2 μl of Temed and 8 μl of ammonium peroxodisulphate solution [20% (v/v) in the phosphate buffer] are added. Eight membrane filters (cellulose acetate, 1.2 μm) are placed on the first glass plate and 19 μl of the enzyme preparation (electric eel type III) (equivalent to 17.27 U per membrane) and 250 μl of the polymer solution are pipetted on to each membrane. The subsequent procedure is the same as described above.

Determination of activity

The enzyme membrane is placed over the ion-sensitive surface of the pH electrode (Ingold) and fixed with a rubber-band. Care must be taken to ensure that the enzyme membrane fits well and without wrinkles on the electrode. On dipping into the buffer, the enzyme electrode shows initial signal U_G. After dipping this electrode into 50 ml of the substrate solution in buffer the electrode shows another signal, U_S. The difference between the two signals is proportional to the

original activity of the enzyme in the membrane, U_0 ($U_0 = U_S - U_G$). The change in signal can be recorded with an X–Y recorder.

Determination of inhibition effect

The original activity, U_0, of the enzyme membrane is determined for a solution of 300 mg l^{-1} acetylcholine chloride (ACh) in buffer. For the inhibition the electrode is incubated in a 1.0 or 0.1 mg l^{-1} dichlorvos solution in buffer. After 30 min the activity, U_I, of the electrode is determined again for the same substrate solution as described above. The difference between the two activities shows the inhibition effect, I [I (%) = $(U_0 - U_I)/U_0 \times 100\%$].

RESULTS AND DISCUSSION

Immobilization by co-cross-linking

Immobilization by co-cross-linking is a commonly used technique and suitable for many enzymes. Bi- or multi-functional reagents react covalently with the enzyme molecules (cross-linking), if catalytic inactive protein is added to both the protein and the enzyme (co-cross-linking), to give macromolecular aggregates. The formation of covalent bonds between reagent and enzyme can lead to changes in the three-dimensional structure of the enzyme, which is necessary for the catalysis, and therefore to decreases in activity. On the other hand, this technique can be applied quickly and easily [5,8]. The cross-linking agent mostly used is glutaraldehyde [5]. Different mechanisms have been described for the immobilization reaction with glutaraldehyde. On the one hand the reaction between the aldehyde groups of the glutaraldehyde and free amino groups of the enzyme has been reported [5]. As enzymes have more than one free amino group, a macromolecular immobilization product can be formed. On the other hand, a reaction is possible between the amino groups of the protein and an α,β-unsaturated aldehyde (Michael addition reaction), which is formed by dehydration of an aqueous glutaraldehyde solution [9,10]. The immobilization by co-cross-linking with glutaraldehyde and albumin offers the possibility of immobilizing the enzyme directly on the ion-sensitive surface of the pH electrode. Such a procedure has been already described for AChE [7].

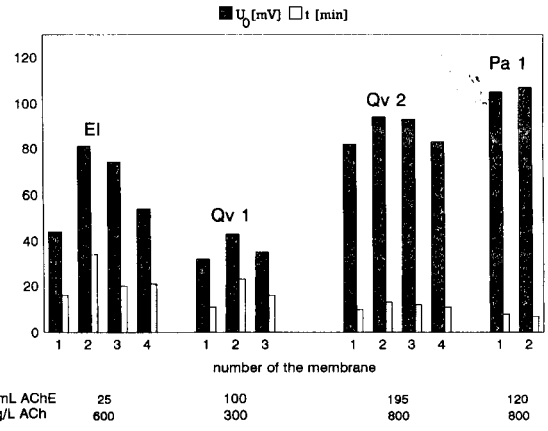

Fig. 1. Comparison of the immobilization product according to the original activity and the steady-state times. El = co-cross-linking on to the ion-sensitive surface of the electrode; Qv = co-cross-linking in a membrane (1 = method 1; 2 = method 2); Pa 1 = trapping in polyacrylamide membrane method 1. U_0 = Original activity; t = time; u = enzyme units.

Co-cross-linking on the electrode

The advantage of immobilization directly on the ion-sensitive surface of a pH electrode by co-cross-linking with glutaraldehyde and bovine serum albumin is the rapid and easy procedure and the long shelf-life (electrodes stored cool in buffer are stable for over 50 days without a serious decrease in activity [7]).

Four electrodes produced in the same batch (a maximum of fifteen electrodes can be produced in the same process [7]) show different original activities, U_0, and vary in the time they take to reach steady-state activity (steady-state time) (Fig. 1). The gelation of the albumin–enzyme solution begins after adding the cross-linking agent glutaraldehyde. The thickness of the enzyme layer on the electrode depends on the viscosity of the immobilization solution. Immediately after adding glutaraldehyde the viscosity of the solution is the same as that of water. Dipping the electrodes into the solution then does not lead to the forma-

tion of an enzyme membrane on the surface of the electrodes. With containing gelation of the enzyme–albumin solution the viscosity of the solution increases. The more viscous the solution, the thicker will be the enzyme layer formed on the electrode. The activity of the enzyme electrode depends on the concentration of enzyme in the enzyme layer. The thicker the enzyme membrane on the electrode, the greater is the content of enzyme in the enzyme layer of the electrode and the higher is the activity of the electrode. Hence this method is not suitable for producing enzyme electrodes that are comparable with respect to activity and time of measurement.

The dependence of the activity on the concentration of the substrate ACh is illustrated in Fig. 2. The threshold value depends on the one hand on the kinetics of the enzyme reaction and on the other hand on the diffusibility of the substrate through the enzyme membrane and the diffusibility of the protons produced. The inhibition of electrode 1 (Fig. 1) with 0.1 mg l^{-1} dichlorvos solution in buffer is shown in Fig. 3.

Immobilization in membranes

This immobilization technique produces enzyme membranes that can be contacted with the pH-sensitive area of a flat-surface electrode by turning the membrane over on the electrode. The

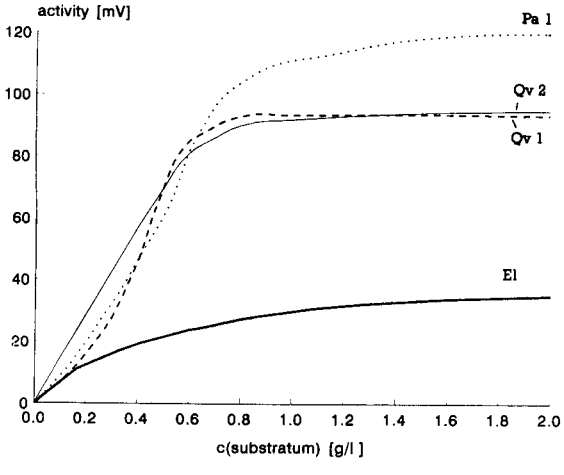

Fig. 2. Behaviour of the sensors with increasing substrate concentrations. Abbreviations as in Fig. 1.

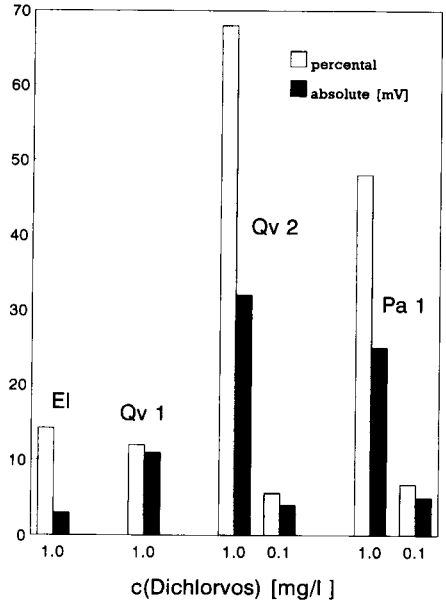

Fig. 3. Comparison of inhibition with dichlorvos of the immobilization products. Abbreviations as in Fig. 2.

membrane has to be fixed with a rubber-band. The exchange of the used enzyme membranes is quickly and easily effected without the risk of damaging the pH-sensitive surface of the electrode. The membranes are stored separately from the electrode in a refrigerator.

Method 1

First immobilizations in a membrane were carried out by dipping a membrane into the immobilization solution instead of an electrode.

In the same process three enzyme membranes were produced. By means of this technique it was possible to dip membrane filters into the immobilization solution until the gelation had not proceeded too much. Because of the large amount of enzyme, as many enzyme membranes as possible should be produced. This technique also was not successful in producing membranes that are comparable in activity and steady-state time. Figure 1 shows the activities and the steady-state times of three enzyme membranes produced from the same charge. The differences in the membranes are slightly smaller than the difference in electrodes produced by immobilization directly on the surface of the electrode. This is due to the

thickness of the enzyme membrane, which is mainly influenced by the thickness of the membrane filter. Also, this technique does not lead to enzyme membranes with the some concentration of enzyme. For each membrane the viscosity of the solution and therefore the content of enzyme in each membrane are different. In principle, however, membranes with a short steady-state time (membrane 1, Fig. 1) can be produced with the described technique. The dependence of the activity of membrane 3 (Fig. 1) on increasing substrate concentration is shown in Fig. 2. The form of the graph is similar to that for the electrode produced by immobilization directly on the surface of the electrode.

Inhibition tests with 1.0 mg l^{-1} dichlorvos solution in buffer of membrane (Fig. 1) resulted in a decrease in activity of 12% after an incubation period of 30 min determined with a substrate concentration of 800 mg l^{-1} ACh (Fig. 3).

Method 2

An immobilization procedure for glucose oxidase or glutamate oxidase has been described, involving spraying its solution of cellulose triacetate, glutaraldehyde and an amine on a glass plate. After drying, a thin cellulose triacetate membrane was formed. For immobilization this membrane was placed in glutaraldyde solution and then in a solution of the enzyme after a fixed incubation period. Subsequently the membrane was pressed between watch-glasses and stored cool overnight to complete the reaction [11,12]. This method was modified by using a commercial membrane filter.

The material of the carrier membrane is not important for the immobilization procedures. The properties of the materials differ only in the stability of the resulting enzyme membranes. Enzyme membranes with cellulose nitrate as the carrier membrane are damaged more quickly during turning over the flat-surface pH electrode, in spite of careful handling, than are enzyme membranes with cellulose acetate as the carrier membrane. Membranes with cellulose acetate retain the form of the electrode after removal from the electrode and can often be used without the risk of damage.

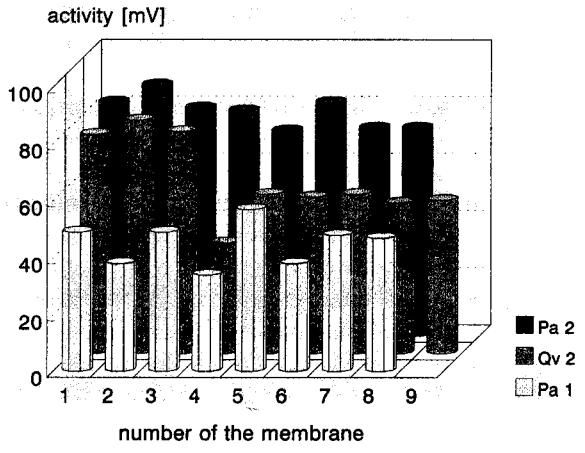

Fig. 4. Original activities of membranes produced in the same process. Abbreviations as in Fig. 1.

The measured values shown in Fig. 1 demonstrate clearly the advantages of this method. The steady-state time and therefore the time of measurement are shorter in each instance and comparable from membrane to membrane. Figure 4 shows the original activities of nine membranes produced in the same process. However, the activities of these membrane are not comparable. Hence this technique is not suitable for manufacturing enzyme membranes with the same original activities. During removal of the membranes from the watch-glasses (immobilization procedure) an amount of immobilization product is retained on the watch-glasses, and this amount is not the same for each membrane.

The characteristics of these enzyme membranes do not differ from these of membranes produced by dipping the membrane filter into the immobilization solution. The signal of the electrode as a function of the substrate concentration is illustrated in Fig. 2. This membrane also shows a limit of saturation of the substrate above a substrate concentration of 800 mg l^{-1}.

The shelf-life should be comparable to that of electrodes produced by co-cross-linking on the surface of the electrode, because of the same immobilization reaction. Membrane 1 (Fig. 1) was stored cool for a long period, during which time the activity was determined regularly. Figure 5 shows the activities during this period referred to

the original activity on the day of production. After 49 days the retained activity was 73% of the original activity.

Corresponding to the shorter steady-state times, the behaviour of these membranes against inhibitors is more sensitive (Fig. 3). Inhibition with a solution of 0.1 mg l^{-1} dichlorvos in buffer leads to an inhibition of 5.6% (4 mV).

Trapping in polyacrylamide

Immobilization by trapping fixes the enzyme in a polymer network by physical trapping. The enzyme itself does not take part in any chemical reaction which could possibly change the structure of the enzyme. The polymer forms a mesh structure around the enzyme. The pore size has to be small enough to retain the enzyme but wide enough to make possible the diffusion of the substrate and product molecules in the structure. The polymer mostly used for trapping of enzymes is polyacrylamide, known from electrophoresis. The enzyme is trapped by the cross-linking reaction between *N,N'*-methylenebisacrylamide and acrylamide [5]. The gel produced can be characterized by the total concentration of solid (acrylamide + cross-linker) (%*T*) and the amount of cross-linker (%*C*) [13,14]:

$$\%T = [(g_A + g_B)/V] \times 100$$

$$\%C = [g_B/(g_A + g_B)] \times 100$$

where g_A = amount of acrylamide (g), g_B = amount of methylenebisacrylamide (g) and V = volume.

The smaller is T, the greater is the pore size of the gel by a constant value of C. The gel formed by the reaction between acrylamide and *N,N'*-methylenebisacrylamide is not stable enough for it to be attached to a flat-surface pH electrode. The gel can be stabilized by pouring a membrane filter into the polymer.

Method 1

Similarly to the co-cross-linking in a membrane, this method also forms enzyme membranes, which can be contacted with a flat-surface pH electrode. The different pore sizes of the membrane filters, which are used for stabilization, have no effect on the activity of the enzyme membranes (Table 1).

TABLE 1

Original activities and steady-state times of different membranes with 240 U of AChE in 2 ml of polymer solution measured with 800 mg l^{-1} ACh

Pore size (μm)	Activity (mV)	Steady-state time (min)
0.45	105	8
1.2	107	7

These membranes reach the steady-state signal markedly quicker than the membranes used before (Fig. 1). The original activities of eight membranes produced in the same process are shown in Fig. 4. As can be seen, these membranes also do not have the same original activity. The dependence of the signal on the substrate concentration is shown in Fig. 2. The form of the graph is comparable with that of the other graphs. These membranes also show saturation above substrate concentrations of 800 mg l^{-1} ACh.

First inhibition tests showed an inhibition of 5 mV (6.8%) at a dichlorvos concentration of 0.1 mg l^{-1} (Fig. 3). For this inhibition test the determination of the activity was carried out with 800 mg l^{-1} dichlorvos in buffer.

Membranes with different contents of acrylamide. The shelf-life and signal depend on the pore size of the gel. If the pores are large the enzyme is not retained, so the activity of the membranes decreases with time of storage. If the pore size is too small, the resistance of the gel to the diffusion of the substrate molecule is too high, so that the molecule cannot pass through the polymer. For the determination of the optimum polymer composition different polymers were produced and compared with respect to shelf life.

Figure 5 shows the shelf-life and Fig. 6 the original activities and the steady-state times of membranes with different pore sizes. The decreased original activity and the increased steady-state time for the membrane with $T = 30\%$ and $T = 40\%$ (Fig. 6) can be explained by the small pore size of the gel. The substrate molecule

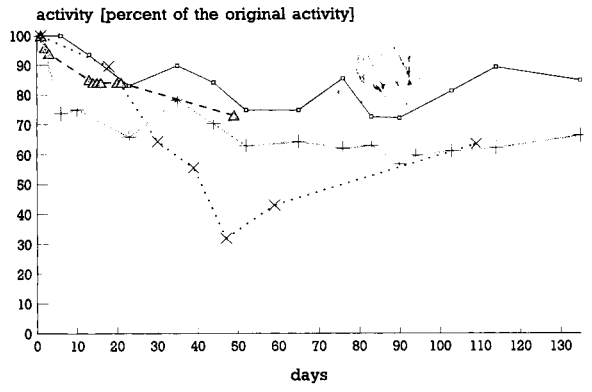

Fig. 5. Effect on activity of storage of the different membranes at 4°C. Abbreviations as in Fig. 1. T = concentration of solids (acrylamide + methylenebisacrylamide). Concentration of cross-linking agent $C = 5\%$.

cannot reach the enzymes in the gel. Another effect is inhibition of the enzyme by the monomer acrylamide, which has to be taken into account by large values for T [15]. Because of its low original activity and high steady-state time, the membrane with $T = 40\%$ was not used further. The optimum composition of the polymer for the immobilization of AChE with respect to the original activity and the steady-state time and the better shelf-life (Fig. 5) is a solid concentration of $T = 20\%$ with a cross-linker concentration of $C = 5\%$.

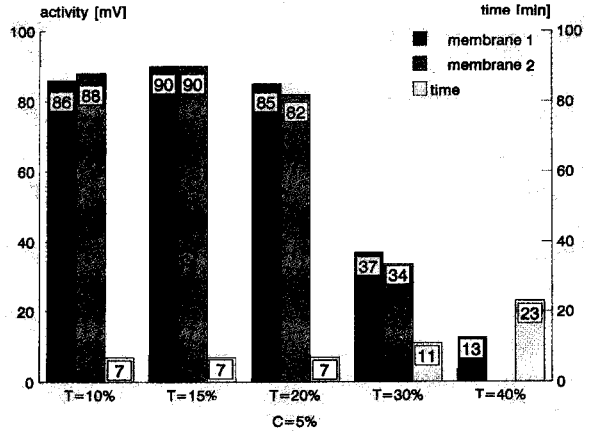

Fig. 6. Comparison of the polyacrylamide membranes (method 1) with different pore sizes. T = concentration of solids (acrylamide + methylenebisacrylamide). Concentration of cross-linking agent $C = 5\%$.

Method 2

To determine the reproducibility of the preparation of the enzyme membranes, eight membranes were produced in the same process and the original activities were compared (Fig. 4). Immobilization by method 2 produces membranes that show the most reproducible activity of each membrane.

Comparison of the immobilization techniques

Immobilization by co-cross-linking directly on the surface of a pH electrode formed a biosensor that is sensitive to a substrate solution. For immobilization the pH electrode was dipped in a solution of albumin, enzyme and glutaraldehyde. Because of the progressive gelation of the immobilization solution, it was not possible to produce membranes with the same thickness on the surface of the pH electrodes. Therefore, the electrodes produced showed different original activities and steady-state times. The handling of these electrodes was difficult: inactive enzyme membranes have to be removed from the pH electrode very carefully because of the risk of damaging the pH-sensitive surface of the electrode; and the enzyme electrode has to be stored cool and before use it must be brought up to the temperature of the test medium.

These disadvantages do not occur on producing enzyme membranes that are not directly coupled to the pH electrode: inactive enzyme membranes can be very easily removed without the risk of damaging the pH-sensitive surface of the electrode; and the membranes are stored cool separately, and for the measurement the electrode does not have to be warmed up.

The immobilization of the enzyme in a membrane can be carried out by trapping in polyacrylamide or by co-cross-linking with albumin and glutaraldehyde pressed between two glass plates. The thickness of the enzyme membrane is fixed by the thickness of the membrane filter. This technique produces enzyme membranes that are more reproducible in original activity and steady-state time than with co-cross-linking on to the ion-sensitive surface of an electrode. The reproducibility of the original activity and

steady-state time of the membranes produced by trapping in polyacrylamide (method 2) was slightly better than by co-cross-linking (method 2) (Fig. 4). The self-life of the polyacrylamide membranes ($T = 20\%$, $C = 5\%$) was slightly better than the shelf-life of the membranes formed by co-cross-linking. The shelf-life of the other polyacrylamide membranes was not better (Fig. 5). A suitable method for the immobilization of AChE was co-cross-linking by albumin and glutaraldehyde in a membrane filter and trapping in a polyacrylamide gel with $T = 20\%$ and $C = 5\%$. The carrier membrane could be a cellulose acetate membrane filter with a pore size of 1.2 μm because of the mechanical stability of this material.

First inhibition tests with the inhibitor dichlorvos showed that the membranes produced by co-cross-linking (method 2) and trapping in polyacrylamide are more sensitive than sensors produced by dipping the electrodes in the immobilization solution and by co-cross-linking in a membrane (method 1) (Fig. 3). In a subsequent paper, the optimization of the sensor for the detection of AChE inhibitors in drinking water will be described [16].

This work was supported by the research fund of Niedersachsen.

REFERENCES

1 A. Näbauer, P. Berg, S. Koch and E. Müller, Labor 2000, (1989) 219.
2 R. Kindervater and R.D. Schmidt, Z. Wasser Abwasser Forsch., 22 (1989) 84.
3 J. Fedrowitz, Energie, 43 (1991) 32.
4 U. Lemke and J. Sander, LABO (1991) 50.
5 W. Hartmeier, Immobilisierte Biokatalysatoren, Springer, Berlin, 1986.
6 J. Montalvo, Jr., and G.G. Guilbault, Anal. Chem., 41 (1969) 1897.
7 G. Schwedt and M. Hauck, Fresenius' Z. Anal. Chem., 331 (1988) 316.
8 G.G. Guilbault, Analytical Uses of Immobilized Enzymes, Dekker, New York, 1984.
9 O. Zaborsky, Immobilized Enzymes, CRC Press, Cleveland, OH, 1973.
10 F.M. Richards and J. Knowles, J. Mol. Biol., 37 (1968) 231.
11 E. Tamiya and I. Karube, Sensors Actuators, 15 (1988) 199.
12 Y.-C. Su and C.-Y. Chen, Proc. Natl. Sci. Counc. B ROC, 11 (1987) 10.
13 T. Mori, T. Sato, T. Tosa and I. Chibata, Enzymologia, 43 (1972) 213.
14 R. Westermeier, in H. Güunzler, R. Borsdorf, W. Fresenius, W. Huber, H. Kelker, I. Luderwald, G. Tölg and H. Wisser, Analytiker-Taschenbuch, Vol. 7, Springer, Berlin, 1989, p. 295–343.
15 T.T. Ngo and K.J. Laidler, Biochim. Biophys. Acta, 377 (1975) 303.
16 K. Stein and G. Schwedt, Wasser, 79 (1992) 211.

Analytica Chimica Acta, 272 (1993) 83–90
Elsevier Science Publishers B.V., Amsterdam

Optimization procedure of open vessel microwave digestion for Kjeldahl nitrogen determination in foods

M.H. Feinberg, J. Ireland-Ripert and R.M. Mourel

Institut National de la Recherche Agronomique, Laboratoire de Chimie Analytique, 16 Rue Claude-Bernard, F-75231 Paris Cedex 05 (France)

(Received 10th August 1992; revised manuscript received 18th September 1992)

Abstract

Wet ashing conditions were optimized for a recently developed open vessel microwave digestion system for Kjeldahl nitrogen determination in various food matrices. Short digestion times in association with maximum nitrogen recovery were sought using methodology based on experimental designs and response surfaces. Microwave digestion was carried out in two complementary periods: decomposition of the organic matrix with sulphuric acid without catalyst and oxidation with hydrogen peroxide. According to the matrix type, each of these two mineralization periods was found to require one or several steps. In order to use response surface methodology, these steps were transposed as experimentally controlled factors of microwave power, time and reagent volumes. The results obtained are illustrated by time–power diagrams indicating the optimum level of each factor and the relative influence of the setting. Digestion by microwaves is shown to allow an appreciable reduction in sample preparation time compared with official methods.

Keywords: Digestion techniques; Experimental design; Optimization methods; Sample preparation; Foods; Kjeldahl; Microwave digestion; Nitrogen

As many analytical methods are rapid or automated, sample preparation is usually the most time-consuming part of a chemical analysis, especially when digestion is involved. Although rapid, non-destructive methods exist for some food products, wet ashing still remains a very general method in food chemistry. For example, one of the limiting factors of the Kjeldahl nitrogen determination in foods is matrix dissolution, as this normally requires more than 2 h, or about 1 h using a heating block, whereas the measurement itself takes only a few minutes with an automated distillation apparatus. Nevertheless, it is used by standardization organizations as an official method in many countries [1].

It has been demonstrated that closed vessel microwave digestion of food samples is efficient for nitrogen determination [2,3]. Recent work has also demonstrated the utility of open vessel microwave digestion for Kjeldahl nitrogen determination in meat products [4]. This paper describes an exhaustive study of optimum wet ashing conditions for all types of foods, using an open vessel microwave digestion system. In particular, short digestion times were sought in addition to maximum nitrogen recovery. In order to obtain results usable by other laboratories, strict methodology based on experimental designs and response surfaces was used.

Correspondence to: J. Ireland-Ripert, Institut National de la Recherche Agronomique, Laboratoire de Chimie Analytique, 16 Rue Claude-Bernard, F-75231 Paris Cedex 05 (France).

EXPERIMENTAL

Nitrogen determination

The principle of sample digestion was to use pure, concentrated sulphuric acid, without addition of any catalyst or salt; the total destruction of the matrix was obtained by adding hydrogen peroxide. This protocol was chosen in order to simplify the digestion, as hydrogen peroxide can be added automatically, and to avoid environmental contamination with the use of catalysts. According to this method, a typical digestion protocol for foods consists in two complementary *periods*: decomposition of the organic matrix with analytical-reagent grade sulphuric acid; and oxidation with 30% hydrogen peroxide, in order to destroy the remaining resistant molecules.

Complete acid decomposition must always be achieved before adding hydrogen peroxide, in order to lessen the risks of possible explosive reactions, which are always possible when hydrogen peroxide is added to undecomposed organic matrices [5]. Depending on the sample, hydrogen peroxide was added in one or several steps, but in all instances heating was stopped for 2 min during its addition; this pause is included in the total digestion time.

After sample dissolution, the digestion vessel was installed in a Kjeltec 1026 (Perstorp) distillation apparatus for NH3 titration according to the Kjeldahl method [6]. To obtain correct distillation, the digestion vessel should not be over one-third filled, which corresponds, under the conditions of this study, to 75 ml of NaOH for 20 ml of H_2SO_4.

Digester programming

The focused microwave digester that was used (Maxidigest MX-350, Prolabo) is composed of a digestion module, containing the microwave generator (magnetron), and a control unit controlling both the magnetron and a multi-channel peristaltic pump used to add reagents to the digestion vessel, where sample dissolution takes place at atmospheric pressure. The ıme control unit can operate up to four digestion modules.

The microwave digestion programme consists in a succession of *steps* characterized by: the power applied, expressed as a percentage of the maximum power of the apparatus (350 W); the time in minutes; and the reagent volume added in ml.

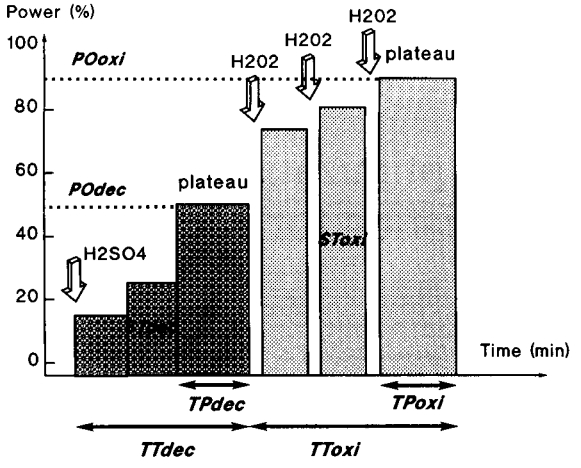

Fig. 1. Typical time–power diagram with selected experimental factors.

Power and time were combined in order to obtain complete decomposition of the sample while avoiding losses from foaming, which would cause the solution to rise into the reflux column. According to the matrix type, each of the above two mineralization periods may require one or several steps. Figure 1 illustrates a typical time–power diagram and indicates the controlled factors used for optimization. The eight controlled factors and their experimental levels are given in Table 1. This type of description is not directly dependent on the experimental device, but represents an attempt to describe, in a formal and universal way, what is generally considered to be an analytical "recipe".

In order to reduce the number of possible controlled factors, some settings were kept constant, as indicated in Table 1. For example, the volume of sulphuric acid (V_{sul}) was set to 20 ml because of the need to maintain a minimum volume of solution in the digestion flask. Similarly, each addition of hydrogen peroxide of 5 ml (V_{oxi}), and as there was always at least one addition of hydrogen peroxide, its total volume is equal to $V_{oxi}ST_{oxi}$.

TABLE 1

Controlled factors and their experimental levels and constant settings

Code	Factor	Unit	Min.	Max.
Period 1: acid decomposition				
ST_{dec}	Number of steps for the decomposition		1	4
PO_{dec}	Maximum power applied for decomposition	%	40	70
		W	140	245
TP_{dec}	Time of the decomposition plateau	min	2	16
TT_{dec}	Total time of the decomposition period	min	2	30
Period 2: Oxidation				
ST_{oxi}	Number of steps for the oxidation		1	3
PO_{oxi}	Maximum power applied for oxidation	%	60	90
		W	210	315
TP_{oxi}	Time of the oxidation plateau	min	2	10
TT_{oxi}	Total time of the oxidation period	min	3	30
	Total digestion time ($TT_{dec} + TT_{oxi}$)	min	5	60

Constant settings

Code	Name	Unit	Value
-	Sample aliquot	g	0.1–2
-	Initial power for decomposition ($ST_{dec} > 1$)	%	15
		W	52
-	Initial power for oxidation ($ST_{oxi} > 1$)	%	70
		W	245
V_{sul}	Volume of sulphuric acid	ml	20
V_{oxi}	Volume of each hydrogen peroxide addition	ml	5

As some samples were freeze-dried and others were fresh, the sample aliquots varied from 0.1 to 2 ± 0.01 g in order to contain a total amount of nitrogen compatible with the method of measurement. The samples were weighed directly in the digestion vessels. For powdered samples, 5 ml of distilled water were added to obtain homogeneous acid attack. Two glass beads were also placed in each digestion flask to regulate boiling and reduce foaming.

The limits of variation of the power of the oxidation period were defined according to the expected temperature in the digestion vessel. It is known that this temperature is a function of power, time and the boiling point of the solution. Preliminary studies with an infrared sensor indicated how the reagent temperature within the digestion vessel varies as a function of time and power. Figure 2 gives an example of this variation for 10 ml of pure sulphuric acid.

Experimental design

The principal aim of this study was to define which settings of the microwave apparatus were the most favourable to obtain efficient sample digestion, but also to evaluate the ruggedness of each factor, in order to predict whether a modification of these settings could have serious consequences on the performances of the apparatus. Thus, all trials were carried out according to the method of experimental design, which allows not only the study of several factors at a time, but also the construction of a predictive model (response surface) which indicates the relative effect of each factor and its eventual interactions with other factors [7].

In general, fractional complete factorial designs were used. When factors were recognized as having little influence, they were maintained fixed in order to reduce the number of trials. In several exceptional cases, when a curved response surface was expected, a Dohlert experimental design [8] was used. This paper will not present all the results obtained, but synthetic diagrams of inter-

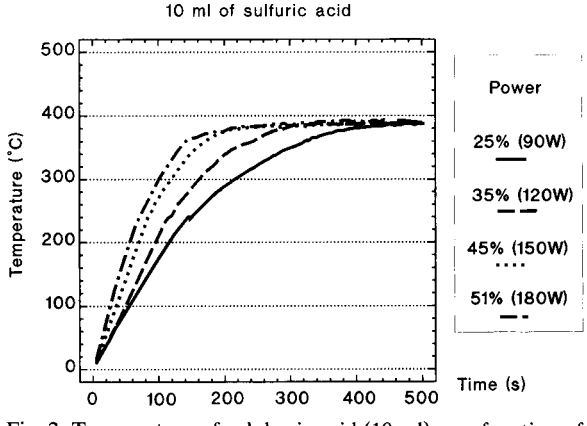

Fig. 2. Temperature of sulphuric acid (10 ml) as a function of time and power.

preted results. On each figure the relative importance of the effect of each significant factor is represented by a + or + + symbol.

Selection of matrices

Foods were selected from a classification established as a function of their concentrations in proteins, carbohydrates and fats as they are given in food composition tables [9], because these three nutrients are known to have an essential role in the problems encountered during mineralization. Figure 3 presents the nine food products chosen clustered in four typical food groups: rich in proteins (fish, chicken, beef, liver); rich in carbohydrates (rice); rich in fats (butter, pâté); and mixed composition (hazelnut, soy flour).

Moreover, in order to evaluate the limiting conditions of digestion, pure L-tryptophan from Fluka (> 99.5% pure), known to be difficult to digest, was also studied.

RESULTS AND DISCUSSION

Recommended time–power programmes for foods

Final recommendations for all matrix types are summarized in Fig. 4; the time–power diagrams indicate the optimum level of each factor and the relative influence of the setting on a scale of + to + + according to its weight.

Foods rich in proteins are fairly easy to dissolve. The acid decomposition period is long, but relatively uncomplicated when the product contains little or no fat or tryptophan (e.g., turkey, chicken and certain fish); for the latter products, the duration of the oxidation step can thus be reduced. In contrast, in the presence of tryptophan it may be necessary to lengthen the decomposition time.

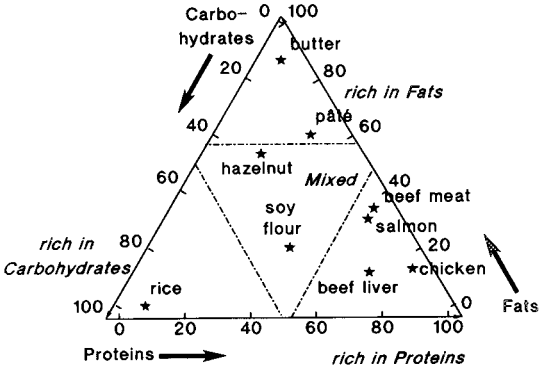

Fig. 3. Food matrix selection as a function of composition.

Foods rich in carbohydrates are the most delicate to digest, because foam formation occurs when an initial power greater than 100 W is applied. With samples of about 1 g, foam rises in the digestion vessel and reaches the reflux column. To avoid this, several *predigestion* steps are necessary at the beginning of the acid digestion period, commencing with low powers, so that decomposition may progress gradually, as illustrated in Fig. 4.

Foods rich in fats, like foods rich in carbohydrates, are liable to foam during acid digestion, and thus necessitate predigestion steps of gradually increasing power. Fats are also difficult to oxidize, and one addition of hydrogen peroxide, even of 15 ml, proves to be insufficient; it is essential to split this volume into at least two aliquots.

Mixed foods contain nearly equivalent percentages of carbohydrates, fats and proteins, which leads to a combination of digestion constraints. Hazelnuts were chosen for their concentration in fats and carbohydrates, and soy flour for its central position in the triangle of food composition (Fig. 3). As shown in Fig. 4, a significant modulation of digestion conditions is observed, resulting in a relative prolongation of the total oxidation time (TT_{oxi}), linked to the fragmented addition of hydrogen peroxide.

Tryptophan

As the nitrogen concentration in tryptophan is known to be 13.72 g per 100 g, it was possible to optimize the recovery. Several experimental designs were necessary to arrive at a recovery of 100%. The results obtained are given in Fig. 5, a time–power diagram indicating the optimum level of each factor.

The total digestion time here is relatively short compared with that of conventional methods.

Only 22 min and a final power of 90% (325 W) are necessary to obtain a recovery of 100% without addition of any catalyst or salt. Factors having statistically significant coefficients in the response surface model are TT_{dec} and TT_{oxi}. This means that time settings must be precise in order to repeat digestion conditions exactly.

Discussion

For typical products of a food category, such as those defined above, it is possible to propose simple, relatively general methods of mineralization by open vessel microwave digestion. For complex foods, on the other hand, the digestion programme can be variable. Nevertheless, the

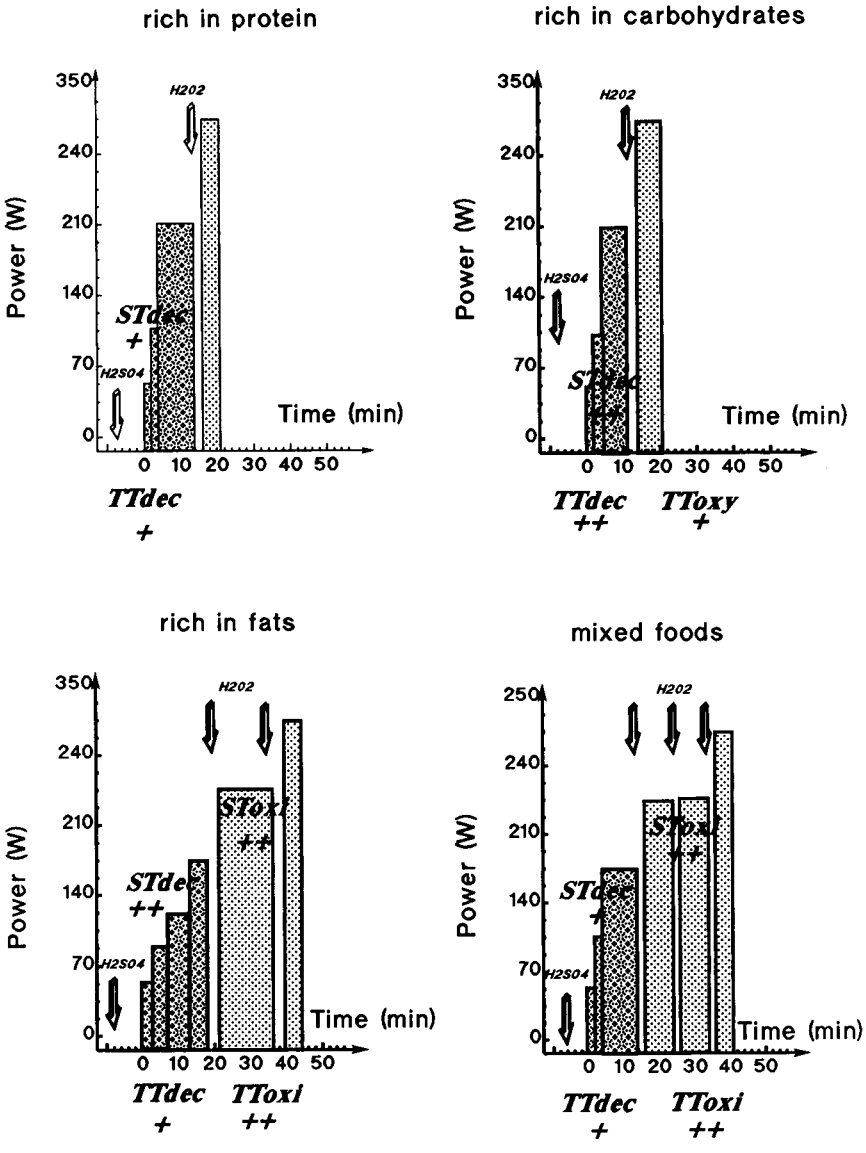

Fig. 4. Recommended time–power programmes for foods (+ indicates the relative influence of the setting).

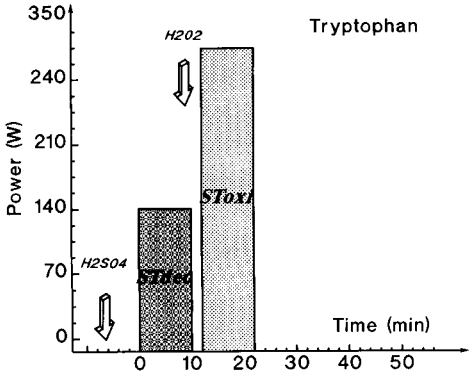

Fig. 5. Optimum time–power programme for tryptophan digestion.

proposed approach allows operating conditions to be defined fairly precisely.

In general, the microwave power to be applied during the acid decomposition (PO_{dec}) and oxidation (PO_{oxi}) periods are not critical. They can be determined without difficulty and proved to be more or less the same for all matrices, and were set to 210 and 310 W, respectively. On the other hand, time factors such as TP_{dec}, TT_{dec}, TP_{oxi} and TT_{oxi} are significant in many models. These factors should then be optimized when adapting the programmes to different matrices. Figure 6 gives an example of the response surface obtained for tryptophan and indicates that drastic changes may occur when time factors are modified. In this

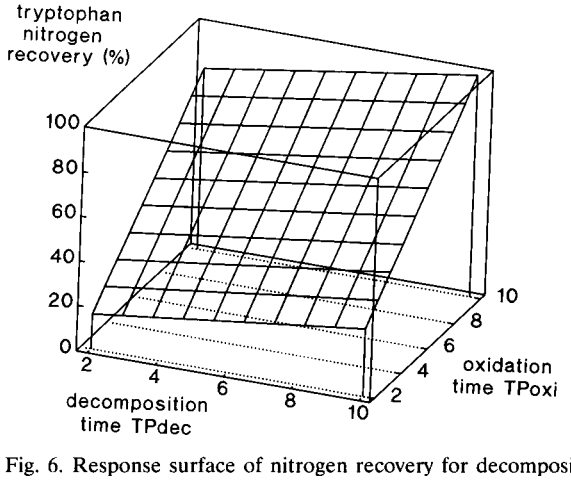

Fig. 6. Response surface of nitrogen recovery for decomposition and oxidation times.

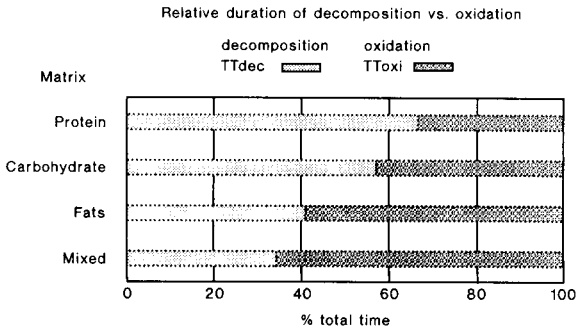

Fig. 7. Relative acid digestion and oxidation times for food matrices.

instance, a reduction in the oxidation time of 1 min may decrease the yield by 10%.

The main difficulty then consists in obtaining a judicious balance between the duration of acid decomposition and that of oxidation. For matrices totally or principally protein, the ratio TT_{dec}/TT_{oxi} is close to 0.8, whereas for difficult matrices the oxidation step is clearly preponderant and nearly twice as long as the acid decomposition period. Figure 7 illustrates the various situations observed during this study and gives guidelines according to the matrix composition.

Complementary optimization

As many reactions occurring within the digestion vessel are not clearly understood, the above results can be considered as guidelines. If very precise digester settings are required before routine analysis of a certain sample type, it may be necessary to perform some preliminary optimization trials. In this case, a general, sixteen-trial saturated experimental factorial design with the four following factors is proposed: the duration of applied power at the acid decomposition plateau (TP_{dec}); the number of steps in the increasing power oxidation phase (ST_{oxi}); the total duration of the oxidation period (TT_{oxi}); and the duration of the final oxidation plateau (TP_{oxi}).

This experimental design is given in Table 2 for the usual factor levels. For high levels of fats, the values for ST_{oxi} should be 2 and 3.

In order to verify that the presence of tryptophan in the matrix did not cause significant errors, recommended digestion conditions for each

TABLE 2

Recommended experimental design for digester setting optimization

Trial No.	TP_{dec}	ST_{oxi}	TT_{oxi}	TP_{oxi}
1	2	1	15	2
2	12	1	15	2
3	2	2	15	2
4	12	2	15	2
5	2	1	30	2
6	12	1	30	2
7	2	2	30	2
8	12	2	30	2
9	2	1	15	10
10	12	1	15	10
11	2	2	15	10
12	12	2	15	10
13	2	1	30	10
14	12	1	30	10
15	2	2	30	10
16	12	2	30	10

Factors kept constant

V_{sul}	Volume of H_2SO_4	20 ml
V_{oxi}	Volume of each addition of H_2O_2	5 ml
ST_{dec}	Number of acid decomposition steps	2
-	Time of predigestion phase	4 min
PO_{dec}	Power at the decomposition plateau	210 W
PO_{oxi}	Power at the final plateau	310 W

category of food, as illustrated at Fig. 4, were applied to 0.1-g samples of tryptophan. The results obtained are given in Table 3. They confirm that increasing time alone or power alone is not sufficient to compensate for the reduction in other factors. For example, the 44 min in the digestion programme for foods rich in fats gives no better recovery than that of the tryptophan programme in 22 min (see Fig. 5). It is therefore necessary to consider the finalization of a digestion procedure

TABLE 3

Recovery of tryptophan as a function of the programme applied

Programme applied	Total time (min)	Recovery (%)
Tryptophan	22	99.42
Proteins	21	95.31
Carbohydrates	21	84.55
Fats	44	93.26

TABLE 4

Collaborative study results for Kjeldahl nitrogen determination in food samples

Matrix	Average (g/kg)	r (g/kg)	R (g/kg)	R.S.D. (r) (%)	R.S.D. (R) (%)
Wheat flour	17.8	0.24	0.38	1.33	2.15
Cocksfoot hay	20.6	0.28	0.55	1.36	2.65
Milk	4.9	0.05	0.09	1.07	1.89
Canned beef meat	30.0	0.53	0.78	1.77	2.60
Powdered egg	76.5	0.90	0.97	1.18	1.27
Casein	138.1	1.75	1.75	1.26	1.26

as a coherent whole, which requires simultaneous adaptation of factors and which justifies the use of experimental designs.

Conclusion

A complementary validation of these different time–power diagrams was performed in the frame of a collaborative study, consisting in the determination of nitrogen in six homogenized food samples by eleven laboratories [10]. Table 4 summarizes the reproducibility (R) and repeatability (r) and their relative standard deviations (R.S.D.) obtained for these matrices when applying the recommended programmes. Although a wide range of variation of the average concentration exists, the performance is very good and the R.S.D. (R) is close to 1.7%.

In conclusion, open vessel microwave digestion seems to allow an appreciable decrease in sample preparation time compared with other methods. Moreover, the use of hydrogen peroxide greatly simplifies this method, whereas official methods require the addition of catalyst and salts. These satisfactory results are associated with flexibility of the instrument settings and good reproducibility of the heating conditions of the microwave digestion procedure. Major drawbacks lie in the difficulty of predicting precisely the behaviour of a new matrix type, because the accuracy of the prediction of response surface models is still poor. Complementary studies are therefore necessary in order to understand better the exact role of microwaves in the digestion process and the influence of matrix characteristics on microwave thermal effect absorption.

REFERENCES

1 Official Methods of Analysis of the Association of Official Analytical Chemists, AOAC, Arlington, VA, 15th edn., 1990.
2 H. Matuziewicz and R.E. Sturgeon, Prog. Anal. Spectrosc., 12 (1989) 21.
3 H.M. Kingston and L.B. Jassie, in H.M. Kingston and L.B. Jassie (Eds.), Introduction to Microwave Sample Preparation, American Chemical Society, Washington, DC, 1988, Chap. 6.
4 D. Didenot, Spectra 2000, No. 146 (1990) 44.
5 C.C. Hach, S.V. Brayton and A.B. Kopelove, J. Agric. Food Chem., 33 (1985) 1117.
6 Norme NF V03–050, Agricultural Food Products — General Directions for the Determination of Nitrogen by the Kjeldahl method, AFNOR, Paris, 1975.
7 S.N. Deming and S.N. Morgan, Experimental Design: a Chemometric Approach, Elsevier, Amsterdam, 1987.
8 M.H. Feinberg and P. Wirth, Analusis, 12 (1984) 490.
9 M.H. Feinberg, J.C. Favier and J. Ireland-Ripert, Répertoire Général des Aliments, Lavoisier Technique and Documentation, Paris, 1991.
10 M.H. Feinberg, J. Ireland-Ripert, C. Suard and R.M. Mourel, to be published.

Analytica Chimica Acta, 272 (1993) 91–97
Elsevier Science Publishers B.V., Amsterdam

Preconcentration of trace metals from sea water with the chelating resin Chelamine

Stéphane Blain, Pierre Appriou and Henri Handel

URA CNRS 322, Faculté des Sciences de Brest, 6 Avenue le Gorgeu, 29287 Brest Cedex (France)

(Received 30th June 1992; revised manuscript received 14th September 1992)

Abstract

The complexing properties (capacity, pH effect, breakthrough curve) of the chelating resin Chelamine, containing a pentamine ligand, were investigated. The resin was used in a column procedure for the preconcentration of Cd(II), Cu(II), Mn(II), Ni(II), Pb(II) and Zn(II) from deionized water and sea water and the recoveries were 93–105 and 91–102%, respectively. The absolute blanks varied from less than 0.6 ng for Cd to 11 ng for Cu, permitting the determination of the above six metals in oceanic water. The accuracy of the method was demonstrated by replicate analyses of the marine reference material CASS-2. The high selectivity of the resin leads to low concentrations of alkali and alkaline earth metal ions in the acidic eluate.

Keywords: Atomic absorption spectrometry; Chelating resin; Preconcentration; Sea water; Trace metals; Waters

Although the sensitivity of analytical instrumentation has increased in recent years, the routine determination of trace metals in complex media such as sea water is still very difficult. Also, a preliminary step is generally required to concentrate the metal ions and to eliminate interfering ions (e.g., alkali and alkaline earth metal ions).

Liquid–solid extraction is commonly used, and the most widely used chelating resin is Chelex 100. Since Riley and Taylor's first work [1], numerous workers have studied and modified the procedure [2–4] or applied it to on-line preconcentration systems [5–7]. These studies demonstrated the ability of Chelex resin to preconcentrate trace metals from sea water, but also revealed some difficulties: partial recovery of some trace metals (e.g., Mn or Cd) with no optimum experimental conditions (e.g., pH during the preconcentration); losses of trace metal (Mn) during the washing step, which elutes the alkali and alkaline earth elements; and high levels of interfering ions in the acidic eluate, leading to the need for a standard addition method for accurate and precise determination of concentration by atomic absorption spectrometry.

The poor selectivity of the chelating agent iminodiacetate is principally responsible of the two last problems. In the Pearson classification [8] the transition metals are soft acids and alkali and alkaline earth metal ions are hard acids. Hence it is clear that the presence of hard acidic sites such as oxygen atoms in the resin will reduce its selectivity.

A chelating agent with only soft basic sites such as nitrogen atoms would be more suitable.

Correspondence to: S. Blain, URA CNRS 322, Faculté des Sciences de Brest, 6 Avenue le Gorgeu, 29287 Brest Cedex (France).

In previous work [9,10], the utilization of tetraazamacrocyclic ligands immobilized for the preconcentration step was investigated, but the low decomplexation rate for some metals (Cu, Ni) with the different synthesized resins reduced their utility in analytical chemistry. Linear polyamines have also been immobilized on various supports [11–13]. Recently, a new commercial chelating resin, Chelamine, has been produced by the immobilization of a pentamine ligand (1,4,7,10,13-pentaazatridecane or tetren) on an organic polymer. This paper reports some properties of this resin and a procedure for preconcentration of trace metals (Cd, Cu, Mn, Ni, Pb, Zn) from sea water with high selectivity.

EXPERIMENTAL

Reagents

Aqueous solutions were prepared with deionized water obtained from a Milli-RO/Milli-Q apparatus (Millipore). The chelating resin Chelamine was purchased from Fluka. All the metal standard solutions and spikes were prepared from commercial standard solutions [NO_3^- was the anion for Pb(II) and Cu(II) and Cl^- for Cd(II), Mn(II), Ni(II) and Zn(II)]. Nitric acid and ammonia solutions were ultrapure (Merck). Tris buffer (1 M) was purified by shaking with Chelamine (2 g per 100 ml) overnight.

Apparatus

A Perkin-Elmer Zeeman 3030 atomic absorption spectrometer equipped with an autosampler AS 60 was used for electrothermal atomic absorption spectrometric (ETAAS) measurements. During the column procedure the flow-rates were controlled with eight-channel peristaltic pumps (Gilson Minipuls 2). The Chelamine resin was packed in columns purchased from Bio-Rad. An automatic collector (Redirac 2212, LKB Biochrom, Cambridge, UK) was used for breakthrough and elution curves.

Storage bottles, labware and columns were cleaned by soaking in hydrochloric acid overnight and rinsing with high-purity water. All the procedures were carried out under a laminar flow hood.

Batch measurements

The chelating resin was preliminarily rinsed with water, 2 M HNO_3, water, 2 M NH_3 and water. For capacity determination the resin was dried under a laminar flow hood and 50 mg of dry resin were gently shaken with 10 ml of 1 g l^{-1} Cu(II) for 24 h. For the pH study, 2 g of wet resin were equilibrated with buffered solutions (citrate, ammonium acetate or Tris) and then shaken with 20 ml of a mixed metal solution [Cd(II), Cu(II), Mn(II), Ni(II), Pb(II), Zn(II) (10 mg l^{-1} each)] for 48 h. The concentrations of the different metals were determined in the supernate by flame AAS.

Breakthrough curves and elution curves

The columns were filled with 1.2 g of wet resin and successively rinsed with 50 ml of water, 5 ml of 2 M HNO_3, 10 ml of water, 10 ml of water containing 600 μl of 2 M NH_3 and 10 ml of water at a flow-rate of 1 ml min^{-1}. A 1-l volume of a mixed metal ion solution [Cd(II), Cu(II), Mn(II), Ni(II), Pb(II), Zn(II) (10 mg l^{-1} of each metal)] was pumped through the column at 0.3 ml min^{-1}. Fractions of 10 ml of the effluent were collected in 15-ml glass tubes and analysed by flame AAS. The columns were rinsed with 10 ml of water and the metals were eluted with 5 ml of 2 M HNO_3 under gravity flow. Fractions of 0.5 ml of the acid eluate were collected and analysed by flame AAS.

Recoveries of spikes

The columns were prepared as described in the previous section. A 35-ml volume of deionized water was spiked (or not, for blank determination) with 50 μl of (1 mg l^{-1}) standard solutions [Cd(II), Cu(II), Mn(II), Ni(II), Pb(II), Zn(II)]. The pH was adjusted to 8.0 ± 0.2 with 2 M NH_3 and 1 M Tris solution, then the solutions were passed through the columns at the appropriate flow-rate fixed with a peristaltic pump. The columns were rinsed with 20 ml of deionized water and the metals were eluted with 4 ml of 2 M HNO_3 in PTFE tubes. For the determination of spike recoveries in sea water the same procedure was used. The sea water was oceanic water collected in the North Atlantic acidified to pH < 2 and stored in clean polyethylene bottles. The

metal concentrations in the acidic eluate were determined by ETAAS.

Column procedure

Eight columns were prepared as described. The previously determined amounts of 2 M NH_3 and 1 M Tris were added to the sample to adjust the pH to 8.0 ± 0.2. The samples were then passed through the columns at 0.3 ml min^{-1}. The columns were rinsed with 20 ml of water and eluted with 4 ml of 2 M HNO_3.

Selectivity

After sea water has been passed through the resin, the column was rinsed with fractions of 5 ml of deionized water. These fractions were analysed for Ca(II) and Mg(II) by flame AAS and for Na(I) and K(I) by flame emission spectrometry. The amounts of alkali and alkaline earth elements were also determined in this manner in the final acidic eluate.

RESULTS AND DISCUSSION

Resin properties in batch system

Capacity. The capacity was found to be 1.0 ± 0.1 mmol g^{-1} for Cu(II) at pH 5. This value is the same as that indicated by the manufacturer for Zn(II). It is lower than the capacity of Chelex (3.7 mmol g^{-1}) [14] but higher than those of some resins previously used (e.g., 8-hydroxyquinoline on SiO_2, 0.062 mmol g^{-1} [15]; 8-hydroxyquinoline on Fractogel, 0.29 mmol g^{-1} [16]; tetraazamacrocycle impregnated on macroporous polymer, 0.34 mmol g^{-1} [10]). Saturation of the resin was completed in less than 1 h and half saturation was achieved in less than 2 min. In the same manner decomplexation of the Cu(II)-saturated resin was completed in less than 1 min. These properties are compatible with utilization of the column for the preconcentration step.

pH dependence. In Chelamine, the ligand, grafted on the organic matrix, contains five nitrogen atoms. The properties (thermodynamic and kinetic) are very dependent on the protonation of these different basic sites. They could not be deduced completely from pK and complexation constants (Table 1) [17] because immobilization of the ligand interferes with its thermodynamic properties. The uptake of six metals at a concentration of 10 mg l^{-1} by the batch system in various buffered solutions in the pH range 1–8 was studied. The results are presented in Fig. 1. Three types of complexation could be distinguished: Cu(II), which has the highest complexation constant, is complexed at pH close to 2; Mn(II), which has the lowest complexation constant, was not completely recovered even at pH 8. For the other metals the recovery was 100% for

TABLE 1

Thermodynamic datas for the pentamine: pK_a values and logarithm of global formation constant K of the complex [17] of the metal

pK_a value	Metal	Log K
pK_1 = 9.54	Cd	14.0
pK_2 = 9.05	Cu	22.8
pK_3 = 8.10	Mn	7.6
pK_4 = 4.70	Ni	17.4
pK_5 = 2.66	Pb	10.5
	Zn	15.1

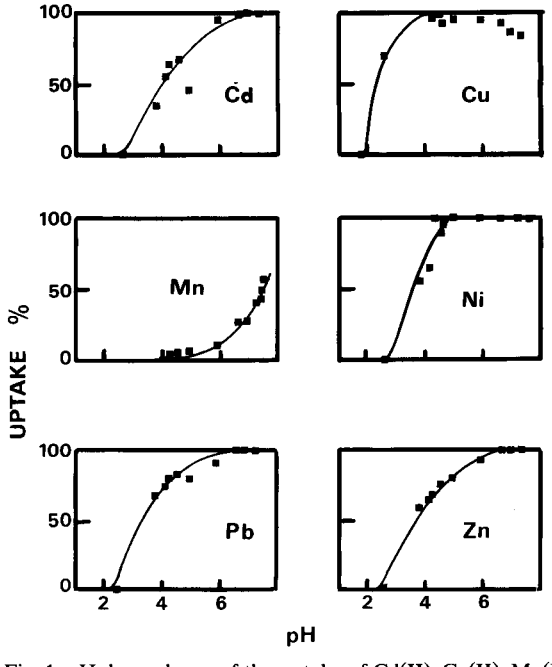

Fig. 1. pH dependence of the uptake of Cd(II), Cu(II), Mn(II), Ni(II), Pb(II) and Zn(II) with Chelamine in a batch procedure.

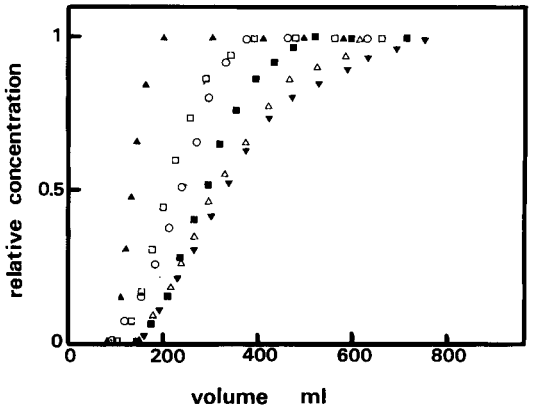

Fig. 2. Breakthrough curve of: ▼, Cu(II); □, Cd(II); ▲, Mn(II); △, Ni(II); ■, Pb(II) and ○, Zn(II) for 0.4 mg of dry Chelamine resin at flow-rate 0.3 ml min^{-1}.

pH > 6.5. It is interesting that even though Pb has a lower complexation constant than Zn(II), Ni(II) and Cd(II) (see Table 1), its pH curve does not differ from the others. The reasons for this are not clear but a similar observation has been made with 2,2′-diaminodiethylamine on cellulose [12].

Column procedure

Breakthrough curve. The breakthrough curves presented in Fig. 2 are in good agreement with the results in the previous section for pH dependence. The Mn curve rises sharply as soon as 100 ml of the multi-metal solution had passed through the column. On the other hand, Cu(II) shows the lowest slope, in accordance with its high complexation constant. For the intermediate metals it is interesting that Pb(II) seems to have more affinity for the resin than was expected from the complexation constant. This is also consistent with the pH observations reported in the previous section.

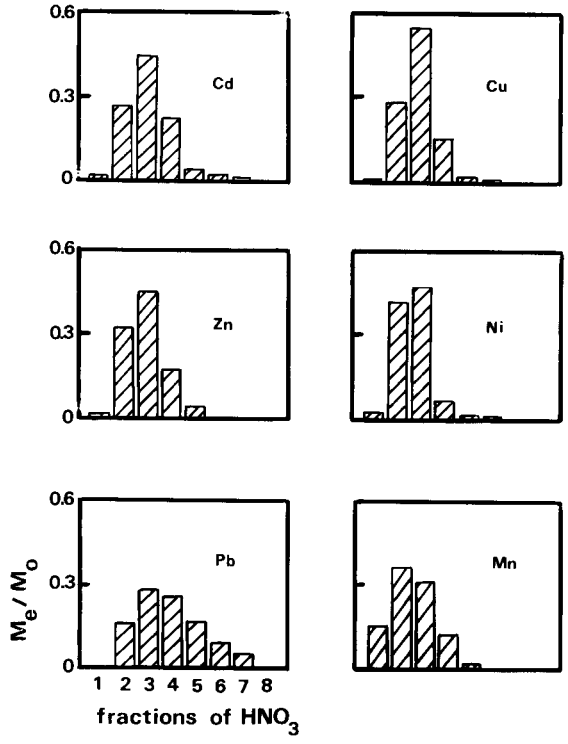

Fig. 3. Elution curves with 2 M HNO_3 (0.5 ml fractions) under gravity flow for Cd(II), Cu(II), Mn(II), Ni(II), Pb(II) and Zn(II). M_0 = total amount of metal loaded on the resin; M_e = amount of metal eluted in the acidic fraction.

Elution curves. The elution curves were obtained on the metal-saturated columns after the breakthrough curve experiments. The amounts of metal sequestered on the columns were much higher than those in a real preconcentration procedure for trace metals from sea water. Figure 3

TABLE 2

Influence of flow-rate of the sample and amount of resin loaded in the column on the uptake (%) of Cu(II) and Mn(II)

Sample	Flow-rate (ml min^{-1})	Metal	Mass of resin (g) [a]		
			0.1	0.2	0.4
Deionized water	1	Mn	77 ± 5	88 ± 4	75 ± 10
		Cu	85 ± 10	98 ± 9	105 ± 10
Deionized water	0.3	Mn	102 ± 8	91 ± 13	102 ± 14
		Cu	80 ± 6	98 ± 9	105 ± 10
Sea water	0.3	Mn	–	64 ± 9	96 ± 9
		Cu	–	89 ± 16	102 ± 8

[a] Mean and confidence interval at the 95% level for four determinations.

TABLE 3

Recoveries (%) of spikes (50 ng) from deionized water and sea water

Sample	Recovery (%) [a]					
	Cd	Cu	Mn	Ni	Pb	Zn
Deionized water	93 ± 6	105 ± 10	94 ± 11	108 ± 16	94 ± 5	100 ± 4
Sea water	98 ± 12	102 ± 15	96 ± 9	91 ± 10	91 ± 7	98 ± 13

[a] Mean and confidence interval at the 95% level for four determinations.

shows that all metal ions were eluted with 4 ml of 2 M HNO_3 under gravity flow. This result is a very important improvement, allowing the use of polyamine-containing resin. Indeed, it has been reported previously [10] that with a tetraaza-macrocycle-impregnated macroporous polymer, the decomplexation rates for some transition metals were so slow that complete recovery could not be obtained [e.g., Cu(II), Ni(II)] even when a low flow-rate (0.1 ml min^{-1}) is used. The difference between the cyclic and linear polyamine kinetics can be explained by the fact that tetraazamacrocycles have no extremity. Protonation of nitrogen atoms and solvatation of metal ion require that the macrocycle folds, and this step is unfavourable and leads to very slow rates of decomplexation. Also, the cleavage of the first Cu–N bond of Cu(1,4,8,11-tetraazacyclotetradecane)$^{2+}$ is slower than that of Cu(1,4,8,11-tetraazaundecane)$^{2+}$ by factors of 10^4–10^5 [18].

Recoveries of spikes. Among the metals studied, Mn and Cu present the lowest and the highest affinity for Chelamine. The effect of the flow-rate and the amount of resin loaded in the column on recoveries of spikes with these two ions was studied. The results are summarized in Table 2.

In deionized water, a complete recovery of spike was achieved with 0.2 g of dry resin and a flow-rate of 0.3 ml min^{-1}. Increasing the flow-rate to 1 ml min^{-1} led to a loss of Mn, even when 0.4 g was loaded in the column. Higher amounts of resin were not investigated because the volume of acidic solution required for elution and also the volume of sample to be processed would need to be increased in order to maintain a good concentration factor. For sea water, 0.4 mg of resin at a flow-rate of 0.3 ml min^{-1} gave satisfactory recoveries of Mn and Cu. The column procedure for preconcentration of trace metals from sea water was carried out under these conditions.

Table 3 gives the results obtained for the six metals studied in deionized water and sea water. All the ions were quantitatively recovered from both media.

Blank and limit of detection. The blank of the method was determined with replicate analyses of deionized water loaded with the same amounts of reagents as used in the preconcentration procedure for sea water. The results are summarized in Table 4. Assuming that $3s_B$ represents the limit of detection of the procedure [19], this value was

TABLE 4

Absolute blank and detection limit

Metal	Absolute blank (ng) [a]	Standard deviation (ng) [b]	Limit of detection (ng l^{-1}) [c]
Cd	0.6 ± 0.2	0.3	2.3
Cu	11.0 ± 0.4	0.4	3
Mn	1.8 ± 0.4	0.5	3.8
Ni	10 ± 2	2.4	18
Pb	1.2 ± 0.4	0.4	3
Zn	5.6 ± 4	4.4	33

[a] Mean and confidence interval at the 95% level for eight determinations. [b] For eight determinations. [c] For 400 ml of sample.

TABLE 5

Analysis of CASS-2

Metal	Concentration ($\mu g\ l^{-1}$)	
	This work [a]	Certified value [b]
Cd	0.029 ± 0.008	0.019 ± 0.004
Cu	0.70 ± 0.08	0.675 ± 0.039
Mn	2.0 ± 0.2	1.99 ± 0.15
Ni	0.26 ± 0.05	0.298 ± 0.036
Pb	0.014 ± 0.007	0.019 ± 0.006
Zn	1.9 ± 0.3	1.97 ± 0.12

[a] Mean and precision expressed as 95% tolerance limit (three determinations). [b] Precision expressed as 95% tolerance limit.

TABLE 6

Selectivity of the resin: determination of the volume of water required to rinse the column and determination of the concentration (mg l^{-1}) of the interferent ions Na(I), K(I), Ca(II) and Mg(II) in the acidic eluate

Resin	Metal	Fraction of 5 ml of rinsing water				Acidic eluate (4 ml)
		1	2	3	4	
Chelamine, first utilization	Ca	150	5	0.5	0	20
	Mg	350	10	1.5	0.1	30
	Na	3000	140	30	3	44
	K	100	0.9	0.6	0.2	0.1
Chelamine after regeneration	Ca	120	2.8	0	0	134
	Mg	350	8.5	0.1	0	250
	Na	2600	40	4.9	3.8	44
	K	100	0.9	0.3	0.1	0.7

calculated for the six metals with 400 ml of sample. The results are low enough to permit the determination of traces of metals in the open ocean water.

Accuracy and precision. The accuracy of the method was verified by determination of Cd(II), Cu(II), Mn(II), Ni(II), Pb(II) and Zn(II) in certified standard coastal sea water (CASS2) from the Chemistry Division of the National Council of Canada. Table 5 shows that the concentrations determined with the Chelamine resin are statistically indistinguishable from the certified values.

Selectivity. One of the principal challenges in preconcentration is the elimination of interfering ions (alkali and alkaline earth metals). If too high levels of these ions are present, a standard addition method should be employed, which increases the time of analysis.

The minimum volume of deionized water required to rinse the column after sample had been pumped through the column was investigated. Table 6 shows that 20 ml of water permit the cations trapped in the pores of the resin to be eliminated. The analysis of the acidic eluate (reported in Table 6) shows that the affinity of the resin for the alkali and alkaline earth metal ions is low but not zero. The ligand is not responsible for this because the complexation constants of these ions are extremely low. The organic matrix can also complex some cations. It is important to note that the amount of interfering ions sequestered by the resin increases after several regenerations with HNO_3 and storage between the successive procedures in slightly acidic solution. This indicates that oxygenated sites are probably created within the matrix. However, the relatively low levels of alkali and alkaline earth metal ions present in the acidic eluate make direct determination (without standard addition) possible.

Conclusion

Chelamine resin offers a very interesting and inexpensive alternative to Chelex for the preconcentration of trace metals from sea water. This work has demonstrated that Cu(II), Ni(II), Cd(II), Mn(II), Pb(II) and Zn(II) were quantitatively recovered from sea water. The selectivity of the resin permits standard calibration methods to be used for the ETAAS determination of metal concentrations in the eluate.

REFERENCES

1 J.P. Riley and D. Taylor, Anal. Chim. Acta, 40 (1968) 479.
2 H.M. Kingston, I.L. Barnes, T.J. Brady, T.C. Rains and M.A. Champ, Anal. Chem., 50 (1978) 2064.
3 A.J. Paulson, Anal. Chem., 58 (1986) 183.
4 S.-C. Pai, P.-Y. Whung and R.-L. Lai, Anal. Chim. Acta, 211 (1988) 257.
5 Y. Liu and J.D. Ingle, Jr., Anal. Chem., 61 (1989) 520.
6 A. Siriraks, H.M. Kingston and J.M. Riviello, Anal. Chem., 62 (1990) 1185.
7 E.A. Novikov, L.K. Shpigun and Yu.A. Zolotov, Anal. Chim. Acta, 230 (1990) 157.
8 R. Pearson, J. Chem. Educ., 45 (1968) 581.
9 S. Blain, P. Appriou, H. Chaumeil and H. Handel, Anal. Chim. Acta, 232 (1990) 331.

10 S. Blain, P. Appriou and H. Handel, Analyst, 116 (1991) 815.
11 J. Dingman, S. Siggia, C. Barton and C. Hiscock, Anal. Chem., 44 (1972) 1351.
12 J.A. Smits and R.E. Van Grieken, Anal. Chem., 52 (1980) 1479.
13 D.E. Leyden, G.H. Lutrell, Anal. Chem., 47 (1975) 1612.
14 R. Rosset, Bull. Soc. Chim. Fr., 8 (1964) 1845.
15 S. Nakashima, R.E. Sturgeon, S.N. Willie and S.S. Berman, Fresenius' Z. Anal. Chem., 330 (1988) 592.
16 W.M. Landing, C. Haraldsson and N. Paxeus, Anal. Chem., 58 (1986) 3031.
17 R.M. Smith and A.E. Martell, Critical Stability Constants, Plenum, New York, 1975.
18 L.-H. Chen and C.-S. Chung, Inorg. Chem., 27 (1988) 1880.
19 Analytical Methods Committee, Analyst, 112 (1987) 199.

Analytica Chimica Acta, 272 (1993) 99–103
Elsevier Science Publishers B.V., Amsterdam

Direct determination of trace elements in indium phosphide by atomic absorption spectrometry

E. Milella

CNRSM, Centro Nazionale Ricerca e Sviluppo Materiali, via G. Marconi 147, 72023 Mesagne, Brindisi (Italy)

E. Sentimenti, G. Mazzetto, L. Meregalli and M. Battagliarin

Temav SpA, Centro Ricerche Venezia, Via delle Industrie 39, 30175 Venezia Porto Marghera, Venice (Italy)

(Received 25th July 1992)

Abstract

A method for the atomic absorption spectrometric determination of important impurities in indium phosphide (InP) is described. Results are compared with those obtained by glow discharge mass spectrometry. To avoid accidental contamination, no preconcentration was used. The detection limits are as low as 10^{14}–10^{16} atoms cm^{-3}. This method gives the possibility of checking rapidly the amount of impurities in InP polycrystals and dopants in InP single crystals by a relatively inexpensive technique.

Keywords: Atomic absorption spectrometry; Indium phosphide; Semiconductors; Trace elements

Considerable interest has been shown recently in III–V semiconducting materials. The substantial progress made over the last decade in the preparation and processing of these materials, together with the development of highly reliable devices, has led to great sophistication of optoelectronics technology. The properties of indium phosphide (InP), a typical representative together with gallium arsenide of the III–V semiconductor class, make it of increasing interest in important areas such as optoelectronics, microwave manufacturing and high-frequency field effect transistors (FETs). InP has a wide energy gap and higher electronic mobility than semiconductors such as silicon and germanium.

Temav (Venice) have developed an industrial prototype process for the production of InP epitaxy-ready substrates. The overall process consists of the production and characterization of the raw materials used, the production and characterization of indium phosphide wafers and the recycling of scraps and slimes. Indium phosphide as a polycrystal is obtained by the very high-pressure synthesis (VHPS) method and the single crystal is then grown by the liquid-encapsulated Czochralsky (LED) method. The steps after growing include orientation, cylindrical and surface grinding, cutting of slices and grinding of edges. The thickness, flatness and surface characteristics of each substate are checked. The manufacture of epitaxy-ready product is conducted in a class 10 clean room.

As some well known impurities strongly affect the electrical features of semiconductors, even at trace levels (Table 1), it is necessary to control accurately the quality both of the materials being used and of the (intermediate) products at each stage of the synthesis. Also, the efficiency and

Correspondence to: E. Milella, CNRSM, Centro Nazionale Ricerca e Sviluppo Materiali, via G. Marconi 147, 72023 Mesagne, Brindisi (Italy).

TABLE 1

Influence of impurities on electrical behaviour of commercial InP

	As	B	Si	S	Zn
Concentration (atoms $cm^{-3} \times 10^{15}$)	4.6	3.8	> 1.1	2.3	0.6
Behaviour	iso [a]	iso [a]	d [a]	d [a]	a [a]

[a] a = Acceptor; d = donor; iso = isoelectronic.

performance of InP devices depend on a low density of dislocations inside the InP crystal.

Methods for the chemical characterization of high-purity indium [1] and red phosphorus [2] by atomic absorption spectrometry (AAS) have been described. During processing, Hall effect characterizations, the evaluation of the number of dislocations by the etch pit density method and chemical analysis by glow dicharge mass spectrometry and AAS are carried out.

In indium phosphide crystals, residual impurities such as Fe, Si and Sn are thought to play an electrical role in semi-insulation, and isoelectrical impurities such as As, Ga and Sb are thought to be effective in reducing the dislocation density. Consequently, the determination of specific elements must be very accurate and precise. Various methods have been used to determine the amounts of trace elements in bulk InP. Stripping voltammetry [3], "chemicospectrography" [4,5], spark-source mass spectrometry [6], secondary-ion mass spectrometry [7–9] and radioactivation analysis [10,11] are well established techniques.

In this paper the application of flame, Zeeman-effect graphite furnace and hydride generation AAS for the determination of twenty elements at trace levels in indium phosphide is described. The impurity in question was not isolated prior to its determination in order to minimize any accidental contamination. The detection limits [12] for these impurity elements are necessary to establish the quality of undoped InP crystals [13].

EXPERIMENTAL

Instrumentation

A Perkin-Elmer Model 5000 atomic absorption spectrometer equipped with a Model HGA-500 thermal programmer, pyrolytic graphite-coated graphite tube, a L'vov platform, a Model AS-40 autosampler, a Model 056 strip-chart recorder and a Model MHS-20 hydride generation system was used. A deuterium and a tungsten background corrector were used in flame AAS and Zeeman-effect background correction was applied in graphite furnace AAS. High-purity (> 99.999%) argon and nitrogen were used as purge gases.

Reagents

Deionized water, obtained with a Milli-Q water purifier (Millipore), was used throughout. Reagents included hydrochloric and nitric acid (Ultrex, 2 Baker), urea (Merck), EDTA (Riedel-de Haën) and potassium iodide (Merck).

Working standard solutions were prepared daily from 1 mg ml^{-1} stock standard solutions of each element.

Flame and graphite furnace AAS

In a 50-ml volumetric flask, place 1 g of indium phosphide and 10 ml of hydrochloric acid (1 + 1) and gently heat the solution to dryness. Add 5 ml of nitric acid and repeat the same procedure. Add 5 ml of nitric acid and dilute to the mark with water.

TABLE 2

Instrumental setting used in Zeeman-effect graphite furnace AAS determinations

Parameter	Dry	Char 1	Char 2	Atomize	Cool 1	Cool 2
Temperature (°C)	150	[a]	[a]	[a]	500	20
Ramp (s)	20	20	3	0	3	2
Hold (s)	20	20	5	5	5	10
Gas flow-rate (ml min^{-1})	300	300	0	0	300	300

[a] Element-specific temperatures are given in Table 3.

TABLE 3

Element-specific parameters in graphite furnace AAS determinations

Element	Wavelength (nm)	Slit (nm)	Sample volume (μl)	Location [a]	Char 1 (°C)	Char 2 (°C)	Atomize (°C)
Ag	328.1	0.7	10	STPF	650	650	2400
Al	309.3	0.7	10	STPF	1500	1500	2500
Au	242.8	0.7	20	STPF	800	800	2700
Bi	306.8	0.7	30	STPF	650	650	2400
Cd	228.8	0.7	10	STPF	700	700	2300
Co	242.5	0.2	5	Wall	1400	1400	2500
Cr	357.9	0.7	10	Wall	1400	1400	2500
Cu	324.7	0.7	10	STPF	900	900	2500
Fe	248.3	0.2	10	Wall	1400	1400	2700
Ga	287.4	0.7	10	STPF	800	800	2400
Mn	279.5	0.2	10	STPF	1400	1400	2700
Mo	313.3	0.7	20	Wall	1800	1800	2700
Ni	232.0	0.2	5	Wall	1400	1400	2500
Pb	283.3	0.7	30	STPF	750	750	2500
Si	251.6	0.2	10	Wall	1400	1400	2650
Sn	286.3	0.7	10	STPF	900	900	2500

[a] STPF = stabilized-temperature platform furnace.

For the determination of Al, Mg, Si and Zn, place 1 g of sample in a polyethylene volumetric flask and add, gently, 10 ml of HCl (1 + 1). Heat and, after complete dissolution, cool to room temperature and dilute with water to the appropriate volume. All the samples, standards and blank solutions were subjected to same procedures.

Tables 2 and 3 give the instrumental conditions used for the determination by graphite furnace AAS, using the blank to zero the instrument and the standard solutions to determine the standard deviation and the detection limit. The following operating conditions were employed in flame AAS determinations: flow spoiler in the nebulizer chamber, concentration mode, integra-

TABLE 4

Hydride generation programme

Parameter	As	Bi	Sb
Wavelength (nm)	193.7	223.0	217.6
Band width (nm)	0.7	0.2	0.2
Mode	$NaBH_4$	$NaBH_4$	$NaBH_4$
Purge 1 (s)	30	30	30
Reaction (s)	10	8	10
Purge 2 (s)	40	40	40
Cell temperature (°C)	700	750	850
Light source	EDL [a]	EDL [a]	EDL [a]
Sample volume (ml)	2	2	2
Diluent	5 ml of 20% HCl	6 ml of 5% HCl	5 ml of 5% HCl
Reductant	3% $NaBH_4$ + 1% NaOH	3% $NaBH_4$ + 1% NaOH	3% $NaBH_4$ + 1% NaOH
Chemical modifier	2 ml of 10% EDTA	2 ml of 10% EDTA	2 ml of 10% EDTA

[a] EDL = electrodeless discharge lamp.

tion time 5 s, expansion factor 10, air–acetylene flame and a warm-up period of 20 min.

Hydride generation AAS

Bismuth. Dissolve 1 g of InP sample, in a Teflon-lined bomb, in 10 ml of water and 10 ml of mixture of nitric acid–hydrochloric acid (1 + 3). After 1 h, heat at 65°C for 2 h. Cool to room temperature and pass nitrogen through the apparatus for 15 min to expel most of the acid and nitrogen vapours. Add 2 g of urea to eliminate completly nitrogen oxides and dilute to 25 ml with water. The solution is then ready for analysis.

In a reaction vessel, mix 2 ml of sample solution, 6 ml of 5% (v/v) HCl and 2 ml of 10% (w/v) EDTA and begin the analysis.

Arsenic. Repeat the same procedure as for bismuth. Mix 2 ml of sample solution, 1 ml of 10% (w/v) KI, 5 ml of 20% (v/v) HCl and 2 ml of 10% (w/v) EDTA. The reduction of arsenic(V) to arsenic(III) takes about 1 h to complete at room temperature. The solution is then ready for analysis.

Antimony. Transfer 2 ml of sample solution obtained with the same procedure as used for bismuth into a reaction vessel. Add 5 ml of 5% (v/v) HCl, 1 ml of 10% (w/v) KI and 2 ml of 10% (w/v) EDTA. As the reduction to Sb(III) occurs instantaneously, the solution may be analysed at once.

The instrumental conditions used for each element are given in Table 4.

RESULTS AND DISCUSSION

For elements such as Si, Al and Fe, many difficulties in eliminating accidental contamination arise; this is also due to the presence of these elements in materials commonly used in the laboratory. Better results are to be expected after reducing ambient contamination. However, the results for Fe were better than those reported in other work and obtained by AAS [14].

Using hydride generation AAS, prereduction with KI for As and Sb was necessary to achieve higher peak-height sensitivities [15]. For As, Bi and Sb, if no masking agent is added, indium precipitates in the form of very fine particles, preventing the correct development of volatile hydrides [1].

Table 5 gives the detection limits calculated using the expression

$$C_L = 4.604 S_b / m$$

where 4.604 is the value of Student's t for four degrees of freedom and at the 99.5% confidence level, S_b is the standard deviation of the blank and m is the slope of the calibration graph.

The accuracy of the method and the results of the analyses were compared with those obtained by glow discharge mass spectrometry (GDMS). The samples for GDMS analysis were cut into pins, etched in 5% high-purity-bromine–methanol solution and rinsed in methanol. The pins were sputtered for 30 min in an argon plasma to remove residual surface contaminants before starting the analysis. A possible drawback of the GDMS technique is the sampling procedure, via sputtering, is applied to a restricted area of the specimen and the determination of some ele-

TABLE 5

Detection limits

Element	Detection limit	
	ng g^{-1}	atoms cm^{-3}
Ag	20	5.35×10^{14}
Al	140	1.50×10^{16}
As	90	1.56×10^{15}
Au	70	1.02×10^{15}
Bi	100	1.38×10^{15}
Cd	6	1.54×10^{14}
Co	140	6.85×10^{15}
Cr	4	2.21×10^{14}
Cu	30	1.36×10^{15}
Fe	50	2.58×10^{15}
Ga	30	1.24×10^{15}
Mg	70	8.31×10^{15}
Mn	8	4.20×10^{14}
Mo	40	1.20×10^{15}
Ni	90	4.43×10^{15}
Pb	60	8.36×10^{14}
Sb	90	2.13×10^{15}
Si	200	2.05×10^{16}
Sn	30	7.29×10^{14}
Zn	90	3.97×10^{15}

TABLE 6

Comparison of results of analyses by GDMS and AAS

Element	Concentration found (ng g^{-1})	
	GDMS	AAS
Ag	< 0.7	< 20
Al	< 0.07	< 140
As	48	< 90
Au	–	< 70
Bi	< 0.3	< 100
Cd	15	13
Co	0.8	< 140
Cr	< 0.25	< 4
Cu	27	< 30
Fe	< 0.4	< 50
Ga	< 10	< 30
Mg	< 0.1	< 70
Mn	< 0.3	< 8
Mo	< 0.3	< 40
Ni	< 0.4	< 90
Pb	< 1.1	< 60
Sb	< 0.6	< 90
Si	< 0.07	< 200
Sn	< 24	< 30
Zn	8.5	< 90

ments could be affected by inhomogeneity in their bulk distribution.

Table 6 shows the results of the analysis of a high-purity InP single crystal obtained by GDMS (VG 9000 instrument) and by AAS. The agreement between the two techniques appears to be very good, even taking in account the better performance of GDMS mainly in terms of sensitivity. Hence AAS can be considered a as a practicable technique for the characterization of InP polycrystals and for the determination of dopants in single crystals.

The detection limits calculated allow the determination of concentrations [16] of p-dopants such as Cd (10^{16}–10^{18} atoms cm^{-3}), Fe (10^{16}–10^{17} atoms cm^{-3}), Ag (10^{16}–10^{18} atoms cm^{-3}), Cr (10^{16}–10^{19} atoms cm^{-3}), Cu (10^{15}–10^{17} atoms cm^{-3}), Zn (10^{17}–10^{19} atoms cm^{-3}) and Mg (10^{18}–10^{19} atoms cm^{-3}) and n-dopants such as Sn (10^{17}–10^{19} atoms cm^{-3}) and Si (10^{16}–10^{19} atoms cm^{-3}).

In the analysis of commercial products it is often found that the purity claimed is incorrect. The method described in this paper offers the possibility of the rapid determination of the elements present in InP by the relatively inexpensive technique of AAS.

The authors acknowledge financial support from the Fondo ENI per la Ricerca of the ENI Group.

REFERENCES

1 E. Sentimenti, G. Mazzetto and G. Pannocchia, Anal. Chim. Acta, 234 (1990) 425.
2 E. Sentimenti, G. Mazzetto and E. Milella, Report No. 3 Temav Centro Ricerche Venezia Laboratory, Venice, 1990.
3 L.S. Kopanskaya and A.T. Russu, Zh. Anal. Khim., 28 (1973) 2182.
4 B.D. Brodskaya, M.A. Notkina, S.A. Korneeva and N.P. Men'shova, Zh. Anal. Khim., 21 (1966) 1447.
5 N.A. Rudnev, L.I. Pavlenko and G.I. Malofeeva, Tr. Kom. Anal. Khim. Akad. Nauk SSSR, 16 (1968) 99.
6 M. Gauneau, A. Rupert, M. Minier, O. Rengreny and R. Coquille, Anal. Chim. Acta, 135 (1982) 193.
7 Y. Gao, Surf. Interface Anal., 14 (1989) 552.
8 M. Gauneau, R. Chaplein and A. Rupert, Microsc. Spectrosc. Electron., 9 (1984) 451.
9 T. Tanaka, Y. Homma and S. Kurosawa, Anal. Chem., 60 (1988) 58.
10 R. Lacroix, G. Blondiaux, A. Giovagnoli, M. Vallon, J.L. Debrun, R. Coquille and M. Gauneau, J. Radioanal. Nucl. Chem., 83 (1984) 91.
11 K.M. Kobayashi and K. Kudo, J. Radioanal. Nucl. Chem., 84 (1984) 291.
12 C. Liteanu and I. Rica, Statistical Theory and Methodology of Trace Analysis, Horwood, Chichester, 1980.
13 H.M. Ortner, Quality—Challeges and Opportunities, Proceedings of the 31st Annual Conference of the European Organization for Quality Control (EOQC), Munich, June 1987, Vol. 1, Deutsche Gesellschaft für Qualität, Frankfurt, 1987, pp. 443–445.
14 G. Zhou, Fenxi Huaxue, 15 (1987) 806.
15 H.W. Sinemus, M. Mekker and B. Welz, At. Spectrosc., 2 (1981) 81.
16 B. Tuck, Atomic Diffusion in III–V Semiconductors, Higer, Bristol, 1988.

Analytica Chimica Acta, 272 (1993) 105–114
Elsevier Science Publishers B.V., Amsterdam

In situ concentration of mercury vapour in a palladium-coated graphite tube: determination of mercury by atomic absorption spectrometry

Xiu-Ping Yan and Zhe-Ming Ni

Research Centre for Eco-Environmental Sciences, Academia Sinica, P.O. Box 2871, Beijing 100085 (China)

Qin-Lin Guo

Institute of Physical Chemistry, Peking University, Beijing (China)

(Received 11th May 1992; revised manuscript received 16th September 1992)

Abstract

A method was developed for the determination of mercury by cold vapour generation electrothermal atomic absorption spectrometry with in situ concentration in a palladium-coated graphite tube. The mercury vapour generated by using $NaBH_4$ is rapidly trapped in the graphite tube, coated with $PdCl_2$, at 250°C and atomized at 2200°C. The experimental results show that the trapping efficiency for mercury by $PdCl_2$ is better than that by reduced palladium. Reduction of $PdCl_2$ to palladium metal gives less favourable mercury trapping. Calibration is achieved with simple aqueous solutions. An absolute detection limit (3σ) of 31.4 pg, corresponding to a concentration detection limit of 628 pg l^{-1} for 50-ml samples, is obtained. The characteristic mass is 114 pg. The precision for ten replicate determinations is 2.0% (relative standard deviation) at the 1-ng level and 1.8% at the 5-ng level. The method was successfully applied to the determination of mercury in certified water samples, sea water and waste water. The most favourable aspects of the method are its simplicity, high-speed and good reproducibility.

Keywords: Atomic absorption spectrometry; Mercury; Preconcentration; Waters

To establish sources of mercury contamination and to evaluate levels of mercury pollution, extensive research on mercury determination has been carried out. In particular, cold vapour atomic absorption spectrometry (CVAAS) has received great attention owing to its simplicity, high sensitivity and relative freedom from interferences [1,2]. In order to lower the detection limit and to improve the sensitivity further, the combination of CVAAS with noble metal amalgamation techniques has been investigated [2–7]. Usually the copper, silver, gold and platinum metals were used for this purpose [6]. However, there are two disadvantages with this amalgamation technique [8]. First, the efficiency of mercury collection may be impaired by moisture or other gaseous reaction products which poison the surface of the amalgamation medium, necessitating occasional cleaning. Second, during heating of the collector to release the mercury, a gas flow is used to transport the vapour to the absorption cell, which means that the sensitivity is flow-rate limited; Slight changes in the flow-rate between measurements will also impair the reproducibility [8].

To circumvent these problems, methods for the determination of mercury have been devel-

Correspondence to: Zhe-Ming Ni, Research Centre for Eco-Environmental Sciences, Academia Sinica, P.O. Box 2871, Beijing 100085 (China).

oped using a combination of cold vapour generation, trapping in a porous gold-plated graphite minitube [9], a gold-coated [10,11] or a platinum-lined graphite tube [8], followed by atomic absorption spectrometric detection. In earlier work, Siemer and Hageman [9] used porous gold-plated graphite minitubes (CRA-63) mounted in a specially designed holder as filters to collect mercury from a gas stream drawn through the reaction cell by a vacuum pump. Owing to the variation in the blank levels obtained, the reported detection limit was 14 ng l^{-1} [9]. Methods developed by Lee et al. [10] and Hladky et al. [11] using a gold-coated graphite furnace as both mercury trapping medium and atomization cell permit the determination to be carried out at ng l^{-1} levels. Unfortunately, in the method proposed by Lee et al. [10], the commercially available electrothermal atomizer (CRA-90) needed modification so that it could be coupled directly to a mercury vapour generator [10]. This poses a problem in applying this method to routine analysis. Further, in these methods [10,11], an additional pretreatment step was required to reduce the gold(III) to the metal before mercury trapping.

Baxter and Frech [8] reported the possibility of using a platinum-lined graphite furnace for mercury determination and obtained a detection limit (2σ) of 2 ng l^{-1} for 50-ml samples. However, the adsorption of mercury in a platinum-lined furnace was slow and a collection time of more than 5 min was needed to achieve the maximum absorbance signal. In the method reported by Hladky et al. [11], a much longer collection time, over 20 min, was used to trap mercury in a gold-coated tube.

Chemical modification techniques are widely used in electrothermal atomic absorption spectrometry (ETAAS). Palladium is a very effective chemical modifier and can be used to stabilize many elements to several hundred degrees higher than the temperatures possible with current methods [12–22]. The use of palladium-coated tubes as both the hydride-trapping medium and atomization cell greatly improved the sensitivity and detection limits for hydride-forming elements [23–25].

In this work, a method was developed for the determination of mercury by in situ concentration of mercury in a $PdCl_2$-coated graphite tube with subsequent ETAAS detection. There is no need to modify the graphite furnace in this method. Moreover, no additional pretreatment step for the reduction of palladium salt is required before mercury trapping. The mercury vapour can be effectively adsorbed by the $PdCl_2$-coated tube within 20 s. The most favourable aspects of this method are its simplicity, high speed and good reproducibility. The valence state of palladium on the graphite surface after heat treatment was studied using x-ray photoelectron spectrometry (XPS).

EXPERIMENTAL

Instrumentation

The measurement of analyte absorbance was carried out in the peak height mode under "gas stop" conditions using a Perkin-Elmer Model 4000 atomic absorption spectrometer with deuterium background corrector, equipped with an HGA-400 graphite furnace and a Model 056 chart recorder. A mercury hollow-cathode lamp was used as the line source at 253.7 nm. The sample introduction port of the graphite tube was enlarged to a diameter of 2.5 mm with a drill bit. Pyrolytic graphite-coated graphite tubes were used.

Mercury vapour was generated in a laboratory-built hydride generator, HG-100 [26], into which sodium tetrahydroborate solution and sample solution were introduced by two channels of a peristaltic pump. The mercury vapour evolved was stripped from the solution and swept into the preheated palladium-coated graphite tube using an argon purge gas. The generator assembly and sequence of operations used to generate and trap mercury vapour were similar to the earlier detailed description [23,26].

The x-ray photoelectron spectra were measured at room temperature using an ESCA LAB-5 (VG Scientific) surface spectrometer which had a base pressure of 4×10^{-13} bar. Mg $K\alpha$ x-radiation ($h\nu = 1253.6$ eV) was used. The XPS data were recorded and processed by a PDP LS 11/2

TABLE 1

Recommended experimental conditions

Wavelength	253.7 nm	Uptake rate of $NaBH_4$ solution	6 ml min^{-1}
Band width	0.7 nm	Uptake rate of HCl solution	6 ml min^{-1}
Lamp current	4 mA	$NaBH_4$ concentration	2% (w/v)
Carrier gas flow-rate	570 ml min^{-1}	HCl concentration	0.5 mol dm^{-3}

computer. The binding energy scale was calibrated by assigning a value of 284.5 eV to the C 1*s* signal of graphite.

Reagents

All chemicals were of analytical-reagent grade. A stock standard solution of mercury (1000 μg ml^{-1}) was prepared by dissolving mercury(II) chloride in deionized water. Working standard solutions were obtained through appropriate dilution of the stock standard solution just before use.

Solutions of sodium tetrahydroborate of 1%, 1.5%, 2%, 4% and 6% (w/v) were prepared daily or as required by dissolving $NaBH_4$ in deionized water and used without further filtration or stabilization.

Palladium solution (1000 μg ml^{-1}) was prepared by dissolving palladium(II) chloride in dilute nitric acid and subsequently diluting with deionized water. Palladium solutions of 25, 50, 100, 200, 300 and 400 μg ml^{-1} were obtained by diluting the above solution with deionized water.

Procedure

Mercury vapour generation, adsorption and ETAAS measurement were done as follows. A 50-μl aliquot of 200 μg ml^{-1} Pd as $PdCl_2$ solution was injected into the graphite tube with an Eppendorf microlitre pipette fitted with disposable polypropylene tip, and dried at 100°C. The tip of the quartz tube connected with the outlet of the hydride generator was inserted into the sample introduction port at the centre of the graphite tube and was held near the opposite interior wall. When the furnace reached the adsorption temperature, the $NaBH_4$ solution and acid sample solution containing mercury were delivered to the hydride generator. The mercury vapour evolved was swept into the furnace with argon and adsorbed on the graphite tube coated with $PdCl_2$. When the adsorption was complete, the quartz hydride delivery tube was automatically withdrawn from the furnace, and the analyte was atomized at 2200°C. The recommended experimental conditions and furnace programme are summarized in Tables 1 and 2.

Graphite platforms were used as base materials on which three samples were prepared for subsequent investigations by XPS. Samples 1 and 2 were prepared by repeating the following operation five times: 20 μl of 200 μg ml^{-1} Pd as $PdCl_2$ solutions were injected on to the graphite platform, dried at 100°C for 30 s, and then heated at 250°C (sample 1) or 900°C (sample 2) for 40 s. Sample 3 containing $PdCl_2$ and Hg was prepared

TABLE 2

Furnace programme

Step	Temperature (°C)	Ramp time (s)	Hold time (s)	Internal gas flow	Procedure
1	100	5	50	Normal	Dry Pd solution
2	250	5	5		Insert quartz tube
			40	Normal	Generate and trap mercury vapour
			5		Remove quartz tube
3	2200	1	5	Stopped	Atomization
4	2650	1	2	Normal	Clean the furnace

as follows: the operation of injection and drying of the $PdCl_2$ solution was the same as for sample 1, the mercury vapour was adsorbed by $PdCl_2$ at 250°C for 40 s and this process was repeated until a required amount (μg level) of sample was accumulated. After the graphite tube had been cooled to room temperature, the platform was removed and transferred into the vacuum system of the x-ray photoelectron spectrometer for XPS measurement.

RESULTS AND DISCUSSION

Effect of ascorbic acid and heat pretreatment

In direct aqueous sample introduction in ETAAS, it has been reported that steps taken to ensure that the palladium modifier was reduced to the metal as early as possible greatly improved its performance. The palladium modifier could be reduced, for example, by hydrogen–argon (5 + 95), ascorbic acid or preheating palladium modifiers to 1000°C before injecting analytes [27–29]. In this work, the effects of ascorbic acid and heat pretreatment on the mercury trapping were investigated in order to establish whether the reduction of $PdCl_2$ was a prerequisite for mercury trapping.

The results in Fig. 1 show that the adsorption efficiency of mixed $PdCl_2$–ascorbic acid for mercury (curve b) is much lower than that of $PdCl_2$ alone (curve a). Figure 2a indicates that the trapping efficiency for Hg by $PdCl_2$ decreases as the pretreatment temperature increases. However, the results in Fig. 2b show that the pretreatment temperature has no influence on the trapping efficiency of mixed $PdCl_2$–ascorbic acid, as the $PdCl_2$ has been reduced to the metal by ascorbic acid. It is well documented that palladium salts would be reduced to metallic palladium in a graphite tube at temperatures around 500°C or on mixing with a reducing reagent such as ascorbic acid [27,28,30,31].

From the above results, it is evident that the reduction of $PdCl_2$ to the metal is less favourable for mercury trapping. This is contrary to the results obtained from the direct injection method, in which higher sensitivities are usually achieved

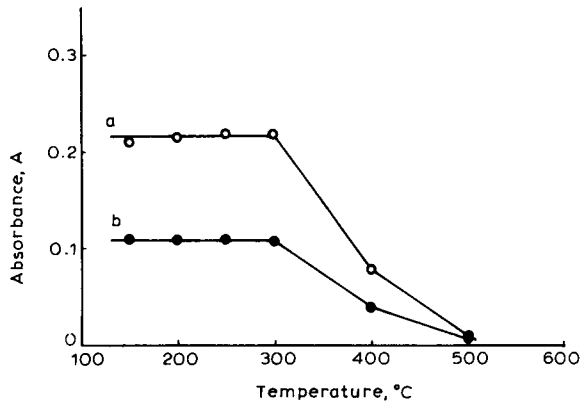

Fig. 1. Effect of adsorption temperature on the peak absorbance of 5 ng of mercury generated in 0.5 mol l^{-1} HCl and 2% (w/v) $NaBH_4$: (a) 50 μl of 200 μg ml^{-1} Pd as $PdCl_2$; (b) 50 μl of 200 μg ml^{-1} Pd as $PdCl_2$ + 20 μl of 1% (w/v) ascorbic acid.

when the reduced palladium is used as a matrix modifier [27,28,30,31]. Therefore, $PdCl_2$ was used to trap mercury vapour with no addition of ascorbic acid or heat pretreatment. In order to investigate further the mechanism of mercury trapping, the oxidation state of the palladium on the graphite surface was studied by XPS.

Optimization of experimental parameters

Adsorption temperature and collection time. As can be seen from Fig. 1, the maximum ab-

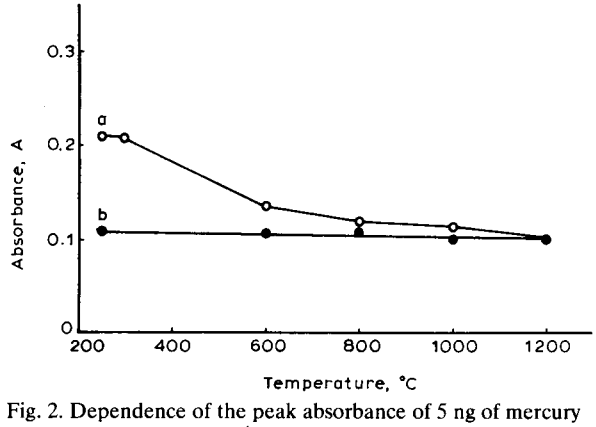

Fig. 2. Dependence of the peak absorbance of 5 ng of mercury generated in 0.5 mol l^{-1} HCl and 2% (w/v) $NaBH_4$, adsorbed at 250°C, on pretreatment temperature: (a) 50 μl of 200 μg ml^{-1} Pd as $PdCl_2$; (b) 50 μl of 200 μg ml^{-1} Pd as $PdCl_2$ + 20 μl of 1% (w/v) ascorbic acid.

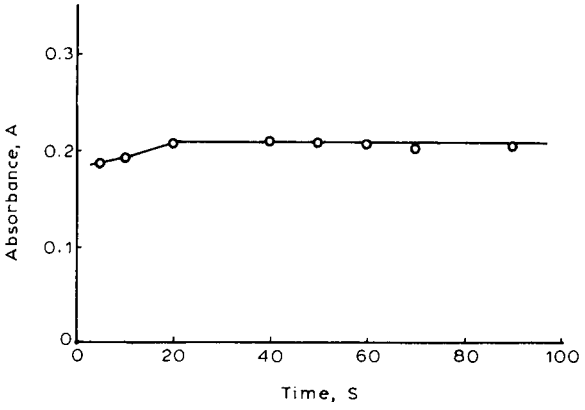

Fig. 3. Influence of collection time on the peak absorbance of 5 ng of mercury generated in 0.5 mol dm^{-3} HCl and 2% (w/v) $NaBH_4$, adsorbed at 250°C in the $PdCl_2$-coated graphite tube.

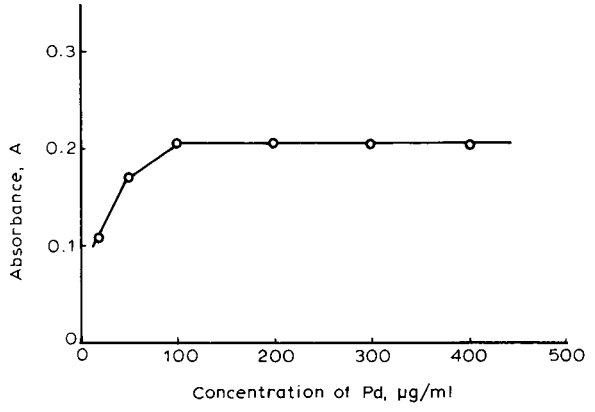

Fig. 4. Effect of Pd concentration on the peak absorbance of 5 ng of mercury generated in 0.5 mol l^{-1} HCl and 2% (w/v) $NaBH_4$, adsorbed at 250°C in the graphite tube coated with $PdCl_2$.

sorbance of mercury is obtained with adsorption temperatures between 150 and 300°C using either (a) $PdCl_2$ or (b) mixed $PdCl_2$–ascorbic acid as an adsorber. Above 300°C the trapping efficiency rapidly decreases. This is probably due to the reduction of $PdCl_2$ to the metal (curve a) and incomplete adsorption of mercury (curves a and b) at higher temperatures. In subsequent experiments, a temperature of 250°C was selected for mercury trapping.

Figure 3 shows the dependence of the peak absorbance of mercury on collection time. Even a collection time of 20 s is sufficient for trapping mercury in a $PdCl_2$-coated tube; no significant change in the absorbance is observed as the collection time increases further. These results imply that mercury vapour can be rapidly adsorbed by the graphite tube coated with $PdCl_2$. To ensure that all of the mercury vapour was completely adsorbed, a collection time of 40 s was used.

Amount of palladium added. The influence of the concentration of Pd solution on the trapping efficiency was examined when the volume of Pd solution injected was kept at 50 µl. The results in Fig. 4 show that the trapping efficiency increases significantly as the concentration of Pd solution increases from 25 to 100 µg ml^{-1}, then levels out above 100 µg ml^{-1}.

The effect of the volume of Pd solution injected on the trapping efficiency was also investigated for a constant 10 µg of Pd. No significant change in the trapping efficiency was found when the volume of Pd solution injected varied from 10 to 100 µl. These results suggest that the adsorption of mercury in the $PdCl_2$-coated tube depends only on the amount of Pd added. All subsequent experiments utilized a 50-µl injection volume of 200 µg ml^{-1} Pd solution.

Carrier gas flow-rate The variation of the mercury absorbance with carrier gas flow-rate was examined under the recommended conditions, and is illustrated in Fig. 5. It is obvious that a carrier gas flow-rate of 480 ml min^{-1} is necessary to strip the generated mercury vapour completely

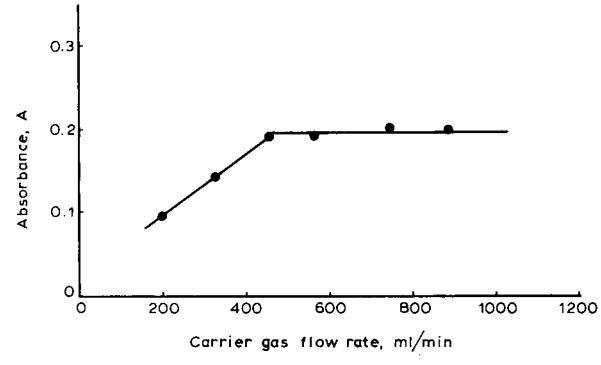

Fig. 5. Influence of carrier gas flow-rate on the peak absorbance of 5 ng of mercury generated at 0.5 mol l^{-1} HCl and 2% (w/v) $NaBH_4$, trapped in the $PdCl_2$-coated tube at 250°C.

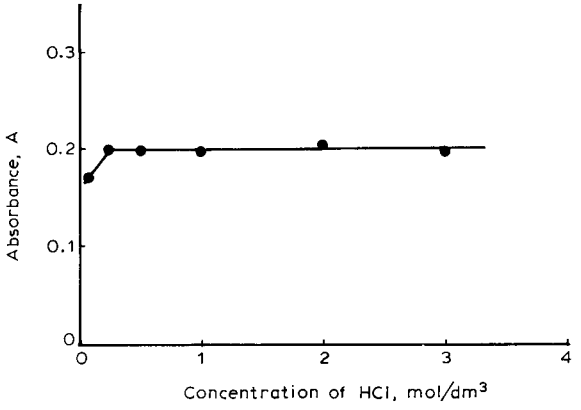

Fig. 6. Dependence of the peak absorbance of 5 ng of mercury generated in 2% (w/v) $NaBH_4$, trapped in the $PdCl_2$-coated tube at 250°C, on HCl concentration.

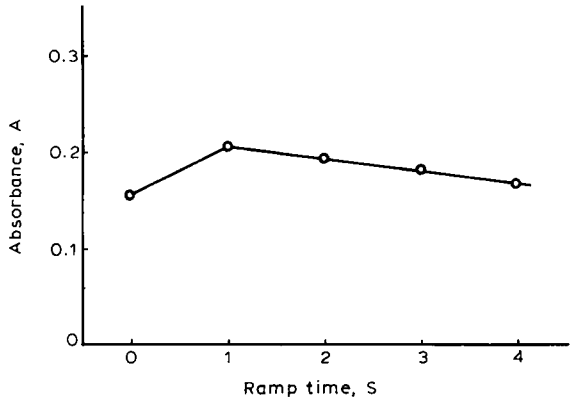

Fig. 8. Influence of heating rate on the peak absorbance of 5 ng of mercury generated in 0.5 mol l^{-1} HCl and 2% (w/v) $NaBH_4$, trapped in the $PdCl_2$-coated tube at 250°C.

from the solution. A carrier gas flow-rate of 570 ml min^{-1} was used.

HCl and $NaBH_4$ concentrations. Figure 6 shows the influence of HCl concentration on the peak absorbance of mercury. Below 0.25 mol l^{-1} the mercury absorbance increases with increasing concentration of HCl, but above 0.25 mol dm^{-3} it remains almost unchanged. A concentration of 0.5 mol l^{-1} HCl was needed for the generation of mercury vapour.

The variation of the peak absorbance of mercury with the concentration of $NaBH_4$ is depicted in Fig. 7. Obviously, below 1.5% (w/v) the peak absorbance increases rapidly with increasing concentration of $NaBH_4$. However, above 1.5% (w/v) the mercury absorbance gradually decreases as the concentration of $NaBH_4$ increases. It seems unreasonable to conclude that excessive $NaBH_4$ will hinder the generation of mercury vapour. However, as interaction between Pd species and H_2 at low furnace temperatures has been suggested [27], the hydrogen generated by excessive $NaBH_4$ may decrease the trapping efficiency through reduction of palladium chloride to metallic palladium, which is less favourable for the adsorption of mercury, as described above. For subsequent experiments 2% (w/v) $NaBH_4$ solution was used.

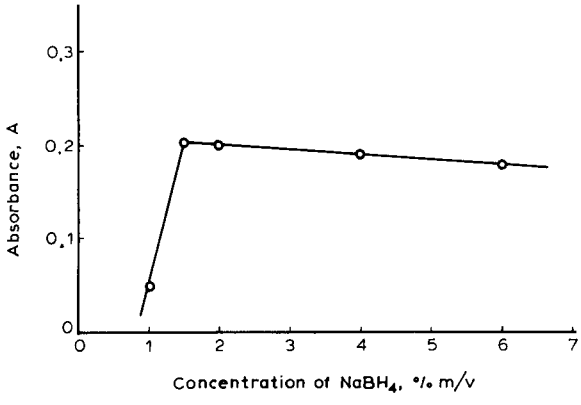

Fig. 7. Variation of the peak absorbance of 5 ng of mercury generated in 0.5 mol l^{-1} HCl, trapped in the $PdCl_2$-coated tube at 250°C, with $NaBH_4$ concentration.

Heating rate and atomization temperature. For the determination of refractory elements, the "maximum power" mode is often required to achieve maximum sensitivity, as fast heating increases the rate of analyte release. However, for the analysis of highly volatile mercury, the "maximum power" mode is unnecessary. Figure 8 depicts the influence of ramp time in the atomization step on the peak absorbance of mercury. The highest signal is obtained using a ramp time of 1 s rather than "maximum power". Although rapid heating facilitates the release of analyte from the graphite surface, it also speeds up the dissipation of gaseous analyte atoms within the atomizer through expulsion. Therefore the "maximum power" mode is not favourable for mercury determination.

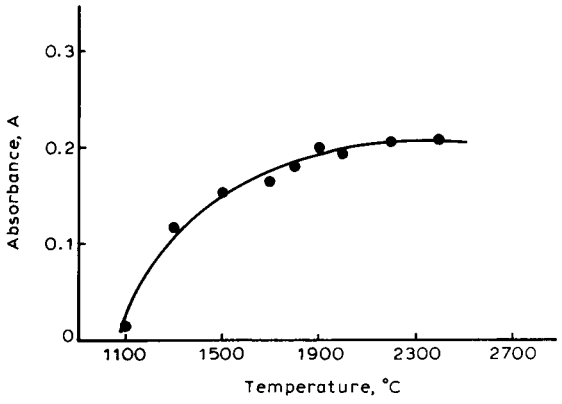

Fig. 9. Effect of atomization temperature on the peak absorbance of 5 ng of mercury generated in 0.5 mol l^{-1} HCl and 2% (w/v) $NaBH_4$, adsorbed in the $PdCl_2$-coated tube at 250°C.

Figure 9 shows the dependence of the peak absorbance of mercury on atomization temperature. The optimum atomization temperature ranges from 1900 to 2400°C. Compared with the direct aqueous solution injection method for mercury determination in which a palladium modifier was used and optimum atomization temperatures of 900–2400°C were obtained [12,13], the mercury adsorbed by $PdCl_2$ seems to be more difficult to atomize. This probably results from the different stabilization and atomization mechanisms. A temperature of 2200°C was chosen for atomization.

TABLE 4

Determination of mercury in standard water samples [a]

Sample	Concentration (ng ml^{-1})	
	Certified	Determined [b]
GSBZ 50016-90 Hg 1400203 (China)	4.9 ± 1.0	4.8 ± 0.4
GSBZ 50016-90 Hg 1410104 (China)	14.7 ± 1.4	14.5 ± 0.2

[a] Standard water samples were prepared and certified by the China Environmental Monitoring Station, Beijing. [b] Mean ± standard deviation based on triplicate determinations.

Analytical results

The results for the recovery of mercury added to water samples are summarized in Table 3. The recoveries are in the range 96–103%. The slope of the calibration graph prepared with standard aqueous solutions was found to be almost identical with that of the standard additions plot prepared for water samples, so calibration was achieved with a simple calibration graph.

The results for certified water samples given in Table 4 show that the concentrations of mercury determined by the present method are in good

TABLE 3

Recovery of mercury from water samples

Sample	Hg in water (ng)	Hg added (ng)	Total Hg found (ng)	Recovery (%)
GSBZ 50016-90 Hg 1400203 (China)	4.90	4.00	8.90	100
		6.00	11.20	103
GSBZ 50016-90 Hg 1410104 (China)	7.05	2.50	9.58	101
		5.00	12.11	101
Sea water 1	0.09	5.00	5.20	102
		10.00	10.10	100
Sea water 2	0.06	5.00	5.18	102
		10.00	9.80	97
Waste water 1	0.05	5.00	4.90	97
		10.00	10.10	101
Waste water 2	0.06	5.00	4.85	96
		10.00	10.00	99

TABLE 5

Determination of mercury in water samples

Sample	Concentration (ng ml^{-1}) [a]
Sea water 1	0.18 ± 0.01
Sea water 2	0.12 ± 0.02
Waste water 1	0.10 ± 0.01
Waste water 2	0.11 ± 0.02

[a] Mean ± standard deviation based on triplicate determinations.

agreement with the certified values. Results for sea water and waste water are given in Table 5.

Figures of merits

A characteristic mass of 114 pg was obtained, where characteristic mass is defined as the amount of analyte that provides a defined peak absorbance of 0.0044. The absolute detection limit, based on the variability of the blank (3σ), is 31.4 pg. This corresponds to a concentration detection limit of 628 pg l^{-1} for 50-ml samples.

The precision of the method was evaluated by replicate determinations for 1 ng and 5 ng of mercury. The relative standard deviations for ten replicate determinations are 2.0% for 1 ng and 1.8% for 5 ng of mercury. The regression equation for the calibration graph is $y = 0.0386x + 0.0005$ with a correlation coefficient of 0.9998 ($n = 8$), where x = the analyte mass (ng) and y = peak absorbance. The calibration graph is linear up to 30 ng, corresponding to a linear range of three orders of magnitude. The blank is found to be 5 pg.

Adsorption mechanism

Palladium is a very useful chemical modifier for ETAAS. Recently, a great deal of interest has be generated in the mechanism of palladium as a chemical modifier [25,27–29,32–36]. The formation of intermetallics between palladium and the analytes has been ascribed as the primary mechanism by which palladium stabilizes elements in ETAAS [33,34,36]. The high efficiency and universal effect of palladium modifiers are due to the fact that the palladium metal can be easily formed from its compounds [29]. Differences in the physical form of the palladium obtained by various reduction methods may influence the performance of the palladium modifier [28]. The effective hydride trapping in a palladium-coated graphite tube has been explained by the catalytic activity of the palladium metal [24,25].

In order to elucidate the mechanism of mercury trapping in the graphite-tube coated with $PdCl_2$, the effects of the physical and the chemical forms of the palladium on mercury adsorption were investigated. Scanning electron micrographs showed that the size and distribution of palladium particles on the graphite surface were different depending on the reduction method used [28]. When ascorbic acid was used as a reducing agent, relatively small particles of palladium were obtained, but they were not evenly distributed; with the case of using hydrogen as a reducing agent, most of the palladium particles appeared to be clustered together; however, preheating a palladium solution to 1000°C resulted in a considerable variation in palladium particle size. Although the physical form of palladium produced by ascorbic acid reduction is different from that obtained by preheating the palladium modifier to 1000°C, as mentioned above, no significant changes in the peak absorbance of mercury were found (see Figs. 1b and 2). This suggests that the physical form of palladium has no significant influence on mercury trapping.

To evaluate the role of the chemical form of palladium in mercury adsorption, XPS was used to identify the chemical state of elements. Figure 10a shows the 3*d* XP spectrum of palladium for pure $PdCl_2$ powder. The $3d_{3/2}$ and $3d_{5/2}$ binding energies are 343.50 and 338.12 eV, respectively, in good agreement with the tabulated values [37]. The 3*d* XP spectrum of palladium for the $PdCl_2$ deposit prepared by heating at 250°C on the graphite surface is depicted in Fig. 10b. In comparison with the 3*d* XP spectrum of pure $PdCl_2$, no significant shift in the 3*d* binding energies is observed, implying that $PdCl_2$ has not been converted into the metal on the graphite surface at 250°C. However, the 3*d* spectrum in Fig. 10c, obtained from the $PdCl_2$ deposit heated at 900°C, significantly shifts to lower binding energies of 341.12 eV for the $3d_{3/2}$ and 335.78 eV for the $3d_{5/2}$ level, corresponding to the values for

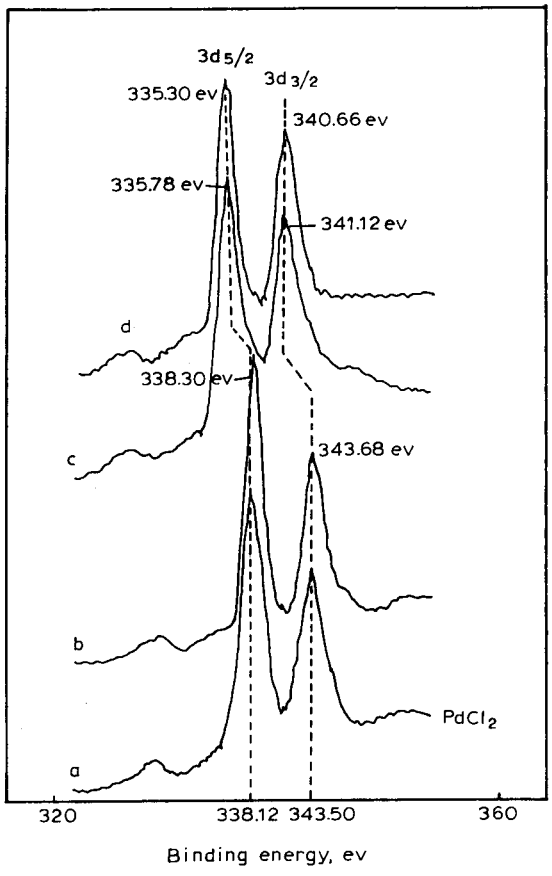

Fig. 10. Palladium 3*d* x-ray photoelectron spectra for (a) pure $PdCl_2$ powder; (b) $PdCl_2$ deposit, heated at 250°C on the graphite platform; (c) $PdCl_2$ deposit, heated at 900°C on the graphite platform; (d) $PdCl_2$ deposit on which Hg was adsorbed at 250°C.

metallic palladium [37]. This indicates that $PdCl_2$ has been reduced to palladium metal on the graphite surface at 900°C. Therefore, the reduction of $PdCl_2$ to the metal by preheating or ascorbic acid treatment is responsible for the considerable decrease in the mercury trapping efficiency.

The much higher trapping efficiency for Hg by $PdCl_2$ than by the reduced palladium can be ascribed to the chemical reaction that occurred between $PdCl_2$ and Hg. It has been reported that $PdCl_2$ could be used to remove mercury vapour in the original vapour stream due to the reaction $PdCl_2 + Hg \rightarrow Pd + HgCl_2$ [38,39]. According to this reaction, palladium metal and mercury(II) chloride seem to be formed during mercury trapping. Figure 10d shows the 3*d* XP spectrum of palladium for a $PdCl_2$ deposit on which mercury vapour was trapped at 250°C. In contrast with Fig. 10b, it can be seen that introducing mercury vapour to the $PdCl_2$ surface (Fig. 10d) makes the binding energies of Pd $3d_{5/2}$ and $3d_{3/2}$ shift to 335.30 and 340.66 eV, respectively, close to those of metallic palladium [37]. A binding energy of 99.42 eV for the Hg $4f_{7/2}$ level was also observed by XPS (not shown), nearly corresponding to that of metallic mercury [37]. It is possible that mercury(II) chloride produced from the oxidation of mercury vapour by $PdCl_2$ was reduced to metallic mercury by the reducing atmosphere in the graphite tube during mercury trapping.

The possibility of intermetallic compound formation between mercury and palladium during mercury trapping still exists, although no significant evidence of this formation can be provided by XPS experiments as the binding energy shifts of $3d_{3/2}$ and $3d_{5/2}$ shown in Fig. 10c and d are less than 0.6 eV. Hedman et al. [40] studied the electronic structure of some palladium alloys (Cu–Pd, Rh–Pd, Ag–Pd and Au–Pd) by XPS and found no significant shifts (not more than 0.3 eV) of Pd 3*d* binding energies for these alloys. Vesely and Langer [41] investigated the binding energies of some simple compounds of Zn, Cu, Cd and Hg and pointed out that in general the chemical shifts of these elements were fairly small. As no XPS results for the Hg–Pd system are available, it is assumed that the chemical shifts of Pd 3*d* and Hg 4*f* in this system are very small. Hence it is difficult to confirm the presence of intermetallic formation between mercury and palladium during mercury trapping by XPS. However, the fact that the reduced palladium did trap mercury vapour at temperatures of 150–300°C indicates that an intermetallic compound or alloy is probably formed between Hg and Pd. The rapid oxidation of mercury vapour by $PdCl_2$ makes the $PdCl_2$ more favourable for mercury trapping than the reduced metal.

This work was supported by the China National Science Foundation under Grant No. 29170240.

REFERENCES

1 G. Topping and J.M. Pirie, Anal. Chim. Acta, 62 (1972) 200.
2 B. Welz, M. Melcher, H.W. Sinemus and D. Maier, At. Spectrosc., 5 (1984) 37.
3 W.F. Fitzgerald and G.A. Gill, Anal. Chem., 51 (1979) 1714.
4 R. Dumarey, R. Dams and J. Hoste, Anal. Chem., 57 (1985) 2638.
5 W.H. Schroeder, Environ. Sci. Technol., 16 (1982) 394A.
6 N.S. Bloom and E.A. Crecelius, Mar. Chem., 14 (1983) 49.
7 G.A. Gill and W.F. Fitzgerald, Mar. Chem., 20 (1987) 227.
8 D.C. Baxter and W. Frech, Anal. Chim. Acta, 225 (1989) 175.
9 D.D. Siemer and L. Hageman, Anal. Chem., 52 (1980) 105.
10 S.H. Lee, K.H. Jung and D.S. Lee, Talanta, 36 (1989) 999.
11 Z. Hladky, J. Risova and M. Fisera, J. Anal. At. Spectrom., 5 (1990) 691.
12 Z.-M. Ni and X.-Q. Shan, Spectrochim. Acta, Part B (1987) 937.
13 X.-Q. Shan and Z.-M. Ni, Acta Chim. Sin., 37 (1979) 261.
14 X.-Q. Shan, Z.-M. Ni and L. Zhang, At. Spectrosc., 5 (1984) 1.
15 X.-Q. Shan, Z.-M. Ni and L. Zhang, Talanta, 31 (1984) 150.
16 L.-Z. Jin and Z.-M. Ni, Can. J. Spectrosc., 26 (1981) 219.
17 X.-Q. Shan, Z.-N. Yuan and Z.-M. Ni, Can. J. Spectrosc., 31 (1986) 35.
18 L.M. Voth-Beach and D.E. Schrader, Spectroscopy, 1 (1986) 49.
19 G. Schlemmer and B. Welz, Spectrochim. Acta, Part B, 41 (1986) 1157.
20 B. Sampson, J. Anal. At. Spectrom., 3 (1988) 465.
21 L.M. Beach, Spectroscopy, 2 (1987) 21.
22 I. Lindberg and E. Lundberg, J. Anal. At. Spectrom., 3 (1988) 497.
23 L. Zhang, Z.-M. Ni and X-Q. Shan, Spectrochim. Acta, Part B, 44 (1989) 339.
24 P.S. Doidge, B.T. Sturman and T.M. Rettberg, J. Anal. At. Spectrom., 4 (1989) 251.
25 R.E. Sturgeon, S.N. Willie, G.I. Sproule, P.T. Robinson and S.S. Berman, Spectrochim. Acta, Part B, 44 (1989) 667.
26 Z.-M. Ni, H.-B. Hang, A. Li, B. He and F.-Z. Xu, J. Anal. At. Spectrom., 6 (1991) 385.
27 T.M. Rettberg and L.M. Beach, J. Anal. At. Spectrom., 2 (1989) 45.
28 L.M. Voth-Beach and D.E. Schrader, J. Anal. At. Spectrom., 2 (1987) 45.
29 A. Volynsky, S. Tikhomirov and A. Elagin, Analyst, 116 (1991) 145.
30 Z. Grobenski, W. Erler and U. Voellkopf, At. Spectrosc., 6 (1985) 91.
31 Z. Zhuang, P. Yang, L. Luo, X. Wang and B. Huang, Can. J. Appl. Spectrosc., 36 (1991) 9.
32 J.E. Teague-Nishimura and T. Tominaga, Anal. Chem., 59 (1987) 1647.
33 X.-Q. Shan and D.-X. Wang, Anal. Chim. Acta, 315 (1985) 173.
34 W. Wendle and G. Mulller-Vogt, J. Anal. At. Spectrom., 3 (1988) 63.
35 B. Welz and G. Schlemmer, Spectrochim. Acta, Part B, 41 (1986) 1157.
36 D.L. Styris and D.A. Redfield, presented at the XV Federation of Analytical Chemistry and Spectroscopy Societies (FACSS) meeting, October 30–November 4, 1988, Boston, MA, abstract No. 22.
37 C.D. Wagner, W.M. Riggs, L.E. Davis, J.F. Moulder and G.E. Muilenberg, Handbook of X-Ray Photoelectron Spectroscopy, Perkin-Elmer, Norwalk, CT, 1979.
38 C.H. James and J.S. Webb, Trans. Inst. Min. Metall., 73 (1964) 633.
39 R.L. Windham, Anal. Chem., 44 (1972) 1334.
40 J. Hedman, M. Klasson, R. Nilsson, C. Nordling, M.F. Sorokina, O.I. Kljushnikov, S.A. Nemnonov, V.A. Trapeznikov and V.G. Zyryanov, Phys. Scr., 4 (1971) 195.
41 C.J. Vesely and D.W. Langer, Phys. Rev. B, 4 (1971) 451.

Analytica Chimica Acta, 272 (1993) 115–124
Elsevier Science Publishers B.V., Amsterdam

Evaluation of different data-processing options for a flow system with a well-stirred mixing chamber

James M. Jordan [1], Steven H. Hoke and Harry L. Pardue
Department of Chemistry, Purdue University, West Lafayette, IN 47907–1393 (USA)

(Received 15th July 1992; revised manuscript received 24th September 1992)

Abstract

This paper describes the evaluation of several data-processing options for a flow-based sample processor with a well-stirred mixing chamber. Data-processing options evaluated include peak-height, peak-area and time-interval methods with different choices of reference points. Results are compared with theoretical expectations and effects of experimental parameters on the different methods are compared by using relative error coefficients. It is found that theoretical equations based on a kinetic model for the system describe shapes of calibration equations very well and predict slopes of calibration plots to within a few percent of experimental values. These results show that other less rigorous treatments can lead to conclusions that are valid only for selected sets of circumstances.

Keywords: Flow system; Calibration plots; Data processing

There have been many approaches to flow-based sample processors in which unsegmented flow streams were used in conjunction with efficient mixing chambers [1–5]. A recent variant of this general approach involved intercalation of aliquots of sample into flowing streams that flushed them into mixing chambers and subsequently to detection systems [6,7].

The earlier version [6] of this general approach involved parallel flow streams, a small mixing chamber and relatively fast flow-rates such that fixed ratios of sample and reagent were mixed very rapidly. The latter version [7] involved a single flow stream, a relatively large mixing chamber and relatively slow flow-rates such that variable ratios of sample and reagent were mixed over a relatively long time period. The transient nature of the response from this latter system has led to several differences of opinion regarding the nature of the approach as well as the correct mathematical treatment of the responses [7–12]. This and a related study [13] were undertaken because several issues related to this system remain unresolved.

The original treatment [7] was based on the perception that the method was a titration and resulted in equations that were valid only for a limited set of operating conditions. A later pair of papers [8,9] provided a more general mathematical treatment that was intended to be applicable for a wide variety of operational options and experimental conditions. It was stated in a later paper [11] that unecessary assumptions were made earlier [8,9]. Although different symbols were used in the later paper [11], the same mathematical treatment as described earlier [8,9] was used to develop response equations. However, an alternative approach was used [11] to develop relation-

Correspondence to: H.L. Pardue, Department of Chemistry, 1393 Brown Building, Purdue University, West Lafayette, IN 47907-1393 (USA).
[1] Present address: The Procter & Gamble Company, International Technology Coordination, Laundry & Cleaning Products, 6060 Center Hill Road, Cincinnati, OH 45224 (USA).

ships between measured time intervals and analyte concentration. It was argued in a subsequent paper [12] that in fact the more recent treatment [11] had included hidden assumptions that resulted in mathematical expressions and subjective conclusions that were valid only for specialized circumstances.

To date, these arguments have been based primarily on mathematical treatments rather than detailed experimental studies. The present study was undertaken in part to test the validity of the mathematical treatments reported to date [7–9,11,12,14,15]. Also, although a variety of measurement and data-processing approaches should be applicable to this sample-processing approach, most studies have focused on the time-interval procedure described originally [7]. Accordingly, this study also included an evaluation of alternative measurement and data-processing options including peak-height and peak-area methods.

EXPERIMENTAL

Instrumentation and reagents

The instrument system and reagents were as described previously [13,15]. Triiodide ion was used as a tracer and was detected amperometrically. The time-controlled sampling approach described earlier [13] was used for all data reported here. After loading sample into the sample loop, the reagent stream was diverted through the sample loop for a controlled period that was long enough to flush the desired volume of sample from the sample loop but short enough that some sample remained in the loop after the reagent stream was diverted away from the sample loop and into the mixing chamber. In this way, the trailing edge of the sample aliquot which mixed with reagent was not introduced into the mixing chamber. Thus, sample introduction approached plug flow more closely and there was much better agreement between experimental and theoretical results than with conventional approaches to sample introduction.

Electrolysis currents from the amperometric detector were converted to voltages, digitized and stored on a disk by using an on-line microprocessor. The data were subsequently transferred to a supermicro computer for long-term storage, data processing and display.

Error coefficients

One goal of this study was to compare effects of different variables on different measurement and data-processing options. These comparisons were facilitated by computing relative error coefficients for each of the variables studied for each measurement/data-processing approach.

Relative error in concentration, RE(%), is defined as

$$\mathrm{RE}(\%) = 100\ \Delta C/C \qquad (1)$$

where ΔC is the concentration error produced by a change in some variable and C is the concentration at the point where the error coefficient is determined. The *relative error coefficient*, REC (%), is the relative error in concentration per unit change in the variable of interest. This is expressed as

$$\mathrm{REC}(\%) = 100\ (\Delta C/C)/\Delta V \qquad (2)$$

where ΔV is the change in the variable of interest.

Eqn. 2 can be used directly by determining the concentrations, C_1 and C_2, corresponding to values, V_1 and V_2, of the variable of interest and computing $\Delta C = C_2 - C_1$ and $\Delta V = V_2 - V_1$. For situations in which concentration changes vary non-linearly with the variable, care must be exercised to ensure that the change in the variable is sufficiently small that misleading results are not obtained.

For sufficiently small changes in a variable, the concentration change can be described as

$$\Delta C = (\mathrm{d}C/\mathrm{d}V)\Delta V \qquad (3)$$

where $\mathrm{d}C/\mathrm{d}V$ is the slope of a plot of C vs. V at a particular point along the curve. Substituting this into Eqn. 2 we obtain

$$\mathrm{REC}(\%) = 100(\mathrm{d}C/\mathrm{d}V)/C \qquad (4)$$

which is more useful for non-linear relationships between concentration and the variable of interest.

For situations for which it is possible to establish a linear relationship between the measure-

ment objective, S, and concentration, we can write

$$S = (dS/dC)C + I \quad (5)$$

where S is the measurement objective, dS/dC is the slope (sensitivity) of a calibration plot of S vs. C and I is any intercept that exists. Rearranging Eqn. 5 to be explicit in C, and substituting into Eqn. 4, we have

$$REC(\%) = 100(dC/dV)(dS/dC)/(S - I) \quad (6)$$

where all terms have been defined above. For situations in which $(dC/dV)(dS/dC) = dS/dV$, Eqn. 6 reduces to

$$REC(\%) = 100(dS/dV)/(S - I) \quad (7)$$

It is noted here that the measurement objective, S, can be as simple as a measured signal such as peak current or it can be a complex mathematical function such as the integral of current vs. time (peak area) or an exponential function such as $\exp(f/V_g)\Delta t$. The principal requirement is that it satisfies the linear relationship in Eqn. 5.

RESULTS AND DISCUSSION

Response curves

Figure 1 illustrates a typical set of response curves for different concentrations of the tracer, triiodide. The ordinate has been converted to concentration units (rather than measured current) to facilitate comparison of experimental and theoretical results. Such data were used to evaluate the time-interval, peak-height and peak-area data-processing methods. We begin with the time-interval method because of the controversy that has been associated with this method [7–9,11,12].

Time-interval approach

Most applications of this approach have assumed a linear relationship between the measured time interval and the logarithm of analyte concentration [7,10,11,16]. In fact, it was stated recently [11] that the linear relationship between Δt and ln C can be proven mathematically without any approximations. In a more recent study [12], a rigorous mathematical treatment was used to suggest that the relationship between Δt and ln C is inherently non-linear and that linear relationships should be expected only for special sets of circumstances. It was also suggested that there are different alternatives for using the time-interval approach that depend upon the positions of reference points on the transient responses between which time intervals are measured. These suggestions were evaluated experimentally in this study.

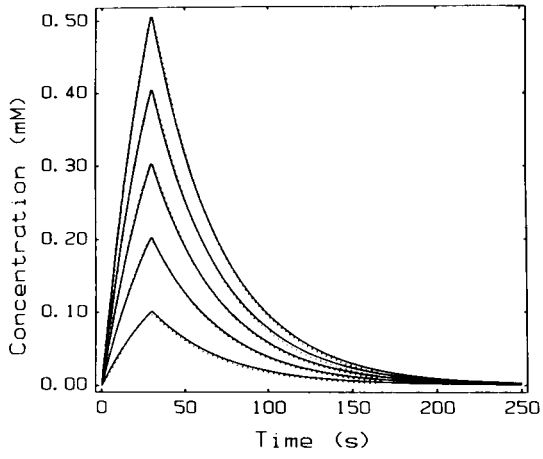

Fig. 1. Response curves for different concentrations of triiodide. (·····) Experimental, (———) theoretical; $V_s = 0.5$ ml, $V_g = 0.7017$ ml, $f = 0.0167$ ml s^{-1}, C_{as}^{o} (bottom to top) = 0.2, 0.4, 0.6, 0.8, and 1.0 mmol l^{-1}.

To avoid problems that could result from slow chemical reactions, we chose to use a tracer (I_3^- with amperometric detection [17]) to test the different approaches. Conclusions reached are applicable directly to situations in which products of fast chemical reactions are monitored because the leading and trailing edges of such responses mimic the leading and trailing edges of responses for a tracer (Eqns. A1 vs. A15 and A3 vs. A24 in [12]).

This study was limited to just three measurement options which are judged sufficient to evaluate the validity of the suggestions made earlier [12]. The three options involved: (a) the same reference points on the leading and trailing edges of the peaks; (b) different reference points on the

leading and trailing edges of the peaks; and (c) different reference points on the leading edges of the peaks. In addition to evaluating the Δt vs. ln C relationships, we also evaluate alternative modes of utilizing the data.

Leading / trailing edges, equal reference points. The simplified relationship (Eqn. 8b in [12]) between the measured time interval and analyte concentration is

$$\Delta t = (V_g/f)\ \ln\left\{\left[(C_{as}^{o} - C_{ag}^{rp})/C_{ag}^{rp}\right] \times \left[\exp(V_s/V_g) - 1\right]\right\} \quad (8a)$$

where Δt is the time interval, V_g is the volume of the mixing chamber, f is the flow rate, C_{as}^{o} is analyte concentration in the sample, C_{ag}^{rp} is the analyte concentration in the gradient chamber at the reference points (rpn) between which the time intervals are measured, and V_s is sample volume. It is clear from inspection of this relationship that Δt should vary linearly with ln C_{as}^{o} only when the reference-point concentration is much less than analyte concentration in the original sample (i.e. $C_{ag}^{rp} \ll C_{as}^{o}$). It is also clear that the relationship should become more non-linear as the reference-point concentration becomes larger relative to initial analyte concentration.

Figure 2 shows plots of experimental values of Δt vs. ln C_{as}^{o} for five different reference-point concentrations as well as predicted responses based on Eqn. 8a and the conditions in the legend of Fig. 1. Predicted responses agree well with experimental results. Also, as expected, the plots become more non-linear as the reference-point concentrations are increased from 0.035 mmol l^{-1} to 0.2 mmol l^{-1}.

Results are presented in this format to address directly issues related to the relationship between Δt and ln C_{as}^{o} [11,12]. However, for practical applications of this approach to the determination of analyte concentration, other presentation formats are more useful. For example, Eqn. 8a can be arranged into the form

$$\exp\left[(f/V_g)\Delta t\right] = \left\{\left[\exp(V_s/V_g) - 1\right]/C_{ag}^{rp}\right\}C_{as}^{o} + \left[1 - \exp(V_s/V_g)\right] \quad (8b)$$

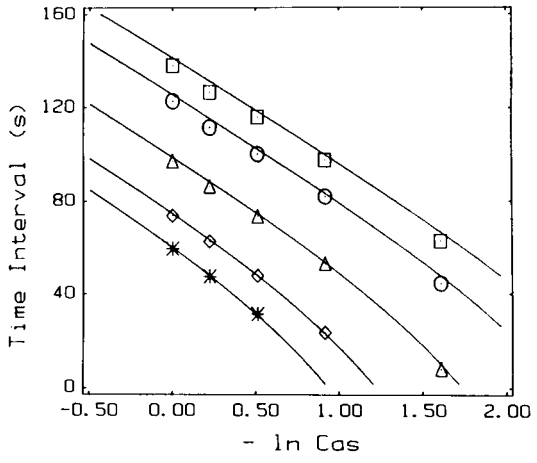

Fig. 2. Calibration results for time-interval method with equal reference points on leading and trailing edges. Conditions as in Fig. 1 except: (*,◇,△,○,□) experimental; (———) theoretical; reference points (mmol l): (*) 0.2; (◇) 0.15; (△) 0.09; (○) 0.05; (□) 0.035.

This equation suggests a linear relationship between the exponential, $\exp[(f/V_g)\Delta t]$, and analyte concentration which should be more useful for quantitative purposes.

Figure 3 includes plots of experimental and theoretical results for one set of conditions. The experimental results confirm the linear relationship between the exponential function and concentration predicted by Eqn. 8b. Also, there is reasonable agreement between experimental and theoretical results. Although the agreement in

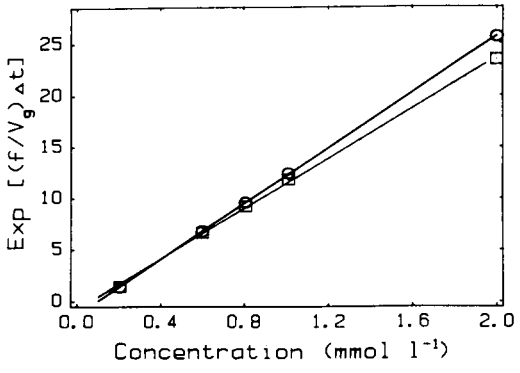

Fig. 3. Linearized calibration plots for time-interval option. Conditions: $V_s = 0.60$ ml, $V_g = 0.7017$ ml, $f = 0.0333$ ml s^{-1}, $C^{rp1} = C^{rp2} = 0.10$ mmol l^{-1}. (□) Experimental; (○) theoretical.

Fig. 3 does not appear to be as good as that in Fig. 2, the logarithmic scale in Fig. 2 (and elsewhere) tends to compress differences.

Least-squares statistics for the two plots are summarized in the first two rows of Table 1. The experimental slope is about 9% lower than the theoretical slope based on Eqn. 8b and values of parameters (f, V_g, V_s, C^o_{as} and C^{rp}_{ag}) used in the study. This difference is somewhat larger than had been expected but is not unreasonable. The exponential function "amplifies" small errors in Δt or the controlled parameters such that agreement does not appear to be as good as that for logarithmic plots such as those in Fig. 2.

Leading / trailing edges, different reference points. The equation for the expected relationship between the time interval and analyte concentration when Δt is measured between different reference points, $t^{rp1} \neq t^{rp2}$, on the leading and trailing edges of the peak is

$$\Delta t = (V_g/f)\ln\left\{\left[\left(C^o_{as} - C^{rp1}_{ag}\right)/C^{rp2}_{ag}\right] \times\left[\exp(V_s/V_g) - 1\right]\right\} \quad (9a)$$

where C^{rp1}_{ag} and C^{rp2}_{ag} are the reference-point concentrations on the leading and trailing edges.

Results in Fig. 4 compare experimental results and theoretical expections for four different sets of reference points. Again, there is good agreement between experiment and theory. As expected by examination of Eqn. 9a, best linearity

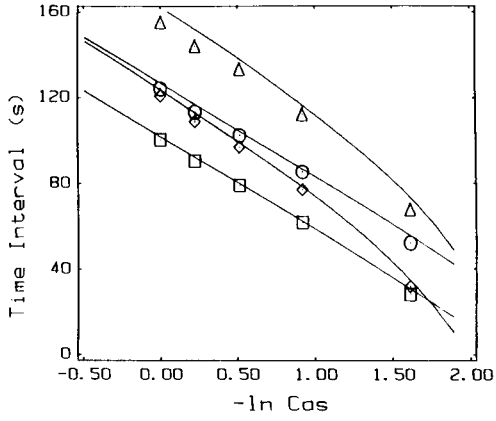

Fig. 4. Calibration results for time-interval method with different reference points on leading and trailing edges. Conditions as in Fig. 1 except: (□,◇,○,△) experimental; (———) theoretical; reference points (mmol l^{-1}) (C^{rp1}/C^{rp2}): (○) 0.02/0.05; (□), 0.02/0.09; (◇), 0.09/0.05; (△) 0.09/0.02.

between Δt and ln C is obtained for smallest values of the reference-point concentration on the leading edge when $C^{rp1}_{ag} \ll C^o_{as}$.

Equation 9a is easily rearranged into the form

$$\exp\left[(f/V_g)\Delta t\right] = \left\{\left[\exp(V_s/V_g) - 1\right]/C^{rp2}_{ag}\right\} C^o_{as} + \left\{\left[1 - \exp(V_s/V_g)\right]C^{rp2}_{ag}/C^{rp1}_{ag}\right\} \quad (9b)$$

A plot of $\exp[(f/V_g)\Delta t]$ vs. concentration is similar to that in Fig. 3. Least-squares statistics for the plots are presented in the third and fourth

TABLE 1

Results for linearized calibration equations for the time-interval method [a]

	Slope (S.D.)	Intercept (S.D.)	Standard error	Correlation coefficient
Leading / trailing edges; equal reference points [b]				
Experimental	12.2 (0.19)	−0.76 (0.21)	0.25	0.9996
Theory	13.5 (0.05)	−1.3 (0.05)	0.07	0.9999
Leading / trailing edges; different reference points [c]				
Experimental [e]	12.2 (0.16)	−0.15 (0.17)	0.21	0.9997
Theory	13.4 (0.03)	−0.62 (0.04)	0.04	0.9999
Leading edge; different reference points [d]				
Experimental	16.8 (0.88)	1.01 (0.97)	1.19	0.996
Theory	19.9 (0.07)	−0.92 (0.08)	0.09	0.9999

[a] Conditions: $V_s = 0.6$ ml, $V_g = 0.7071$ ml; $f = 0.0333$ ml s^{-1}. Reference points (mmol l^{-1}): [b] $C^{rp1} = C^{rp2} = 0.1$; [c,d] $C^{rp1} = 0.05$; $C^{rp2} = 0.10$; [e] Slope = 19.7, intercept = 0.70, $r = 0.999$ when result for highest concentration ($\Delta t = 0.63$ s) is deleted.

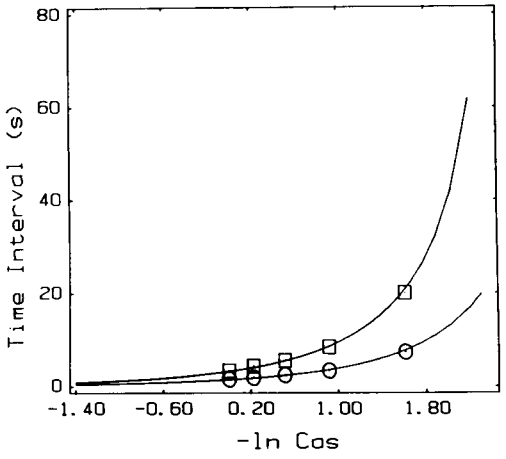

Fig. 5. Calibration results for time-interval method with different reference points on leading edge. Conditions as in Fig. 1 except: (○,□) experimental; (———) theoretical; reference points (mmol l^{-1})(C^{rp1})/C^{rp2}): (○) 0.02/0.09; (□) 0.02/0.05.

rows of data in Table 1. As with the previous example, the experimental slope is about 9% low relative to the expected value.

Reference points on leading edge. Equation 10a represents the relationship between the time interval and analyte concentration when both reference points are on the leading edge of the peak.

$$\Delta t = (V_g/f)\ \ln\left[\left(C^{o}_{as} - C^{rp1}_{ag}\right)/\left(C^{o}_{as} - C^{rp2}_{ag}\right)\right] \qquad (10a)$$

Experimental and predicted results for two sets of reference points are shown in Fig. 5. Agreement is quite good, confirming the validity of the approach and the relationship describing it.

To obtain a relationship that is linear in concentration, Eqn. 10a is rearranged into the form

$$\left\{1 - \exp\left[-(f/V_g)\Delta t\right]\right\}^{-1} = \left(1/\Delta C^{rp}_{ag}\right)C^{o}_{as} - \left(C^{rp1}_{ag}/\Delta C^{rp}_{ag}\right) \qquad (10b)$$

where ΔC^{rp}_{ag} is the difference between the reference points ($\Delta C^{rp}_{ag} = C^{rp2}_{ag} - C^{rp1}_{ag}$). Although this is not a particularly convenient relationship for hand calculations, it presents no problem for computer processing and helps to demonstrate the generality of the concepts involved. Plots of $\{1 - \exp[-(f/V_g)\Delta t\}^{-1}$ vs. concentration were linear with scatter similar to that in Fig. 3. Linear least-squares statistics for this option are given in the last two rows of Table 1. Although the difference between the two slopes (15%) is larger than that for the other two data sets, it should be noted that the measured time interval for that largest concentration is very short (0.63 s) and differs by only 0.08 s from the expected value (0.55 s). When this one point is dropped, the slope is 19.72 which differs by only 1.5% from the expected value. This approach would be most useful for systems with much larger time constants.

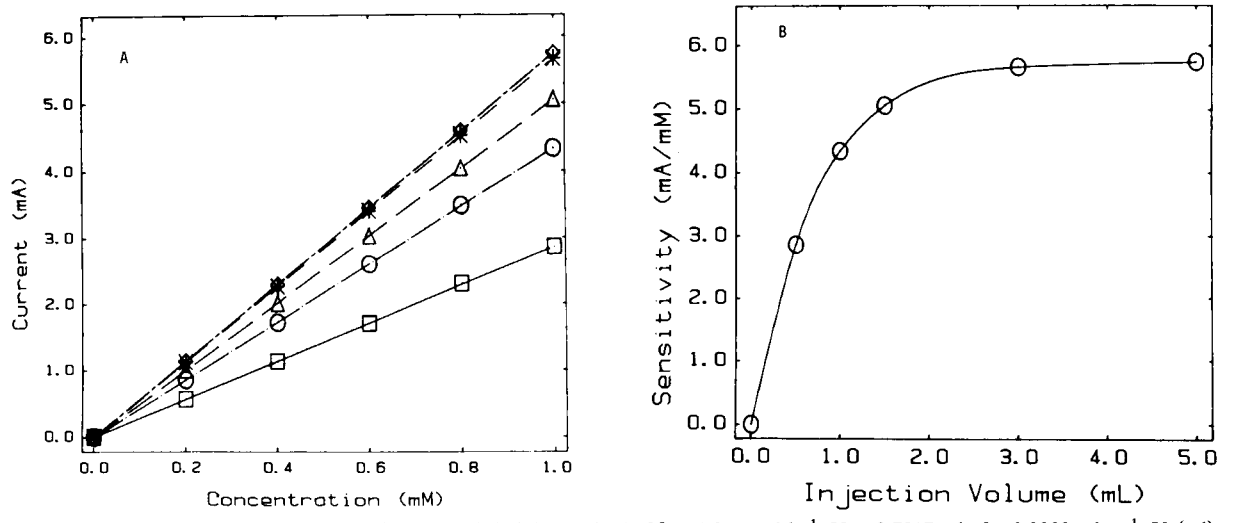

Fig. 6. Effects of sample volume on results for peak-height method. C^{o}_{as} = 1.0 mmol l^{-1}, V_g = 0.7017 ml, f = 0.0333 ml s^{-1}, V_s (ml): (□) 0.5; (○) 1.0; (△) 1.5; (*) 3.0; (◇) 5.0. (A) Measured current vs. concentration. (B) Sensitivity vs. sample volume.

These results confirm the validity of the mathematical treatments described earlier [8,9,12,14, 17] and the viability of the alternative time-interval approaches suggested earlier [12]. However, there is no reason to limit the utility of this sample-processing approach to time-interval methods and two alternative approaches, peak-height and peak-area methods, are discussed in the following sections.

Peak-height method

Peak heights for data such as those in Fig. 1 were measured and related to concentration. As long as measured currents remained in the linear range of the detector, peak current varied linearly with concentration for a wide range of sample volumes (see Fig. 6A) and flow-rates and three different volumes of the mixing chamber.

Peak currents were converted to concentration by using the calibration data for the detector and these peak concentrations varied linearly with sample concentration as expected (Eqn. A2 in [12]). Results for a typical data set ($V_s = 0.60$ ml, $V_g = 0.7017$ ml, $f = 0.0333$ ml s^{-1} and $C^o_{as} = 0.2$, 0.6, 0.8, 1.0 and 2.0 mmol l^{-1}) yielded the following least-squares statistics

$$C^p_{as} = (0.575 \pm 0.0035)C^o_{as} + (0.0012 \pm 0.0035)\ \text{mmol}\ l^{-1}$$

with $r^2 = 0.99985$ and standard error of the estimate, $s_{yx} = 0.0056$ mmol l^{-1}. The theoretical value of the slope, $1 - \exp(-V_s/V_g)$, is 0.5747, showing excellent agreement between theory and experiment.

Peak areas

As expected, peak areas varied linearly with analyte concentration. Plots of peak area vs. analyte concentration were similar to those in Fig. 6A except that ordinate values varied between 0 and 800 mA s. A linear least-squares fit of area vs. concentration (conditions as described above for peak-height results) yielded

$$A(\text{mA s}) = 99.4 \pm 0.75C^o_{as}\ (\text{mmol}\ l^{-1}) - (0.3 \pm 0.5)\text{mA s}$$

with $s_{yx} = 0.62$ mA s and $r^2 = 0.9998$.

Based upon equations developed earlier [8,9], Tyson [16] has shown that the peak area [concentration and time (Ct) units] is given by

$$\text{Area(Ct)} = (V_s/f)C^o_{as} \quad (11a)$$

where C^o_{as} is the initial analyte concentration, V_s is sample volume and f is the flow-rate. To express the area in terms of measured current, a sensitivity (slope) factor, b, must be used as follows

$$\text{Area(mA s)} = b(V_s/f)C^o_{as} \quad (11b)$$

where b is the sensitivity of the detector (mA mmol^{-1} l) for changes in analyte concentration. It follows that a plot of area(mA s) vs. initial

TABLE 2

Relative error coefficients for sample volume, flow-rate and volume of mixing chamber

Sample volume [a]	Peak height		Peak area		Time interval
	Experimental (S.D.)	Theory	Experimental (S.D.)	Theory	Experimental (S.D.)
	Sample volume [a] (% μl^{-1})				
Small	0.22 (0.007)	0.220	0.30 (0.015)	0.29	0.46 (0.02)
Large	0.05 (0.00)	0.045	0.10 (0.002)	0.10	0.21 (0.01)
	Flow-rate [a] (% μl^{-1} s)				
Small	1.45 (0.016)	0.000	−7.47 (0.01)	−4.0	98 (3.5)
Large	0.05 (0.022)	0.000	−4.46 (0.04)	−4.0	75 (54)
	Volume of mixing chamber [b] (% μl^{-1})				
Small	0.10 (0.005)	0.11	0.017 (0.007)	0.00	0.66

[a] $C^o_{as} = 1.0$ mmol l^{-1}, $f = 0.0333$, 0.0250, 0.167 ml s^{-1}, $V_g = 0.7017$ ml, V_s (small) = 0.33, 0.34, 0.35, 0.36, 0.37 ml, V_s (large) = 0.5, 1.0, 1.5 ml, n = 3. [b] $C^o_{as} = 1.0$ mmol l^{-1}, $f = 0.0333$ ml s^{-1}, $V_g = 0.617$, 0.719, 0.931 ml, $V_s = 0.33$, 0.35, 0.37 ml, n = 3.

analyte concentration should have a slope equal to bV_s/f. For the least-squares results given above, $b = 5.56$ mA mmol^{-1} l, V_s is 0.6 ml and $f = 0.0333$ ml s^{-1}. Accordingly, the expected slope is (5.56 mA mmol^{-1} l) × (0.6 ml)/(0.0333 ml s^{-1}) = 100.2 mA s mmol^{-1} l. The experimental value of 99.4 mA s mmol^{-1} l is in excellent agreement with this expected value.

Error coefficients

The error coefficients described above represent an effective way to compare effects of different parameters on results obtained for different measurement/data-processing options. Experimental values of relative error coefficients for sample volume, flow-rate and chamber volume are summarized in Table 2 for each of the three options evaluated in this study. Experimental values were obtained by using Eqn. 7 for the peak-height and peak-area options and Eqn. 4 for the time-interval option. Equation 7 was implemented by computing least-squares slopes of peak current (see Fig. 6B) or area vs. each variable at the values of interest. Equation 4 was implemented by computing apparent concentration values based on experimental values of the different parameters, evaluating least-squares slopes, dC/dV, of concentration vs. each variable, and using those in Eqn. 4. Theoretical values are also included for the peak-height and peak-area methods; these theoretical values are based on equations in Table 3.

TABLE 3

Expressions for relative error coefficients [a] for peak-height and peak-area methods

	REC	Ref.
Peak-height option		
Sample volume	$\{V_g[\exp(V_s/V_g)-1)]\}^{-1}$	12
Chamber volume	$V_s\{V_g^2[\exp(V_s/V_g)-1]\}^{-1}$	13
Peak-area option		
Sample volume	V_s^{-1}	14
Flow-rate	$-f^{-1}$	15

[a] Expressions must be multiplied by appropriate factors (e.g. 100 for percent and 10^{-3} ml μl^{-1}) to obtain desired units.

Equation 7 was used as a starting point for the theoretical equations in Table 3. Development of two example equations is illustrated here. For the peak-height method, we have $S \propto [1 - \exp(V_s/V_g)]C_{as}^o$ (Eqn. A2 in [12]). To evaluate the effect of sample volume, one obtains $dS/dV_s \propto (1/V_g)[\exp(V_s/V_g)]$ and substituting this along with the expression for S into Eqn. 7 assuming that $I \approx 0$ and simplifying, we obtain Eqn. 12 in Table 3.

As noted above (Eqn. 11b), peak area is proportional to the volume of sample used and initial analyte concentration and inversely proportional to flow-rate $[S_A \propto (V_s/f)C_{as}^o)$. It follows that $dS_A/df \propto -(V_s/f^2)C_{as}^o$; substituting this along with S_A into Eqn. 7, assuming that $I \approx 0$ and simplifying, we obtain Eqn. 15 in Table 3, which represents the expected effect of flow rate on relative errors for concentrations obtained from peak areas. Other equations in Table 3 were obtained by similar procedures. We have not yet developed analogous equations for time-interval approaches.

There is excellent agreement between experimental and theoretical results for effects of sample volume and chamber volume. The largest discrepancies occur for effects of flow rate when small sample volumes are used. We are unable to explain these discrepancies.

Changes in sample volume have similar effects on error coefficients for peak-height, peak-area and time-interval methods wereas changes in flow-rate have the largest effects on peak-area and time-interval methods. Changes in the volume of the mixing chamber have the largest effects on the peak-height and time-interval methods.

Discussion

Results presented here confirm predictions made earlier [12] that several different approaches can be used to collect and process data from flow-based sample-processing systems with a well-stirred mixing chamber. Options include several variants of the time-interval method as well as peak-height and peak-area options. The study also illustrates alternative and potentially more useful ways of using time-interval methods

and introduces experimental and theoretical approaches to the concept of error coefficients that are useful in comparing different options. Although applied here to a flow system, these concepts are applicable to virtually any type of analytical system.

Results in this paper are also relevant to controversial issues related to the time-interval option. In discussing our earlier studies [8,9], Tyson [11] stated "Pardue and Fields ··· make unnecessary approximations in deriving their final peak-width equations ···". Discussing a proposed equation for the relationship between the measured time interval and analyte concentration (Eqn. 9 in [11]), it was stated further that "Thus, without any approximations, Δt_{eq} is a linear function of ln C_m^s" where C_m^s is the analyte concentration (C_{as}^o in the papers criticized). When the symbols in that equation are changed to correspond to those in the original papers [8,9] it is easily shown that the equation is in fact identical to Eqn. 7a in our original paper [8] if the reference-point analyte concentration, $[A]_g^{ep}$, is set equal to zero. As noted earlier [12], this condition (reference-point concentration equal to zero) is the only circumstance for which the cited equation (Eqn. 9 in [11]) is strictly correct. Accordingly, this is a hidden assumption in the derivation of the equation cited above. Thus, we had already developed essentially the same equation in our original study [8] without using any approximations. However, we were not satisfied with an equation that was valid only for a very restrictive set of conditions but rather wanted equations that would be valid for a wide variety of conditions. Some arithmetic errors not-withstanding, we accomplished that goal. We introduced approximations only to emphasize conditions that must be met for the semilogarithmic relationship described initially [7] to be valid.

Results obtained in the present study validate the kinetic model on which the equations were based, the mathematical approach in the original study [8,9] and the more general equations developed in subsequent studies [12,14,17]. Moreover, contrary to conclusions upon which criticisms of our studies were based [11], results in Figs. 2, 4 and 5 show that there are many more situations for which the measured time interval varies nonlinearly with the logarithm of analyte concentration than situations for which the relationship is linear. The rigorous mathematical treatment of this system as well as careful experimental studies show that without any question, a linear relationship between the measured time interval and the logarithm of concentration will be strictly valid only for very specific sets of circumstances. More importantly, the linear relationship will be valid only for certain concentration ranges for any given set of experimental conditions and suggestions to the contrary are misleading.

Finally, the error coefficients described herein can be used to identify what variables should be controlled most closely and what degree of control is required to achieve a given level of reliability by any of the different approaches. They can also be used to compare what levels of reliability can be expected by the different methods for given degrees of control of different variables.

This work was supported by Grant No. GM-13326-24 from the National Institutes of Health.

REFERENCES

1 K.E. Hallikainen and D.J. Pompeo, Instruments, 25 (1952) 335.
2 W.J. Blaedel and R.H. Laessig, Anal. Chem., 36 (1964) 1617.
3 W.J. Blaedel and G.P. Hicks, Anal. Chem., 34 (1962) 388.
4 G. Nagy, Zs. Feher, K. Toth and E. Pungor, Anal. Chim. Acta, 100 (1978) 181.
5 H.A. Mottola, CRC Crit. Rev. Anal. Chem., 4 (1975) 229.
6 D. Sanderson, J.A. Bittikofer and H.L. Pardue, Anal. Chem., 44 (1972) 1934.
7 J. Ruzicka, E.H. Hansen and H. Mosbaek, Anal. Chim. Acta, 92 (1977) 235.
8 H.L. Pardue and B. Fields, Anal. Chim. Acta, 124 (1981) 65.
9 H.L. Pardue and B. Fields, Anal. Chim. Acta, 124 (1981) 39.
10 K.K. Stewart, Anal. Chem., 55 (1983) 931A.
11 J.F. Tyson, Anal. Chim. Acta, 179 (1986) 131.
12 H.L. Pardue and J.M. Jordan, Anal. Chim. Acta, 220 (1989) 23.
13 J.M. Jordan and H.L. Pardue, Anal. Chim. Acta, 270 (1992) 195.

14 H.L. Pardue and P. Jager, Anal. Chim. Acta, 179 (1986) 169.
15 J.M. Jordan, Theoretical Treatment of Gradient Chamber and Single-Bead String Reactor Flow-Injection Systems with Emphasis on Evaluation of an Error-Compensating Method for Data Analysis, Ph.D. Thesis, Purdue University, West Lafayette, IN, 1991.
16 J.F. Tyson, Anal. Chim. Acta, 214 (1988) 57.
17 P. Jager and H.L. Pardue, Anal. Chim. Acta, 187 (1986) 343.

Analytica Chimica Acta, 272 (1993) 125–134
Elsevier Science Publishers B.V., Amsterdam

Evaluation of a predictive curve-fitting method for processing data from flow systems

Part 1. Flow system with a mixing chamber

James M. Jordan [1], Michael D. Love and Harry L. Pardue
Department of Chemistry, Purdue University, West Lafayette, IN 47907–1393 (USA)

(Received 15th July 1992; revised manuscript received 24th September 1992)

Abstract

This paper describes the evaluation of a curve-fitting predictive approach to processing data from a flow system with a well-stirred mixing chamber. The method utilizes data from the leading edges of response peaks to predict the response that would be measured if sufficient sample were used to give a steady-state response. Advantages of the method under optimal conditions include a 10-fold reduction of dependency on sample volume relative to a peak-height method, a 20- to 65-fold reduction of dependency on flow-rate relative to a peak-area method, and extended linear ranges in situations involving nonideal detector response and situations involving slow reaction kinetics. Limitations include a requirement for larger sample volumes and degraded error coefficients for flow-rate relative to a peak-height method and chamber volume relative to a peak-area method. The new approach is judged to offer complementary features relative to peak-height and peak-area methods.

Keywords: Flow system; Curve fitting; Data processing

Quantitative methods based on transient responses tend to be less rugged than their equilibrium counterparts because transient responses usually depend more on experimental variables than equilibrium conditions. Accordingly, it has been suggested that kinetic-based methods should not be used if equilibrium-based methods are available [1].

Unfortunately, there are many situations in which other criteria strongly favor the use of transient responses. In such situations, the approach usually used to compensate for the larger dependency on experimental variables is to control those variables within very tight tolerances. This can be both difficult and expensive for unskilled personnel working with nonideal samples in poorly controlled environments. For example, whereas it is quite easy for skilled personnel in controlled laboratory environments to control variables such as sample volume, flow-rate and sample matrices within narrow tolerances, it may not be so easy for unskilled personnel processing large numbers of nonideal samples in poorly controlled environments to do so. A better solution would be to develop and use measurement and data-processing methods that are less dependent on experimental variables.

Several such methods have been developed [2–5]. By using such methods with chemical kinetic processes, it has been possible to reduce

Correspondence to: H.L. Pardue, Department of Chemistry, 1393 Brown Building, Purdue University, West Lafayette, IN 47907-1393 (USA).
[1] Present address: The Procter & Gamble Company, International Technology Coordination, Laundry & Cleaning Products, 6060 Center Hill Road, Cincinnati, OH 45224 (USA).

effects of experimental variables by factors of 10- to 100-fold. Although the same principles should apply to transient responses from physical and physico-chemical systems, there have been few analogous studies of such systems. This study was undertaken to evaluate the hypothesis that the same types of error-compensating methods that have been developed for chemical kinetic processes can be used to improve the ruggedness of methods based on transient responses of physical and physico-chemical processes.

As an initial test of this hypothesis we chose a flow system with a well-stirred mixing chamber [6,7]. This system was chosen for the initial study because the transient response is reasonably well understood [8] making it possible to compare experimental findings with theoretical expectations. The data-processing approach evaluated is one we call a *predictive-kinetic method* [9]. In this approach, data collected early in the transient response are used to predict the signal that would be measured if the response were monitored to steady state [10,11]. Frequently the predicted steady-state responses depend much less on experimental variables than the transient data from which they were predicted. Consequently, these predictive methods are frequently more rugged than methods based strictly on transient responses.

The predictive method was implemented by fitting a first-order model [8] to data from the leading edges of peak-shaped responses for both a tracer and a chemical reaction with complex stoichiometry and nonideal kinetic behavior. Results obtained with the predictive method are compared with results obtained with peak-height and peak-area methods.

EXPERIMENTAL

Reagents and instrumentation

Reagents and instrumentation were as described previously [12,13]. For tracer studies, the reagent and sample streams contained 0.15 mol l^{-1} potassium iodide and 0.142 mol l^{-1} phosphate buffer (pH 6.0) and the sample stream also contained variable concentrations of triiodide as the analyte (tracer). For studies involving a chemical reaction (iodate + iodide + hydrochloric acid), the reagent stream contained 0.15 mol l^{-1} each of potassium iodide and potassium iodate in deoxgenated water and the sample stream contained 0.15 mol l^{-1} potassium iodide and variable concentrations of hydrochloric acid as the analyte. Samples were introduced by the time-controlled method [12,13] and triiodide (both as a tracer and as the product of the reaction among iodide, iodate and hydrochloric acid) was detected amperometrically by platinum electrodes in a thin-layer flow cell. Data were acquired on-line with custom-built circuitry interfaced to a microcomputer. Data were transferred to a supermicrocomputer for long-term storage, processing and display.

Data processing

Peak heights were measured in the usual way. Data from the leading edges of response peaks were used to predict signals expected if sufficient sample were used to give steady-state responses. The equation for the leading edge [8,12,13] is

$$I_t = I_{ss}\{1 - \exp[(-f/V_g)t]\} + I_o \qquad (1)$$

where I_t, I_{ss}, and I_o are currents at time t, steady state and zero time, respectively, and f and V_g are flow-rate and chamber volume, respectively. The steady-state current, I_{ss} is computed and related to analyte concentration. Several approaches used to predict the steady-state current are discussed briefly below. The same data range was used for all sample volumes and was selected empirically to provide accurate values of steady-state responses for the smallest volume selected. It was selected to represent about 85% of the leading edge of the smallest peak processed.

Iterative option. Details of the nonlinear curve-fitting process have been described elsewhere [10,11]. The only change is to replace absorbance in the initial equations with the time-dependent current measured in this study. As in previous studies, the Marquardt algorithm [14] was used and the iterative process was continued until the change in the χ^2 statistic between successive approximations was less than 0.01%.

Direct computation. If the "fixed" parameters, f, V_g and I_o, in Eqn. 1 are known, then it is possible to compute steady-state current directly from one or more values of I_t. Use of multiple values of I_t provides the effect of signal averaging but use of fixed values of f, V_g and I_o obviously removes the possibility of compensating for changes in these variables. To permit the use of this direct-computation option and still have the possibility of compensating for changes in f and V_g, we used the Guggenheim [15] and Kezdy-Swinbourne [16] methods to quantify apparent values of f/V_g (effectively a first-order rate constant) for each set of time-dependent responses. These experimentally determined values of f/V_g were then used in the direct-computation mode (Eqn. 1).

Modified nonlinear regression. The convergence time for the nonlinear regression program is dependent on the initial estimates provided; the better the initial estimates, the shorter the convergence time. The nonlinear regression program was modified so that results of the direct-computation method could be used as initial estimates of the steady-state signal.

RESULTS AND DISCUSSION

All uncertainties are reported at the level of one standard deviation unit (±S.D.). Relative error coefficients [REC(%)] are used to compare effects of experimental variables on different data-processing approaches. As described earlier, the relative error coefficient is the percent error in concentration caused by a given change in the variable of interest [12]. Unless stated otherwise all fits to experimental data are made with the unmodified nonlinear regression method.

Response curves

Figure 1A represents a set of experimental response curves for four different volumes of a fixed concentration of triiodide used as a tracer in the flow system. The three smaller peaks represent sample volumes (V_s = 1.0 and 1.5 ml) too small to give steady-state responses whereas the largest peak represents a sample volume large enough to give a well-defined steady-state response. Figure 1B shows the same response curves with a predicted response (solid curve) obtained by fitting Eqn. 1 to the leading edge of the smallest peak. The predicted curve is not only superimposed upon large fractions of the leading edges of all the peaks but also is nearly superimposed upon the steady-state response of the largest volume. Thus, by using the leading edges of such peaks for small volumes it is possible to predict the signal expected if sufficient sample were used to give a steady-state response.

Because the leading edges of experimental and fitted responses in Fig. 1B are so completely

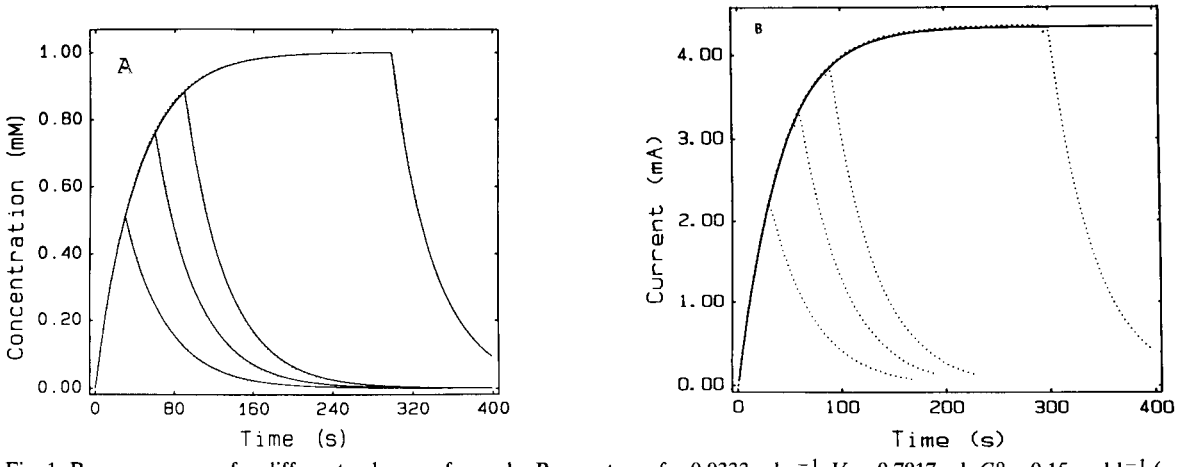

Fig. 1. Response curves for different volumes of sample. Parameters: f = 0.0333 ml s^{-1}, V_g = 0.7017 ml, C_I^o = 0.15 mol l^{-1} (carrier and sample streams), C_{as}^o = 1.0 mmol l^{-1}, V_s (ml, bottom to top) = 0.5, 1.0, 1.5 and 5.0, polarizing voltage = 200 mV. (A) Experimental data. (B) Experimental data (· · · · · ·) with fit (———) to the leading edge of smallest peak.

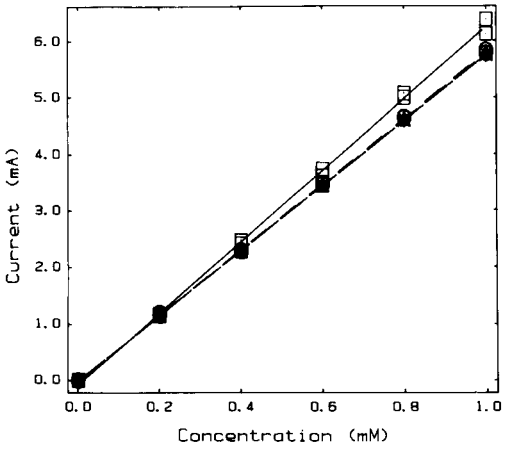

Fig. 2. Calibration plots for predictive method with different injection volumes. Conditions as in Fig. 1 except: V_s (ml) = 0.5 (□), 1.0 (○), 1.5 (△), 3.0 (*) and 5.0 (◇).

superimposed, it could appear that all data contain the same information. This could lead one to conclude that the response at any time could be used to compute the steady-state response and to wonder about the advantage of the predictive method. For example, if one knew the true values of the flow parameters, then one could use these parameters and the current at any time along the leading edge to compute the steady-state response. However, if the flow parameters were to change without one knowing it, then this approach would give incorrect values of the steady-state response whereas the curve-fitting method is expected to give the correct values. This is the principal hypothesis to be tested in this study.

Calibration plots

Figure 2 represents plots of predicted values of steady-state current vs. triiodide concentration for five different volumes of six different concentrations (including zero). The most important observations from these results are that all plots are linear and plots for all but the smallest volume (V_s = 0.5 ml) are virtually superimposed upon one another. The predictive method virtually nullifies the effects of rather large differences in sample volume for all but the smallest volume for which there is insufficient information in the leading edge of the peak to permit accurate prediction of the steady-state response.

As expected, analogous plots for peak heights vs. concentration were linear but sensitivities (slopes) increased with increased sizes of sample volume.

Accuracy / precision

To evaluate the potential accuracy of the peak-height and predictive options, data were obtained for six samples containing triiodide concentrations between 0 and 2 mmol l^{-1} with all other conditions being the same (V_s = 1.00 ml, f = 0.0333 ml s^{-1} and V_g = 0.7017 ml). Calibration data (I vs. C) obtained independently were used to compute peak concentrations and steady-state concentrations from measured values of peak height and predicted values of steady-state current. Linear-least-squares statistics were then obtained for computed values of peak and steady-state concentrations vs. prepared concentrations.

For the peak-height results, the least-squares equation for computed peak concentration (y) vs. prepared concentration (x) is

$$y = (0.75 \pm 0.007)x + (7.04 \pm 7) \times 10^{-3} \text{ mmol } l^{-1}$$

with a standard error of the estimate of s_{yx} = 0.011 mmol l^{-1} and correlation coefficent of r = 0.998. The standard error of the estimaye represents very small scatter (11 μmol l^{-1}) about the least-squares lines and the intercept also is quite small relative to the data range. The slope is very close to the expected value (Eqn. A2 in [8]) of 0.760. The data are presented in this form, C^p vs. C° to illustrate the degree of agreement with theory; obviously, the least-squares equation shown could be used as a calibration equation to compute concentrations in unknown samples.

For the predictive method, the least-squares equation for predicted steady-state concentration (y) vs. prepared concentration (x) is

$$y = (1.016 \pm 0.004)x - (4 \pm 4) \times 10^{-3} \text{ mmol } l^{-1}$$

with s_{yx} = 0.0065 mmol l^{-1} and r = 0.99997. The slope is very close to unity as expected, the intercept is close to zero and the standard error of the estimate reflects very little scatter about the least-squares line.

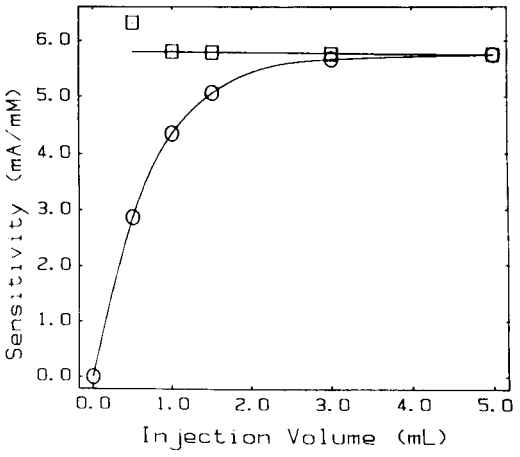

Fig. 3. Effects of sample volume on calibration sensitivity. Conditions as in Fig. 1: peak height (○), predictive method (□).

We conclude that in the absence of interferences both the peak-height and the predictive methods can be used to quantify analyte with high degrees of reliability. The predictive method has the advantage of reduced dependencies on variables.

To evaluate the imprecision of the results, ten runs were made on a solution containing 1.015 mmol l^{-1} triiodide with the same conditions mentioned earlier in this section. Average values and standard deviations were 0.759 ± 0.0052 mmol l^{-1} for the peak concentrations and 1.033 ± 0.030 mmol l^{-1} for steady-state concentrations. These results are consistent with the general observation that peak-heights tend to be more precise than predictive results. Even so, the imprecision of the predictive method is not unreasonably large.

Error compensation

Figure 3 is a plot of sensitivity (slopes of calibration plots) vs. sample volume. It is clear from this plot that the predictive method depends less on sample volume than the peak-height method for all but the largest volume used which was sufficient to give a steady-state response. With the peak-height method, one must control sample volume within narrow tolerances to achieve high degrees of reliability; with the predictive method the dependence on sample volume is sufficiently low that it is not necessary to control this variable within such tight tolerances to achieve the same levels of reliability.

Error coefficients

To quantify variable dependencies such as those illustrated in Fig. 3, we use relative error coefficients (REC). The relative error coefficient is the percent error in concentration produced by a unit change in the variable of interest (e.g., sample volume). In these studies measured currents varied linearly with concentration with very small background currents for both peak-height and predicted values. For such situations, it is easily shown that the error coefficients can be calculated from the equation

$$\mathrm{REC}(\%) = 100(\mathrm{d}I/\mathrm{d}V)/I \qquad (2)$$

where REC is the relative error coefficient, $\mathrm{d}I/\mathrm{d}V$ is the slope of a plot of current vs. the variable of interest and I is the measured current at the concentration value where the relative error is calculated. In this study, I is either peak height, I_p, or steady-state current, I_{ss}. All relative error coefficients reported below are at 1.0 mmol l^{-1} so that absolute error coefficients can be obtained by dividing reported values by 100 and relative error coefficients at any other concentration can be obtained by dividing reported values by that concentration (mmol l^{-1}).

We evaluated error coefficients for sample volume, flow-rate and chamber volume. Effects of sample volume are illustrated in Fig. 1 and relative error coefficients at two levels of sample volume are summarized in Table 1. Because the modified and unmodified iterative options gave virtually identical results except that the modified option required, fewer iterations, results are reported here only for the unmodified option. As expected, the error coefficients for both peak-height and predictive methods are much lower for larger sample volumes which are closer to that required to give a steady-state response. Also, for this situation in which f and V_g did not vary, the direct-computation method based on known (nominal) values of f and V_g gives error coefficients about one order of magnitude below

TABLE 1

Relative error coefficients (% μl^{-1}) [a] for sample volume for tracer studies and various predictive options (Conditions: $[I_3^-] = 1.0$ mmol l^{-1}, $V_g = 0.7017$ ml)

Flow-rate (ml s^{-1})	Iterative	Direct computation		
		Nominal [b]	Guggenheim	Kezdy-Swinborne
Sample volume (0.33–0.37 ml)				
0.0333	0.18	0.010	–	–
0.0250	0.22	0.010	–	–
0.0167	0.14	0.010	–	–
Average [c]	0.18	0.010	–	–
Sample volume (0.5–1.5 ml)				
0.0333	0.0059	0.00036	0.0045	0.0054
0.0250	0.0029	0.00054	0.0011	0.0011
0.0167	0.0071	0.00055	0.0044	0.0048
Average [c]	0.0053	0.00048	0.0034	0.0038

[a] Computed at $V_s = 0.035$ and 1.0 ml for small and large sample volumes, respectively. [b] Based on known values of f and V_g. [c] Based on 3 to 4 significant figures.

TABLE 2

Relative error coefficients (% μl^{-1} s) [a] for flow-rate for tracer studies and various predictive options (Conditions as in Table 1)

Sample volume (ml)	Iterative	Direct computation		
		Nominal	Guggenheim	Kezdy-Swinborne
Small sample volume				
0.330	0.64	3.2	–	–
0.350	0.52	3.2	–	–
0.370	0.11	3.3	–	–
Average [b]	0.40	3.3	–	–
Large sample volume				
0.5	0.25	3.0	0.28	0.29
1.0	0.01	2.2	0.034	0.034
1.5	0.14	1.8	0.22	0.23
Average [b]	0.13	2.3	0.18	0.23

[a] Computed at $f = 0.0250$ ml s^{-1}. [b] Based on 3 to 4 significant figures.

those of the iterative method and the direct-computation method with determined values of f and V_g. These differences probably reflect the uncertainty in the curve-fitting processes.

Effects of flow-rate for a fixed sample volume, V_s, and analyte concentration, C^o_{as}, are illustrated in Fig. 4. Despite the differences in curve shapes, the curve-fitting method predicts the same value

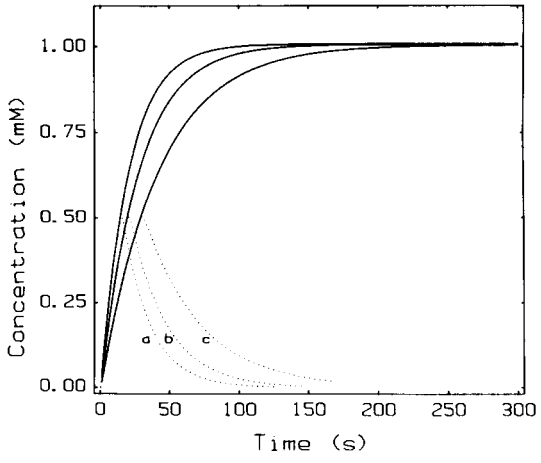

Fig. 4. Response curves at different flow-rates. Conditions as in Fig. 1 except: $V_s = 0.5$ ml, $f = 0.0333$ (a), 0.0250 (b) and 0.0167 ml s^{-1} (c).

of steady-state current for all three data sets. Error coefficients for flow-rate by the different predictive options are summarized in Table 2. The error coefficient for flow-rate is significantly larger than that for sample volume for all data-processing options. The error coefficients for the direct-computation option using nominal volumes of f and V_g are quite large because the computation was done assuming that flow-rate remained constant at 0.0250 ml s^{-1}. By using either the iterative Guggenheim [15] or Kezdy-Swinborne [16] methods to quantify the effective rate constant (f/V_g), the error coefficient was reduced by an order of magnitude relative to the direct-computation method with nominal values of f and V_s.

Error coefficients for chamber volume were determined at three sample volumes; results are summarized in Table 3. On average, the error coefficients for chamber volume are between those for sample volume and flow-rate. As expected, direct-computation methods based on determined values of the apparent rate constant are somewhat better than those based on the nominal value of V_g.

Comparisons with conventional methods

Error coefficients obtained by the predictive methods are compared in Table 4 with results by

TABLE 3

Relative error coefficients (% μl^{-1}) [a] for chamber volume for tracer studies and various predictive options (Conditions: $[I_3^-] = 1.0$ mmol l^{-1}, $f = 0.0333$ ml s^{-1})

Sample volume (ml)	Iterative	Direct computation		
		Nominal	Guggenheim	Kezdy-Swinborne
0.330	0.055	0.10	0.053	0.041
0.350	0.054	0.052	0.041	0.050
0.370	0.028	0.11	0.017	0.052
Average [b]	0.046	0.087	0.037	0.041

[a] At $V_g = 0.719$ ml. [b] Based on 3 to 4 significant figures.

peak-height and peak-area methods [13,17]. Because results based on the use of the Guggenheim and Kezdy-Swinbourne methods for determining the apparent rate constant are very similar, only the former is included in this comparison.

For changes in sample volume, the predictive methods offer only slight improvements over peak-height and peak area at small sample volumes but offer 10- to 20-fold improvements at larger sample volumes.

Regarding flow-rate at small sample volumes, the iterative predictive method offers about 3-fold improvement over the peak-height method and about 20-fold improvement over the peak-area method. At larger sample volumes, the iterative option and the direct-computation option with determined values of the apparent rate constant offer about 60-fold improvement over the peak-area method but are degraded by about 3-fold relative to the peak-height method. This latter result is not surprising because peak height is expected to be independent of flow-rate [8].

Regarding chamber volume, the iterative and direct-computation predictive methods can offer slight (2-fold) improvements relative to the peak-height method but are degraded by a similar amount relative to the peak-area method. Although both the steady-state current and peak area [18] are expected to be independent of the chamber volume, predicted steady-state responses are somewhat less effective than peak areas in compensating for this variable, probably as a result of inaccuracies associated with the predictive process.

Linearity

In all studies reported above, triiodide concentrations were limited to the known linear range of the detector. In a subsequent study conditions were changed such that triiodide concentrations at peak levels would exceed the linear range of the detector. Figure 5 illustrates results obtained by using the iterative predictive option and the peak-height method. The predictive method ex-

TABLE 4

Relative error coefficients for tracer studies and different data-processing options (Conditions except when varied: $[I_3^-] = 1.0$ mmol l^{-1}, $f = 0.0250$ ml s^{-1}, $V_g = 0.7017$ ml, $V_s = 0.350$ ml [a], $V_s = 1.0$ ml [b])

Iterative	Predictive		Peak height	Peak area	Improvement ratio [c]	
	Direct computation				Pk/It	PA/It
	Nominal	Guggenheim				
Sample volume (% μl^{-1})						
0.18 [a]	0.0102	–	0.22	0.30	1.2	1.6
0.0053 [b]	0.0005	0.0034	0.050	0.10	9.4	19
Flow-rate (% μl^{-1} s) [c]						
0.40 [a]	3.3	–	1.4	−7.4	3.5	19
0.13 [b]	2.3	0.18	0.05	−8.6	0.4	66
Chamber volume (% μl^{-1}) [d]						
0.046 [b]	0.087	0.037	0.10	0.017	2.2	0.4

[a] $V_s = 0.33$–0.37 ml. [b] $V_s = 0.5$–1.5 ml. [c] $f = 0.0167$–0.0333 ml s^{-1}. [d] $V_g = 0.617$–0.931 ml. [e] Peak height (Pk) and peak area (PA) vs. iterative method (It).

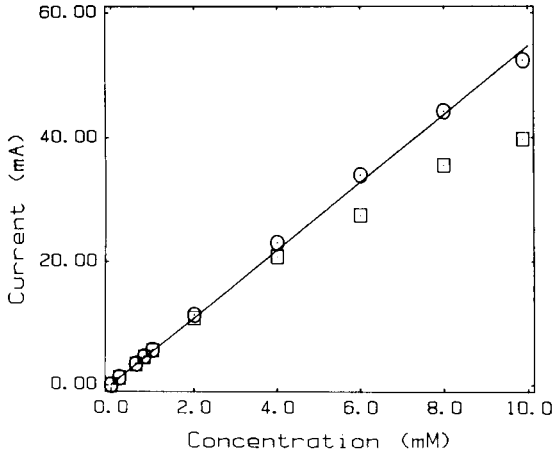

Fig. 5. Comparison of calibration plots for peak-height and predictive options. Conditions as in Fig. 1 except $V_s = 5$ ml and polarizing voltage = 50 mV.

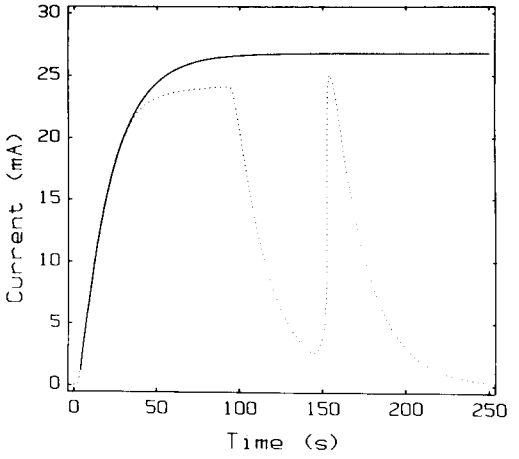

Fig. 6. Experimental and fitted responses for reaction of iodate, iodide and hydrochloric acid. Conditions as in Fig. 1 except: $V_s = 5.0$ ml, iodate (reagent stream) = 150 mmol l^{-1}, hydrochloric acid (sample stream) = 10 mmol l^{-1}. Experimental (·····), fitted (———).

tends the linear range and preserves higher sensitivities at higher concentrations relative to the peak-height method because the former method can be implemented with data low enough on the edge of the peak that they remain in the linear range of the detector.

Kinetic effects

Effects of slow reactions were evaluated by using the reaction among iodide, iodate and acid to produce triiodide. For low acid concentrations, the reagent concentrations remained in excess and the error coefficients for sample volume were consistent with those expected from the studies with triiodide as tracer. However, for larger sample volumes (5.0 ml) and acid concentration (10 mmol l^{-1}), reagent is depleted and the reaction becomes the rate-limiting process. The result is that the amount of product near the peak-height is less than expected.

Figure 6 shows a typical data set for analyte in excess. Although the sample volume is large enough to produce the maximum steady-state response, the maximum signal is less than that expected for a fast reaction. However, by using the predictive method, it is possible to compensate for the slow reaction by extrapolating the data along the leading edge to the expected steady-state value.

The effects on calibration plots are illustrated in Fig. 7. The plot of peak height vs. concentration curves toward the concentration axis at higher concentrations whereas the predicted values of steady-state signals vary linearly with concentration throughout the range examined. Thus, the predictive value can offer extended linearity relative to peak-height methods for situations involving slow reactions.

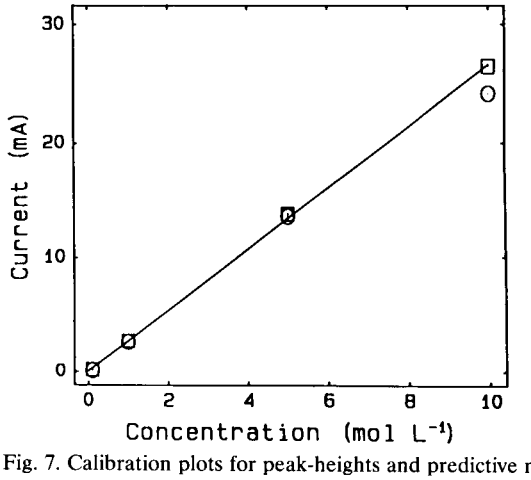

Fig. 7. Calibration plots for peak-heights and predictive methods for slow reactions. Conditions as in Fig. 6: peak-height (○), predictive method (□).

Conclusions

Improvement ratios for error coefficients for selected conditions are summarized in Table 4. The predictive method offers the smaller error coefficients for larger sample volumes. This is expected because data for larger samples require less extrapolation to obtain steady-state responses. For larger sample sizes, the improvement ratios for sample volume are about 10- and 20-fold relative to peak-height and peak-area methods, respectively. Because peak height is expected to be independent of flow-rate for detection of tracers and reaction products [8], the predictive method either offers only modest (3.5-fold) improvement or has a larger error coefficient than peak height. However, the predictive method provided 20- to 70-fold improvements in the error coefficients for flow-rate relative to the peak-area method. For changes in the volume of the primary dispersing element, the predictive method yielded a 2-fold improvement relative to peak height and was 2.5-fold worse than the peak-area method even though both responses are expected to be independent of the volume of the dispersing element. Although it is relatively easy to control most of these variables in well-controlled laboratory environments, it may not be so easy to do so in poorly-controlled environments that exist in manufacturing and field situations. These are the situations in which the low variable dependencies of the predictive method will likely be most useful. However, even in well-controlled laboratory environments, the ability to compensate for slow reaction kinetics and non-ideal nonlinear detector response such as that illustrated for peak heights in Fig. 5 may prove very attractive.

The principal limitation of the predictive method is that it requires somewhat larger ratios of sample volume to chamber volume than either the peak-height or peak-area methods. For any given flow manifold, the latter options probably can be used successfully with smaller sample volumes than the predictive method as described herein. However, there may be other approaches to using the predictive method or other error-compensative approaches [2–5] that will overcome this limitation. In any event, this study has shown that the predictive method is complementary to the more conventional options, offering both advantages and limitations under different circumstances. The method of choice will depend upon those conditions that are most difficult to control under a given set of circumstances.

Future studies will focus on more complex flow systems such as single-bead string-reactors and open tubular columns. The principal problem with these more complex manifolds will be the selection of appropriate mathematical models for the fitting process. Although the responses from these systems are much more complex than that considered in this study, our experience with other types of complex transient responses such as chromatographic responses lead us to expect that we can apply the approach successfully to these more complex flow manifolds.

This research was supported by Grant No. GM-13326-24 from the National Institutes of Health.

REFERENCES

1 H.A. Mottola and H.B. Mark, Jr., Anal. Chem., 58 (1986) 264R.
2 R.C. Harris and E. Hultman, Clin. Chem. (Winston-Salem, NC), 29 (1983) 2079.
3 P.D. Wentzell and S.R. Crouch, Anal. Chem., 58 (1986) 2855.
4 H.L. Pardue, Anal. Chim. Acta, 216 (1989) 69.
5 H.A. Mottola, Kinetic Aspects of Analytical Chemistry, Wiley, New York, 1988.
6 J. Ruzicka, E.H. Hausen and H. Mosbaek, Anal. Chim. Acta, 92 (1977) 235.
7 J.F. Tyson, Anal. Chim. Acta, 179 (1986) 131.
8 H.L. Pardue and J.M. Jordan, Anal. Chim. Acta, 220 (1989) 23.
9 B.L. Bacon and H.L. Pardue, Clin. Chem., 35 (1989) 360.
10 G.E. Mieling and H.L. Pardue, Anal. Chem., 50 (1978) 1611.
11 G.E. Mieling, H.L. Pardue, J.E. Thompson and R.A. Smith, Clin. Chem. (Winston-Salem, NC), 25 (1979) 1581.
12 J.M. Jordan and H.L. Pardue, Anal. Chim. Acta, 270 (1992) 195.
13 J.M. Jordan, Theoretical treatment of gradient chamber and single-bead string reaction flow-injection system with emphasis on evaluation of an error-compensating method

for data analysis, PhD Thesis, Purdue University, West Lafayette, IN, 1991.
14 P.R. Bevington, Data Reduction and Error Analysis for the Physical Sciences, McGraw-Hill, New York, NY, 1969, pp. 235–242.
15 E.A. Guggenheim, Phil. Mag. J. Sci., 2 (1926) 538.
16 J.H. Espenson, Chemical Kinetics and Reaction Mechanisms, McGraw Hill, New York, 1981, p. 25.
17 J.M. Jordan, S.H. Hoke and H.L. Pardue, Anal. Chim. Acta, 272 (1993) 115.
18 J. Tyson, Anal. Chim. Acta, 214 (1988) 57.

Analytica Chimica Acta, 272 (1993) 135–138
Elsevier Science Publishers B.V., Amsterdam

Flow-injection extraction spectrophotometric determination of chromium(VI) with the benzyltributylammonium cation

S.A. Barakat, D. Thorburn Burns and Michael Harriott

Department of Analytical Chemistry, The Queen's University of Belfast, Belfast BT9 5AG (UK)

(Received 1st July 1992)

Abstract

Chromium(VI) can be determined spectrophotometrically at 365 nm after flow-injection extraction into chloroform of the ion associate benzyltributylammonium dichromate. The carrier stream was distilled water, merged with 1.0 M sulphuric acid solution, the reagent stream was 0.5% (w/v) benzyltributylammonium chloride solution. The injection rate was 20 h^{-1}. The calibration graph was linear up to 20 $\mu g\ ml^{-1}$ and the detection limit (3 × baseline noise) was 0.5 $\mu g\ ml^{-1}$ Cr(VI) based on 250-μl injection volumes. The system has been applied to the determination of chromium in steels.

Keywords: Flow injection; Spectrophotometry; Benzyltributylammonium dichromate extraction; Chromium

Although there are many excellent selective and sensitive spectrophotometric methods for most common metals the same is not true for metalloids, non-metals or anions in general [1] or oxo anions in particular [2]. This accounts for the lack of flow-injection spectrophotometric methods for anions where, so far, less than 15% of 3000 or so published FIA papers deal with this topic [3], of which 24 concern chromium(VI) [4–27]. These papers are all based on relatively non-selective, single-phase, oxidation reactions of diphenylcarbazide [4–21], ferroin [22,23], brucine [24] or a leuco dye [25,26] apart from one dealing with an onium ion-pair extraction [27]. Extraction of dichromate as an onium ion-pair can be achieved quite selectively [28,29]. We now report on the adaption of an earlier [29] manual method for flow-injection analysis of dichromate utilising benzyltributylammonium as the ion-pairing cation.

Correspondence to: D.T. Burns, Department of Analytical Chemistry, The Queen's University of Belfast, Belfast BT9 5AG (UK).

EXPERIMENTAL

Apparatus

Absorbances were measured at 365 nm with a Pye Unicam SP6-550 UV–visible spectrophotometer fitted with a 30-μl, 10-mm, special optical quartz cell (Hellma) and recorded with Phillips 825 recorder. Solutions were pumped using a fixed speed proportioning pump (Technicon) fitted with Acidflex pump tubes for the organic phase and Tygon pump tubes for the aqueous phases. Samples were injected using a four-way Rheodyne valve fitted with by-pass coil. Flow lines were PTFE tubing (0.5 and 0.8 mm i.d.). The flow system is shown diagrammatically in Fig. 1. Omnifit three-way connectors were used at

the mixing points, "Hex" for mixing aqueous phases and "Tee" for mixing organic and aqueous phase (segmenter).

The phase separator was constructed according to the design of Al-Wehaid [30] and fitted with a 1-μm pore size PTFE porous membrane (Zefluor, Gelman Sciences).

Reagents and solutions

A stock solution of 1000 μg ml^{-1} chromium (VI) was prepared by dissolving 2.830 g of potassium dichromate (AnalaR, BDH, previously dried to constant weight at 140°C) in 1 l of distilled water. More dilute solutions of chromium(VI) were prepared as required.

Benzyltributylammonium chloride (Fluka, purum, > 98% as Cl) was used as supplied. A stock 0.5% (w/v) solution was prepared in distilled water.

Stock solution of 500 μg ml^{-1} chromium(III) was prepared by dissolving 2.401 g of chromium (III) potassium sulphate dodecahydrate (AnalaR, BDH) in 500 ml of distilled water. More dilute solutions of chromium(III) were prepared as required.

Cerium(IV) sulphate solution, 0.05 M, was prepared by dissolving 15.81 g of ammonium cerium(IV) sulphate in 500 ml of 1 M sulphuric acid.

All other reagents were of analytical grade, and doubly distilled water was used throughout.

General procedure

Samples and standards were examined using the flow system illustrated in Fig. 1, under the specified conditions. Peak heights were measured.

Procedure for steel samples

For samples containing 3–6% chromium, such as high-speed tool steels, dissolve accurately weighed 0.1-g samples in 10 ml of 20% (v/v) sulphuric acid in 250-ml conical flasks by warming. Add 1 ml of concentrated nitric acid and simmer gently until all carbides are decomposed. Add 2 ml of (1 + 1) sulphuric acid and evaporate carefully to fumes. Cool. Add 50 ml of water and warm to dissolve the soluble salts. Cool and if necessary filter through a Whatman No. 540 filter paper into a 100-ml volumetric flask. Wash the residual solids with a small volume of hot (1 + 99) sulphuric acid followed by water and dilute to volume. Mix well.

Pipette an aliquot of the sample solution (containing about 500–1000 μg of chromium) into a 250-ml beaker, make up to 20 ml with water, add 2 ml of concentrated sulphuric acid and 5 ml of 0.05 M cerium(IV) solution. Heat the solution on a steam bath for 25 min, cool to room temperature, and transfer quantitatively to a 100-ml volumetric flask and make up to volume with distilled water. The peak-height absorbances were meas-

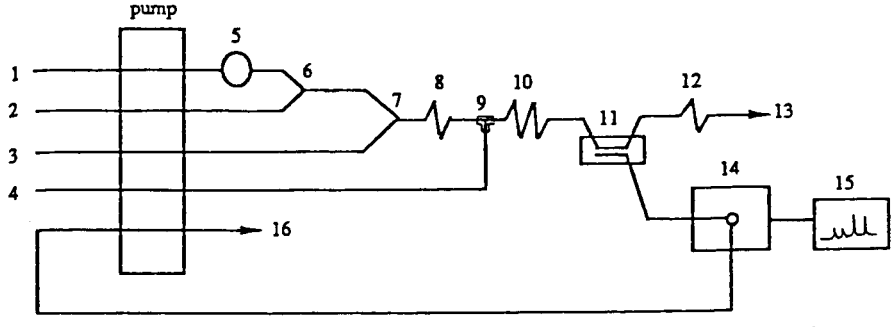

Fig. 1. Schematic diagram of the flow-injection system: (1) distilled water 0.70 ml min^{-1}; (2) 1.0 M sulphuric acid 0.70 ml min^{-1}; (3) onium cation 0.68 ml min^{-1}; (4) chloroform at 0.70 ml min^{-1}; (5) sample injector; (6,7) mixing points ("Hex"); (8) mixing coil (15 cm × 0.5 mm i.d.); (9) segmenter ("Tee"); (10) extraction coil (300 cm × 0.5 mm i.d.); (11) phase separator; (12) restrictor coil; (13) aqueous waste; (14) spectrophotometer; (15) recorder; (16) organic waste pumped at 0.68 ml min^{-1}.

ured in the flow system (Fig. 1) for triplicate injections of each sample. The amount of chromium present was evaluated from a calibration graph (0–20 μg ml^{-1} Cr) prepared by using aliquots of standard chromium(III) solution, oxidizing with cerium(IV) and proceeding as for steel samples. For samples containing 0.1–1% chromium increase the sample weights to 0.3–0.5 g. For samples which contain large amounts of manganese [where some of Mn(II) can be oxidized to Mn(VII) by cerium(IV)], add 5% (w/v) sodium nitrite solution dropwise until the colour of permanganate disappears, before diluting the samples to volume.

RESULTS AND DISCUSSION

The main experimental variables were examined using a fixed sample concentration and injection volume (15 μg ml^{-1} Cr, 250 μl).

The peak heights were found to be independent of the length of the extraction coil from 2.0 to 4.0 m; 3.0 m was chosen for routine use because this gave a convenient resistance to flow and decreased the risk of leakage in the phase-separator block.

The effect of sulphuric acid concentration was investigated by varying the concentration from 0 to 2 M. The peak heights were found to increase with acid concentration up to 0.25 M and were independent of acid concentration up to at least 2 M. A reagent stream of 1 M was therefore used.

The onium cation concentration was varied from 0 to 2% (w/v). The peak heights increased rapidly with onium cation concentration up to 0.5% and decreased slowly thereafter. A reagent concentration of 0.5% (w/v) was therefore chosen.

The length of the reaction coil was varied from 25 to 300 cm. The peak heights decreased slightly above 25 cm, so that 25 cm was used.

The effect of injection volume on peak shape was examined. The volume of sample injected was varied from 100 to 1000 μl by changing the length of the sample loop in the injection valve. Although the peak heights increased with increasing sample volume they also became broader; 250 μl volumes were a convenient compromise between sensitivity and sample throughput.

TABLE 1

Effect of diverse ions on the determination of chromium(VI) (10 μg)

Ion [a]	Ion–Cr(VI) (w/w)	Peak height change (%)
Fe(III)	1000	–
Zn(II), Co(II), Pb(II), Mn(II), V(V), W(VI), Mo(VI)	100	–
Al(III)	100	10.6
	50	–
Ni(II)	100	31
	10	5.3
	5	–
Cu(II)	100	28
	10	10.6
	5	–
Mn(VII)	10	835
	1	58
	10 [b]	–
Nitrate	1000	–
Perchlorate	1000	−83
	100	–
Chloride	1000	28
	10	–
Fluoride	200	–

[a] Cations added as nitrate salts, anions added as sodium or potassium salts. [b] After addition of sodium nitrite (dropwise until the colour of permanganate disappears).

The possible interferences of various ions were checked for the determination of 10 μg of chromium as dichromate under the conditions of the general procedure. The results are summarised in Table 1. The only ion of interest in steel analysis that interfered was manganese(VII). This interference was overcome by dropwise addition of 5% (w/v) sodium nitrite solution prior to diluting the samples to volume.

A linear calibration was obtained over the range 0–20 μg ml^{-1} Cr(VI) at 365 nm. For the determination of 15 μg ml^{-1}, the relative standard deviation was 0.70% (n = 10) and the detection limit (3 × baseline noise) was 0.51 μg ml^{-1}. The results for the determination of chromium in Standard Steel samples (Table 2) were in good agreement with the certificate values. The method is simple to operate and faster (20 injections h^{-1})

TABLE 2

Determination of chromium in steels

Sample	Sample weight (g)	Chromium in steel (%, w/w)	
		Certified [a]	Found [b]
ECRM 082-1	3.0	0.018 ($S = 0.001$) for 10 samples	0.0179 ± 0.006
BCS 219/3	0.5	0.76 (0.75–0.76)	0.757 ± 0.005
BCS 435/1	0.3	0.14 (0.13–0.15)	0.141 ± 0.004
BCS 482	0.1	4.09 (4.06–4.14)	4.077 ± 0.009

[a] Certified range in parentheses. [b] Mean ± standard deviation for 4 replicates.

than conventional manual liquid–liquid extraction. The procedure is similar in sensitivity, precision and interferences to that obtained earlier [27] using pentamethylenebis(triphenyl)phosphonium chloride but is cheaper by a factor of 6.

REFERENCES

1 C.A. Watson, Analyst, 111 (1986) 1353.
2 D.T. Burns, Anal. Proc., 19 (1982) 355.
3 B. Fernandez-Band, P. Linares, M.D. Luque de Castro and M. Valcarcel, Analyst, 116 (1991) 305.
4 S.S. Jorgensen and M.A.B. Regitano, Analyst, 105 (1980) 292.
5 J.C. de Andrade, J.C. Rocha, C. Pasquini and N. Baccan, Analyst, 108 (1983) 621.
6 B. Bubnis, M.R. Straka and G.E. Pacey, Talanta, 30 (1983) 841.
7 R.A. Leach, J. Ruzicka and J.M. Harris, Anal. Chem., 55 (1983) 1669.
8 J.A. Andrade, J.C. Rocha and N. Baccan, Analyst, 109 (1984) 645.
9 C. Pasquini and W.A. De Oliveira, Anal. Chem., 57 (1985) 2575.
10 J.C. de Andrade, J.c. Rocha and N. Baccan, Analyst, 110 (1985) 197.
11 J. Ruz, A. Rios, M.D. Luque de Castro and M. Valcarcel, Fresenius' Z. Anal. Chem., 322 (1985) 499.
12 M.J. Whitaker, Anal. Chim. Acta, 174 (1985) 375.
13 J. Ruz, A. Rios, M.D. Luque de Castro and m. Valcarcel, Anal. Chim. Acta, 186 (1986) 139.
14 J. Ruz, A. Rios, M.D. Luque de Castro and M. Valcarcel, Talanta, 33 (1986) 199.
15 J. Ruz, A. Torres, A. Rios, M.D. Luque de Castro and M. Valcarcel, J. Autom. Chem., 8 (1986) 70.
16 Z. Yu and X. Li, Fenxi Huaxue, 14 (1986) 867.
17 D.J. Malcolme-Lawes and C. Pasquini, J. Autom. Chem., 10 (1988) 25.
18 K. Yoshimura, Analyst, 113 (1988) 471.
19 A.N. Araujo, J.L.F.C. Lima, A.O.S.S. Rangel, J. Alonso, J. Bartroli and R. Barber, Analyst, 114 (1989) 1465.
20 M.K. Beklemisheva and T.V. Rodionova, Vestn. Mosk. Univ., Ser. 2 Khim., 31 (1990) 559.
21 C.C. Chien and Y.M. Chen, Hua Hsueh, 48 (1990) 99.
22 V.V.S.E. Duff and H.A. Mottola, Anal. Chem., 47 (1975) 357.
23 A. Zhang and C. Liu, Yejin Fenxi, 10 (1990) 24.
24 T. Yamane and H.A. Mottola, Anal. Chim. Acta, 146 (1983) 181.
25 C. Martinez-Lozano, T. Perez-Ruiz, V. Tomas and E. Yague, Analyst, 113 (1988) 1057.
26 H. Mueller and E.H. Hansen, Chem. Tech. (Leipzig), 42 (1990) 304.
27 D.T. Burns, N. Chimpalee and M. Harriott, Anal. Chim. Acta, 225 (1989) 241.
28 A.J. Bowd, D.T. Burns and A.G. Fogg, Talanta, 16 (1969) 719.
29 D.T. Burns, M. Harriott and S.A. Barrakat, Anal. Chim. Acta, 259 (1992) 33; and references cited therein.
30 A. Al-Wehald, PhD Thesis, University of Hull, 1987.

Analytica Chimica Acta, 272 (1993) 139–143
Elsevier Science Publishers B.V., Amsterdam

Four-potential-step differential amperometry in a dual-potential sequence mode

Yuzhi Fang, Wei Tong, Pingang He, Rener Wang and Litong Jin

Department of Chemistry, East China Normal University, 3663 Zhong Shan Road (N), Shanghai 200062 (China)

(Received 3rd June 1992; revised manuscript received 11th September 1992)

Abstract

An amperometric waveform was designed for the resolution of overlapped peaks in voltammetry. The waveform is formed by superimposing a small-amplitude square-wave sequence on a dual-amplitude double-pulse sequence. Similar to the principle of dual-wavelength spectrophotometry, cadmium and indium can be determined in the presence of each other.

Keywords: Amperometry; Voltammetry; Cadmium; Indium; Overlapped peaks

In polarography and voltammetry, the determination of two species when their peak potentials are close together and their concentration difference is large, has long been a vexed problem. There are two main approaches to dealing with these overlapping peak problems. In the subtraction method reported by Bond and Grabaric [1], the interfering species is added gradually to a blank solution and the voltammetric curve of the former is subtracted from that of the sample solution until no trace of the overlapping peak remains. The alternative is computational methods, which include pattern classification [2,3], fast Fourier transformation deconvolution [4], Kalman filtering [5] and model function fitting methods [6]. These methods are tedious and time consuming and many of them involve complicated mathematical calculations and are often subjective and arbitrary.

Dual-wavelength spectrophotometry, proposed by Chance [7], has been widely used to handle overlapped absorption peaks [8]. Unfortunately, this has not attracted much attention from electrochemists, and no report of the use of this principle to solve the problems of overlapped voltammetric peaks could be found. To achieve this, a dual-potential waveform must first be designed. On the basis of previous work on normal dual-pulse superimposed four-potential-step differential voltammetry [9] and four-potential-step differential amperometry in a single-pulse sequence mode [10], in this paper a new amperometric waveform in the dual-potential mode is proposed. This dual-potential mode four-potential-step waveform is achieved by superimposing a sequence of small-amplitude (ΔE) square waves on a double-pulse sequence with amplitudes E_A and E_B. The subtraction and addition of the sampling currents on these four potential steps which are antisymmetric with each other can form a net Faradaic current without charging current and background [9,10]. The final current ouptut is obtained through an algorithm similar to that in dual-wavelength spectrophotometry. In this way, the peak overlapping problem can be solved effectively. The determination of cadmium and in-

Correspondence to: Y.-Z. Fang, Department of Chemistry, East China Normal University, 3663 Zhong Shan Road (N), Shanghai 200062 (China).

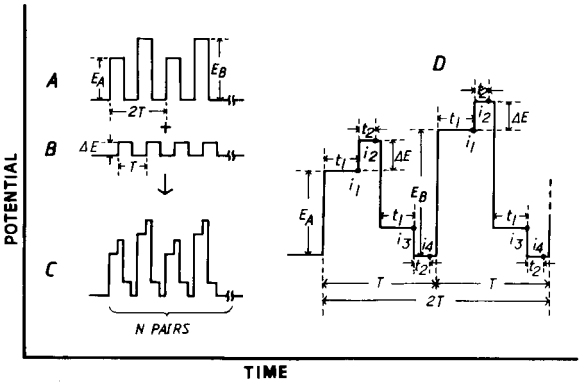

Fig. 1. Waveform of four-potential-step differential amperometry in the dual-potential sequence mode.

dium in the presence of each other gave satisfactory results.

PRINCIPLE

The waveforms for this technique, which will be referred to as four-potential-step differential amperometry in a dual-potential sequence mode, are shown in Fig. 1. This waveform (Fig. 1C) is formed by superimposing a sequence of small-amplitude (ΔE) square waves (Fig. 1B) on a double-pulse sequence with amplitudes E_A and E_B (Fig. 1A).

The periods of the double-pulse sequence and square-wave sequence are $2T$ and T, respectively. Generally, the initial potential of the double-pulse sequence, E_0, is set at the point where no electrochemical reaction (i.e., no Faradaic current) takes place. $(E_0 + E_B)$ is the peak potential (not necessarily) of the species to be determined. $(E_0 + E_A)$ is the iso-current point of the interfering species versus $(E_0 + E_B)$, i.e., the currents for the interfering species at $(E_0 + E_A)$ and $(E_0 + E_B)$ are equivalent. In the first period of the final waveform (Fig. 1C), the sampling currents on the four potential steps of the first pulse (E_A) are combined through subtraction and additions as follows:

$$I_{A,1} = I_{A,1,for} + I_{A,1,rev} = (i_2 - i_1)_{A,1} + (i_4 - i_3)_{A,1} \quad (1)$$

where $I_{A,1}$ is the current output of the first pulse (the potential of which is E_A) in the first period, $I_{A,1,for}$ and $I_{A,1,rev}$ are the differentials of the currents caused by forward and reverse potential steps in this pulse, respectively, and i_1 to i_4 are the sampling currents on these first to fourth potential steps. Because the sampling positions of i_1 and i_3 and of i_2 and i_4 are antisymmetric with each other (i.e., they have the same net potential steps and sampling time but with the opposite direction), according to previous work [9,10] the charging currents in i_1 and i_3 and in i_2 and i_4 have the same magnitude and opposite sign to each other. Therefore, the charging currents in $I_{A,1}$ tend to be offset and $I_{A,1}$ is essentially the Faradaic current. Finally, the average current output, $\bar{I}_A$, in the N pulse period with amplitude E_A is

$$\bar{I}_A = \sum_{j=1}^{N} I_{A,j}/N \quad (2)$$

where $I_{A,j} = I_{A,j,for} + I_{A,j,rev} = (i_2 - i_1)_{A,j} + (i_4 - i_3)_{A,j}$, $I_{A,j,for}$ and $I_{A,j,rev}$ are the differentials of the currents caused by forward and reverse potential steps of the first pulse (with amplitude E_A) in the jth period, respectively.

Similarly, the average current output, $\bar{I}_B$, in the Nth pulse period with amplitude E_B is

$$\bar{I}_B = \sum_{j=1}^{N} I_{B,j}/N \quad (3)$$

where $I_{B,j} = I_{B,j,for} - I_{B,j,rev} = (i_2 - i_1)_{B,j} + (i_4 - i_3)_{B,j}$, $I_{B,j,for}$ and $I_{B,j,rev}$ are the differentials of the currents caused by forward and reverse potential stpes of the second pulses (with amplitude E_B) in the jth period respectively.

$\bar{I}_A$ and $\bar{I}_B$ are primarily the pure Faradaic currents. Thus, the sampling time and pulse period can be reduced without much sacrifice of Faradaic current owing to the long delay. The signal-to-noise ratio is therefore enhanced by increasing the number of pulse periods, N, in the same amount of time.

If (a) and (b) are the two electroactive species which have very closely located peak potentials, their voltammograms will seriously overlap (Fig. 2A). A typical case is the overlap of the voltam-

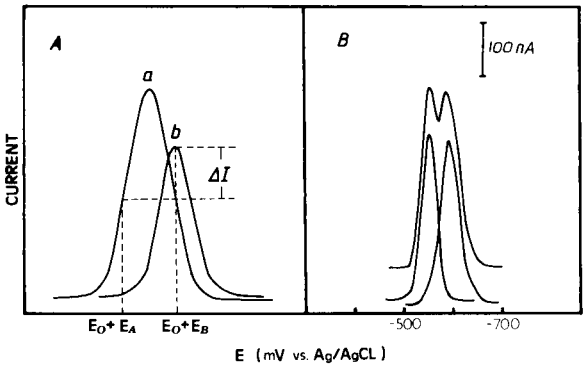

Fig. 2. Principle of four-potential-step differential amperometry for overlapped voltammetric peaks (A) $(E_0 + E_B)$ = the peak potential of the species (b) to be determined; $(E_0 + E_A)$ = the iso-current point of the interfering species (a) versus $(E_0 + E_B)$. (B) Overlap of the normal dual-pulse superimposed four-potential-step differential voltammograms for Cd^{2+} and In^{3+}. Cd^{2+}, 4.0 μg ml^{-1}; In^{3+}, 3.0 μg ml^{-1}; KCl, 0.2 mol l^{-1}; $t_1 = 100$ ms; $t_2 = 60$ ms; $E_0 = -400$ mV; $E_s = 2$ mV; $\Delta E = 10$ mV.

metric peaks of In^{3+} and Cd^{2+} (Fig. 2B), where quantitative analysis is difficult. However, the current responses caused by (a) and (b) are superimposable at a certain potential. Therefore, at a potential $(E_0 + E_A)$,

$$\bar{I}_A = K_{A,a}C_a + K_{A,b}C_b \quad (4)$$

where $K_{A,a}$ and $K_{A,b}$ are the proportionality constants for species (a) and (b) in the pulses with amplitude E_A and C_a and C_b are the concentrations of (a) and (b), respectively.

Similarly, at a potential $(E_0 + E_B)$,

$$\bar{I}_B = K_{B,a}C_a + K_{B,b}C_b \quad (5)$$

where $K_{B,a}$ and $K_{B,b}$ are the proportionality constants for (a) and (b) in the pulses with amplitude E_B.

$(E_0 + E_A)$ is the iso-current point of interfering species (a) versus $(E_0 + E_B)$. Therefore,

$$K_{A,a}C_a = K_{B,a}C_a \quad (6)$$

Hence the current difference, ΔI, of $(E_0 + E_B)$ versus $(E_0 + E_A)$ is

$$\Delta I = \bar{I}_B - \bar{I}_A = (K_{B,b} - K_{A,b})C_b \quad (7)$$

As can be seen in Eqn. 7, ΔI is directly proportional to the concentration of the species (b) to be determined. This forms the basis for quantitative analysis using this method.

Similarly, if (a) is to be determined,

$$K_{A,b}C_b = K_{B,b}C_b \quad (8)$$

$$\Delta I = \bar{I}_A - \bar{I}_B = (K_{A,a} - K_{B,b})C_a \quad (9)$$

where ΔI is directly proportional to the concentration of species (a).

EXPERIMENTAL

The microcomputerized electrochemical system [10] used for this work is based on a Z80 single-board computer. All software is written in Z80 assembly language and stored in EPROM. High-resolution 12-bit A/D and D/A converters were emmployed to achieve high-precision of control potential via a potentiostat circuit. Currents between 1 nA and 1000 μA can be measured. The results were recorded by a Laser Model PP40 four-colour plotter. All experiments were conducted by using an EG&G/PARC Model 303 static mercury drop electrode (SMDE) as the working electrode, Ag/AgCl as the reference electrode and platinum wire as the auxiliary electrode. The entire pulse sequence was performed on a single drop of mercury. All chemicals used were of analytical-reagent grade or better. Doubly distilled water was used throughout.

RESULTS AND DISCUSSION

In practical analysis, the selection of iso-current potentials for the interfering species is important. If (b) is to be determined, one of the potentials is usually chosen at its peak potential, $(E_0 + E_B)$. The iso-current potential of interferent (a) versus $(E_0 + E_B)$ is then selected through experiment. The iso-absorbance point selection method reported by Shibata et al. [8] in dual-wavelength spectrophotometry is also applied. However, the influences of the initial potential, the concentration of interfering species and square-wave amplitude (ΔE) on the iso-current potentials need to be explored further. The sam-

pling time, according to the previous recommendation [10], are $t_1 \geqslant 80$ ms and $t_2 \geqslant 50$ ms. Under these conditions, the blank current is set to zero and the influence of the charging current and background is eliminated. In this work, $t_1 = 100$ ms and $t_2 = 60$ ms were adopted throughout.

Effect of initial potential and concentration of an interferent on the iso-current points of the interfering species

Experiments showed that initial potential, E_0, does not affect the iso-current point of the interferent. When the initial potential is to be changed, one does not have to re-select a new iso-current point. Generally, E_0 is chosen at a potential where no Faradaic current flows. Experiments also demonstrated that the concentration of the interfering species does not affect its iso-current points in a certain concentration range. Once the iso-current points have been determined, they are valid over a fairly wide concentration range. This is convenient for practical sample analysis where the exact concentration of the interferents is usually unknown.

Effect of square-wave amplitude on the iso-current points of an interferent

The effect of the square-wave amplitude, ΔE, on the iso-current points of In^{3+} is illustrated in Fig. 3, which demonstrates that ΔI varies greatly with ΔE whereas E_A and E_B are certain. Therefore, the iso-current points should be determined again while using a different ΔE.

Calibration

The calibration graphs In^{3+} and Cd^{2+} in the presence of 10 μg ml^{-1} of each other using the proposed method are shown in Fig. 4A and B, respectively. ΔI and the concentrations of In^{3+} and Cd^{2+} show a good linear relationship in the concentration range used here. The linear regression equations for In^{3+} and Cd^{2+} are $\Delta I_{In} = 207.4C_{In} - 13.7$ and $\Delta I_{Cd} = 148.0C_{Cd} - 9.8$ and the correlation coefficients are 0.9998 and 0.9997, respectively.

Analysis of cadmium–indium sample

To a KCl solution containing a certain concentration of cadmium different amounts of indium

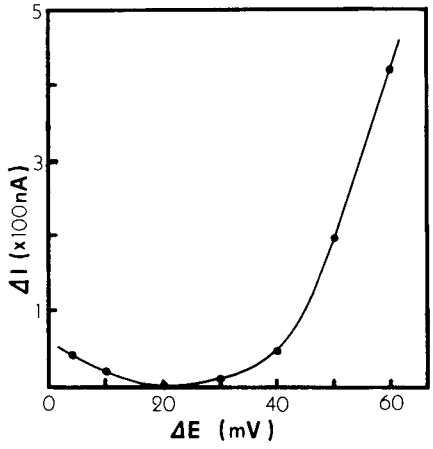

Fig. 3. Effect of square-wave amplitude, ΔE, on the iso-current points of the interferent. KCl, 0.2 mol l^{-1}; In^{3+}, 3.0 μg ml^{-1}; $N = 100$; $t_1 = 100$ ms; $t_2 = 60$ ms; $\Delta E = 20$ mV; $E_0 = -400$ mV; $E_A = -102$ mV; $E_B = -200$ mV.

were added and ΔI was measured at -600 mV vs. -502 mV by the proposed method. The cadmium concentrations obtained are given in Table 1. Similarly, to a KCl solution with a definite concentration of indium were added different amounts of cadmium and ΔI was measured at -546 mV vs. -626 mV. The indium concentrations obtained are given in Table 2. The results

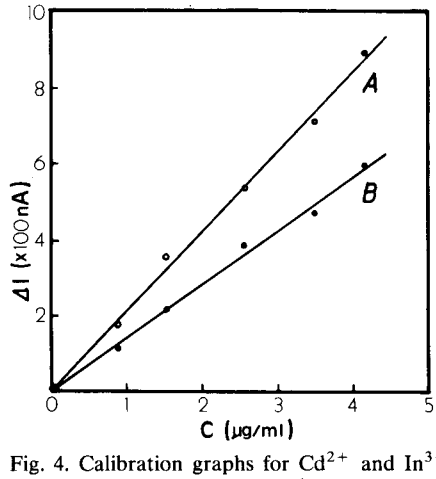

Fig. 4. Calibration graphs for Cd^{2+} and In^{3+} with the proposed method. KCl, 0.2 mol l^{-1}; $N = 100$; $t_1 = 100$ ms; $t_2 = 60$ ms; $\Delta E = 20$ mV. (A) Calibration graph for In^{3+} when $C_{Cd} = 10$ μg ml^{-1}, $E_0 = -400$ mV, $E_A = -146$ mV, $E_B = -226$ mV; (B) calibration graph for Cd^{2+} when $C_{In} = 10$ μg ml^{-1}, $E_0 = -400$ mV, $E_A = -102$ mV, $E_B = -200$ mV.

TABLE 1

Results for the determination of cadmium in the presence of different amounts of indium [a]

Cd^{2+} taken ($\mu g\ ml^{-1}$)	In^{3+} present ($\mu g\ ml^{-1}$)	Cd^{2+} found ($\mu g\ ml^{-1}$)	Error ($\mu g\ ml^{-1}$)
1.91	2.86	1.86	−0.05
1.85	5.56	1.87	+0.02
1.78	8.93	1.80	+0.02
1.64	16.39	1.75	+0.11

[a] $E_A = -102$ mV; $E_B = -200$ mV; other parameters as in Fig. 3.

TABLE 2

Results for the determination of indium in the presence of different amounts of cadmium [a]

In^{3+} taken ($\mu g\ ml^{-1}$)	Cd^{2+} present ($\mu g\ ml^{-1}$)	In^{3+} found ($\mu g\ ml^{-1}$)	Error ($\mu g\ ml^{-1}$)
1.91	2.86	2.10	+0.19
1.85	5.56	1.95	+0.10
1.78	8.93	1.75	−0.03
1.64	16.39	1.62	−0.02

[a] $E_A = -146$ mV; $E_B = -226$ mV; other parameters as in Fig. 3.

demonstrate that the proposed method can be used successfully in the determination of species with overlapped peaks.

The reproducibility of the method is examined for seven parallel determinations of 2.4 $\mu g\ ml^{-1}$ In^{3+} in the presence of 20 $\mu g\ ml^{-1}$ Cd^{2+}. The relative standard deviation was 2.13%.

Conclusion

The principle of dual-wavelength spectrophotometry was applied to solve the problems of overlapped peaks in voltammetry. Using a dual-potential sequence waveform, this permits the elimination of charging current and background, and can be used successfully in the determination of two mixed species with close peak potentials. As dual-wavelength spectrophotometry has long been accepted, the principle of this method is straightforward and easily understood. Generally, the present method is divided into two major procedures: from the normal dual-pulse superimposed four-potential-step voltammograms, locate the corresponding iso-current potential of the interferent versus the peak potential (not necessarily) of the species to be determined; measure the current difference, ΔI, at the peak potential versus the corresponding iso-current point of the interferent. The first step is very important. Although the principle of iso-absorbance selection methods [8] is still applied, as in dual-wavelength spectrophotometry it seems difficult to find the same matrices as for practical samples containing only the interferent in order to locate the iso-current potentials. However, the error caused by this mismatch can be minimized with a similar matrix. Therefore, this method not only provides a simple way to solve the problems of overlapped voltammetric peaks, but also is helpful for carrying out voltammetric analyse without pre-purging of oxygen. In addition, as the potential of the present method returns to its initial point, it is advantageous for electrode cleaning and thus will find great utility in the study of solid electrode and adsorption systems.

This work was supported by a grant from the Foundation of Laboratory of Electroanalytical Chemistry, Changchun Institute of Applied Chemistry, Academica Sinica.

REFERENCES

1 A.M. Bond and B.S. Grabaric, Anal. Chem., 48 (1976) 1624.
2 S.P. Perone and W.F. Gutnecht, Anal. Chem., 42 (1970) 906.
3 R.A. Depalma and S.P. Perone, Anal. Chem., 51 (1979) 825.
4 B.S. Grabaric, R.J. O'Halloran and D.E. Smith, Anal. Chim. Acta, 133 (1981) 349.
5 T.F. Brown and S.D. Brown, Anal. Chem., 53 (1981) 1410.
6 R. Fan and X. Fang, Fenxi Huaxue, 17 (1989) 607.
7 B. Chance, Rev. Sci. Instrum., 22 (1951) 634.
8 S. Shibata, M. Furukawa and K. Goto, Anal. Chim. Acta, 46 (1969) 271.
9 Y. Fang, R. Wang, W. Tong and P. He, Gaodeng Xuexiao Huaxue Xuebao, 13 (1992) 320.
10 Y. Fang, W. Tong, P. He, R. Wang and L. Jin, Electroanalysis, in press.

Analytica Chimica Acta, 272 (1993) 145–150
Elsevier Science Publishers B.V., Amsterdam

Direct electrochemical determination of paracetamol in plasma

I. Christie and S. Leeds

Department of Medicine (Clinical Biochemistry), University of Manchester, Hope Hospital, Salford M6 8HD (UK)

M. Baker and F. Keedy

Department of Clinical Biochemistry, University of Newcastle upon Tyne, Newcastle upon Tyne NE2 4HH (UK)

P. Vadgama

Department of Medicine (Clinical Biochemistry), University of Manchester, Hope Hospital Salford M6 8HD (UK)

(Received 21st June 1991; revised manuscript received 21st September 1992)

Abstract

A simplified, reagentless method for the determination of paracetamol (0–2 mM) in plasma is described, based on the electrochemical oxidation of paracetamol. The technique has been adapted for assay in biological fluids by the use of a permselective cellulose acetate membrane, and an outer diffusion-limiting, microporous polycarbonate membrane treated with dimethyldichlorosilane to impart biocompatibility. The results obtained agreed well with those obtained by a routine enzymic method. The limit of detection is 0.1 mM paracetamol; a range of other drugs was generally without effect.

Keywords: Voltammetry; Membrane electrodes; Paracetamol; Plasma

The estimation of paracetamol plays a vital role in the diagnosis and overall management of a patient with a suspected overdose. Because of the rapid hepatotoxic effects [1] of the drug and the obligatory early therapeutic intervention, analytical methods have been frequently directed towards rapid, simplified analysis, suitable for the emergency laboratory. Early approaches to measurement, such as those based on differential UV absorbance [2] or the indophenol colour reaction following paracetamol hydrolysis to *p*-aminophenol [3] were either too cumbersome for emergency use or lacked selectivity. The nitration method of Glynn and Kendal [4] came to be commonly used, but here interference by salicylate proved a significant drawback. Such chemical methods have been superseded by rapid immunoassay techniques based on enzyme and fluorescent labels [5], and by detection of *p*-aminophenol from the parent compound by a highly selective, enzymic hydrolysis step [6].

The ultimate simplification in analysis, however, would be a paracetamol dip-stick. Electrochemical techniques have begun to be explored more recently as one means of achieving the functionalities of a dry-reagent system [7,8]. The special attraction for medical use is the potential for reagentless assay in an optically opaque solu-

Correspondence to: I. Christie, Department of Medicine (Clinical Biochemistry), University of Manchester, Hope Hospital, Salford M6 8HD (UK).

tion, and for a quantitative readout of either e.m.f. or current, with equipment at a fraction of the cost of most reflectance-based systems.

Paracetamol is electrochemically active at modest polarizing potentials (typically +0.65 V vs. Ag/AgCl). As such, it is a well-recognized interferent at enzyme electrodes where the H_2O_2 product of an oxidase enzyme reaction is detected electrochemically at a polarized working metal electrode [9]. Diffusion-limiting and permselective membranes derived from such a sensor, have been combined here with a simple two-electrode system without enzyme in order to achieve direct detection of paracetamol is plasma.

EXPERIMENTAL

Reagents

Aqueous isotonic phosphate buffer (pH 7.4) was constituted using AnalaR-grade Na_2HPO_4 (BDH, 52.8 mM) and K_2EDTA (BDH, 0.15 mM). Stock standard (10 mM) was made by dissolving paracetamol in the buffer. Bovine serum albumin (BSA) was obtained from Sigma and used as a 5% (w/v) solution in buffer. Dimethyldichlorosilate from BDH, obtained as a 25% (w/v) solution in 1,1,1-trichloroethane, was diluted to 10% of its original concentration in that solvent before use. Therapeutic drug-monitoring control serum was obtained from Bio-Rad (Anaheim, CA). Assigned values for paracetamol in low, medium and high controls were 43–86 μM, 203–365 μM and 560–1135 μM, respectively.

Materials

Neutron track-etched polycarbonate membranes (pore size 0.03 μm, 0.015 μm or 0.01 μm) were obtained from Nuclepore (Pleasonton, CA), and cellulose nitrate membranes (0.45 μm) were purchased from Millipore (Croxley Green, UK). Cellulose acetate powder was from BDH (Poole).

Apparatus

A commercial two-electrode oxygen system (Rank Brothers, Bottisham, Cambridge), comprising a 2 mm diameter platinum working electrode, set in Perspex, and an outer annular 10 mm diameter silver reference electrode, was used for electrochemical detection. Electrodes were polarized between 0.4 and 0.9 V, using a variable-voltage source, and changes in current with time during the measurements were recorded by means of an output to a strip-chart recorder.

Membrane fabrication

Nuclepore membranes were cut to ca. 12-mm squares and either used as received or first dip-coated with dimethyldichlorosilane. Coating was done by 10–30 s immersion in silane solution followed by ca. 2 min rinsing in a jet of distilled water. Cellulose acetate membranes were cast from 1% (w/v) solutions in acetone by the application of 1 ml onto 5-cm square glass plates. Slow rotation of plates enabled uniform films of cellulose acetate to be formed.

Experimental procedure

A ca. 12-mm square cut from the cast cellulose acetate was placed over the platinum working electrode, followed by a Nuclepore membrane. The loose membrane laminate was clamped into place by means of a screw-fit adaptor, which also secured a sample well over the working electrode surface [10]. Single membranes were positioned in the same way. Concentrated stock solutions were added to the buffer to give a final sample volume of 0.5 ml. A similar procedure was adopted for spiking samples of plasma from different patients or of pooled blood, resulting in minimum dilution of the sample, (ca. 2%, v/v). Results were obtained as the difference between a constant baseline and the plateau produced following the step change on paracetamol addition. Fouling and drug control studies and measurement of patients' plasma paracetamol were conducted by replacing buffer in the cell with undiluted BSA, control serum or plasma sample. Measurements were carried out at room temperature (21 ± 2°C).

The correlation study used 10 patient plasma samples obtained from the Clinical Biochemistry Department of Hope Hospital, Salford. Calibration with buffered paracetamol solutions and undiluted plasma measurements were performed

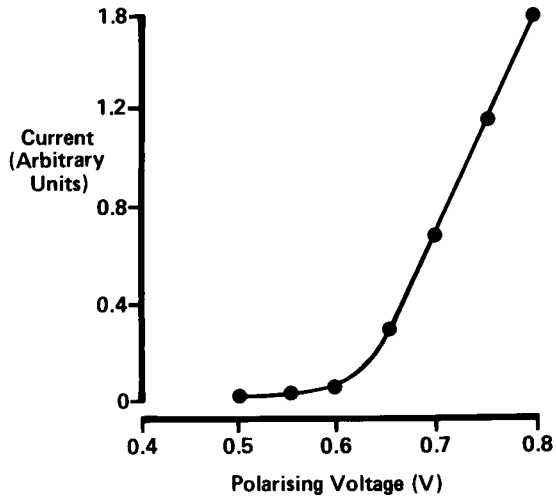

Fig. 1. Voltammogram of paracetamol (0.05 mM) at a bare platinum anode (vs. Ag pseudo-reference).

on an electrode covered by uncoated polycarbonate membrane (0.03 μm pore size) and cellulose acetate and with an applied polarization voltage of +0.65 V vs. Ag/AgCl.

RESULTS

Increasing the polarizing voltage at a bare platinum electrode up to the limit for aqueous solutions resulted in progressively increased, rapid (< 10 s) responses to paracetamol (Fig. 1). While an adequate signal size (lower sensitivity limit ca. 0.01 mM paracetamol) was readily achieved, appropriate for clinical measurement, at high concentrations ($\geqslant 0.5$ mM) a rapid decay in steady-state signals was evident with halving of the signal size in 3–10 min.

The superimposition of a Millipore microporous membrane (0.45 μm pore size) on the electrode not only decreased the signal size, but also altered the current–voltage relationship curve, which now had a plateau region at polarizing voltages above +0.75 V. When cellulose acetate was used, a plateau was retained, and had shifted to lower voltages (Fig. 2), albeit with lower current. A polarizing voltage of +0.65 V was chosen as suitable for subsequent studies, because of the zero-order relationship between current and voltage. With cellulose acetate as a covering membrane (Fig. 3), the linear range was restricted to $\leqslant 2$ mM paracetamol in buffer, but extended up to 5 mM when a polycarbonate membrane was superimposed over the cellulose acetate, though at the expense of reduced signal size. The steady-state signal was achieved in 3–5

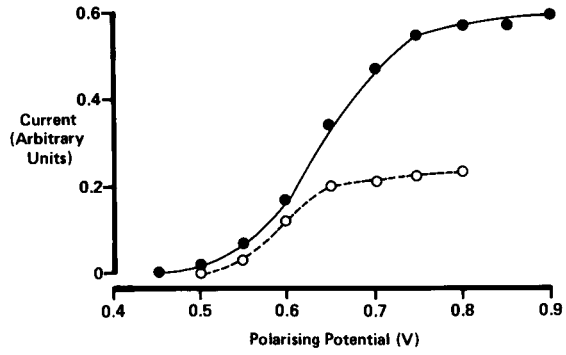

Fig. 2. Voltammograms of paracetamol (0.05 mM) at a platinum anode, with covering (●) Millipore and (○) cellulose acetate membranes (vs. Ag pseudo-reference).

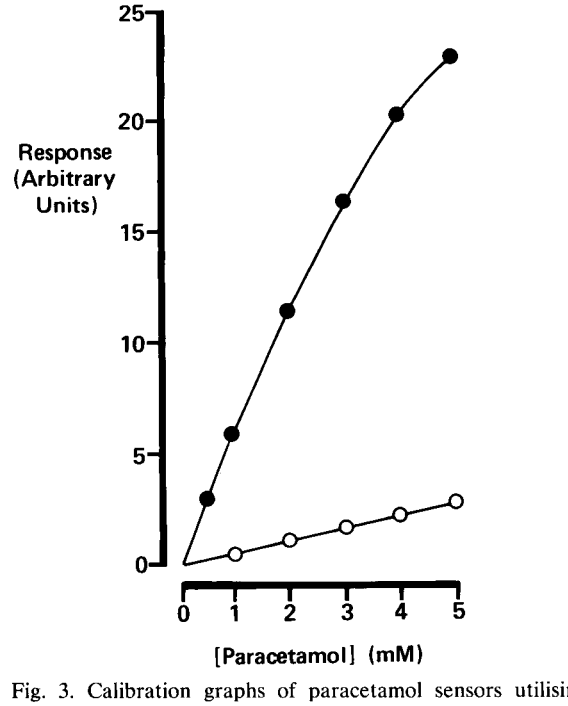

Fig. 3. Calibration graphs of paracetamol sensors utilising covering (●) cellulose acetate, and (○) cellulose acetate overlaid with 0.01 μm polycarbonate membrane.

TABLE 1

Responses to paracetamol and common interferents; effect of including cellulose acetate (CA) covering membrane in addition to polycarbonate (PC)

Drug	Responses (nA)		Response ratios Paracetamol : interferent	
	PC only (0.1 mM)	PC + CA (1.0 mM)	PC only (at equal molarity)	PC + CA (at equal molarity)
Paracetamol	74	172	–	–
Ascorbate	103	10	0.73 : 1	17 : 1
Urate	97	4	0.76 : 1	73 : 1
Glutathione	4	0.7	16.0 : 1	246 : 1
Cysteine	75	5	1 : 1	34 : 1

min, showed no decay, was independent of stirring and pH variations between 6.5 and 8.0 had no effect on signal size.

Table 1 shows the responses obtained to a range of serum interferents, and the high degree of selectivity for paracetamol imparted by the inclusion of a cellulose acetate membrane, as shown by the response ratios.

The glucuronide conjugate of paracetamol gave responses at a bare electrode which were 7% of those of the equimolar parent compound, but this interference became undetectable when a cellulose acetate covering membrane was included. A guide to the discrimination of the electrode for paracetamol was given by exposure to the drug control sera; a calibrated paracetamol electrode comprising silanized 0.03-μm polycarbonate over a cellulose acetate membrane gave responses corresponding to 110, 345 and 900 μM paracetamol, for assigned values of 43–86, 203–365 and 560–1135 μM, respectively. The measured value was higher than the assigned range for the low concentration control, but within the assigned ranges of the medium- and high-concentration control sera. The other drugs present in the control sera had assigned values at three therapeutic levels and were: amikacin, amitriptyline, caffeine, carbamazepine, chloramphenicol, clonazepam, cortisol, cyclosporine, desipramine, digoxin, disopyramide, estriol, ethosuximide, gentamicin, haloperidol, imipramine, kanamycin, lidocaine, lithium, methotrexate, NAPA, netilmicin, nortriptyline, phenobarbital, phenyltoin, primidone, procainamide, propranolol, quinidine, salicylate, streptomycin, theophylline, TSH, T3, T4, tobramycin, valproic acid and vancomycin. The responses to individual drugs were not investigated.

Repeated exposure of the unsilanized electrode (0.03-μm polycarbonate over cellulose acetate) to BSA resulted in a lowering of the elec-

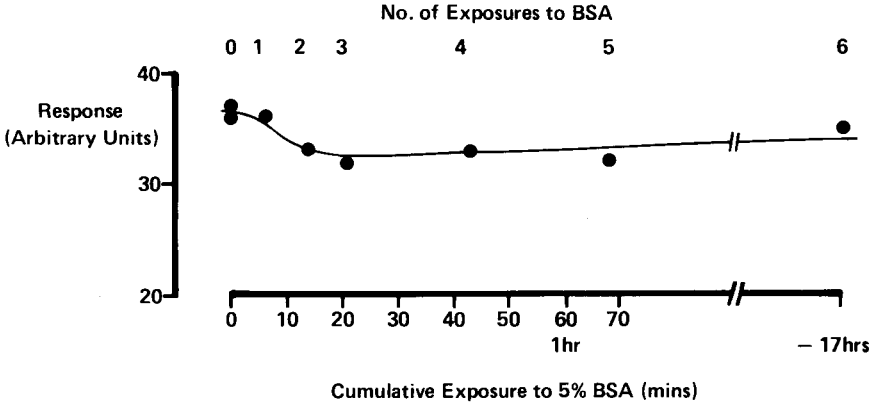

Fig. 4. Response of electrode (unsilanized 0.03 μm polycarbonate + cellulose acetate membranes) to paracetamol (3 mM aqueous solutions) between repeated exposures to 5% BSA.

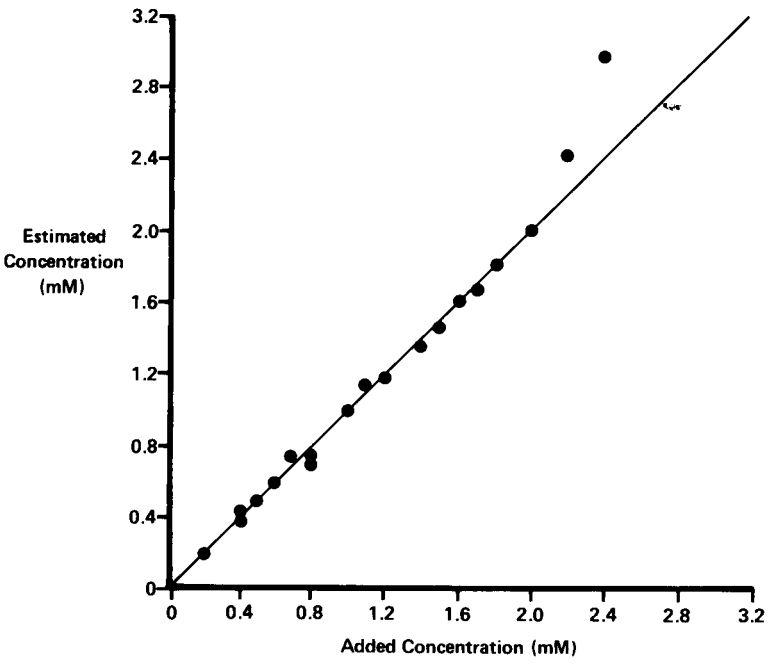

Fig. 5. Recovery of paracetamol added to plasma, using silanized 0.015 μm polycarbonate over cellulose acetate above the electrode ($y = 1.12x - 0.11$, $r = 0.99$).

trode response to 3.0 mM aqueous paracetamol standards (Fig. 4). After the 17-h exposure, the responses to paracetamol in buffer had become reduced by 40% (1 mM), 30% (2 mM) and 29% (3 mM). Problems of signal attenuation were avoided by use of organosilane-treated polycarbonate membranes covering the cellulose acetate. Signals in response to 3.0 mM aqueous paracetamol showed no decrease after a 70-min exposure to 5% BSA. A calibrated electrode with the silanized membranes was found to give a reliable estimation of paracetamol up to 2.0 mM in samples of different patients' plasma, spiked with small quantities ($\leqslant 2\%$, v/v) of paracetamol stock solution (Fig. 5).

Similar spiking of pooled blood at 2.0, 3.0 and 4.0 mM paracetamol resulted in a silanized, precalibrated electrode giving 95, 81 and 79% recovery of the expected paracetamol signal. The comparison of results obtained by the electrochemical method (y) with routine results obtained by enzymic hydrolysis with spectrophotometric detection of a colour reaction with the *p*-aminophenol product (x), showed good correlation ($y = 0.9427x + 0.064$, $n = 7$, $r = 0.9835$) over the range 0–2 mM, even without silanization of the covering polycarbonate membrane. Additionally, four samples showed no detection of paracetamol when assayed by the conventional method (limit of detection 0.1 mM), and these also gave no response by the electrochemical method.

DISCUSSION

Paracetamol is readily oxidizable at polarizing voltages lower than those capable of decomposing water (Fig. 1). The electrochemical reaction is favoured by the thermodynamic stability of the oxidation product *N*-acetyl-*p*-quinoneimine, though undoubtedly there are by-products and a simple two-electron two-proton reaction chemistry is unlikely [11]. With high concentrations at the bare electrode, surface fouling by the rapid deposition of oxidation products most probably led to the decay in signal. The development of plateau voltage regions (Fig. 2) and independence from bulk convection effects are indications of

the reaction-limiting nature of the low-permeability covering membranes selected for the study. The effective surface concentration of paracetamol was lowered by covering electrodes with diffusion-limiting membranes; this was sufficient to enable assay over the entire clinical range of paracetamol without sample dilution (Fig. 3).

Although there is the potential for interference from endogenous electrochemically active species in blood, these can be screened out by the cellulose acetate membrane (Table 1), and as a result do not appear to be significant, as very little bias was shown with plasma (Fig. 5).

Conjugated forms of paracetamol can make up the major proportion of the drug in plasma [12], and it is important that these do not interfere with the assay. The main paracetamol derivatives (the sulphate and glucuronide) have high redox potentials, decreasing interference at +0.65 V, which can be further alleviated by the inclusion of a selective cellulose acetate membrane. The ready discrimination of free from bound is an intrinsic capability of electrochemical methods, and hence could well be advantageous in exploring the true toxic potential of the parent drug in overdose situations; this is particularly so since the electrode is reagentless and could be readily adapted for continuous monitoring of paracetamol. However, the minor metabolites which have a free *p*-hydroxy group could still contribute to the electrode signal. Other interferences from exogenous compounds, including those from drugs, are essentially those encountered with the amperometric glucose enzyme electrode [13], polarized to a similar voltage. The interference found from the control sera is only a problem at low paracetamol levels. The electrochemical interference was not found to be present in clinical samples. At high therapeutic doses, and in overdose, the electrochemical method appears to be a viable screening method at this stage.

Surface fouling by proteins generally distorts the mass-transfer process at amperometric electrodes, so influencing sensitivity (Fig. 4). However, the improved biocompatibility achieved with silanized membranes confirms the benefits demonstrated in an enzyme electrode system of silane resistance to surface adsorbates [10].

The electrochemical system responds only to free paracetamol. At concentrations below 2.0 mM, the high recoveries in plasma (Fig. 5) suggest that there is little protein binding at therapeutic levels. Binding almost certainly increases at toxic levels [14,15], as apparent in the reduced recoveries for 3.0 and 4.0 paracetamol in blood.

The results obtained from patient samples by the electrochemical method show a good correlation with the results from the conventional enzymic method. This indicates that the method developed here is a viable alternative to existing methods, allowing determination of high paracetamol levels in overdose patients, and also possesses the necessary interference-free operation to reliably eliminate paracetamol overdose in clinical diagnosis. Such a simple sensor system would be particularly suited to further development for continuous monitoring of overdose patients with an implanted sensor.

The authors wish to express their gratitude for financial support from SERC and ICI. The paracetamol conjugates were the kind gift of Sterling Winthrop, Northumberland, UK.

REFERENCES

1 J.A. Holm and D. Jacobson, Lancet, i (1986) 804.
2 J.I. Routh, N.A. Shane, E.G. Arredondo and W.G. Paul, Clin. Chem., 14 (1968) 882.
3 M.J. Stewart, P.I. Adriaenssens, D.R. Jarvie and L.F. Prescott, Ann. Clin. Biochem., 16 (1979) 89.
4 J.P. Glynn and S.E. Kendal, Lancet, i (1975) 1147.
5 M. De Laurentis, E. Snyder, K. Chegwidden, P. Khanna and A. Jaklitsch, Clin. Chem., 28 (1982) 1664.
6 C.P. Price, P.M. Hammond and M.D. Scawen, Clin. Chem., 29 (1983) 358.
7 M. Baker and P. Vadgama, Meas. Control. 21 (1988) 53.
8 P.A. Vaughan, L.D.L. Scott and J.F. McAleen, Anal. Chim. Acta, 248 (1991) 361.
9 M. Roddis, Lancet, ii (1981) 634.
10 W.H. Mullen, F.H. Keedy, S.J. Churchouse and P.M. Vadgama, Anal. Chim. Acta, 183 (1986) 59.
11 D.J. Milner, J.R. Rise, R.M. Riggin and P.T. Kissinger, Anal. Chem., 53 (1981) 2258.
12 T.A. White, Lancet, ii (1976) 696.
13 T.K. Chua and I.K. Tan, Clin. Chem., 24 (1978) 150.
14 M.J. Stewart and I.D. Watson, Ann. Clin. Biochem., 24 (1987) 525.
15 F. Kamali, J.R. Fry and G.D. Bell, J. Pharm. Pharmacol., 39 (1987) 150.

Analytica Chimica Acta, 272 (1993) 151–159
Elsevier Science Publishers B.V., Amsterdam

Voltammetry with microelectrodes in wine: determination of the total acidity

M. Antonietta Baldo, Salvatore Daniele and Gian A. Mazzocchin

Department of Physical Chemistry, University of Venice, Calle Larga S. Marta 2137, 30123 Venice (Italy)

(Received 20th May 1992; revised manuscript received 21st September 1992)

Abstract

A voltammetric study of wine was performed in order to ascertain its suitability as a medium for analysis. The electrochemical processes of the probe molecule $Ru(NH_3)_6Cl_3$ and of some electroactive species present in the medium were investigated with a platinum microelectrode and the relevant responses were compared with those obtained with an electrode of the same material of conventional size. The results indicated that with the latter electrode ohmic losses affect the voltammetric processes, whereas no problem arises with the microelectrode. It was also found that the acids present in wine are responsible for a large cathodic wave and its measurement, by voltammetric and chronoamerometric titrations, permitted the determination of the total acidity of wine with a relative standard deviation within 2.5%. The results obtained with this approach were compared with those obtained by the classical method commonly employed for the determination of the total titratable acidity of wine.

Keywords: Amperometry; Voltammetry; Acidity; Chronoamperometry; Microelectrodes; Wines

Small electrodes have received increasing attention for both kinetic studies of the electrode processes and quantitative analyses [1]. In general, their use provides a means of simplifying the procedure of electroanalysis, making it more accessible in more demanding situations [2–5]. Some of the advantageous characteristics are the low current involved with a consequent negligible ohmic drop, the fast response due to a small electrode capacitance and steady-state conditions achievable in a short time. These properties allow microelectrodes to be employed, for instance, directly in resistive media and without the deliberate addition of supporting electrolytes [6–9].

Microelectrodes have been used previously for determinations in real samples directly and without pretreatment [3–5]. This approach is advantageous because the species naturally present, additives and contaminants can be revealed and determined without changing their nature and without modification of the existing chemical equilibria in the sample.

This paper reports an investigation on wine, which is a water–ethanol medium in which the ethanol content ranges from about 7 to 18% (v/v) at 20°C [10,11]. It also contains acids and salts but it is less conductive and more viscous than an aqueous solution having the same ionic strength [11]. Therefore, the use of microelectrodes may be advantageous compared with conventional electrodes, and this aspect was explored.

EXPERIMENTAL

Reagents

Hexammineruthenium(III) trichloride, $Ru(NH_3)_6Cl_3$, was provided by Matthey Bishop and

Correspondence to: S. Daniele, Department of Physical Chemistry, University of Venice, Calle Larga S. Marta 2137, 30123 Venice (Italy).

purified as reported [12]. All inorganic salts, acids and organic compounds were of analytical-reagent grade. The wine samples analysed were Italian red wines (Chianti, Cabernet and Merlot) and white wines (Tocai and Verduzzo from Friuli and Veneto).

Doubly distilled water was used throughout to prepare standard solutions of the reagents. When necessary, the samples were deareated with nitrogen (99.99%) from SIAD.

Electrodes and instrumentation

To prepare a platinum disc microelectrode, a wire of diameter 25 μm was sealed directly in glass as reported previously [13]. For a carbon disc microelectrode, a single carbon fibre 8 μm in diameter was connected with a thin copper wire with silver epoxy and sealed with pure resin in a glass capillary. This was cut perpendicularly to its length to expose the carbon disc. Prior to each measurement, the electrodes were polished with graded alumina powder (down to 0.05 μm) on a polishing microcloth. For comparison, a conventional platinum disc electrode of diameter 3 mm was used. A saturated calomel electrode (SCE) was employed as a reference electrode.

The experiments with microelectrodes were done in a two-electrode cell configuration maintained in a Faraday cage made of sheets of aluminium to reduce external noise. Chronoamperometric (Chr), linear-sweep (LSV) and cyclic voltammetric (CV) waveforms were generated by a PAR 175 function generator; a Keithley 485 picoammeter served as a current-measuring device and data were plotted with Hewlett-Packard 7045 B X–Y recorder. For cyclic voltammetry at conventional electrodes an Amel 472 multipolarograph, equipped with a three-electrode assembly, was employed.

The bulk viscosity of the samples was measured with a Ostwald viscosimeter calibrated with pure water.

pH measurements were made by using a Methrohm 605 pH meter.

Procedure

A 20-ml volume of wine, equilibrated at room temperature, was withdrawn with a syringe from a just uncorked bottle, transferred into the cell previously pre-evacuated and equilibrated with nitrogen and kept under a nitrogen atmosphere. As the levels of oxygen in bottled wine are very low [10,14,15], measurements were performed without bubbling nitrogen before the scan. This procedure avoids losses from the solution of volatile components of wine, such as acetic acid and molecular SO_2, which would accompany the normal deoxygenation step.

RESULTS AND DISCUSSION

Probe of the wine matrix with platinum electrodes

Figure 1a shows a typical voltammogram recorded at a platinum disc microelectrode at a low scan rate on a red wine sample. In the cathodic region a well defined reduction wave L characterized by a half-wave potential ($E_{1/2}$) at -0.710 V is observed, whereas the anodic scan mostly shows evidence of two smaller processes. The cathodic and anodic background current discharges, probably due to the reduction and oxidation of the water in the wine, occur behyond -1.2 and $+1.35$ V respectively. This behaviour is typical also of the white wine samples, particularly in the cathodic region.

For comparison, Fig. 1b shows the voltammogram obtained at a conventional platinum electrode for the same red wine sample as in Fig. 1a. The voltammogram shows distorted and badly defined processes before the solvent discharge. Here the response is probably conditioned by the presence of a considerable ohmic drop.

In order to obtain an insight into this aspect, a series of measurements was made with the two different types of electrodes on a wine sample containing deliberately added hexammineruthenium(III) trichloride as probe molecule. This compound is known to undergo a reversible one-electrode process even in media containing organic substances which can partially cover the electrode surface [16,17]. Figure 2 shows cyclic voltammograms recorded with the micro- and macro-electrodes on this type of solution.

The logarithmic analysis, i.e., the slope of the

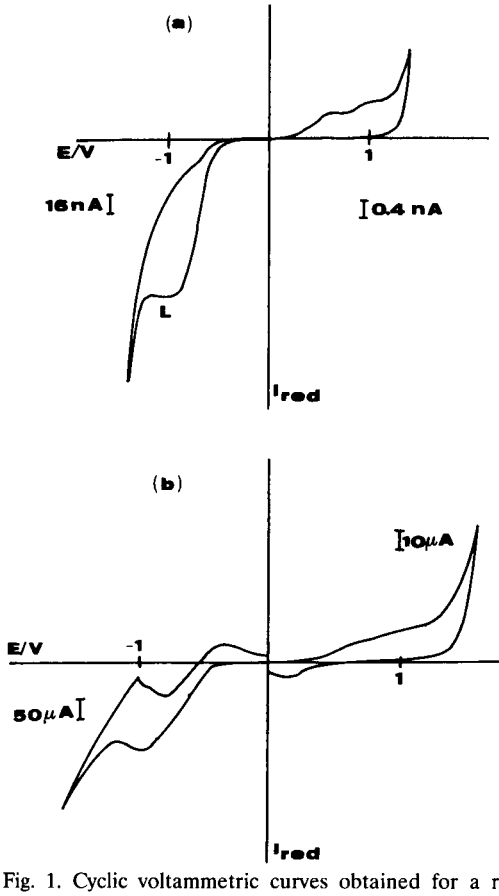

Fig. 1. Cyclic voltammetric curves obtained for a red wine sample (Chianti) at (a) a 12.5-μm radius platinum disc at a scan rate of 10 mV s^{-1} and (b) a 1.5-mm radius disc at a scan rate of 50 mV s^{-1}.

plot of $\log[(i_l - i)/i]$ versus potential (i_l = diffusion limiting current), along with the $E_{1/4} - E_{3/4}$ values for the wave obtained at the micro-

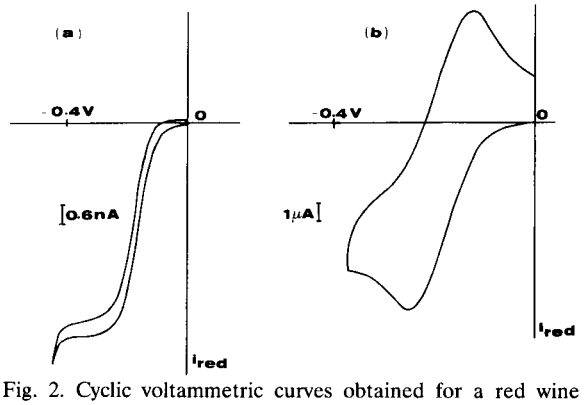

Fig. 2. Cyclic voltammetric curves obtained for a red wine sample fortified with 1 mM $Ru(NH_3)_6Cl_3$ at (a) a 12.5-μm radius platinum disc at a scan rate of 10 mV s^{-1} and (b) a 1.5-mm radius platinum disc at a scan rate of 50 mV s^{-1}.

electrode [18], and the anodic to cathodic peak-potential separations ($E_{p_a} - E_{p_c}$) obtained at the conventional electrode at different scan rates, are reported in Table 1. The values obtained are compared with those found after addition of KCl as supporting electrolyte. From these data it can be inferred that at the microelectrode the responses are almost free from ohmic distortion, whereas at the macroelectrode, in the absence of the supporting electrolyte, considerable distortion arises, similarly to the behaviour observed for wave L in Fig. 1b.

The anodic to cathodic peak separation observed in the reduction process of $[Ru(NH_3)_6]^{3+}$ at the conventional electrode could also be attributed to a slower heterogeneous electron transfer rate, which takes places in wine as a consequence of an inhibition effect caused by

TABLE 1

Effect of solution resistance on voltammetry at micro and conventional electrodes

Electrode radius (cm)	Scan rate (mV s^{-1})	Slope [a] (mV)		$E_{1/4} - E_{3/4}$ [b] (mV)		$E_{p_a} - E_{p_c}$ [c] (mV)	
		Wine	Wine + KCl	Wine	Wine + KCl	Wine	Wine + KCl
12.5×10^{-4}	2	58	58	57	56	–	–
	5	59	59	56	56		
	10	59	58	58	57		
0.15	20					110	60
	50	–	–	–	–	140	70
	100					170	90

[a] Slope of the plot of $\log[(i_l - i)/i]$ vs. E; expected theoretical value at 20°C = $58.1/n$ mV. [b] Expected theoretical value at 20°C = $55.4/n$ mV. [c] Expected theoretical value at 20°C $58.1/n$ mV.

adsorption of organic substances at the electrode surface, in particular of ethanol. Actually, if this were the case a similar phenomenon should also be observed at the microelectrode. However, both the logarithmic analysis and the $E_{1/4} - E_{3/4}$ values reported in Table 1 in the latter instance indicate no departure from the reversible behaviour.

As at the microelectrode slow rates of the heterogeneous electron transfer would lead to larger deviations from the reversible behaviour than that observable at the conventional electrode [18], it can be concluded that the high ($E_{p_a} - E_{p_c}$) values obtained in the latter instance can conceivably be attributed to ohmic drop effects.

Because ethanol is the main organic component of the wine matrix, its effects on the electrochemical reduction of $[Ru(NH_3)]_6]^{3+}$ were examined. For this purpose measurements were made on a 12% (v/v) aqueous ethanol solution containing 1 g l^{-1} KCl. The half-wave potentials and the limiting current values recorded for $[Ru(NH_3)_6]^{3+}$ in water–ethanol (W/E), water (W) and wine are compared in Table 2. The $E_{1/2}$ values differ from one another if taken against SCE, whereas they fall within the experimental error if measured against the $E_{1/2}$ of the ferricinium–ferrocene (Fc^+/Fc) system, as an internal reference, independent on the nature of the solvent [19]. This result means that the above differences in $E_{1/2}$ are due to liquid junction potentials.

The differences observed in the limiting current values can be explained by assuming a change in the diffusion coefficient of the probe molecule due to the change in the viscosities of the media. In Table 2 the measured viscosities and the diffusion coefficients obtained for $[Ru(NH_3)_6]^{3+}$ in the three media are also reported. The diffusion coefficients were calculated from the experimental steady-state limiting current by employing the relationship $i_l = 4nFDcr$ (where n = number of electrons, D = diffusion coefficient, c = bulk concentration, and r = electrode radius) [18]. The product $D\eta$ (where η = viscosity of the medium) for the different media is almost constant, as expected on the basis of the Stock–Einstein equation $D = kT/6\pi\eta r_h$ (k = Boltzmann constant, r_h = hydrodynamic radius of the probe molecule) [20]. Therefore, the decrease in the limiting current values on passing from water to the ethanolic matrices is fully justified on the basis of an increase in the viscosity of the medium.

The overall results obtained indicate that ethanol does not adversely affect the voltammetric behaviour of the probe molecule.

Study of the cathodic region of wine

A series of measurements performed on Italian red and white wines showed that the cathodic wave L in Fig. 1a was present in all the samples analysed; this wave was characterized by a half-wave potential of −0.705 V (±0.010 V), and its height was correlated with the pH of the samples, that is, the higher the wave height, the lower was the pH (see Table 3). Moreover, the voltammograms recorded with a carbon disc electrode on wine samples showed a negative shift of the position of the wave L, and also of the cathodic limit, typical of the overpotential effect for hydrogen evolution on this electrode material with respect to platinum [21].

These results suggested that the cathodic process L could be ascribed to the reduction of

TABLE 2

Half-wave potentials (±2 mV), diffusion limiting currents and diffusion coefficients for $[Ru(NH_3)_6]^{3+}$ and viscosities of different media

Medium	$E_{1/2}$ (V)		$E_{1/2}$ vs. Fc^+/Fc	i_l (nA)	$10^6 D$ ($cm^2\ s^{-1}$)	$10^{-2}\ \eta$ ($kg\ m^{-1}\ s^{-1}$)
	Ru^{3+}/Ru^{2+}	Fc^+/Fc	Ru^{3+}/Ru^{2+}			
W + KCl	−0.183	0.150	−0.333	1.76	7.21	0.98
W/E (12%) + KCl	−0.170	0.164	−0.334	1.31	5.41	1.42
Wine (11.5%)	−0.176	0.156	−0.332	1.22	5.04	1.53

TABLE 3

Comparison between height of wave L and pH for different wine samples

Sample [a]	$i \pm 1$ (nA)	pH ± 0.01
Tocai Friulano		
1	134	3.35
2	130	3.37
Tocai Veneto		
1	147	3.30
2	142	3.32
3	145	3.31
4	164	3.16
Pinot Grigio		
1	138	3.34
2	150	3.27
Verduzzo	176	3.08
Chianti		
1	145	3.31
2	156	3.21
3	150	3.28
Cabernet	144	3.31
Merlot	125	3.45

[a] Numbers represent samples from different Italian companies.

protons released by acidic species present in the samples.

In order to verify this hypothesis, some typical organic acids of different strength and inorganic bases were added to wine. The results obtained indicated that the wave L increased owing to addition of acids characterized by dissociation constants higher than about 10^{-5} M, e.g., tartaric, acetic, citric and lactic acids, whereas it decreased after addition of bases, e.g., sodium hydroxide. A parallel pH check of the same sample showed that a decrease in the pH corresponded to an increase in the wave height and vice versa. Hence the process under investigation should include the reduction of the organic acids characteristic of the matrix, particularly tartaric acid and hydrogentartrate ions present in relatively high concentrations [10]. The contribution of each acid should in principle be discriminated, as the half-wave potential for the reduction of a Brønsted acid to hydrogen becomes increasingly negative as the acidity of the Brønsted acid decreases [22,23]. In contrast, the shape of the cathodic wave L indicates the presence of only one wave, probably due to overlapping reduction processes of the acids involved. These in fact are characterized by dissociation constants that are too close and they probably cannot be differentiated by linear-sweep voltammetry. To demonstrate this hypothesis, measurements were made

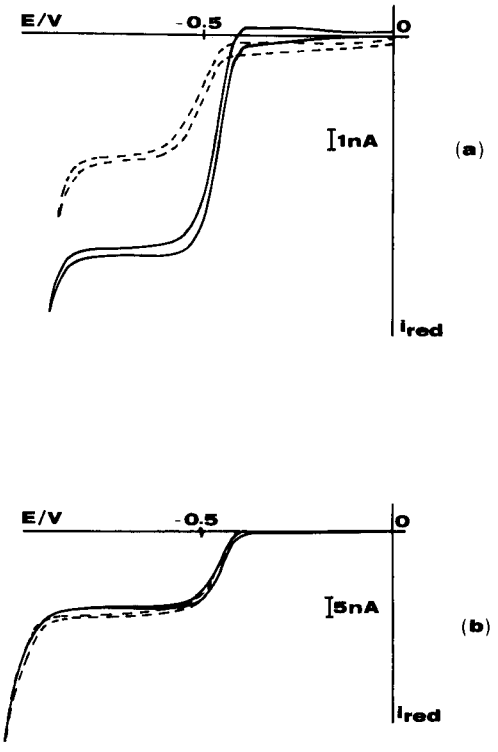

Fig. 3. Cyclic voltammetric curves obtained for solutions in water–ethanol containing 1 g l^{-1} KCl of (a) (full line) 1 mM lactic acid and (dashed line) 1 mM acetic acid and (b) (full line) 1 mM tartaric acid and (dashed line) 1 mM citric acid. 12.5-μm radius platinum disc at a scan rate of 10 mV s^{-1}.

TABLE 4

Half-wave potentials obtained from organic acids at a platinum disc microelectrode (12.5 μm radius) in both water (W) and water–12% (v/v) ethanol (W/E), containing 1 g l^{-1} of KCl

Acid	Equilibrium constants [a]			$E_{1/2(W)}$ ± 0.002 (V)	$E_{1/2(W/E)}$ ± 0.002 (V)
	pKa_1	pKa_2	pKa_3		
Tartaric	3.04	4.37	–	−0.450	−0.445
Citric	3.13	4.76	6.40	−0.455	−0.450
Lactic	3.86	–	–	−0.460	−0.450
Acetic	4.76	–	–	−0.495	−0.490

[a] From [24].

on solutions of tartaric, citric, lactic and acetic acids in water–ethanol mixtures containing KCl to give the typical ionic strength of wine. Fig. 3 shows the voltammograms obtained in these solutions and Table 4 gives the relevant parameter values compared with those observed in aqueous solutions containing KCl as supporting electrolyte.

From Fig. 3 it is evident that the processes are well defined for all the acids investigated, and that they are not inhibited by bubbles of hydrogen formed during the reduction. The half-wave potentials obtained in water–ethanol are more positive (within 10 mV) than those in water. These slight differences can be attributed to the junction potential effect, as demonstrated by referring the $E_{1/2}$ of the acids against that of ferrocene in the two media.

The trend of the half-wave potentials correlates with the relative strength of the different acids employed; the higher the first dissociation equilibrium constant, the less negative is the $E_{1/2}$ value (see Table 4); however, these values from the highest to the lowest fall in the range of about 50 mV, thus precluding the possibility of their separation. A mixture of these acids gave in fact only one wave characterized by an $E_{1/2}$ value that was within the potential range reported in Table 4, depending on the mutual proportions of the different acids.

The half-wave potentials reported in Table 4, even for the weaker acid, are almost 200 mV less negative than the $E_{1/2}$ of wave L observed in wine. Actually, wine is more complex than a water–ethanol containing acids and chloride ions; other substances could play a role in the performance of the electrode, particularly surface-active compounds other than ethanol which may adsorb and consequently change the structure of the double layer. For instance, when to a water–ethanol mixture, containing tartaric acid and KCl, a solution of two other typical components such as sodium metabisulphite and acetaldehyde was added, and after adjusting it to pH 3.3, the cathodic process shifted negatively from −0.445 to about −0.700 V, very close to the $E_{1/2}$ of wave L of wine, whereas the overall limiting current did not change.

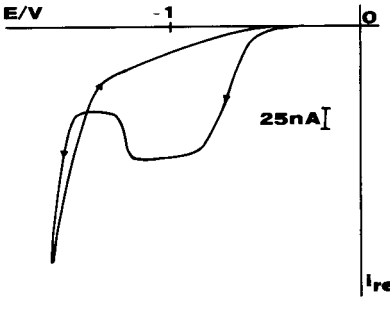

Fig. 4. Cyclic voltammetric curve obtained for a white wine sample (Verduzzo Veneto) at a 12.5-μm radius platinum disc at a scan rate of 10 mV s^{-1}.

The shape of the linear-sweep voltammogram recorded at the microelectrode at a low scan rate is sufficiently sigmoidal for most of samples examined, as expected under non-planar diffusion control [18]. The reduction process responsible for wave L can conceivably be represented by the known CE mechanism:

$$H_nA^{m-} \rightleftharpoons H^+ + H_{(n-1)}A^{(m+1)-} \quad (1)$$

$$H_{(n-1)}A^{(m+1)-} \rightleftharpoons H^+ + H_{(n-2)}A^{(m+2)-} \quad (2)$$

$$H^+ + e- \rightleftharpoons 1/2H_2 \quad (3)$$

where H_nA is a generic polyprotic acid present in wine.

For some white wines the wave exhibited an unexpected current drop, as shown in Fig. 4, probably due to substantial electrode passivation. The most likely explanation may be the formation of a precipitate on the electrode surface, e.g., of the sparingly soluble potassium hydrogen tartrate and calcium tartrate, the precipitation of which can be enhanced by the higher concentration of hydrogen tartrate and tartrate ions achievable at the electrode surface than in the bulk solution, due to the electrode process according to the above general mechanism.

Determination of the total acidity

Voltammetric measurements. The total amount of the species giving rise to the cathodic process L under investigation was quantified by voltammetric titrations by using both the strong base NaOH and tartaric acid as titrants.

In the titrations with NaOH, the decrease in the current height of wave L was recorded as a function of the amount of NaOH added. For concentrations of NaOH ranging from 1 to 20 mM, the calibration graphs were linear, with an average correlation coefficient of 0.998. The end-points were then determined, by extrapolation to zero current, from the straight lines obtained in the titrations. Table 5 gives the acidity values so determined, expressed in meq per litre of NaOH added, for a red wine sample (Chianti) and a white wine sample (Tocai from Friuli). The relative standard deviation of about 1.5% obtained for five determinations indicates the good reproducibility of the method.

In order to verify whether the values obtained could reliably express the titratable acidity of wine, they were compared with those determined in the same samples by using the classical and standardized titration methods with bromothymol blue as indicator and with a potentiometric pH measurement that adopts as titration end-point a pre-established pH value [25]. In this instance the end-point adopted was pH 7.0, as recommended in the standard procedure.

The agreement between the voltammetric and potentiometric results is fairly good, the differences among the acidity values found being within 2%, and the pH value at the end-point of the voltammetric titration being very close to that pre-estabilished in the potentiometric titration (see Table 5). The bromothymol blue method yielded higher acidity values mostly in red wines (+6%), because of the evident difficulty of generating a visible colour change of the dye in this coloured matrix.

TABLE 5

Acidity index of wine

Method	Sample			
	Chianti		Tocai	
	NaOH consumption (meq l^{-1}) [a]	pH [b]	NaOH consumption (meq l^{-1}) [a]	pH [b]
Bromothymol blue	75 (3.8)	7.15	81 (3.5)	7.20
pH-metric	69 (2.1)	7.03	77 (2.3)	7.01
Voltammetric	70 [c] (1.5)	7.07 [d]	78 [c] (1.4)	7.05 [d]

[a] Values in parentheses are R.S.D. (%) from five replicate determinations. [b] Experimental pH at the end of the titrations. [c] Obtained by extrapolation. [d] Obtained after the extrapolated amount of NaOH was added to the wine samples.

TABLE 6

Parameters of calibration graph and titrable acidity values obtained in voltammetric titrations of two wine samples spiked with tartaric acid

Sample	Slope (nA meq $^{-1}$)	Intercept (nA)	r [a]	Titrable acidity (meq l^{-1})
Chianti	4.650	137	0.998	69
Tocai	4.435	151	0.996	76

[a] $n = 8$.

In the titration with tartaric acid (which can also be regarded as a standard addition procedure), an increase in the current height of wave L was recorded as a function of the titrant volume. Tartaric acid was added at concentrations ranging between 4 and 16 meq l^{-1} to obtain linear trends. Table 6 gives the titrable acidity evaluated for the Chianti and the Tocai samples, expressed in meq l^{-1}. The R.S.D. was 2.1% and the mean value thus obtained, compared with that found by voltammetric titration with NaOH, gave differences not greater than 3%.

The influence of oxygen in the determination of the total acidity was also examined. Bottled wine contains very low concentrations of oxygen [10,14,15]; in any case, even considering a wine sample saturated with oxygen (the solubility of O_2 in wine is in the range 5.6–6 ml l^{-1} at 20°C [14]), the limiting current from its reduction, calculated by the equation $i_L = 4nFDcr$ and by assuming $D_0 = 2.12 \times 10^{-5}$ cm^2 s^{-1} [21], ranges from 4.8 to 5.1 nA, which cause a maximum error of 4% for the lowest current reported in Table 3.

Chronoamerometric measurements. To obtain steady-state currents, the measurements can be made by chronamperometry at a time sufficiently long after the imposition of a potential step to a value where the reduction is diffusion controlled.

However, to reach true steady-state conditions,

within 1%, the theoretical analysis predicts 202 s [26] for a disc electrode of 25 μm in diameter and assuming 10^{-5} cm^2 s^{-1} as an average diffusion coefficient for the species involved. Conversely, if a closeness of about 5% is taken as a good approximation to the steady-state current, the time required decreases to 10 s, which is a good arrangement for faster measurements.

Figure 5a shows a typical transient recorded under the latter conditions. The comparison between the experimental currents obtained by chronoamperometry and linear-sweep voltammetry, also reported in Fig. 5a, indicate that the former technique gave current responses 3.4% higher than the latter; hence the contribution of the time-dependent term falls within the theoretical approximation estimated above. It was also necessary to select the base potential, to avoid interferences, and a delay between steps to allow the electrode activation. The waveform applied that gave the best performances is reported in Fig. 5b.

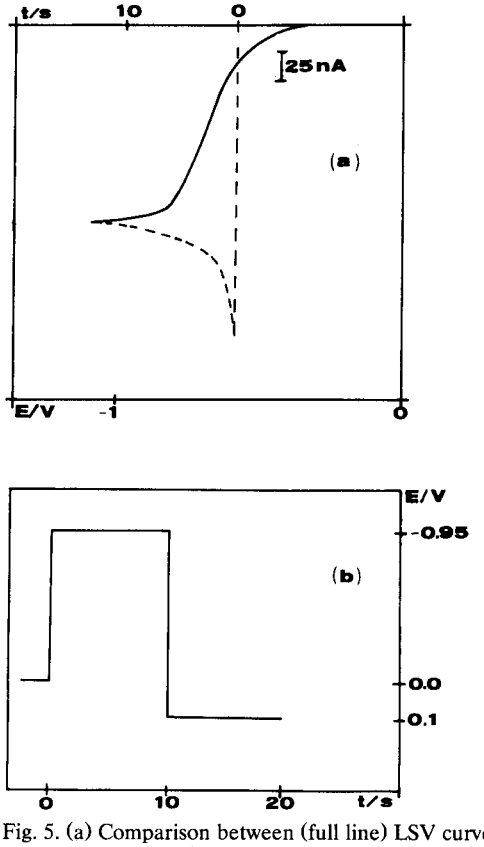

Fig. 5. (a) Comparison between (full line) LSV curve at a scan rate of 10 mV s^{-1} and (dashed line) Chr response to a potential step from 0.00 to −0.95 V vs. SCE obtained for a wine sample at a 12.5-μm radius platinum disc. (b) Waveform applied in the chronoamperometric experiments.

TABLE 7

Chronoamperometric currents recorded for two wine samples

Sample [a]	i [b]	No. of cycles [c]									
		1	2	3	4	5	6	7	8	9	10
A	i_{Chr}	181	176	174	173	172	171	171	171	171	170
	i_{1-5}			175.2 (2.04)							
	i_{1-10}						173	(1.93)			
B	i_{Chr}	162	156	154	153	153	153	153	153	152	152
	i_{1-5}			155.6 (2.43)							
	i_{1-10}						154.1	(1.95)			

[a] A = Verduzzo; B = Chianti. [b] i_{1-5} and i_{1-10} refer to the mean values for 5 and 10 cycles, respectively. [c] Valves in parentheses are R.S.D. (%).

To obtain a datum point, the cycle was generally repeated five times without polishing the electrode; lower current values were observed for the cycles after the first, caused by a slight fouling of the electrode, and the R.S.D. found was within 2.5%. Ten replicates, however, gave a better R.S.D., i.e., less than 2%, the current values after 4–5 cycles being almost constant (R.S.D. < 0.5%). This result suggests the choice of a larger number of cycles than five; however, the time for the analysis would become too long. Hence five cycles can represent a good compromise between reproducibility and time consumption for the analysis. Table 7 gives typical results for a datum point.

The chronoamperometric determination of the total acidity was made by titration with NaOH, using the same concentration range as reported for linear-sweep voltammetric measurements. Each titration point was obtained by running, after the NaOH addition, a series of five chronoamperometric measurements with the waveform shown in Fig. 5b. The mean value after each addition plotted against the volume of titrant gave straight lines with an average correlation coefficient of 0.997. Figure 6 shows typical tran-

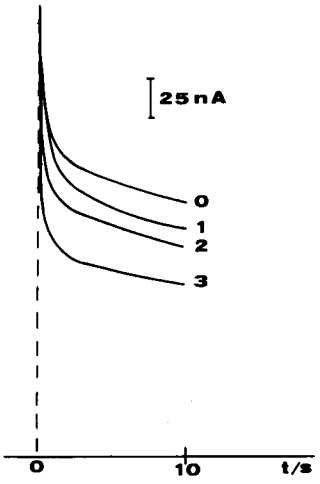

Fig. 6. Chronoamperometric responses to a potential step as in Fig. 5b recorded at a 12.5 μm-radius platinum disc in the titration of a wine sample with NaOH. (0) blank and (1), (2) and (3) with 5, 10 and 20 mM NaOH, respectively.

sients for three additions of NaOH to a sample of wine. The acidity values found by this method were compared with those determined on the same samples by voltammetric titration with NaOH, and the agreement was satisfactory. For instance, for a white wine sample (Verduzzo from Veneto) the NaOH consumption for linear-sweep voltammetry was 62.04 meq l^{-1} and for chronoamperometry 62.56 meq l^{-1}, the difference being $< 1\%$.

The authors thank Professor I. Moret for helpful discussions and Mr. D. Rudello for experimental assistance. Financial aid from the Italian Nazional Research Council (CNR) and Ministry of University (MURST), Rome, is gratefully acknowledged.

REFERENCES

1 R.M. Wightman and D.O. Wipf, in A.J. Bard (Ed.), Electroanalytical Chemistry, Vol. 15, Dekker, New York, 1989, p. 267.
2 M.I. Montenegro, M.A. Queiros and J.L. Daschbach (Eds.), Microelectrodes. Theory and Applications (NATO ASI Series), Kluwer, Dordrecht, 1991.
3 S. Daniele, M.A. Baldo, P. Ugo and G.A. Mazzocchin, Anal. Chim. Acta, 219 (1989) 9.
4 S. Daniele, M.A. Baldo, P. Ugo and G.A. Mazzocchin, Anal. Chim. Acta, 219 (1989) 19.
5 S. Daniele, M.A. Baldo, P. Ugo and G.A. Mazzocchin, Anal. Chim. Acta, 238 (1990) 357.
6 A.M. Bond, M. Fleischmann and J. Robinson, J. Electroanal. Chem., 168 (1984) 299.
7 A.M. Bond, M. Fleischmann and J. Robinson, J. Electroanal. Chem., 180 (1984) 257.
8 M.J. Pena, M. Fleischmann and N. Garrard, J. Electroanal. Chem., 220 (1987) 31.
9 K.B. Oldham, J. Electroanal. Chem., 250 (1988) 1.
10 M.A. Amerine, H.W. Berg, R.E. Kunkee, C.S. Ough, V.L. Singleton and A.D. Webb, The Technology of Wine Making, AVI, Westport, CT, 1982.
11 J. Ribereau-Gayon and E. Peynaud, Analisi e Controllo dei Vini, Edizioni Agricole, Bologna, 1966.
12 R. Pladziewicz, T. Meyer, J.A. Broomhead and H. Taube, Inorg. Chem., 12 (1973) 639.
13 M. Fleischmann, F. Lasserre, J. Robinson and D. Swan, J. Electroanal. Chem., 177 (1984) 97.
14 L. Usseglio-Tomasset, Chimica Enologica, AEB, Brescia, 1978.
15 T. De Rosa and I. Moret, Riv. Vitic. Enol. Conegliano, 5 (1983) 219.
16 E. Sabatani, I. Rubinstein, R. Maoz and J. Sagiv, J. Electroanal. Chem., 219 (1987) 365.
17 E. Sabatani and I. Rubinstein, J. Phys. Chem., 91 (1987) 6663.
18 A.M. Bond, K.B. Oldham and C.G. Zoski, Anal. Chim. Acta, 216 (1989) 177.
19 G. Gritzner and J. Kuta, Pure Appl. Chem., 56 (1984) 461.
20 A. Einstein, Ann. Phys., 19 (1906) 289.
21 R.N. Adams, Electrochemistry at Solid Electrodes, Dekker, New York, 1969.
22 W.C. Barrette, H.V. Johnson and D.T. Sawyer, Anal. Chem., 56 (1984) 1890.
23 S. Daniele, P. Ugo, G.A. Mazzocchin and G. Bontempelli, Anal. Chim. Acta, 173 (1985) 141.
24 A.E. Martell and R.M. Smith, Critical Stability Constants, Vol. 3, Plenum, New York, 1977.
25 Ministero Agricoltura e Foreste, Metodi Ufficiali per i Mosti, i Vini e Gli Aceti, Instituto Poligrafico dello Stato, Rome, 1965.
26 C.G. Zoski, A.M. Bond, E.T. Allinson and K.B. Oldham, Anal. Chem., 62 (1990) 37.

Analytica Chimica Acta, 272 (1993) 161–167
Elsevier Science Publishers B.V., Amsterdam

Synthesis of 2-[2-(4-methylquinolyl)azo]-5-diethylaminophenol and its use for the spectrophotometric determination of nickel

Tomosuke Ishizuki, Masayoshi Tsuzuki, Akio Yuchi, Tadao Ozawa, Hiroko Wada and Genkichi Nakagawa

Department of Applied Chemistry, Nagoya Institute of Technology, Showa, Nagoya 466 (Japan)

(Received 3rd January 1992; revised manuscript received 18th May 1992)

Abstract

2-[2-(4-Methylquinolyl)azo]-5-diethylaminophenol (QADP) was synthesized and the acidity constants of the reagent in 50% (v/v) ethanol and reactions with various metal ions were studied. QADP and its chelates are extracted into chloroform and the molar absorptivities of most complexes are higher than 10^5 l mol^{-1} cm^{-1}. QADP was applied to the selective spectrophotometric determination of nickel. Nickel (0.4–7.2 μg) could be determined by masking cobalt as the Co(III)–ammine complex.

Keywords: UV–Visible spectrophotometry; Nickel

Various heterocyclic azo reagents have been proposed for the spectrophotometric determination of nickel. The molear absorptivities of the nickel chelates with 1-(2-pyridylazo)-2-naphthol (PAN) [1], 1-(2-thiazolylazo)-2-naphthol (TAN) [2] and 1-(2-pyridylazo)-2-naphthol-6-sulphonic acid (PAN-6-S) [3] are about 5×10^4 l mol^{-1} cm^{-1}, whereas those of nickel chelates with 2-[2-(3,5-dibromopyridyl)azo]-5-dimethylaminobenzoic acid (3,5-diBr-PAMB) [4] and 2-(2-benzothiazolylazo)-5-dimethylaminobenzoic acid (BTAMB) [5] are $> 10^5$ l mol^{-1} cm^{-1}. In the methods with 3,5-diBr-PAMB and BTAMB, however, the tolerable amount of cobalt is small.

In 1975, Gusev et al. [6] synthesized 5-(2-quinolylazo)-2-ethylamino-*p*-cresol (2-QAAC) and applied it to the determination of zinc in magnesium alloys. It was expected that *o*-hydroxyazo compounds with a quinoline ring would be more sensitive than those with a pyridine ring. The preparation of 2-quinolylazo compounds, however, is tedious, so that their analytical applications have not been studied in detail.

In this study, a new quinolylazo derivative, 2-[2-(4-methylquinolyl)azo]-5-diethylaminophenol (QADP), was synthesized. This reagent could be prepared much more easily than 2-QAAC. Its application to the spectrophotometric determination of several metals was examined, and the determination of nickel in the presence of cobalt was found to be attractive.

Correspondence to: H. Wada, Department of Applied Chemistry, Nagoya Institute of Technology, Showa, Nagoya 466 (Japan).

EXPERIMENTAL

Preparation of 2-[2-(4-methylquinolyl)azo]-5-diethylaminophenol

The steps involved in the synthesis are as shown in Scheme 1.

The starting material, 2-amino-4-methylquinoline, is not commercially available. The conven-

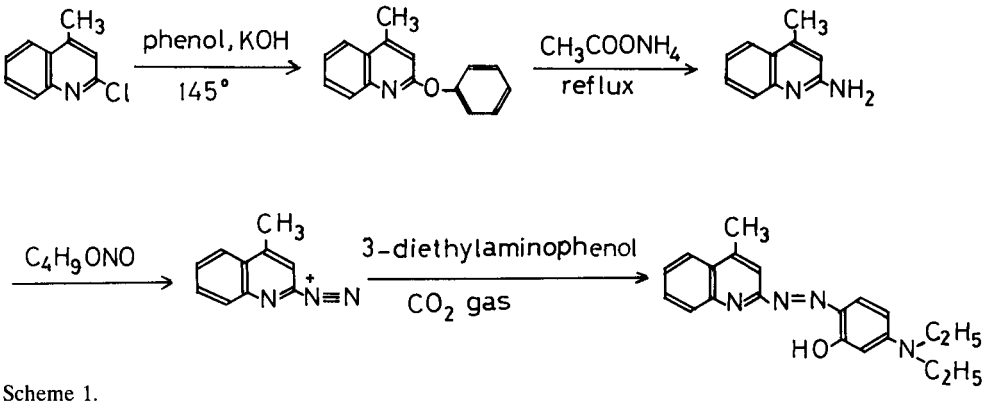

Scheme 1.

tional preparation, which utilizes sodium amide in boiling xylene, is dangerous and gives the amine in low yield [7]. Therefore, a mild reaction was studied for introducing an amino group on the 2-position of quinoline ring. The procedure described previously [8,9] was modified. Potassium hydroxide (3.2 g) and 2-chloro-4-methylquinoline (10 g) were added to molten phenol (50 g) and the mixture was heated on hot-plate at 145°C for 1 h. After cooling, ammonium acetate (90 g) was added and the mixture was refluxed for 4 h. Sodium hydroxide solution (30%, w/v) was added to the mixture with stirring. Crude 2-amino-4-methylquinoline precipitated and was recrystallized from toluene (yield 60%, m.p. 132.5°C; calculated for $C_{10}H_{10}N_2$, C 75.92, H 6.37, N 17.71; found, C 76.14, H 6.28, N 17.78%).

To prepare 2-[2-(4-methylquinolyl)azo]-5-diethylaminophenol, 2-amino-4-methylquinoline in diethyl ether was diazotized with freshly prepared butyl nitrite in the presence of sodium amide under reflux for several hours. After cooling of the solution, 2-diazo-4-methylquinoline was filtered off, washed with diethyl ether and stored in a desiccator over phosphorus pentoxide. Sodium (0.2 g) was added to an ethanol (150 ml) solution of 3-diethylaminophenol (3.4 g) and the diazonium compound (3.5 g). Carbon dioxide was bubbled through the solution for 3 h with stirring. The precipitate was filtered off and washed with a large amount of water. Crude QADP was recrystallized from methanol (decomposed at 230°C; calculated for $C_{20}H_{22}N_4O$, C 71.83, H 6.63, N 16.75; found, C 71.78, H 6.72, N 16.51%).

Reagents and apparatus

QADP reagent was dissolved in ethanol to give a 5×10^{-4} M solution.

Nickel(II), copper(II) and zinc(II) solutions were prepared by dissolving the metals (99.99% purity) in dilute nitric acid. Cobalt(II), cadmium (II) and chromium(III) solutions were prepared from the nitrates, manganese solution from manganese chloride, iron(III) solution from ammonium iron(III) sulphate and vanadium(V) solution from ammonium metavanadate.

The pH buffers used were dilute hydrochloric acid (pH < 2), 1.25 M chloroacetic acid–sodium chloroacetate (pH 2.0–3.5), 1.25 M acetic acid–sodium acetate (pH 3.7–6.0), 0.25 M 3-(*N*-morpholino)ethanesulphonic acid–potassium hydroxide (pH 5.5–7.0), 0.25 M 3-(*N*-morpholino)propanesulphonic acid–potassium hydroxide (pH 6.5–7.9), 1.25 M ammonia–ammonium chloride (pH 8.0–10.0) and carbonate-free sodium hydroxide solution (pH > 10.0).

All chemicals were of analytical-reagent grade. Water was redistilled from a hard glass vessel or purified with a Toray ultra-pure water manufacturing device (Toraypure LV-10T).

A Shimadzu UV-250 spectrophotometer, a Denki Kagaku Keiki IOC-10 pH meter and a Seiko Denshi Kogyo SAS-727 atomic absorption spectrometer were used.

Recommended procedure for the determination of nickel

Place 2 ml of 5 M ammonia–ammonium chloride buffer solution (pH 9) and 0.5 ml of 6%

(w/v) sodium pyrophosphate in a 100-ml separating funnel. Add 0.5 ml of a sample solution, which should contain 0.4–7.2 μg of nickel, then 0.5 ml of 0.4% (w/v) sodium periodate solution and 1 ml of 5×10^{-4} M QADP solution. Extract with 10 ml of chloroform by shaking for ca. 2 min. Transfer 7 ml of this extract into another separating funnel, add 7 ml of 0.01 M sodium diethyldithiocarbamate solution and shake for 20 min. Measure the absorbance of the organic phase at 547 or 584 nm in a 1-cm cell against chloroform.

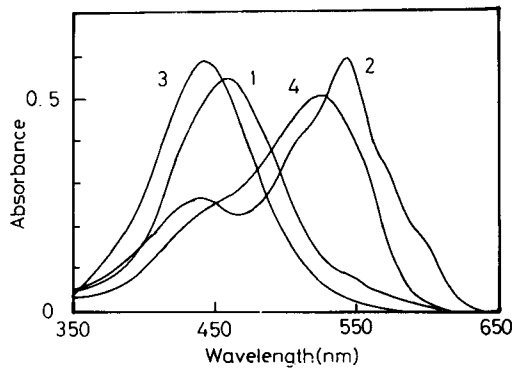

Fig. 1. Absorption spectra of QADP at different pH: (1) 1.3 M HCl; (2) pH 3.0; (3) pH 7.3; (4) pH 12.9. Conditions: 1.1×10^{-5} M QADP, 0.1 M KNO_3, 50% (v/v) ethanol.

RESULTS AND DISCUSSION

Acidity constants of QADP

As QADP is sparingly soluble in water, the acidity constants were determined in 50% (v/v) aqueous ethanol. The absorption spectra of QADP solutions at different pH values are shown in Fig. 1. The QADP solution is yellow (λ_{max} = 457 nm) at "pH" $\approx$ 0, reddish violet (λ_{max} = 544 nm) at "pH" 2–3, yellow (λ_{max} = 446 nm) at "pH" 6–10 and red (λ_{max} = 526 nm) at "pH" $\approx$ 13. The dissociation equilibria of QADP can therefore be written as in Scheme 2.

The three successive adicity constants are defined by $K_{a_1} = a_{H^+}[H_2L^+]/[H_3L^{2+}]$, $K_{a_2} = a_{H^+}[HL]/[H_2L^+]$ and $K_{a_3} = a_{H^+}[L^-]/[HL]$, where a_{H^+} is the apparent activity of hydrogen ion measured in 50% ethanol solution by means of a pH meter equipped with a glass electrode which was calibrated with the two aqueous standard buffers. The acidity constants K_{a_2} and K_{a_3} were determined from the relationship between absorbance and "pH" by using a non-linear least-squares method. The pK_{a_1} value was too small to be accurately determined. The acidity constants obtained are given in Table 1 together with those of 2-(5-bromo-2-pyridylazo)-5-diethylaminophenol (5-Br-PADAP). QADP has a higher basicity than 5-Br-PADAP.

Reactions with metal ions

As shown in Table 2, QADP reacts with various metal ions to form reddish violet chelates. These chelates are sparingly soluble in water, but are soluble in some organic solvents such as ethanol and chloroform. The absorption spectra

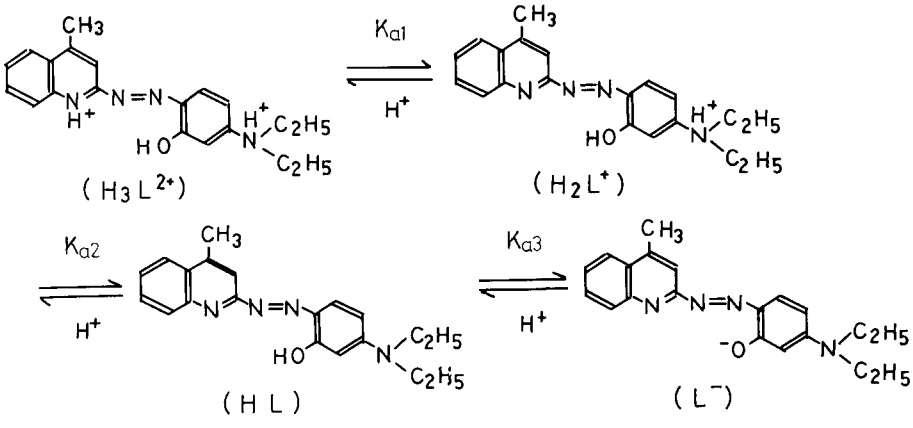

Scheme 2.

TABLE 1

Aciditiy constants at an ionic strength of 0.1 M (KNO_3) in 50% (v/v) aqueous ethanol at 25°C

Acidity constant	QADP	5-Br-PADAP [a]
pK_{a_1}	<1	0.1
pK_{a_2}	3.99	2.02
pK_{a_3}	12.0	11.3

[a] From [10].

of some metal chelates in 50% (v/v) ethanol are shown in Fig. 2. From the results of the molar ratio and continuous variation methods, most metal ions examined predominantly form ML_2 chelates, except vanadium(V), which forms an ML chelate. Copper(II) forms an ML chelate with QADP in acidic medium and an ML_2 chelate in neutral or alkaline medium as with pyridylazophenols. The molar absorptivities of the ML_2 complexes except for that of Co(III) are appreciably higher than 10^5 l mol^{-1} cm^{-1}.

Extraction of metal ions with QADP into chloroform was also studied. Some typical spectra of QADP complexes in chloroform are shown in Fig. 3 and absorption maxima and molar absorptivities are summarized in Table 2. Except for the

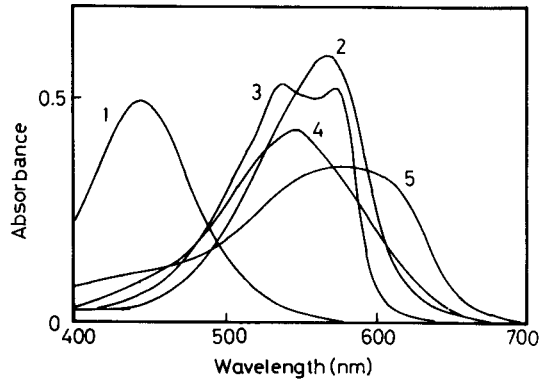

Fig. 2. Absorption spectra of QADP complexes in the presence of excess metal ions [9.4×10^{-6} M QADP, 0.05 M acetic acid–sodium acetate (pH 6.0), 50% (v/v) ethanol]. 1 = QADP only; 2 = Cu, 2.0×10^{-5} M; 3 = Ni, 2.1×10^{-5} M; 4 = Co, 2.1×10^{-5} M, in the presence of ascorbic acid; 5 = Co, 2.1×10^{-5} M, in the presence of KIO_4.

Co(III) complex, the absorptivities of the metal chelates in chloroform were slightly lower than those in ethanol. The pH dependence of the extraction was examined by measuring the absorbance of the chloroform phase (Fig. 4). The pH range of constant absorbance was the widest (> 5) for nickel among the metal ions examined.

TABLE 2

Absorption maxima and molar absorptivities of metal–QADP complexes

Metal ion	Water–ethanol (50%, v/v)		Chloroform		Mole ratio M:L
	λ_{max} (nm)	ϵ ($\times10^4$ l mol^{-1} cm^{-1})	λ_{max} (nm)	ϵ ($\times10^4$ l mol^{-1} cm^{-1})	
None	446	5.2	454	5.2	–
Cu(II)	568	6.4	568	4.9	1:1
	568	11.2	568	9.7	1:2
Ni(II)	539	12.8	547	10.3	1:2
	574	12.4	584	8.0	
Co(II) [a]	545	11.3	548	10.4	1:2
Co(III) [b]	580	7.5	580	8.2	1:2
Fe(II) [a]	565	10.2	557	8.2	1:2
	764	2.1	771	1.9	
Zn(II)	533	12.2	540	11.5	1:2
	565	13.2	573	10.3	
Cd(II)	532	12.2	540	10.9	1:2
	569	15.1	574	10.6	
V(V)	616	6.3	–	–	1:1

[a] In the presence of ascorbic acid. [b] In the presence of KIO_4.

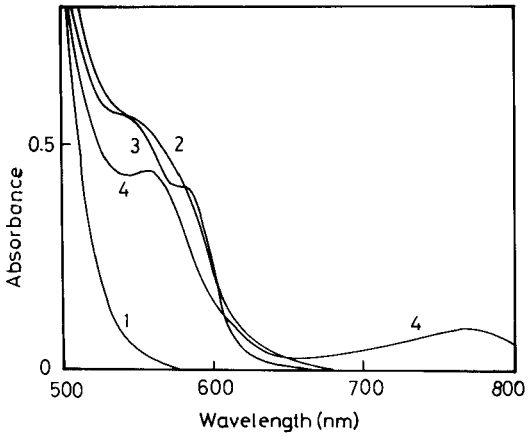

Fig. 3. Absorption spectra of QADP and its metal complexes extracted into chloroform (4.9×10^{-5} M QADP). 1 = QADP only, pH 8.0; 2 = Cu, 5.2×10^{-6} M, pH 9.1; 3 = Ni, 4.9×10^{-6} M, pH 8.3; 4 = Fe, 5.0×10^{-6} M, pH 5.7, in the presence of ascorbic acid.

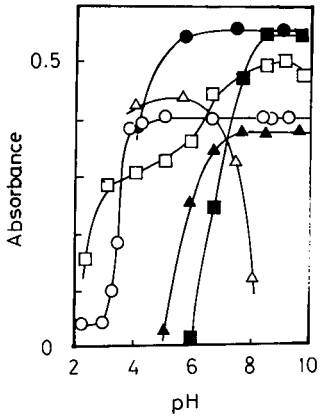

Fig. 4. Effects of pH on extraction of metal–QADP complexes in chloroform (5.0×10^{-5} M QADP, 5.0×10^{-6} M metal ion). ○ = Ni(II); ● = Co(II); △ = Fe(II); ▲ = Zn(II); □ = Cu(II); ■ = Cd(II). Ascorbic acid was added to the aqueous phase for Co(II) and Fe(II) and potassium sodium tartrate for Zn(II) and Cd(II).

Experimental conditions for the determination of nickel

Shaking for 2 min was sufficient for quantitative extraction. Constant and maximum absorbance was obtained in the presence of at least a three-fold excess of the reagent. The nickel chelate of QADP has absorption maxima at 547 and 584 nm. By measuring the absorbance at 547 nm a higher sensitivity was obtained, but the reagent blank was slightly larger; absorbance at 584 nm was measured for the determination. Under the recommended conditions, the calibration graph for nickel was linear up to 1.2×10^{-5} M. The detection limit (3σ) for nickel was 8×10^{-7} M. The relative standard deviation for eight replicate determinations of 5.34 μg of nickel was 0.6%.

Effects of other metal ions

QADP reacts with various metal ions, most of which interfere with the determination of nickel. Interference especially from cobalt is critical. In previous studies with 3,5-diBr-PAMB [4] and BTAMB [5], sodium pyrophosphate and sodium oxalate, respectively, were used for masking of cobalt. However, tolerable limits for cobalt were 0.3 μg in the BTAMB method and 1.0 μg in the 3,5-diBr-PAMB method. Previously interference from cobalt could be eliminated by the formation of the cobalt(III)–amminecomplex in the aqueous

TABLE 3

Results of back-washing with various solutions

Metal ion	Absorbance at 584 nm						
	Before washing	After washing with					
		EDTA [a]	KI [b]	$Na_2S_2O_3$ [c]	HCl [d]	AcOH–AcONa [e]	DDTC [f]
Cu(II)	0.390	0.282	0.405	0.342	0.020	0.240	0.010
Zn(II)	0.390	0.078	0.116	0.120	0.020	0.020	0.007
Cd(II)	0.494	0.018	0.028	0.022	0.020	0.020	0.008
Fe(III)	0.164	0.062	0.304	0.182	0.138	0.158	0.036
Ni(II)	0.402	0.408	0.410	0.405	0.314	0.410	0.400

[a] 1×10^{-4} M, pH 6. [b] 0.05 M, pH 6. [c] 0.01 M, pH 6. [d] 0.01 M. [e] 0.05 M, pH 4. [f] 0.01 M, pH 9.

TABLE 4

Determination of nickel in artificial samples

Taken (μg)						Ni found (μg)
Ni	Co	Cu	Fe	Zn	Cd	
1.50	14.2					1.51
4.32	88.4					4.42
1.50	14.2	1.59				1.53
1.50	14.2		13.9			1.52
5.76	44.3	5.0	46.5	8.8	16.9	5.86

phase[3], and the masking procedure was applied in the present method. Potassium periodate (0.5 ml of 0.4% solution) and 2 ml of 5 M ammonia–ammonium chloride buffer were sufficient for masking Co up to 90 μg. The absorbance of the nickel chelate did not decrease. The masking with ammonia could not be applied to the method using 3,5-diBr-PAMB and BTAMB because of deterioration of the absorbance of the nickel chelate[4,5].

To eliminate interferences from other metal ions such as Cu(II), Zn(II), Cd(II) and Fe(III), back-washing of the organic phase with various complex-forming agents was studied. The results are given in Table 3. Using 0.01 M sodium diethyldithiocarbamate (DDTC) solution, only the nickel complex remained in the organic phase. If DDTC was used as a masking reagent in the aqueous phase, the extraction of nickel–QADP chelate was retarded. Although the iron(III)–QADP complex remained slightly in the chloroform phase, it could be masked by adding 0.5 ml of 6% (w/v) sodium pyrophosphate solution to the aqueous phase before addition of QADP. The tolerable amounts of metal ions in the determination of 4 μg of nickel were as follows: 90 μg of Co, at least 250 μg of Fe, 15 μg of Cu, 40 μg of Zn, 80 μg of Cd, 20 μg of Mn and at least 40 μg of Cr.

Determination of nickel in artificial samples

The method was applied to the determination of nickel in artificial samples containing Co, Cu and Fe and satisfactory results were obtained (Table 4).

The results of the extraction–spectrophotometric determination of nickel with various heterocyclic azo compounds are summarized in Table 5. The present reagent was much more sensitive than PAN and TAN. Although the sensitivity is less than those of the 3,5-diBr-PAMB and BTAMB methods, the proposed method is selective and very simple for the determination of nickel in the presence of moderate amounts of cobalt.

TABLE 5

Extraction–spectrophotometric determination of nickel with various heterocyclic azo compounds in chloroform

Reagent	Conditions	λ_{max} (nm)	ϵ ($\times 10^4$ l mol^{-1} cm^{-1})	Ref.
QADP	pH 4–10	584	8.0	This work
		547	10.3	
PAN	pH 4–10	570	5.0	1
TAN	pH 4–10	595	4.0	2
PAN-6S	pH 4–10, TPA [a]	572	5.6	3
3,5-DiBr-PAMB	pH 4.5–10	618	14.5	4
BTAMB	pH 8.5–9.5	635	11.7	5

[a] Tetraphenylarsonium chloride.

REFERENCES

1 G. Nakagawa and H. Wada, Nippon Kagaku Zasshi, 84 (1963) 636.
2 H. Wada and G. Nakagawa, Anal. Lett., 1 (1968) 687.
3 K. Ohshita, H. Wada and G. Nakagawa, Anal. Chim. Acta, 140 (1982) 291.
4 T. Katami, T. Hayakawa, M. Furukawa and S. Shibata, Analyst, 109 (1984) 731.
5 T. Katami, T. Hayakawa, M. Furukawa and S. Shibata, Anal. Sci., 1 (1985) 33.
6 S.I. Gusev, E.M. Nikolaeva and E.A. Pirozhkova, Zh. Anal. Khim., 30 (1975) 3.
7 R.N. Shreve, E.H. Riechers, H. Rubenkoenig and A.H. Goodman, Ind. Eng. Chem., 32 (1940) 177.
8 J.C.E. Simpson and P.H. Wright, J. Chem. Soc., 1707 (1948).
9 G. Jacini, Gazz. Chim. Ital., 70 (1940) 621.
10 D.A. Johnson and T.M. Florence, Talanta, 22 (1975) 253.

Analytica Chimica Acta, 272 (1993) 169–178
Elsevier Science Publishers B.V., Amsterdam

Extraction constants of Te^{4+}, Sb^{3+}, Se^{4+}, MoO_2^{2+} and Ga^{3+} with dithiocarbamates

Jem-Mau Lo, Chu-Chieh Lin and Si-Jung Yeh

Institute of Nuclear Science, National Tsing Hua University, Hsinchu 30043 (Taiwan)

(Received 12th June 1992)

Abstract

The extraction constants of metal dithiocarbamates [$M(DTC)_m$] were determined by a substoichiometric extraction method. The metal ion under investigation together with a reference metal ion whose extraction constant is certified was studied in 0.1 and 1 M HCl; both metal ions were labelled with radioisotopes and kept at the same concentration. A series of substoichiometric amounts of dithiocarbamate ligand together with chloroform were mixed with the solution containing the two metal ions; the solution mixtures were shaken until equilibrium of the metal–DTC reactions was attained. The distribution ratios of the two metals between the organic and aqueous phases were simultaneously determined by comparing the respective radioactivities of aliquots from both phases. The extraction constants of the metal dithiocarbamates could be obtained from the observed distribution ratios after calculation according to a previously derived equation. The logarithmic extraction constants defined as $1/m \log\{[M(DTC)_m]/[M^{m+}][DTC^-]^m\}$ for Te^{4+}, Sb^{3+}, Se^{4+}, MoO_2^{2+} and Ga^{3+} were found to be 15.1, 15.0, 10.7, 9.3 and 8.1 for the diethyldithiocarbamate form and 15.0, 13.2, 10.3, 8.4 and 6.4 for the tetramethylenedithiocarbamate form.

Keywords: Dithiocarbamates; Extraction constants; Metal dithiocarbamates

Sodium dithiocarbamate (DTC), first synthesized in the 1950s [1], has been extensively used as a powerful separation agent for metals in waters and aqueous solutions. Many analytical studies dealing with this ligand have been reported. Two DTC derivatives, diethyldithiocarbamate (DDC) and tetramethylenedithiocarbamate [also named pyrrolidinecarbodithiolate and pyrrolidinedithiocarbamate (PDC)] have been mostly employed in practice. Compared with other ligands DTC can form very stable complexes or chelates with many metal ions, particularly transition metals. It is of general interest to understand the degree of stability of the various metal–DTC complexes. Extraction constants or two-phase stability constants are often used to denote the degree of stability of metal–DTC complexes. There have been several investigations [2–6] of the extraction order or the extraction constants of a variety of metal ions with DTC. Likussar and Boltz [2,3] used the maximum of the continuous variations plot in terms of normalized absorbance to determine the extraction constants of some metal–DTC complexes. Wyttenbach and Bajo [4] determined the extraction order of several metal DDCs by a radiometric method. Previously, a two-step extraction technique [5] and a substoichiometric extraction technique [6] for the determination of the extraction constants of metal ions with DTC were reported. The former was designed for determining extraction constants for metal–DTC complexes of low stability and the latter for determining extraction constants for very stable metal–DTC complexes. In essence,

Correspondence to: Jem-Mau Lo, Institute of Nuclear Science, National Tsing Hua University, Hsinchu 30043 (Taiwan).

the two-step extraction technique is a direct method and the substoichiometric extraction technique is a comparative method to determine the extraction constants of metal–DTC complexes. Extraction constants of various metal–DTC complexes cover several orders of magnitude. It is not easy to determine the extraction constants of metal–DTC complexes of high stability by general analytical methods, as indicated by Likussar and Boltz [2,3]. The substoichiometric extraction method suggested [6] was found to be able to resolve this problem and was successfully applied to determine accurately the extraction constants of Hg^{2+}, Bi^{3+}, In^{3+}, Cd^{2+}, As^{3+} and Fe^{2+} with DTC.

This work is an extension of the application of the substoichiometric extraction technique [6] to determine the extraction constants of Te^{3+}, Sb^{3+}, Se^{4+}, MoO_2^{2+} and Ga^{3+} with dithiocarbamates (including DDC and PDC). All metal ions were carefully controlled at the specified valent states to exclude the presence of their higher oxidation states.

THEORY

In this work, the determination of an unknown extraction constant of a certain metal–DTC complex is based on the use of a metal–DTC complex as a reference whose extraction constant is certified. Here M^{m+} is denoted as the metal ion of interest whose extraction constant with DTC is to be determined and N^{n+} as the metal ion with a certified extraction constant with DTC. $K_{M(DTC)_m}$ and $K_{N(DTC)_n}$ are the extraction constants of M^{m+} and N^{n+} with DTC, defined as $[M(DTC)_m]_{org}/[M^{m+}][DTC^-]^m$ and $[N(DTC)_n]_{org}/[N^{n+}][DTC^-]^n$, respectively. In experiments, both metal ions, M^{m+} and N^{n+}, are labelled with respective radioisotopes and adjusted to the same concentration at 1×10^{-3} M in 0.1 or 1 M hydrochloric acid. Aliquots of the solution mixture of the metal ions are taken and extracted into chloroform with a series of substoichiometric amounts of DTC ligand. Shaking for a sufficiently long time is needed for the metal–DTC extraction to attain equilibrium. Equal aliquots from both phases are then withdrawn for radioactivity measurements. The distribution ratios of either the metal M or the metal N, denoted as D_{*M} and D_{*N}, can thus be simultaneously determined. Thereafter, $K_{M(DTC)_m}$ can be conveniently but accurately calculated from the certified $K_{N(DTC)_n}$ value and the experimental values, D_{*M} and D_{*N}, in accordance with the equation derived previously [6]:

$$R^m = AK_{M(DTC)_m} + BK_{M(DTC)_{m-1}Cl}(D_{*N})^{-1/n} + CK_{M(DTC)_{m-2}Cl_2}(D_{*N})^{-2/n} + \cdots \quad (1)$$

where

$$R = (D_{*M})^{1/m}/(D_{*N})^{1/n}$$

$$A = \frac{(\alpha_{N^{n+}})^{m/n}}{[K_{N(DTC)_n}]^{m/n}(\alpha_{M^{m+}})}$$

$$B = \frac{(\alpha_{N^{n+}})^{(m-1)/n}[Cl^-]}{[K_{N(DTC)_n}]^{(m-1)/n}(\alpha_{M^{m+}})}$$

$$C = \frac{(\alpha_{N^{n+}})^{(m-2)/n}[Cl^-]^2}{[K_{N(DTC)_n}]^{(m-2)/n}(\alpha_{M^{m+}})}$$

and $\alpha_{M^{m+}}$ and $\alpha_{N^{n+}}$ are side-reaction coefficients as defined by Ringbom [7]. In practice, R^m versus $(D_{*N})^{-1/n}$ is plotted as $y = f(x)$ according to the distribution ratios observed. An equation fitted to the curve is calculated by a least-squares error method [8] using a computer program. By comparing the coefficients in the $y = f(x)$ relationship obtained and those in Eqn. 1, the extraction constant of the metal–DTC complex, i.e., $K_{M(DTC)_m}$ can be calculated. It is worth noting that chloride-mixed metal–DTC complexes may exist in some of the extraction systems and their extraction constants, $K_{M(DTC)_{m-x}Cl_x}$, can also be determined simultaneously.

EXPERIMENTAL

Reagents

All chemicals were of analytical-reagent grade from Merck. The extractant, TlDTC, was synthe-

sized as described [6]. Subboiling redistilled water (ca. 92°C) was used throughout. All containers were washed with detergent, immersed in nitric acid in (1 + 1) overnight and then rinsed with redistilled water several times.

Specified metal ions labelled with radioisotopes

Sb^{3+} labelled with ^{124}Sb. An appropriate amount of Sb_2O_3 was irradiated in the Tsing Hua Open-Pool Reactor (THOR) with a neutron flux of ca. 2×10^{12} n cm^{-2} s^{-1}. The irradiated Sb_2O_3 was dissolved in hot concentrated HCl by heating and then diluted to 2×10^{-3} M in 1 M HCl.

Te^{4+} labelled with ^{123}Te. An appropriate amount of Te metal was irradiated in the reactor, then the irradiated metal was dissolved in concentrated HNO_3 and evaporated nearly to dryness but not baked. The evaporation was repeated after adding water by heating nearly to dryness. Finally, the white precipitate of TeO_2 was dissolved in 1 M HCl and the concentration of Te^{4+} was adjusted to 2×10^{-3} M in 0.1 M HCl.

MoO_2^{2+} labelled with ^{99}Mo. An appropriate amount of MoO_3 was irradiated in the reactor. The irradiated MoO_3 was dissolved in concentrated ammonia solution in a water-bath and evaporated to dryness. Then the solid was dissolved in concentrated HNO_3 and heated nearly to dryness. Finally, 0.1 M HCl was added to make a 2×10^{-3} M MoO_2^{2+} solution in 0.1 M HCl.

Cu^{2+} labelled with ^{64}Cu, Zn^{2+} labelled with ^{65}Zn and Cd^{2+} labelled with ^{115}Cd. An appropriate amount of Cu, Zn or Cd metal was irradiated in the reactor. The irradiated metal was dissolved in concentrated HNO_3 and then the solution was evaporated to dryness in a water-bath. Finally, the metal ion was diluted to 2×10^{-3} M in 0.1 M HCl.

Ga^{3+} labelled with ^{72}Ga. An appropriate amount of Ga_2O_3 was irradiated in the reactor, then it was dissolved in aqua regia in a water-bath and evaporated to dryness. Finally, the solid was dissolved in 0.1 M HCl and diluted to make a 2×10^{-3} M Ga^{3+} solution in 0.1 M HCl.

Se^{4+} labelled with ^{75}Se. An appropriate amount of Se metal was irradiated in the reactor, then it was dissolved in concentrated HNO_3 in a water-bath and evaporated nearly to dryness. Finally, the solid was dissolved in 1 M HCl and diluted with water to 2×10^{-3} M in 0.1 M HCl.

Substoichiometric extraction

The metal ion to be investigated for its extraction constant was mixed with a reference metal ion with a certified extraction constant. Both metal ions were adjusted to the same concentration of 1×10^{-3} M in 0.1 or 1 M HCl, and the respective radionuclides were added as tracers. Then a series of substoichiometric amounts of the extractant NaDDC, APDC or TlDTC was added to the aqueous solution followed by chloroform; both phases were of the same volume. The mixture was shaken mechanically for 2 h at 25 ± 0.1°C (amplitude 3 cm; frequency, 2 s^{-1}). The conditions for all the substiochiometric extractions were set as shown in Table 1. After standing for 30 min, aliquots of both phases were taken and their

TABLE 1

Conditions for substoichiometric extractions [a]

Metal ion to be investigated (M^{m+})		Reference metal ion (N^{n+})		Medium	Extractant
Specified ion	$\alpha_{M^{m+}}$	Specified ion	$\alpha_{N^{n+}}$		
1×10^{-3} M Te^{4+}	2.06×10^9 [14]	1×10^{-3} M Cu^{2+}	2.0076 [15]	0.1 M HCl	TlDTC
1×10^{-3} M Sb^{3+}	1.35×10^5 [9]	1×10^{-3} M Cu^{2+}	19.98 [15]	1.0 M HCl	TlDTC
1×10^{-3} M Se^{4+}	2.06×10^9 [18]	1×10^{-3} M Cd^{2+}	6.27 [16]	0.1 M HCl	TlDTC
1×10^{-3} M MoO_2^{2+}	7.29 [9]	1×10^{-3} M Cd^{2+}	6.27 [16]	0.1 M HCl	TlDTC
1×10^{-3} M Ga^{3+}	1.025 [9]	1×10^{-3} M Zn^{2+}	1.12 [17]	0.1 M KCl (plus 0.01 M HCl)	NaDDC or APDC

[a] The α values are constants which can be calculated from the overall stability constants of the metal–chloride complex in 0.1 or 1 M chloride medium. Numbers in square brackets are literature references.

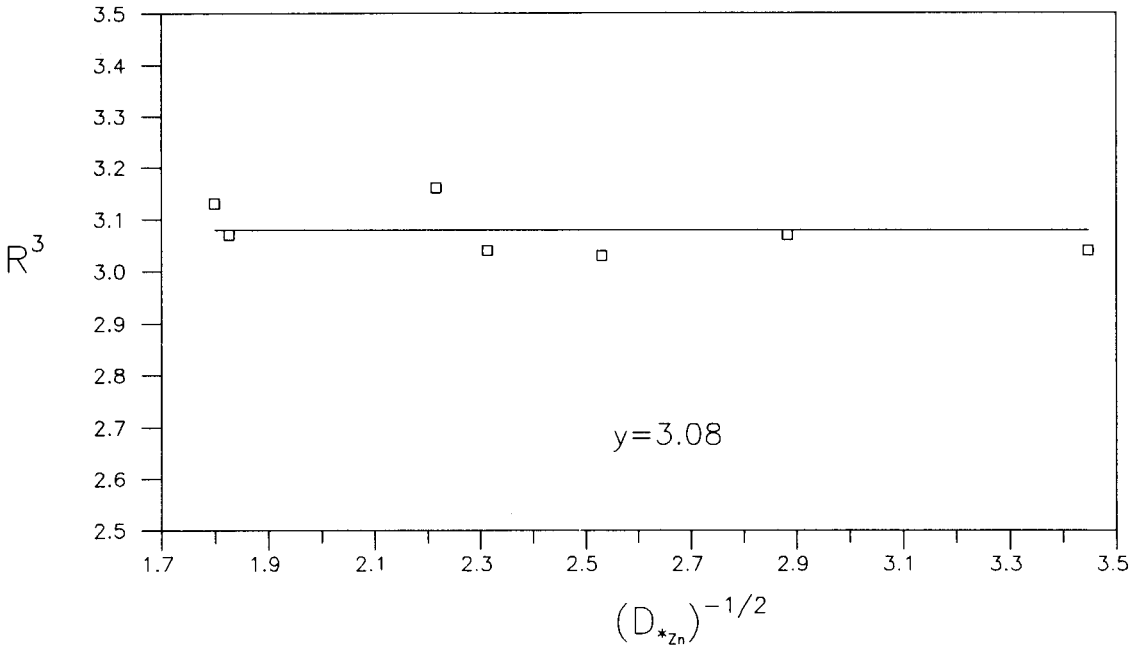

Fig. 1. Substoichiometric extraction of Ga^{3+}–Zn^{2+} pair with NaDDC.

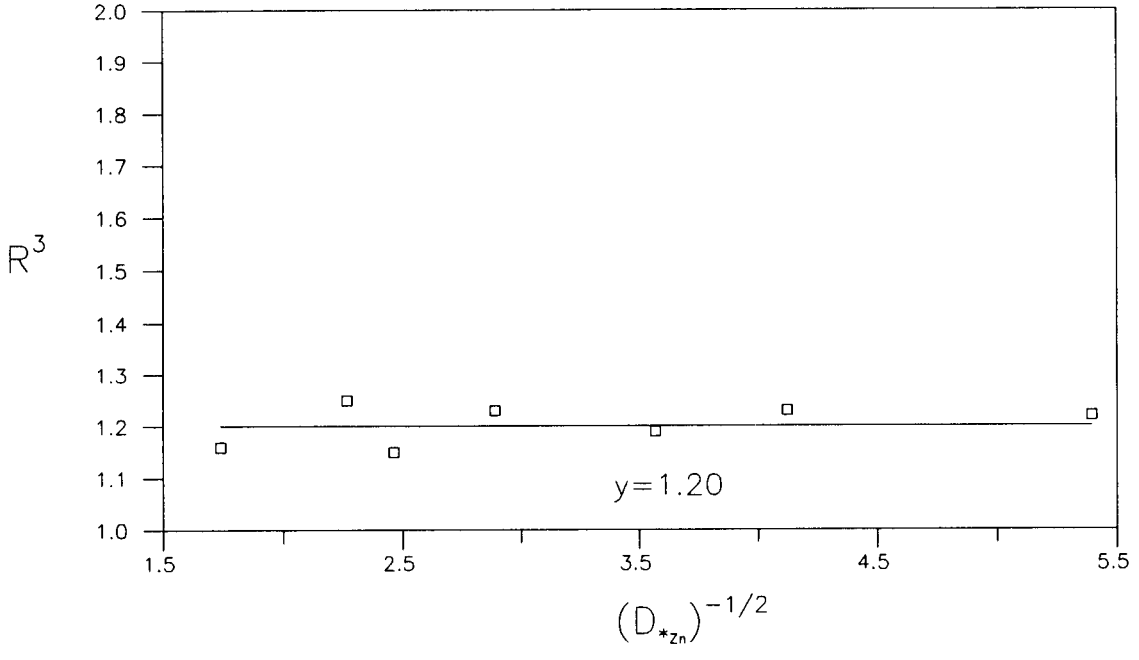

Fig. 2. Substoichiometric extraction of Ga^{3+}–Zn^{2+} pair with APDC.

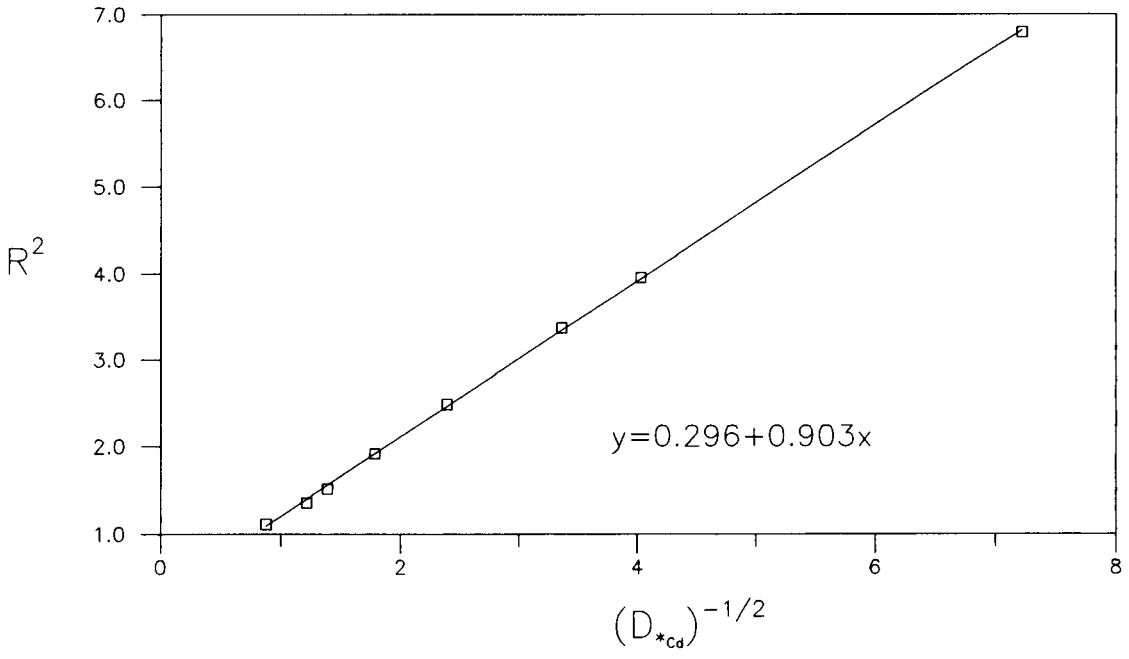

Fig. 3. Substoichiometric extraction of MoO_2^{2+}–Cd^{2+} pair with TlDDC.

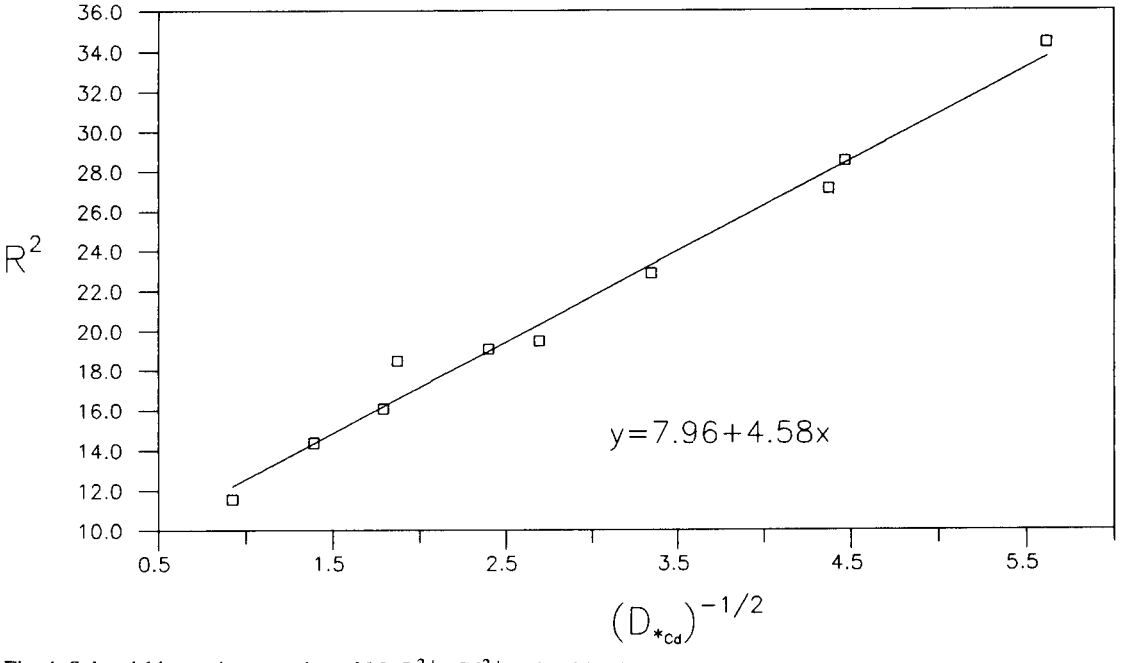

Fig. 4. Substoichiometric extraction of MoO_2^{2+}–Cd^{2+} pair with TlPDC.

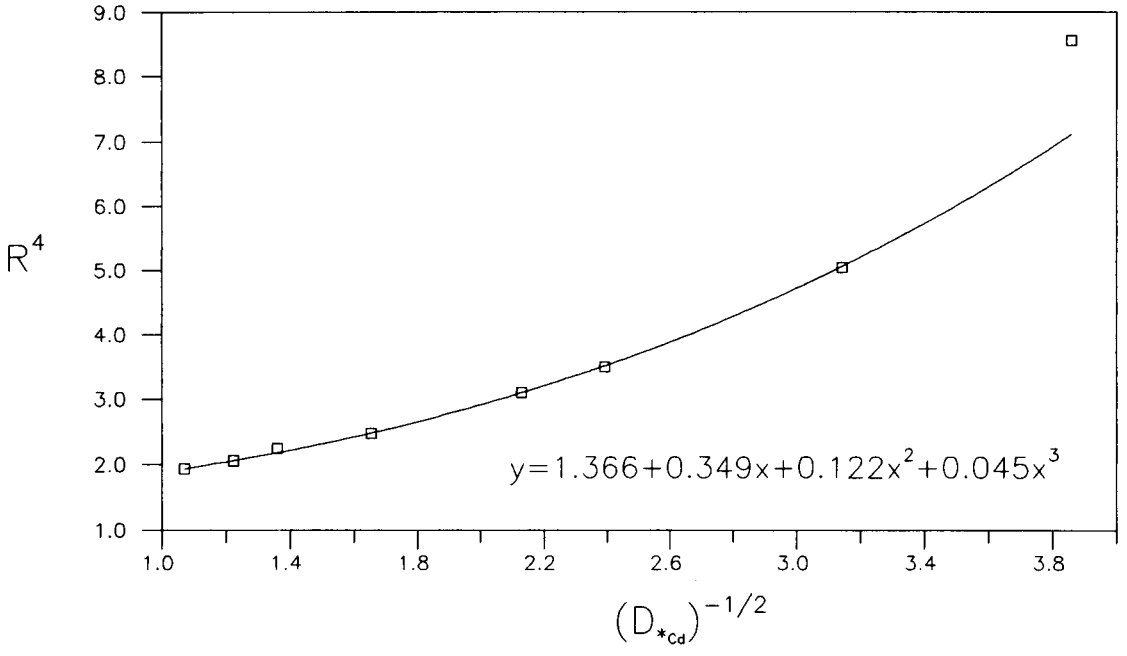

Fig. 5. Substoichiometric extraction of Se^{4+}–Cd^{2+} pair with TlDDC.

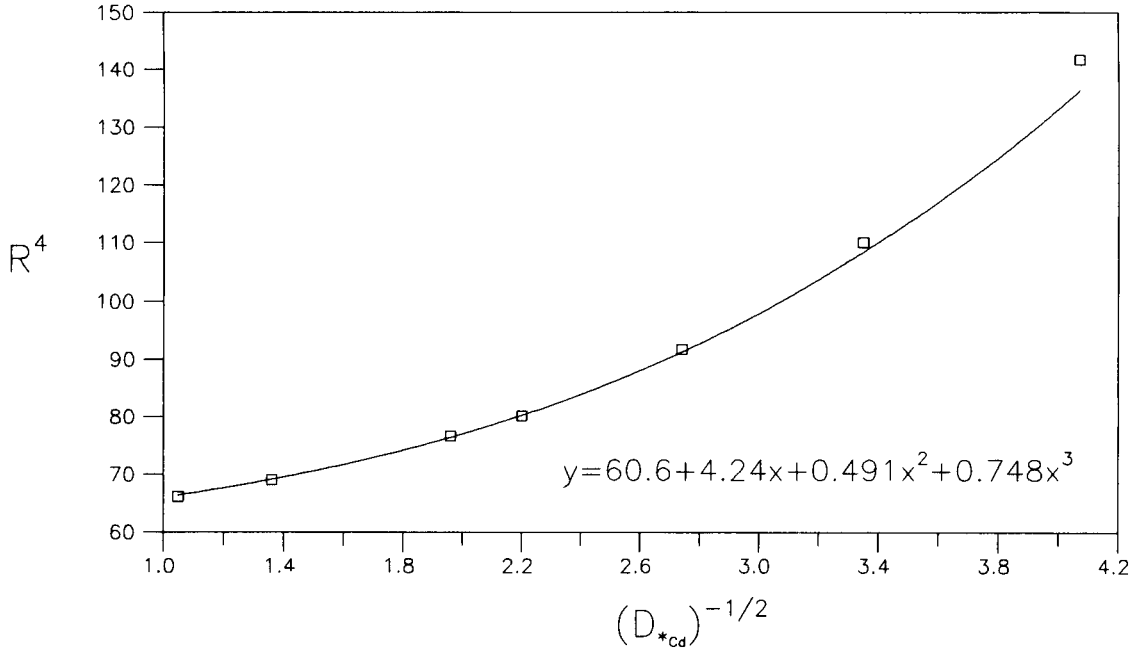

Fig. 6. Substoichiometric extraction of Se^{4+}–Cd^{2+} pair with TlPDC.

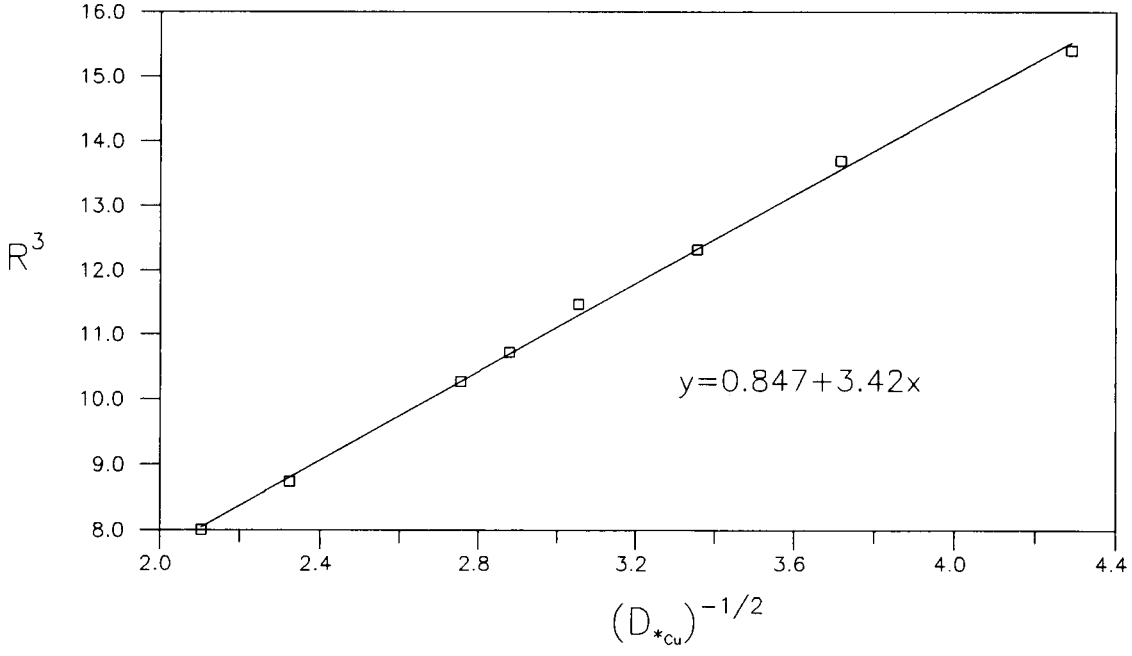

Fig. 7. Substoichiometric extraction of Sb^{3+}–Cu^{2+} pair with TlDDC.

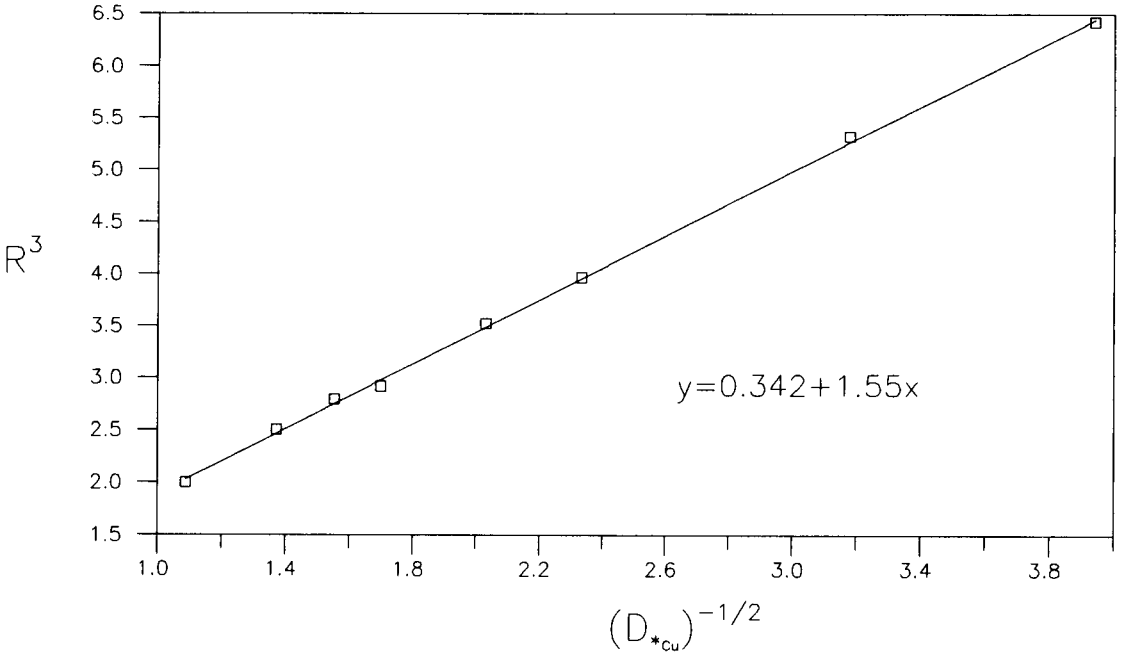

Fig. 8. Substoichiometric extraction of Sb^{3+}–Cu^{2+} pair with TlPDC.

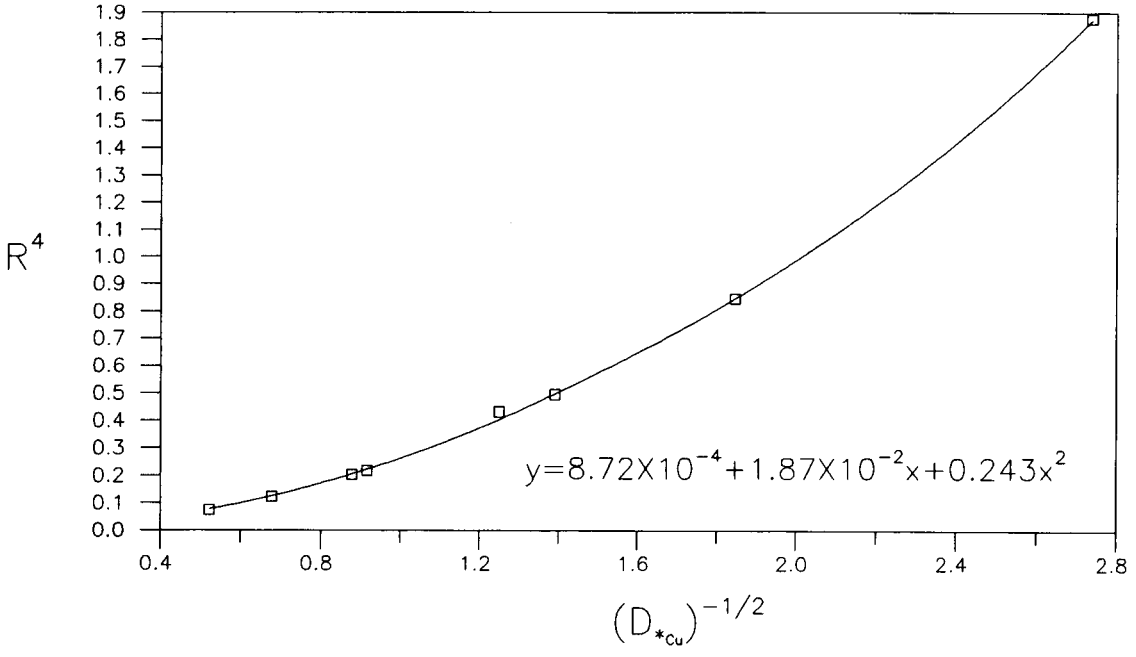

Fig. 9. Substoichiometric extraction of Te^{4+}–Cu^{2+} pair with TlDDC.

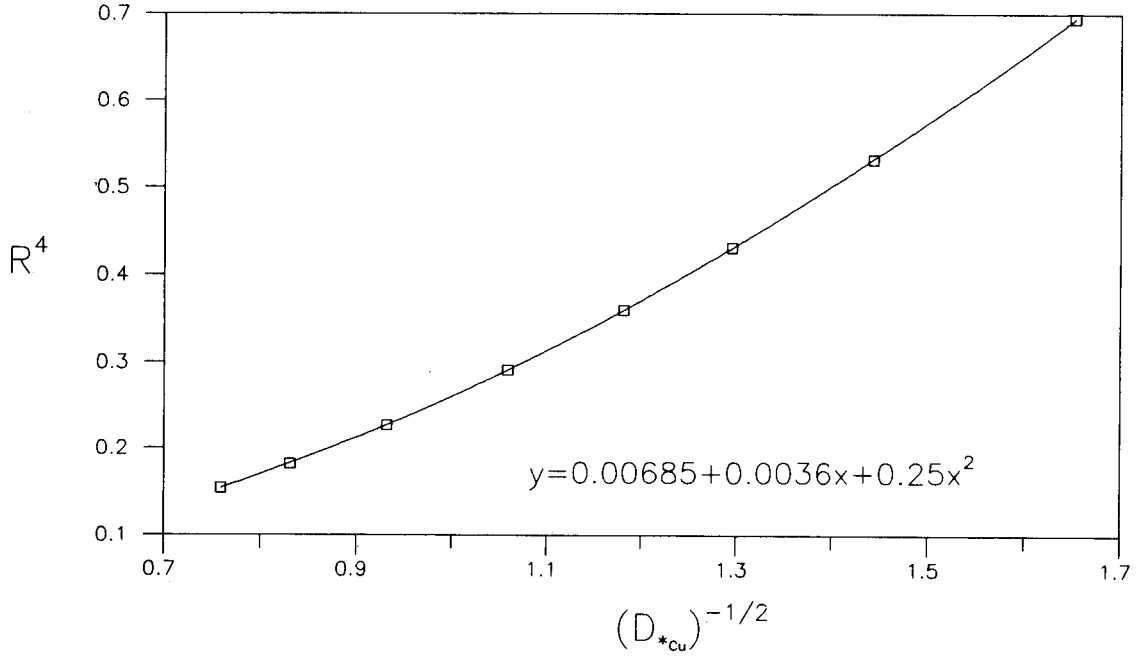

Fig. 10. Substoichiometric extraction of Te^{4+}–Cu^{2+} pair with TlPDC.

radioactivities measured in a high purity germanium detector connected with a Model 4096 multi-channel analyser.

RESULTS AND DISCUSSION

During the 1960s, the combination of the substoichiometric extraction technique with isotope dilution analysis (IDA), so-called substoichiometric IDA, was introduced, by means of which improved selectivity and accuracy could be realized [10,11]. In 1980, the substoichiometric extraction technique was used for the determination of the extraction constants of metal–DTC complexes for the first time [6]. It should be noted that the substoichiometric extraction for determining the extraction constant is different from the use in IDA. In this work, the technique is simply utilized to provide reliable distribution ratios of the

TABLE 2

Extraction constants of metal–DTC complexes and chloride–mixed metal–DTC complexes

Metal ion	Ligand	$\frac{1}{m}\log K_{M(DTC)}$	$\frac{1}{m}\log K_{M(DTC)_{m-1}Cl}$	$\frac{1}{m}\log K_{M(DTC)_{m-2}Cl_2}$	$\frac{1}{m}\log K_{M(DTC)_{m-3}Cl_3}$	Ref.
Au^{3+}	DDC		27.2	23.0		21, 22
Pd^{2+}	DDC	32.5	22.3			20
Hg^{2+}	PDC	19.4	13.6			12
	DDC	20.3	13.8			6
Ag^{+}	DDC	19.3 (18.1)				23, 24
Te^{4+}	PDC	15.0	11.6	8.5		This work
	DDC	15.1	12.1	9.3		This work
Sb^{3+}	PDC	13.2	9.5			This work
	DDC	15.0	10.7			This work
Po^{4+}	DDC	14.1				19
Bi^{3+}	PDC	12.4	8.6	5.3		12
	DDC	13.8	9.7	5.6		6
Cu^{2+}	PDC	11.9				2
	DDC	13.4				13
Ni^{2+}	DDC	12.0				24
Se^{4+}	PDC	10.3	8.4	6.5	4.9	This work
	DDC	10.7	8.9	7.1	5.3	This work
In^{3+}	PDC	8.4	5.9			12
	DDC	9.7				13
Pb^{2+}	PDC	8.1				5
	DDC	9.5				5
Cd^{2+}	PDC	8.7				12
	DDC	9.4	5.6			6
MoO_2^{2+}	PDC	8.4	5.0			This work
	DDC	9.3	5.0			This work
As^{3+}	PDC	7.1	4.9			12
	DDC	8.1	6.0			6
Ga^{3+}	PDC	6.4				This work
	DDC	8.1				This work
Zn^{2+}	PDC	6.9				5
	DDC	7.9				5
Fe^{2+}	PDC	6.3	3.5			12
	DDC	7.7				6
Tl^{+}	PDC	6.4				5
	DDC	7.2				5
Mn^{2+}	PDC	3.6				5
	DDC	7.0				5

metals in both phases, from which the extraction constant of metal–DTCs can be accurately calculated.

Figures 1–10 show the R^m vs. $(D_{*N})^{-1/n}$ plots each for the substoichiometric extraction of a pair of a certain metal ion with its extraction constant under investigation and the corresponding reference metal ion with certified extraction constants using extraction with NaDDC, APDC, TlDDC or TlPDC into chloroform. The equations of the form $y = f(x)$ fitted to the respective curves via a least-squares error method are also given. The extraction constants of the simple metal–DTC complexes and the co-existing chloride–mixed metal–DTC complexes were calculated by comparing the coefficients in the $y = f(x)$ equations with the corresponding values in Eqn. 1. All the extraction constants obtained are given in Table 2, together with the values reported in the literature. Table 2 shows clearly not only the extraction order but also the magnitude of the extraction constants for the various metal–DTC complexes.

The authors are indebted to Kuo-Shyan Lin for assistance with the computing work.

REFERENCES

1 A. Hulanicki, Talanta, 14 (1967) 1371.
2 W. Likussar and D.F. Boltz, Anal. Chem., 43 (1971) 1273.
3 W. Likussar and D.F. Boltz, Anal. Chem., 43 (1971) 1265.
4 A. Wyttenbach and S. Bajo, Anal. Chem., 47 (1975) 2.
5 L.H. Shen, S.J. Yeh and J.M. Lo, Anal. Chem., 52 (1980) 1882.
6 S.J. Yeh, J.M. Lo and L.H. Shen, Anal. Chem., 52 (1980) 528.
7 A. Ringbom, Complexation in Analytical Chemistry, Interscience, New York, 1963.
8 G.R. Gilmore, J. Radioanal. Chem., 48 (1979) 91.
9 L.G. Sillen and A.E. Martell, Stability Constants of Metal-Ion Complexes, Part I, Chemical Society, London, 1964.
10 N. Suzuki and K. Kudo, Anal. Chim. Acta, 32 (1965) 456.
11 J. Ruzicka and J. Stary, Talanta, 10 (1963) 287.
12 J.M. Lo, L.H. Shen and S.J. Yeh, J. Radioanal. Nucl. Chem. Articles, 88 (1985) 313.
13 L.H. Shen, MS Thesis, National Tsing Hua University, Hsinchu, Taiwan, 1978.
14 L.G. Sillen, Stability Constants, Supplement No. 1, Chemical Society, London, 1971.
15 D.F.C. Morris and E.L. Short, J. Chem. Soc. (1962) 2672.
16 P. Kivalo and R. Luoto, Suom. Kemistil. B, 30 (1957) 163.
17 D. Dryssen and M. De Jesus Tavares, in D. Dryssen, J.-O. Liljenzin and J. Rydberg (Eds.), Solvent Extraction Chemistry, North Holland, Amsterdam, 1967, p. 465.
18 Y.M. Chang, MS Thesis, National Tsing Hua University, Hsinchu, Taiwan, 1982.
19 J.M. Lo and C.M. Wai, Anal. Chim. Acta, 148 (1983) 327.
20 G.B. Briscoe and S. Humphries, Talanta, 16 (1969) 1403.
21 J.M. Lo, C.L. Tseng and S.J. Yeh, Anal. Chim. Acta. 126 (1981) 191.
22 H. Chermette, J. Colonat and J. Tousset, Anal. Chim. Acta, 88 (1977) 331.
23 E. Still, Fin. Kemistsamf. Medd., 73 (1964) 90.
24 J. Stary and K. Kratzer, Anal. Chim. Acta, 40 (1968) 93.

PUBLICATION SCHEDULE FOR 1993

	S'92	O'92	N'92	D'92	J	F	M	A	M
Analytica Chimica Acta	267/1 267/2	268/1 268/2	269/1 269/2	270/1 270/2	271/1 271/2	272/1 272/2 273/1–2	274/1 274/2	275/1 275/2	276/1 276/2
Vibrational Spectroscopy		4/1			4/2		4/3		

INFORMATION FOR AUTHORS

Manuscripts. The language of the journal is English. English linguistic improvement is provided as part of the normal editorial processing. Authors should submit three copies of the manuscript in clear double-spaced typing on one side of the paper only. *Vibrational Spectroscopy* also accepts papers in English only.

Abstract. All papers and reviews begin with an Abstract (50–250 words) which should comprise a factual account of the contents of the paper, with emphasis on new information.

Figures. Figures should be prepared in black waterproof drawing ink on drawing or tracing paper of the same size as that on which the manuscript is typed. One original (or sharp glossy print) and two photostat (or other) copies are required. Attention should be given to line thickness, lettering (which should be kept to a minimum) and spacing on axes of graphs, to ensure suitability for reduction in size on printing. Axes of a graph should be clearly labelled, along the axes, outside the graph itself. All figures should be numbered with Arabic numerals, and require descriptive legends which should be typed on a separate sheet of paper. Simple straight-line graphs are not acceptable, because they can readily be described in the text by means of an equation or a sentence. Claims of linearity should be supported by regression data that include slope, intercept, standard deviations of the slope and intercept, standard error and the number of data points; correlation coefficients are optional.

Photographs should be glossy prints and be as rich in contrast as possible; colour photographs cannot be accepted. Line diagrams are generally preferred to photographs of equipment.

Computer outputs for reproduction as figures must be good quality on blank paper, and should preferably be submitted as glossy prints.

Nomenclature, abbreviations and symbols. In general, the recommendations of the International Union of Pure and Applied Chemistry (IUPAC) should be followed, and attention should be given to the recommendations of the Analytical Chemistry Division in the journal *Pure and Applied Chemistry* (see also *IUPAC Compendium of Analytical Nomenclature, Definitive Rules*, 1987).

References. The references should be collected at the end of the paper, numbered in the order of their appearance in the text (*not* alphabetically) and typed on a separate sheet.

Reprints. Fifty reprints will be supplied free of charge. Additional reprints (minimum 100) can be ordered. An order form containing price quotations will be sent to the authors together with the proofs of their article.

Papers dealing with vibrational spectroscopy should be sent to: Dr J.G. Grasselli, 150 Greentree Road, Chagrin Falls, OH 44022, U.S.A. Telefax: (+1-216) 2473360 (Americas, Canada, Australia and New Zealand) or Dr J.H. van der Maas, Department of Analytical Molecule Spectrometry, Faculty of Chemistry, University of Utrecht, P.O. Box 80083, 3508 TB Utrecht, The Netherlands. Telefax: (+31-30) 518219 (all other countries).

0003-2670/93/$06.00

This issue is printed on acid-free paper.

PRINTED IN THE NETHERLANDS

Capillary Electrophoresis

Principles, Practice and Applications

by **S.F.Y. Li**, *National University of Singapore, Singapore*

Journal of Chromatography Library Volume 52

Capillary Electrophoresis (CE) has had a very significant impact on the field of analytical chemistry in recent years as the technique is capable of very high resolution separations, requiring only small amounts of samples and reagents. Furthermore, it can be readily adapted to automatic sample handling and real time data processing. Many new methodologies based on CE have been reported. Rapid, reproducible separations of extremely small amounts of chemicals and biochemicals, including peptides, proteins, nucleotides, DNA, enantiomers, carbohydrates, vitamins, inorganic ions, pharmaceuticals and environmental pollutants have been demonstrated. A wide range of applications have been developed in greatly diverse fields, such as chemical, biotechnological, environmental and pharmaceutical analysis.

This book covers all aspects of CE, from the principles and technical aspects to the most important applications. It is intended to meet the growing need for a thorough and balanced treatment of CE. The book will serve as a comprehensive reference work and can also be used as a textbook for advanced undergraduate and graduate courses. Both the experienced analyst and the newcomer will find the text useful.

Contents:

1. Introduction. Historical Background. Overview of High Performance CE. Principles of Separations. Comparison with Other Separation Techniques. **2. Sample Injection Methods.** Introduction. Electrokinetic Injection. Hydrodynamic Injection. Electric Sample Splitter. Split Flow Syringe Injection System. Rotary Type Injector. Freeze Plug Injection. Sampling Device with Feeder. Microinjectors. Optical Gating. **3. Detection Techniques.** Introduction. UV-Visible Absorbance Detectors. Photodiode Array Detectors. Fluorescence Detectors. Laser-based Thermooptical and Refractive Index Detectors. Indirect Detection. Conductivity Detection. Electrochemical Detection. Mass Spectrometric Detection. **4. Column Technology.** Uncoated Capillary Columns. Coated Columns. Gel-filled Columns. Packed Columns. Combining Packed and Open-Tubular Column. **5. Electrophoretic Media.** Electrophoretic Buffer Systems. Micellar Electrokinetic Capillary Chromatography. Inclusion Pseudophases. Metal-complexing Pseudophases. Other Types of Electrophoretic Media. **6. Special Systems and Methods.** Buffer Programming. Fraction Collection. Hyphenated Techniques. Field Effect Electroosmosis. Systematic Optimization of Separation. **7. Applications of CE.** Biomolecules. Pharmaceutical and Clinical Analysis. Inorganic Ions. Hydrocarbons. Foods and Drinks. Environmental Pollutants. Carbohydrates. Toxins. Polymers and Particles. Natural Products. Fuel. Metal Chelates. Industrial Waste Water. Explosives. Miscellaneous Applications. **8. Recent Advances and Prospect for Growth.** Recent Reviews in CE. Advances in Injection Techniques. Novel Detection Techniques. Advances in Column Technology. Progress on Electrolyte Systems. New Systems and Methods. Additional Applications Based on CE. Future Trends. **References. Index.**

1992 xxvi + 586 pages
Price: US$ 247.00 / Dfl. 395.00
ISBN 0-444-89433-0

"Everything seems to be there, any detection system you have ever dreamed of, any capillary coating, enough electrolyte systems to saturate your wits, and more..."
"...by far the most thorough and comprehensive book in the field yet to appear."
P.G. Righetti, Milan

ORDER INFORMATION

For USA and Canada
ELSEVIER SCIENCE PUBLISHERS
Judy Weislogel
P.O. Box 945
Madison Square Station,
New York, NY 10160-0757
Tel: (212) 989 5800
Fax: (212) 633 3880

In all other countries
ELSEVIER SCIENCE PUBLISHERS
P.O. Box 211
1000 AE Amsterdam
The Netherlands
Tel: (+31-20) 5803 753
Fax: (+31-20) 5803 705

US$ prices are valid only for the USA & Canada and are subject to exchange rate fluctuations; in all other countries the Dutch guilder

ELSEVIER
SCIENCE PUBLISHERS